Unified Zero-Current-Transition Techniques for High-Power Three-Phase PWM Inverters

Yong Li

Dissertation submitted to the faculty of the
Virginia Polytechnic Institute and State University
in partial fulfillment of the requirements for the degree of

Doctor of Philosophy
in
Electrical Engineering

Fred C. Lee, Chairman
Dushan Boroyevich
Jason J. Lai
Dan Chen
Guo-Quan Lu

March 29, 2002
Blacksburg, Virginia

Key words: Soft switching, zero-current transition, three-phase PWM inverters, motor drives

Copyright 2002, Yong Li

Unified Zero-Current-Transition Techniques for High-Power Three-Phase PWM Inverters

Yong Li

(ABSTRACT)

This dissertation is devoted to a unified and comprehensive study of zero-current-transition (ZCT) soft-switching techniques for high-power three-phase PWM inverter applications. Major efforts in this study are as follows: 1) Conception of one new ZCT scheme and one new ZCT topology; 2) Systematic comparison of a family of ZCT inverters; 3) Design, implementation and experimental evaluation of two 55-kW prototype inverters for electric vehicle (EV) motor drives that are developed based on the proposed ZCT concepts; and 4) Investigation of the ZCT concepts in megawatts high-frequency power conversions. The proposed ZCT techniques are also applicable to three-phase power-factor-correction (PFC) rectifier applications.

In order to minimize switching losses, this work first proposes a new control scheme for an existing three-phase ZCT inverter circuit that uses six auxiliary switches. The proposed scheme, called the six-switch ZV/ZCT, enables all main switches, diodes and auxiliary switches to be turned off under zero-current conditions, and in the meantime provides an opportunity to achieve zero-voltage turn-on for the main switches. Meanwhile, it requires no modification to normal PWM algorithms. Compared with existing ZCT schemes, the diode reverse-recovery current is reduced significantly, the switching turn-on loss is reduced by 50%, the resonant capacitor voltage stress is reduced by 30%, and the current and thermal stresses in the auxiliary switches are evenly distributed.

However, a big drawback of the six-switch ZV/ZCT topology, as well as of other types of soft-switching topologies using six auxiliary switches, is the high cost and large space associated with the auxiliary switches. To overcome this drawback, this work further proposes a new three-phase ZCT inverter topology that uses only three auxiliary switches— the three-switch ZCT. The significance of the proposed three-switch ZCT topology is that, among three-phase soft-switching inverters developed so far, this is the only one that uses *fewer* than six auxiliary switches and still has the following three features: 1) soft commutation for all main switches, diodes and auxiliary switches in all operation modes; 2) no modification to normal PWM

algorithms; and 3) in practical implementations, no need for extra resonant current sensing, saturable cores, or snubbers to protect the auxiliary switches.

The proposed six-switch ZV/ZCT and three-switch ZCT inverters, together with existing ZCT inverters, constitute a family of three-phase ZCT inverters. To explore the fundamental properties of these inverters, a systematic comparative study is conducted. A simplified equivalent circuit is developed to unify common traits of ZCT commutations. With the visual aid of state planes, the evolution of the family of ZCT inverters is examined, and their differences and connections are identified. Behaviors of individual inverters, including switching conditions, circulating energy, and device/component stresses, are compared.

Based on the proposed six-switch ZV/ZCT and three-switch ZCT techniques, two 55-kW prototype inverters for EV traction motor drives have been built and tested to the full-power level with a closed-loop controlled induction motor dynamometer. The desired ZCT soft-switching features are realized together with motor drive functions. A research effort is carried out to develop a systematic and practical design methodology for the ZCT inverters, and an experimental evaluation of the ZCT techniques in the EV motor drive application is conducted. The design approach integrates system optimization with characterizations of the main IGBT device under the ZCT conditions, selection, testing and characterization of the auxiliary devices, design and selection of the resonant inductors and capacitors, inverter loss modeling and numerical analysis, system-level operation aspects, and layout and parasitic considerations. Different design aspects between these two ZCT inverters are compared and elaborated. The complexity of the 55-kW prototype implementations is compared as well. Efficiencies are measured and compared under a group of torque/speed points for typical EV drive cycles.

Megawatts high-frequency power conversion is another potential application of the ZCT techniques. The integrated gate commutated thyristor (IGCT) device is tested and characterized under the proposed six-switch ZV/ZCT condition, and the test shows promising results in reducing switching losses and stresses. Improvements in the IGCT switching frequency and simplification of the cooling requirements under ZCT operations are discussed. In addition, a generalized ZCT cell concept is developed based on the proposed three-switch ZCT topology. This concept leads to the discovery of a family of simplified multilevel soft-switching inverters that reduce the number of auxiliary switches by half, and still maintain desirable features.

To my wife Hong-Yan

Acknowledgements

I would like to acknowledge my great debt to my advisor, Dr. Fred C. Lee, for providing me the invaluable opportunity to study in CPES of Virginia Tech, and for his guidance, encouragement and support during my studies. His profound knowledge, creating thinking and consistent encouragement have been the source of inspiration through the course of this work.

I wish to express my sincere gratitude to my professors, Dr. Dushan Boroyevich and Dr. Jason Lai, for their precious guidance and advice on my research and studies.

I am grateful to my committee members, Dr. Dan Chen and Dr. Guo-Quan Lu, for their contributions to this work.

I would like to thank my fellow CPES students and scholar who are involved in the PNGV (Partnership for a New Generations of Vehicles) project, including Mr. Huijie Yu, Mr. Mao Ye, Dr. Jae-Young Choi, Mr. Wei Dong, Mr. Matthew Turner, Mr. Michael Pochet, Mr. Jerry Francis, Mr. Dimos Katsis, and Dr. Xiaochuan Jia, for their useful discussions during the course of the research and help in the inverter hardware fabrication and testing.

I would like to convey my thanks to Mr. Kevin Motto for his interests in applying the ZCT concepts in the IGCT device and for his co-work in testing the IGCT device under the ZCT conditions, to Dr. Wei Chen for his discussions on the design of resonant inductors, to Dr. Johan Strydom for his discussions on the loss calculation of the resonant inductors, to Mr. Yuming Bai for his discussions on the characteristics of IGBT devices, and to Dr. Zhenxian Liang for his help in packaging the auxiliary devices of the three-switch ZCT inverter. Thanks also to Dr. Hengchun Mao for his discussions on ZCT techniques.

I cherish the experience of studying, working and playing together with my friendly colleagues in CPES, including Dr. Yuxin Li, Mr. Changrong Liu, Mr. Qun Zhao, Mr. Zhenxue Xu, Mr. Dengming Peng, Ms. Xiaoyan Wang, Mr. Jianwen Shao, Dr. Fengfeng Tao, Dr. Sam Ye, Mr. Peter Barbosa, Mr. Francisco Canales, Dr. Dong-Ho Lee, Mr. Jia Wu, Mr. Xiukuan Jing, Mr. Yongxuan Hu, Mr. Kaiwei Yao, Mr. Peng Xu, and Mr. Josep Pou. I am indebted to CPES staffs, Ms. Teresa Shaw, Ms. Linda Gallagher, Ms. Trish Rose, Ms. Elizabeth Tranter, Ms. Leslie Farmer, Mr. Steve Chen, Ms. Marianne Hawthorne, Mr. Robert Martin, Mr. Joseph Price-O'Brien, and Ms. Ann Craig, for their assistance and cooperation. I also thank CPES editor, Ms.

Amy Shea, for her efforts in editing the manuscripts of this dissertation as well as some of my publications.

Deep in my heart is my love to my grandmother Mu Tian-Lu, who brought me up and gave me unconditional love. My appreciations are due to my parents, Li Ze-Quan and Huang Shang-Xu, whose everlasting encouragement and love have accompanied me through my entire course of study. I also wish to thank my younger brother, Li Peng, for the good and bad moments we shared together.

Last but not least, I would like to thank my wife *Hong-Yan*, for her love, understanding and support. Without her sacrifice and hard work, especially during the past half year since our daughter *Ying-Nan* was born, this dissertation would not have been possible. I hope this achievement can be a relief to my family, and I can spend more time to play with my little *Ying-Nan.*

This work is supported by General Motors, DaimlerChrysler, Ford, and the U.S. Army under the PNGV program, and by Office of Naval Research under the EMALS/EARS program. This work made use of ERC Shared Facilities supported by the National Science Foundation under Award Number EEC-9731677.

TABLE OF CONTENTS

LIST OF ILLUSTRATIONS

LIST OF TABLES

Chapter 1
Introduction

1.1. Background

Three-phase pulse-width-modulation (PWM) inverters are widely used in motor drives, uninterruptible power supplies (UPSs), and utility interfaces. In order to achieve high performance and high power density, higher switching frequency is desired, because it greatly affects the control bandwidths and system ripples and determines the size of passive components. For this reason, in power supplies and utility applications, the inverters are normally designed with the highest achievable switching frequency. In motor drive applications, such as electric vehicle (EV) traction drives, higher switching frequencies can reduce the acoustic noises as well as torque and speed ripples. Moreover, in modern advanced megawatts power conversion systems, such as Electromagnetic Aircraft Launch Systems (EMALS), in which the fundamental limits of high-power semiconductor devices are being reached, high switching frequencies and small system ripples are the mandatory design requirements [D1].

However, the high-switching-frequency operation of three-phase PWM inverters is thermally limited by the switching losses of the power devices; the current handling capability of the devices, which also affects the inverter power density, is electrically limited by the dynamic switching stresses of the devices at turn-on and turn-off transitions. The purpose of soft-switching techniques is to decease or eliminate the overlap between voltage and current prior to switching transitions. The use of soft switching can alleviate some of the problems associated with the non-ideal switching characteristics of the devices, and can provide an effective means for increasing switching frequencies with reduced switching losses and stresses.

Soft switching is accomplished through the assistance of auxiliary circuits, which consist of resonant components and auxiliary switches that trigger the resonance. There are three major expectations for a three-phase soft-switching inverter. First, the overall system switching losses should be reduced, which requires soft commutation for all main switches, diodes, and auxiliary switches in all operation modes. Secondly, the soft-switching topology should not cause compromise to the inverter control performance. For this reason, piggyback, which means that the implementation of soft switching requires no modification to normal PWM algorithms developed for hard-switching inverters, is a desirable architecture for soft-switching topologies. Since for decades researchers have accumulated knowledge based on hard-switching topologies, the piggyback architecture can offer such advantages as compatibility with well-proven control techniques, short design cycles, and easy acceptance by industry. Thirdly, the auxiliary circuits should be simple and low-cost, in particular with minimum numbers of auxiliary switches. Besides these three expectations, which mainly deal with topologies and controls, practical issues in high-power soft-switching inverters must also be considered. The practical issues include systematic design methodologies to optimize soft-switching performance and evaluations of the advantages and limitations of soft-switching inverters for particular applications using state-of-the-art devices and components.

In recent years, various soft-switching techniques have been developed. As can been seen in Figure 1.1, according to the placement of auxiliary circuitry, three-phase voltage-source soft-switching inverters can be classified into two categories: DC-side topologies and AC-side topologies [F1]. In the DC-side topologies [B1]-[B18], dominant techniques are the resonant DC-link and quasi-resonant DC-link inverters, which normally use fewer than six auxiliary switches. In the AC-side topologies [C1]-[C21], there are basically two techniques, zero-voltage

transition (ZVT) and zero-current transition (ZCT). For the ZVT inverters, topologies with six auxiliary switches and topologies with fewer than six auxiliary switches have been developed; for existing ZCT inverters, six auxiliary switches are required.

The basic concept of ZCT is as follows: During a switching transition, the current flowing through the outgoing device is forced to reduce to zero prior to the turn-off of this device; when the switching transition is over, normal PWM operation resumes. This dissertation is devoted to a unified and comprehensive study of the ZCT technique in high-power three-phase PWM inverter applications. In order to establish the motivation and objectives for this work, existing soft-switching inverter techniques will be briefly reviewed in the following section, and then the outline of the dissertation will be provided.

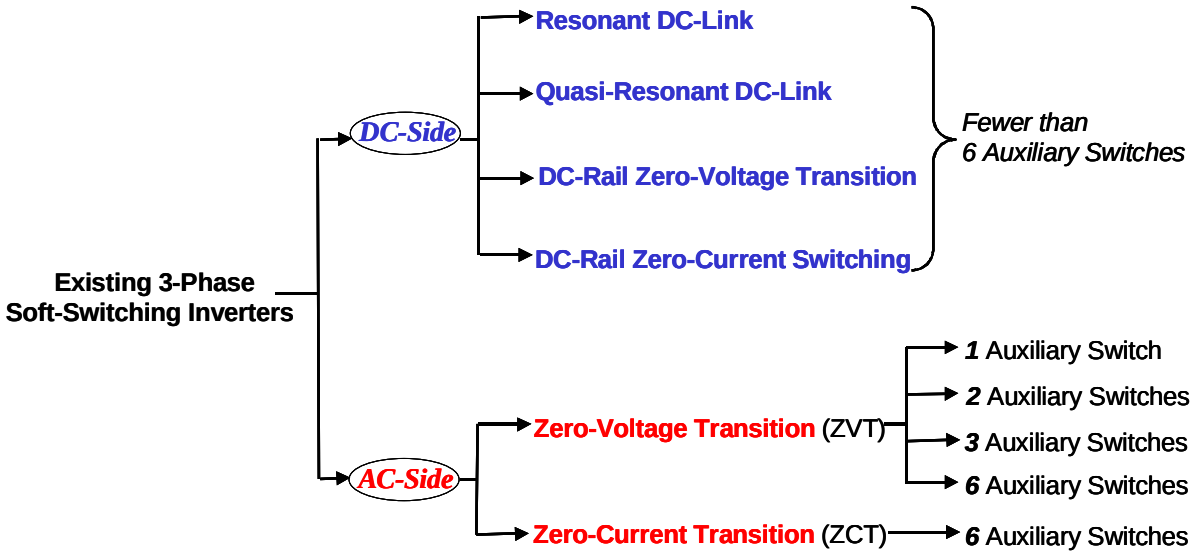

Figure 1.1. Existing three-phase soft-switching inverters.

1.2. Review of Existing Three-Phase Soft-Switching Inverters

1.2.1. DC-Side Soft-Switching Inverters

In a DC-side soft-switching inverter, an auxiliary circuit, which normally uses fewer than six auxiliary switches, is inserted between the input DC power supply and the main bridges in order to achieve soft switching for the main bridges. The DC-side soft-switching topologies are classified into four groups: resonant DC-link inverters [B1]-[B10], quasi-resonant DC-link inverters [B11]-[B15], DC-rail ZVT inverters [B16] [B17], and DC-rail zero-current-switching inverters [B18].

1.2.1.1. The Resonant DC-Link (RDCL) Inverters

Many problems with conventional hard-switching inverters are due to the stiff DC bus, so a lot of research has focused on making the DC bus "softer" at switching transitions. For this purpose, the RDCL inverter was proposed to provide a zero bus voltage condition at every resonant cycle in order to allow zero-voltage turn-on of the main switches. The original RDCL inverter proposed by Divan [B1] does not use auxiliary switches, and it imposes substantial voltage stress (> 2.5 times the DC bus voltage V_{dc}) across the devices. This high voltage can be clamped to 1.3~1.4 times V_{dc} using one auxiliary switch, as shown in Figure 1.2, but the added components result in cost and reliability penalties [B2]. Instead of using PWM control, the RDCL inverters have to use discrete pulse modulation (DPM), which normally causes undesirable sub-harmonic oscillations [B3]. Some techniques tried to provide PWM control for the RDCL inverters [B4], but the PWM range is very limited. Moreover, testing results show that it is difficult to maintain correct DC bus resonance under heavy load conditions [F7].

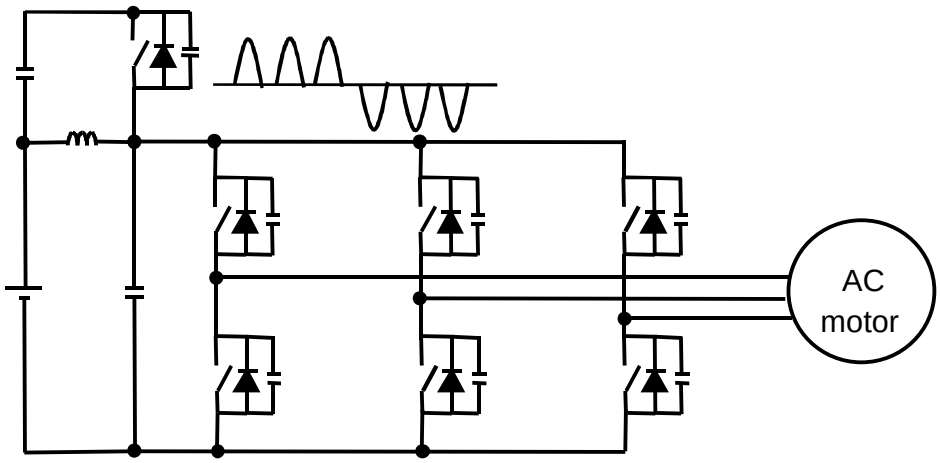

Figure 1.2. The resonant DC-link (RDCL) inverter [B2].

Several improved versions were proposed to overcome the drawbacks of the RDCL inverters and to provide PWM control, using either one auxiliary switch [B5]-[B7] or two auxiliary switches [B8] [B9]. There are various names for these improved versions in literatures, yet they all put a series resonant inductor in the DC rail; thus, in this dissertation, they are grouped into the RDCL inverter category. These improved topologies still suffer from overvoltage and reliability problems. Although they are capable of PWM control in some situations, they have been found to not be fully compatible with true PWM due to a minimum dwell time created by the clamping mode in the inverter operation mode [B10]. Individually, the coupled inductor in the passive clamped topology proposed by Chen [B6] is bulky and difficult to design. In the DC-voltage-notch inverter proposed by Ageligis [B7], the clamp switch is turned on and off under hard-switching conditions, and the zero-voltage switching might be lost during transients. The DC-voltage-notch inverter proposed by Lai [B8] needs an initialization circuit to control the initial inductor current, which increases the complexity. The auxiliary switches in the topology proposed by Salama [B9] are turned off with high current, which results in enormously high losses in the auxiliary circuit.

1.2.1.2. The Quasi-Resonant DC-Link (QRDCL) Inverters

In order to avoid the high voltage stress and to enable PWM control, several QRDCL topologies were proposed, which are also referred to as parallel resonant DC-link (PRDCL) inverters [B11]. Unlike the RDCL inverters, the way to implement the auxiliary circuit in the QRDCL inverters is to put an auxiliary switch in the DC rail and a controlled resonant branch in parallel with the main bridge circuit, as shown in Figure 1.3. During normal operations, the DC-rail switch passes input power directly to the main bridge. During switching transitions, the DC-rail switch separates the main bridge from the input power, and the resonant branch can provide soft-switching conditions in a resonant manner. However, normal PWM schemes usually need to be modified in order to synchronize the switching actions of the main switches, which typically causes additional switching events in the main switches, and increases the ripple of output current. The DC-rail switch has to conduct the full load current of the inverter, and is turned off under a hard-switching condition with high current in every switching cycle. As a consequence, the conduction loss and switching loss in the auxiliary switch are much higher than those of the main switches.

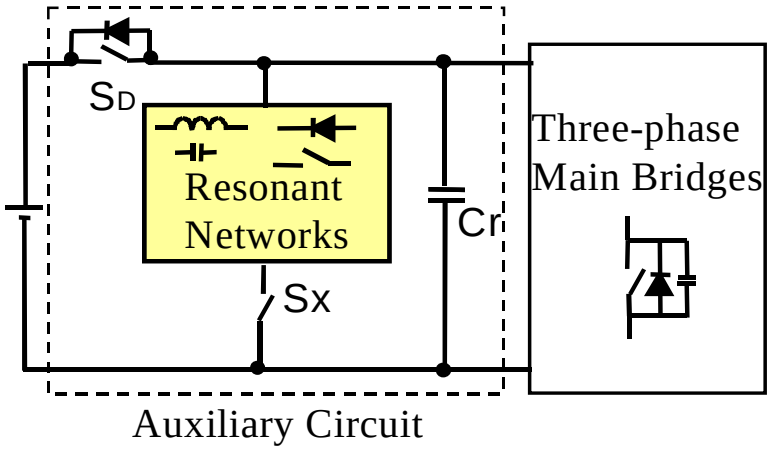

Figure 1.3. A concept diagram of the family of quasi-resonant DC-link (QRDCL) inverters.

The auxiliary circuits in QRDCL inverters normally are complicated. The PRDCL topology proposed by He [B11] uses four auxiliary switches. These switches are turned off with high current, and one of them must withstand a high voltage stress. Another slightly simplified PRDCL topology proposed by Cho [B12] requires three auxiliary switches. Derived from the auxiliary resonant commutation pole (ARCP) inverter [C1] [C2], the auxiliary QRDCL inverter proposed by DeDoncker [B13] uses three auxiliary switches. In addition to the drawbacks common to QRDCL topologies, this auxiliary QRDCL inverter has a charge balance problem in the split DC bus capacitors. The QRDCL proposed by Malesani [B14] uses two auxiliary switches, but the control timing is complex and difficult to adjust for a wide operation range. The QRDCL proposed by Chen [B15] also uses two auxiliary switches, but the coupled inductor used in the auxiliary circuit is bulky and can cause high magnetic loss.

1.2.1.3. The DC-Rail ZVT Inverters

The three-phase DC-rail ZVT inverters proposed by Wang [B16] adopt the ZVT concept that was originally developed by Hua for DC/DC converters [A1] [A2] [A8]. In theory, as shown in Figure 1.4, two auxiliary switches are needed. However, one is in series with the DC rail, causing high conduction loss; the other is turned off at high current. Consequently, the implementation of the auxiliary switches is complicated—three MOSFETs in parallel with an IGBT as the DC-rail switch, and three MOSFETs in parallel as the other auxiliary switch. Another version of the DC-rail ZVT topologies is the ZVT boost rectifier proposed by Jiang [B17], in which the DC-rail switch is changed into a diode. Because the negative DC-link current is blocked by the diode, the bi-directional power flow is impossible. Thus, this ZVT boost circuit can not be used for inverters.

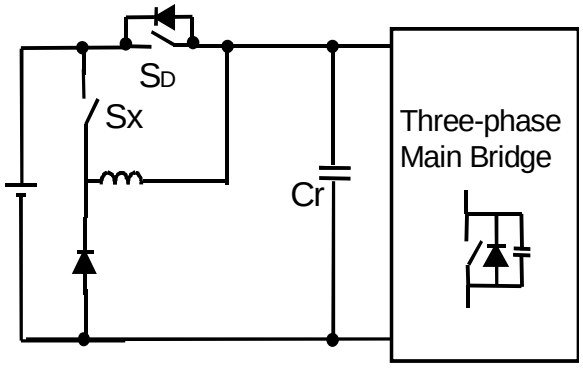

Figure 1.4. The DC-rail ZVT inverter [B16].

1.2.1.4. The DC-Rail Zero-Current-Switching Inverter

The zero-current-switching topology proposed by Tomasin [B18] uses two auxiliary switches to reduce the main switch turn-off loss, as shown in Figure 1.5. It requires synchronized turn-off for the main switches, which generally causes more switching actions than those resulting from conventional space-vector modulation (SVM) schemes. In addition, because the auxiliary switches are placed in series with the DC link and are turned off with high current, high conduction loss and turn-off loss are caused. Furthermore, a resonant inductor is connected in series with each main switch, and therefore can cause excessively high voltage stress if for any reason the zero-current turn-off is not achieved.

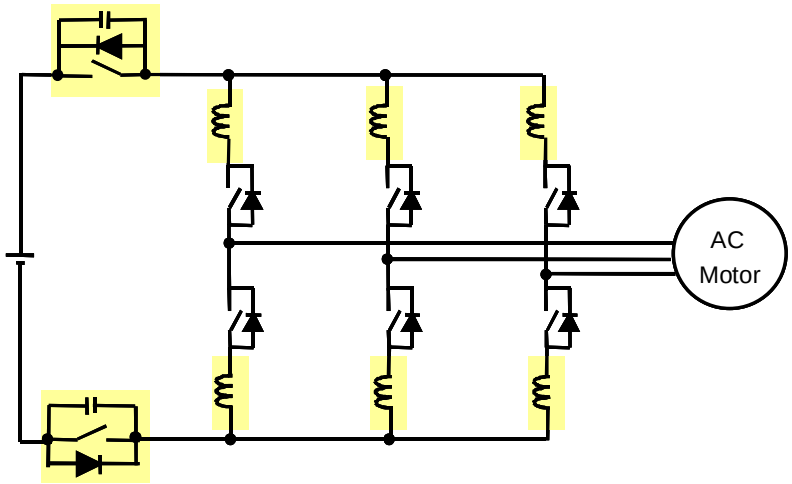

Figure 1.5. The DC-rail zero-current-switching inverter using two auxiliary switches [B18].

1.2.2. AC-Side Soft-Switching Inverters

In high-power applications, it is preferable to place the auxiliary circuit on the AC side of the main bridges. With the auxiliary circuit out of the main power path, the conduction loss can be reduced. The AC-side soft-switching inverters can be grouped as either ZVT or ZCT topologies. The ZVT inverters consist of topologies using six and fewer auxiliary switches, and the existing ZCT inverters use six auxiliary switches.

1.2.2.1. AC-Side ZVT Inverters Using Six Auxiliary Switches

The ARCP inverter proposed by McMurray [C1] and DeDonker [C2] achieves zero-voltage turn-on for main switches and zero-current turn-off for auxiliary switches. The switching turn-off loss is partially reduced with the help of snubber capacitors. A circuit diagram of the ARCP inverter is shown in Figure 1.6. It can be seen that a bulky split DC capacitor bank is required in the ARCP inverter in order to create a midpoint in the DC bus, which is critical for the correct operation of ZVT commutation. However, the split DC capacitor bank causes a severe charge balance problem, which is worse when the inverter line frequency is low. Due to the midpoint, in some situations normal SVM schemes must be modified. Consequently, the ARCP inverter is not a completely piggyback structure. Because the auxiliary switches for each phase are in a back-to-back configuration, and there is no current-returning path from the resonant inductor to the DC bus, an additional over-voltage protection circuit must be used for the auxiliary switches in practical implementations, which increases the complexity.

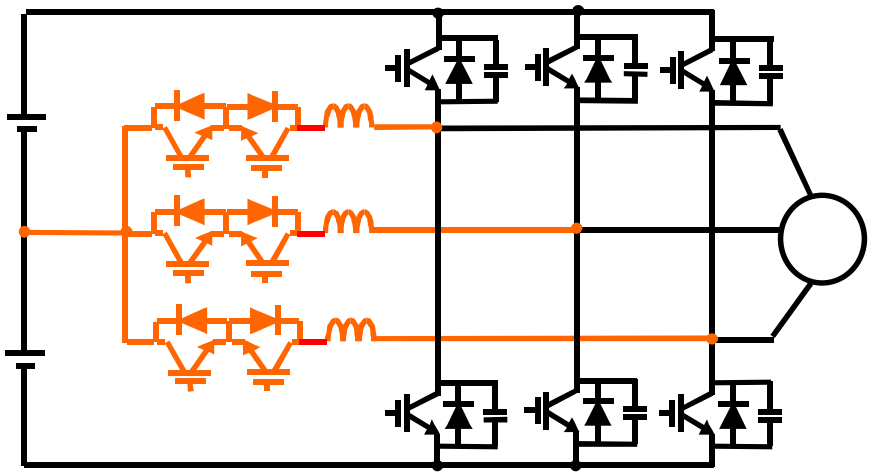

Figure 1.6. The ARCP inverter [C1] [C2].

The ZVT inverter with coupled inductor feedback, which was originally proposed by Barbi [A3] [A4] and Lee [A5] [A6] for DC/DC converters, and developed by Frame [C3] and Yuan [C4] for three-phase inverters, achieves zero-voltage turn-on for main switches and near-zero-current turn-off for auxiliary switches. The switching turn-off loss is also reduced with the help of snubber capacitors. A circuit diagram is shown in Figure 1.7. This topology offers several advantages over the ARCP. First, all problems associated with the split DC capacitor bank are avoided, and the ZVT operation requires no modification to normal SVM schemes. Second, the peak current stress of the auxiliary switches is half of that of the main switches, and the auxiliary switches share the same bridge configuration as the main switches; thus, small-sized six-pack modules can be used. Third, there is no need for additional over-voltage protection for the auxiliary switches in implementations, because the voltage stress is clamped to the DC bus. However, the major problem with this topology is the use of coupled inductors, which are normally bulky and difficult to design, especially in high-power applications.

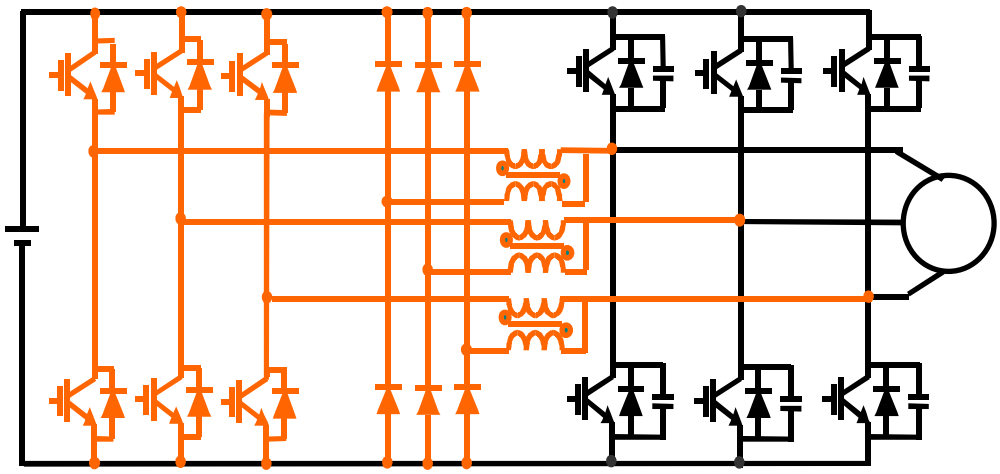

Figure 1.7. The ZVT inverter with coupled inductor feedback [C3] [C4].

The auxiliary resonant snubber ZVT inverter (RSI) proposed by Lai [C5]-[C7] achieves zero-voltage turn-on for main switches and zero-current turn-off for auxiliary switches. Also, the switching turn-off loss is reduced with the help of snubber capacitors. Unlike the ARCP inverter, the RSI does not require a split DC capacitor bank in the DC bus. Unlike the ZVT inverter with coupled inductor feedback, the RSI does not use bulky coupled inductors. However, the RSI requires modification to normal SVM schemes. It cannot use the optimal SVM; instead, it has to use the non-adjacent SVM, which is limited to only a certain few applications, such as permanent magnetic motor drives, but is not suitable for induction motor drives. Similar to the ARCP, implementations require that an additional over-voltage protection circuit be used for the auxiliary switches.

1.2.2.2. The AC-Side ZVT Inverters Using Fewer Than Six Auxiliary Switches

Although the above-mentioned ZVT topologies have the potential to reduce switching losses and thus increase switching frequencies, all requires six auxiliary switches. The associated high device count, cost and large space make the industry hesitant to apply these techniques. In order

to provide simple, low-cost solutions, a number of AC-side ZVT topologies using fewer than six auxiliary switches have been suggested.

Research efforts have been conducted to reduce the number of auxiliary switches in the ARCP inverter. As shown in Figure 1.8(b), an approach proposed by Eckel [C8] uses a single IGBT as the auxiliary switch for one phase leg, thus uses only three auxiliary switches for the three-phase circuit. The auxiliary IGBT S_x is combined with four diodes in a bridge rectifier configuration. The major problem with this simplified topology is the turn-off of the auxiliary switch. With the conventional ARCP circuit in Figure 1.8(a), one auxiliary switch can conduct resonant current in only one direction. The simplified topology, however, allows S_x to conduct resonant current in both directions. Thus, S_x must to be turned off precisely at the moment when the resonant current decreases to zero at the end of ZVT commutations. If the gate driver signal for S_x stays on for too long, the resonant current will build up again in the reverse direction, and the desirable ZVT commutation cannot be realized. As a consequence, extra zero-current detection circuits, saturable cores, and snubbers to protect the auxiliary switches must be included. Therefore, this simplified configuration is not preferred in practical implementations. Using an approach similar to that in Figure 1.8(b), another simplified ZVT topology using three auxiliary switches together with coupled inductors was suggested by Choi [C9], but it suffers the same drawbacks for practical implementations.

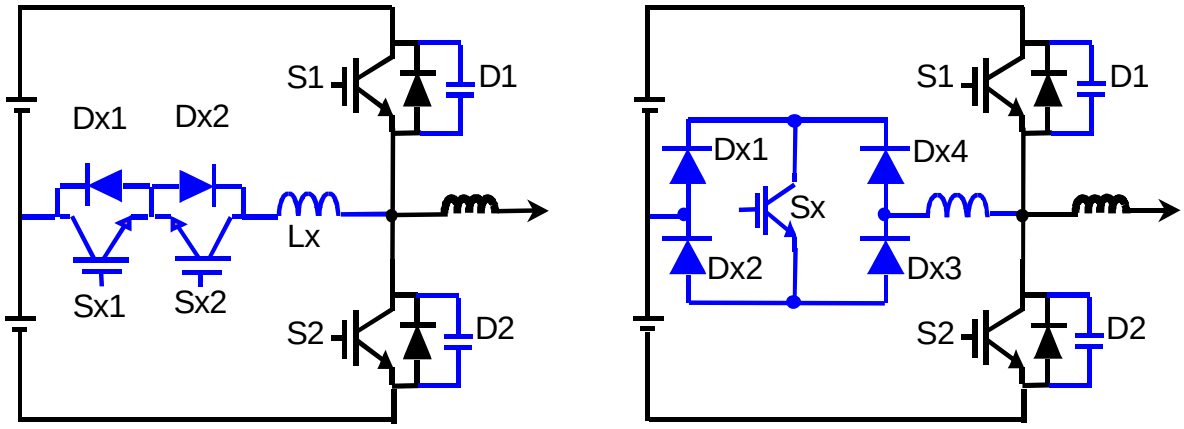

Figure 1.8. A simplification to the ARCP inverter:
(a) the conventional ARCP inverter using two auxiliary switches per phase leg; and
(b) the simplified version using only one auxiliary switch per phase leg [C8].

As shown in Figure 1.9, the topologies proposed by Vlatkovic [C10] [C11], Mao [C12] and Li [C13], use one or two auxiliary switches, and constitute a family of simplified ZVT inverters. In order to achieve soft transition for six main switches by using fewer auxiliary switches, these simplified ZVT inverters require a synchronized turn-on of the main switches. Although they can achieve the main switch turn-on under zero voltage [C10], or 1/3 DC-bus voltage [C12], or 1/4 DC-bus voltage [C13], additional hard turn-off events in the main switches are caused by the modified SVM schemes. One auxiliary circuit has high conduction loss [C10], and the auxiliary switches of another circuit are turned off under hard switching [C12]. Complicated bulky coupled inductors are required in the circuit proposed in [C13] in order to reduce the peak current of the auxiliary switches. An evaluation indicates that these low-cost ZVT inverters actually have worse efficiency than hard-switching inverters [F4] [F19]. Following an approach similar to that used in previous work [C12] [C13], an improved ZVT inverter with two auxiliary switches was proposed by Choi [C14]. Its implementation, however, was found to be quite complicated: Besides the two auxiliary switches as similarly required in the circuits suggested in

[C12] [C13], a number of extra auxiliary switches, either magnetic switches composed of saturable cores or thyristor switches, were necessary [C15] [C16].

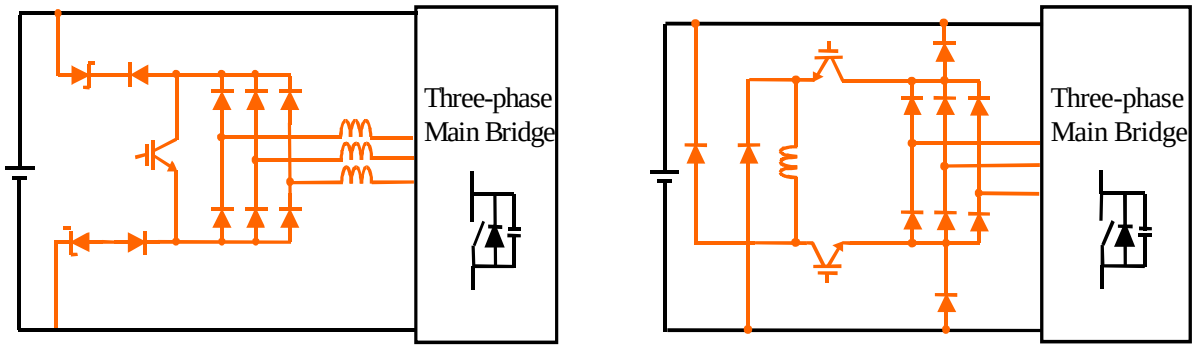

(a) (b)

Figure 1.9. The simplified ZVT inverters with reduced number of auxiliary switches:
(a) using one auxiliary switch [C10]; and
(b) using two auxiliary switches [C12].

1.2.2.3. The ZCT Inverters

Diode reverse recovery and turn-off loss are the dominant causes of switching losses for high-power minority-carrier devices, such as isolated gate bipolar transistors (IGBTs), gate-turn-off thyristors (GTOs), and the integrated gate commutated thyristors (IGCTs) [E20]. Zero-voltage-switching topologies can eliminate the turn-on losses, which are mainly caused by the diode reverse recovery. Zero-voltage-switching topologies can also reduce the turn-off loss with the assistance of snubber capacitors. However, a large snubber capacitance must be required in order to reduce the turn-off loss to a satisfactory level. Yet a large snubber capacitance causes high voltage/current distortion due to the "zero-current clamp" effect in high-frequency operations [F2] [F3]. Moreover, if for any reason the zero-voltage turn-on is not achieved, the energy stored in the snubber capacitors will dump directly into the switch, causing excessive turn-on loss. On the other hand, ZCT techniques force to zero the current flowing through an outgoing device prior to its turn-off, and can thus significantly reduce these two dominant

sources of switching loss without the use of passive snubbers. The ZCT inverter proposed by Hua achieves zero-current turn-off for the main switches [C19], and the improved ZCT inverter proposed by Mao also achieves soft turn-off for the main diodes and zero-current turn-off for the auxiliary switches [C20]. The major issues with the improved ZCT inverter are as follows: 1) six auxiliary switches are required; 2) certain amount of current still remains in the main diodes when the opposite main switches are turned on, and the turn-on of the main switches still occurs under full DC-link voltage; and 3) there is a high resonant capacitor voltage stress.

1.2.3. Multilevel Soft-Switching Inverters

Recently, multilevel inverters have played an important role in megawatts high-frequency power conversions, because they can provide higher voltage capability and lower output voltage distortion using existing devices, without the complications inherent in the series connection of low-voltage devices [D1]-[D8]. Soft switching is useful in increasing the switching frequency and current handling capabilities of multilevel inverters. Normally, existing soft-switching techniques for two-level inverters, as reviewed in Section 1.2.2, can be extended for use in multilevel inverters. Thus, the obtained multilevel soft-switching inverters have advantages and disadvantages similar to those of their two-level counterparts.

A passive-clamped resonant DC-link zero-voltage switching concept, which is similar to prior research [B6], was introduced into three-level inverters by Yi [D9]. However, two DC-rail auxiliary switches are placed in the main power path, causing high power loss. An investigation into a 1.5-MVA three-level quasi-resonant DC-link inverter equipped with the IGCTs, which was conducted by Brucher [D10], shows that the total losses of this inverter were 55% higher than those in a normal snubberless hard-switching inverter.

Regarding the application of the AC-side techniques to multilevel inverters, a three-level ZVT topology using a concept similar to that of the ARCP [C1] [C2] was proposed by Cho [D11]. Besides drawbacks comparable to those in the ARCP inverter, the auxiliary switches in Cho's circuit are subject to 1.5 times the main switch blocking voltage, which significantly raises the cost for the auxiliary circuit. Using the concept of ZVT with coupled inductor feedback [C3] [C4], a three-level ZVT inverter was developed by Yuan [D12] [D13]. Using the improved ZCT scheme [C20], a three-level ZCT inverter was proposed by Mao [D14]; this three-level ZCT topology has been employed for superconductive magnetic energy storage (SMES) [D15] and power electronics building block (PEBB) [D16] applications. A drawback common to these ZVT and ZCT three-level inverters, however, is the high cost, large space and complexity associated with the auxiliary circuits: Four auxiliary switches are required for one phase leg, and 12 auxiliary switches are required for the three-phase circuits.

1.3. Motivation and Objectives

The preceding discussion of the current status of soft-switching techniques for three-phase PWM inverters indicates the need for further research in this subject. Specifically, three areas need to be addressed.

(1) Minimization of Switching Losses

As indicated in the preceding discussion, not all soft-switching inverters can achieve higher overall efficiency than the hard-switching inverter. In order to predict the trend in switching loss reduction and efficiency improvement, a theoretical analysis of the major existing soft-switching inverters was conducted in the Partnership for a New Generation of Vehicles (PNGV) project [F19]. As can be seen in Figure 1.10, the ARCP ZVT, the coupled-inductor ZVT, and the ZCT

can achieve higher efficiency than the hard-switching inverter, but the simplified ZVT with one or two auxiliary switches actually have worse efficiency. Thus, the ARCP ZVT, coupled-inductor ZVT and the ZCT are worthy of further development and evaluation.

Since the switching losses consist of both turn-on and turn-off losses, the ideal soft-switching feature would be zero-voltage turn-on and zero-current turn-off of the main switches, and meanwhile soft commutation of the auxiliary switches. However, so far no soft-switching inverter has this kind of ideal feature. For the ARCP and coupled-inductor ZVT inverters, although the turn-off loss can be partially reduced by snubber capacitors, the snubber capacitors have a limited ability to further reduce the turn-off loss. On the other hand, for the ZCT inverter, not only are the turn-off losses of both the main and auxiliary switches eliminated by the zero-current turn off, but also the turn-on loss can be reduced by the soft commutation. Therefore, this dissertation chooses the ZCT topology as a research object, and will explore and develop advanced ZCT schemes that can further reduce the switching losses.

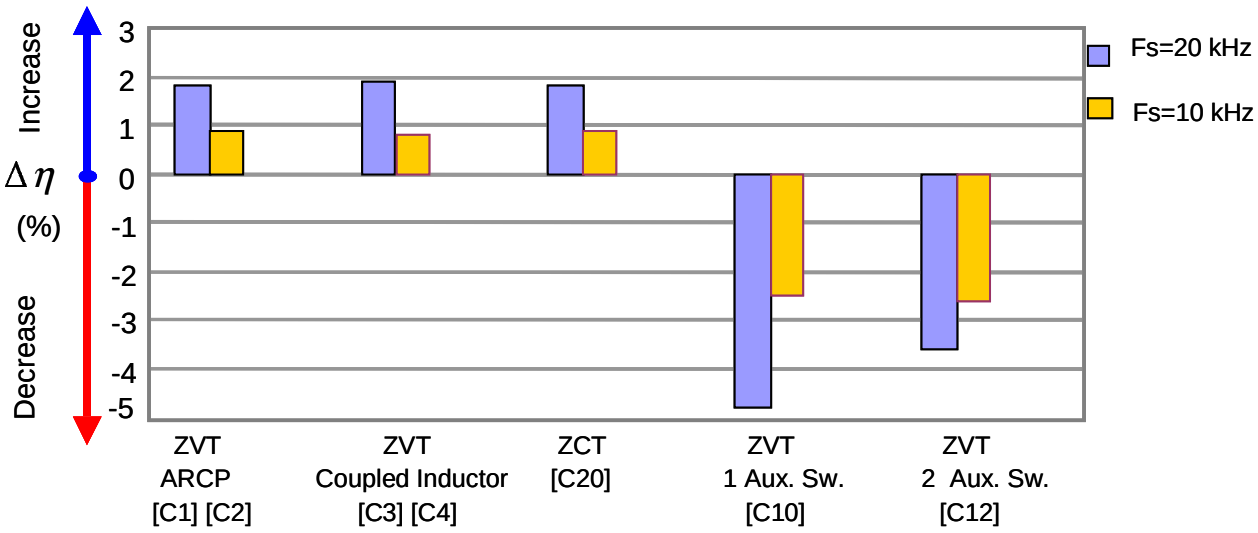

Figure. 1.10. A theoretical comparison of the efficiencies of existing soft-switching inverters conducted in the PNGV project [F19].
(Condition: V_{dc}=324 V, I_{Load_rms}=200 A, power factor= 0.9, six step SVM, modulation index=0.86)

(2) Simplification of Auxiliary Circuits

Most existing soft-switching topologies with fewer than six auxiliary switches have fundamental drawbacks in performance. On the other hand, those with six auxiliary switches are costly and complicated. Another research objective, therefore, is to explore simple low-cost soft-switching topologies that use a reduced number of auxiliary switches and still achieve the following features: 1) they realize soft commutation for all main switches, diodes and auxiliary switches at all operation modes and 2) in the meantime they requires no modification to normal PWM algorithms. As discussed earlier, a lot of effort has been made towards simplifying the ZVT topologies, but the resultant ZVT topologies are still undesirable. Starting from the other category of the soft-switching topology family, this dissertation will explore and develop simplified ZCT topologies that still maintain desirable features.

(3) Issues in Practical Applications

As in all engineering, the effects and variations of actual soft-switching inverters are strongly dependent on applications. Different requirements of applications as a function of power level and frequency (which are coupled with the characteristics of devices and components), as well as proper design and implementations, determine the success of the entire concept. With state-of-the-art devices and components, there are important practical issues that need to be closely examined, including systematic design methodologies for optimizing soft-switching performance and evaluations of the advantages and limitations of soft-switching inverters for particular applications.

Two application examples are used to demonstrate the developed ZCT concepts and to address practical issues. One is the EV traction motor drive application, for which thorough design, hardware implementation, testing, and evaluation on 55-kW prototype ZCT inverters are

conducted. The other is the megawatts high-frequency power conversion application, for which a characterization of the IGCT device under ZCT conditions is carried out, and a generated ZCT cell concept is developed to simplify auxiliary circuitry in multilevel soft-switching inverters.

Overall, through new concept exploration, theoretical analysis, prototype design, implementation, testing and evaluation, this dissertation will provide a unified and comprehensive study of ZCT techniques for high-power three-phase PWM inverter applications. Since rectifiers and inverters are symmetrical to each other, the ZCT techniques discussed in this dissertation are also applicable to three-phase power-factor-correction (PFC) rectifiers.

1.4. Dissertation Outline

This dissertation is arranged as follows.

Chapter 2 explores soft-switching solutions that can minimize the total switching losses. It proposes a new control scheme for a three-phase ZCT inverter circuit that uses six auxiliary switches— the six-switch ZV/ZCT inverter. The proposed scheme enables all main switches, diodes, and auxiliary switches to be turned off under zero-current conditions, and in the meantime provides an opportunity to achieve zero-voltage turn-on of the main switches. Compared with existing ZCT schemes, the diode reverse-recovery current is reduced significantly, the switching turn-on loss is reduced by 50%, the resonant capacitor voltage stress is reduced by 30%, and the current and thermal stresses in the auxiliary devices are evenly distributed. Meanwhile, the proposed scheme requires no modifications to normal PWM algorithms.

Chapter 3 explores simple low-cost soft-switching topologies that can achieve desirable features. It proposes a new ZCT inverter topology that requires only three auxiliary switches—

the three-switch ZCT. With considerable reductions in device count, cost, and size from existing topologies, the proposed three-switch ZCT inverter realizes zero-current turn-off for all main and auxiliary switches, and provides soft commutation for all diodes. Meanwhile, it still requires no modification to normal PWM algorithms.

Neither the six-switch ZV/ZCT scheme nor the three-switch ZCT topology requires any additional resonant current sensing, saturable cores, or snubbers to protect the auxiliary switches in practical implementations. Operation principles, general design criteria, and experimental verifications for both new concepts are presented respectively, in Chapters 2 and 3.

Chapter 4 is a comparative study of a family of ZCT inverters. The family of ZCT inverters consists of five schemes for the six-switch ZCT inverter circuit (which includes the new ZV/ZCT scheme proposed in Chapter 2) and the simplified three-switch ZCT topology proposed in Chapter 3. A simplified equivalent circuit is presented to unify the common traits of ZCT commutations. With the visual aid of state planes, the evolution of the ZCT inverter technique is examined, and the differences and connections between these ZCT inverters are identified. Behaviors of individual inverters, including switching conditions, circulating energy, and device/component stresses, are compared. Suggestions for practical applications are provided.

Based on the proposed six-switch ZV/ZCT and three-switch ZCT techniques, two 55-kW prototype inverters for EV traction motor drives have been built and tested to the full-power level with a closed-loop controlled induction motor dynamometer. The desired ZCT soft-switching features are realized together with motor drive functions.

Chapter 5 presents in detail the design considerations of these two 55-kW ZCT inverters. The design approach integrates system optimization with switching characterization of the main IGBT devices under the ZCT conditions, selection, testing and characterization of the auxiliary

devices, design and selection of the resonant inductors and capacitors, inverter loss modeling and numerical analysis on methods to minimize the total inverter losses, system-level operation aspects, and layout and parasitic considerations. Different design aspects between these two ZCT inverters are compared and elaborated.

Chapter 6 presents the prototype implementations of these two 55-kW ZCT inverters, reports the steady-state test results, and conducts an experimental evaluation of ZCT techniques for the EV drive application. The complexity of the 55-kW prototypes is compared, in terms of the numbers and ratings of all the devices and components that are actually used, overall size, and compatibility with hard-switching inverters. The ZCT inverter operations are fully characterized under the dynamometer tests, for both electrical and thermal properties. Efficiencies are measured and compared under a group of torque/speed points for typical EV drive cycles.

Chapter 7 is an investigation of the ZCT techniques in megawatts high-frequency power conversion applications. It first presents an experimental characterization of the IGCT device under the proposed six-switch ZV/ZCT condition, which shows promising results in reducing switching losses and stresses. Then, it discusses the improvement of the IGCT switching frequency as well as simplification on the cooling system under the ZCT operation. Following the proposed three-switch ZCT topology, this chapter also develops a generalized ZCT cell concept to simplify auxiliary circuitry in multilevel soft-switching topologies. The simplified multilevel soft-switching topologies reduce the number of auxiliary switches by half compared to existing topologies and still maintain desirable soft-switching features.

Chapter 8 provides the conclusions of this dissertation and suggests directions for future research.

Chapter 2

A Three-Phase Soft-Transition Inverter with A New Control Scheme for Zero-Current and Zero-Voltage Switching — The Six-Switch ZV/ZCT Inverter

As discussed in Chapter 1, ZCT techniques are better candidates for minimizing the total switching losses in high-power inverters. This chapter proposes a new soft-transition control scheme for a three-phase ZCT inverter circuit that uses six auxiliary switches— the six-switch ZV/ZCT inverter. It enables all main switches, diodes, and auxiliary switches to be turned off under zero-current conditions, and provides an opportunity to achieve zero-voltage turn-on of the main switches. Compared with existing ZCT schemes, the diode reverse-recovery current is substantially reduced, the switching turn-on loss is reduced by 50%, the resonant capacitor voltage stress is reduced by 30%, and the current and thermal stresses in the auxiliary devices are evenly distributed. Meanwhile, the proposed scheme requires no modifications to normal PWM algorithms. The operation principles and general design criteria, including a detailed analysis based on the state-plane technique, are described. The circuit operation is verified with a 5-kW prototype converter. Significant reductions in switching losses and stresses, as compared to existing techniques, are experimentally demonstrated.

2.1. Previous Research on Three-Phase ZCT Inverters

The basic concept of ZCT is as follows: During a switching transition, the current flowing through the outgoing device is forced to reduce to zero prior to the turn-off of this device; when the switching transition is over, normal PWM operation resumes. This is accomplished by the addition of an auxiliary circuit that generates a resonant current to divert the current through the

main device prior to the switching transition. Figure 2.1 shows a commonly used three-phase ZCT inverter circuit that uses six auxiliary switches, called the six-switch ZCT inverter. In this circuit, there are three auxiliary circuit networks paralleled to the main switch bridge; each network consists of two auxiliary switches and one *LC* resonant tank. There are two basic features associated with this circuit: The first is its piggyback structure – each auxiliary circuit network is independently responsible for the soft transition of one phase leg of the main circuit, thus the execution of soft transition requires no modification to normal PWM algorithms developed for hard-switching inverters; and second, voltage stresses across all the main and auxiliary switches/diodes are kept to the DC bus voltage, and no auxiliary components are in series with the main power flowing path.

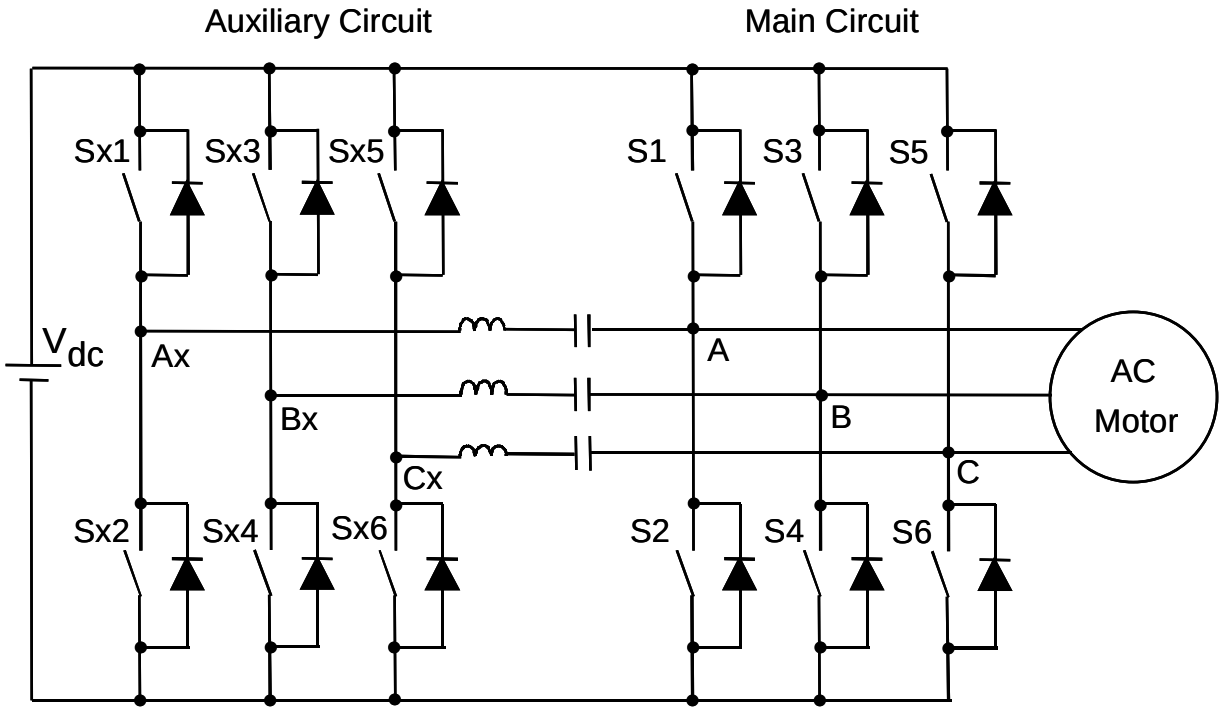

Figure 2.1. Circuit configuration of the six-switch ZCT inverter.

Historically, research with the ZCT inverter circuit configuration shown in Figure 2.1 goes back to the forced current commutation techniques for the SCRs [A9], for which the McMurray inverter is an example of voltage source inverters [C17] [C18]. The McMurray inverter can provide zero-current turn-off for all main and auxiliary switches, but it does not solve the diode reverse-recovery problem at the main switch turn-on transitions. In addition, the auxiliary switches, which are normally unidirectional SCRs without anti-parallel diodes, must block bi-directional voltage and withstand more than twice the DC bus voltage.

For modern gate-controlled devices such as IGBTs with anti-parallel diodes, the McMurray inverter is not appropriate. These modern devices do not block the reverse voltage; instead, they can allow reverse current to flow through the anti-parallel diodes. Therefore, a circuit arrangement with a look similar to that of the McMurray inverter, but with the main and auxiliary switches changed into unidirectional voltage blocking and bi-directional current flow devices, was proposed by Hua for the ZCT operation [C19]. Figure 2.2 shows one phase leg of the ZCT inverter circuit, in which S_1 and S_2 are the main switches, S_{x1} and S_{x2} are the auxiliary switches, and the inductor L_x and capacitor C_x constitute a resonant tank. Hua's scheme, however, has severe drawbacks— it does not solve the diode reverse-recovery problem, and it requires that the auxiliary switches be turned off at the full load current. It simply shifts the turn-off loss from the main switches to the auxiliary switches, without any improvement in overall system efficiency.

An improved ZCT control scheme was proposed by Mao [C20]; it extends the basic ZCT concept to the turn-on transition, and thus reduces the diode reverse-recovery current and switching turn-on loss. Its basic idea is to activate one auxiliary switch for a short time at both turn-on and turn-off transitions of the diagonally located main switch. Mao's ZCT scheme also

extends the auxiliary switch gate signals until the resonant current reverses its direction and flows through its anti-parallel diode, so the auxiliary switches are turned off under a zero-current condition. The switching patterns and operational waveforms are shown in Figure 2.3. With Mao's ZCT scheme, however, the main switches are still turned on under the full DC bus voltage, and a certain amount of current still remains in the main diode when the opposite main switch is turned on, which causes switching losses associated with the diode reverse-recovery current. In addition, Mao's ZCT scheme causes high resonant capacitor voltage stress, which is twice the DC bus voltage. Furthermore, in every switching cycle, one auxiliary switch must be activated *twice*, while the other auxiliary switch is idling. This kind of switching pattern brings undesirable uneven distribution of current and thermal stresses among the auxiliary devices within the inverter load current line cycles.

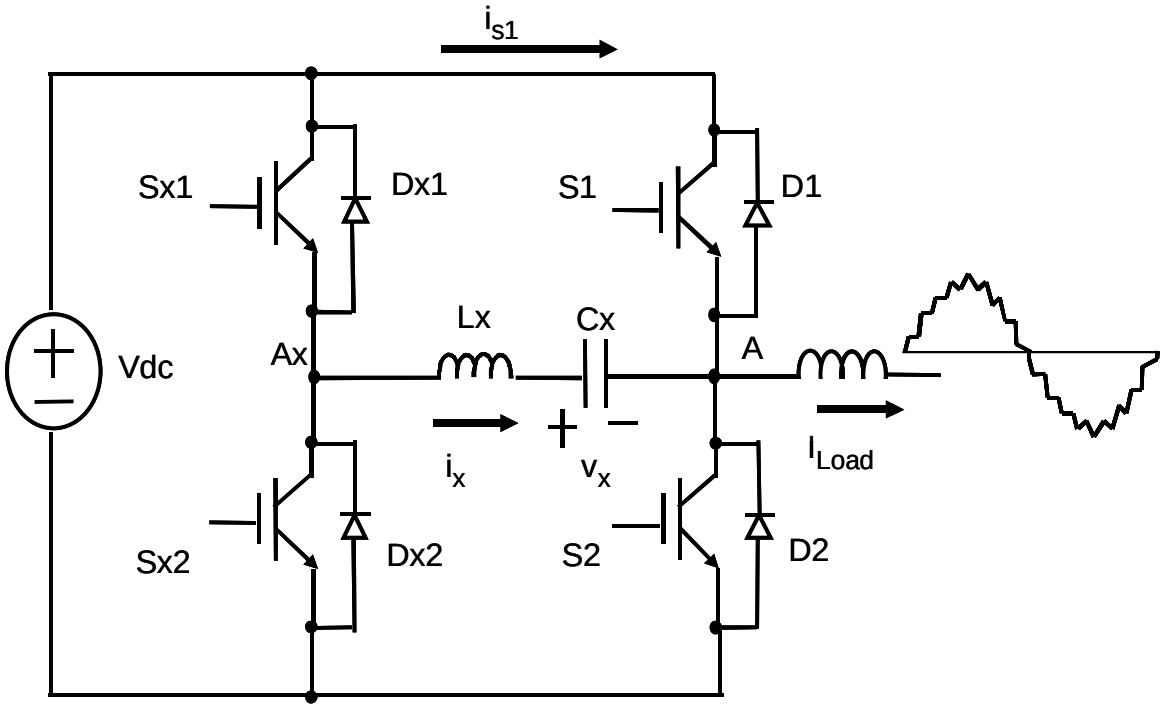

Figure 2.2. Detailed one phase-leg circuit of the six-switch ZCT inverter.

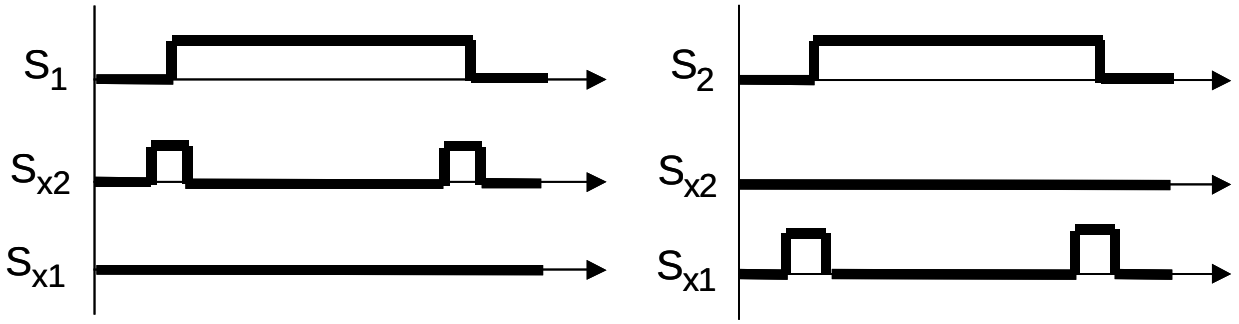

(i) I_{Load}>0 Case (ii) I_{Load}<0 Case

(a)

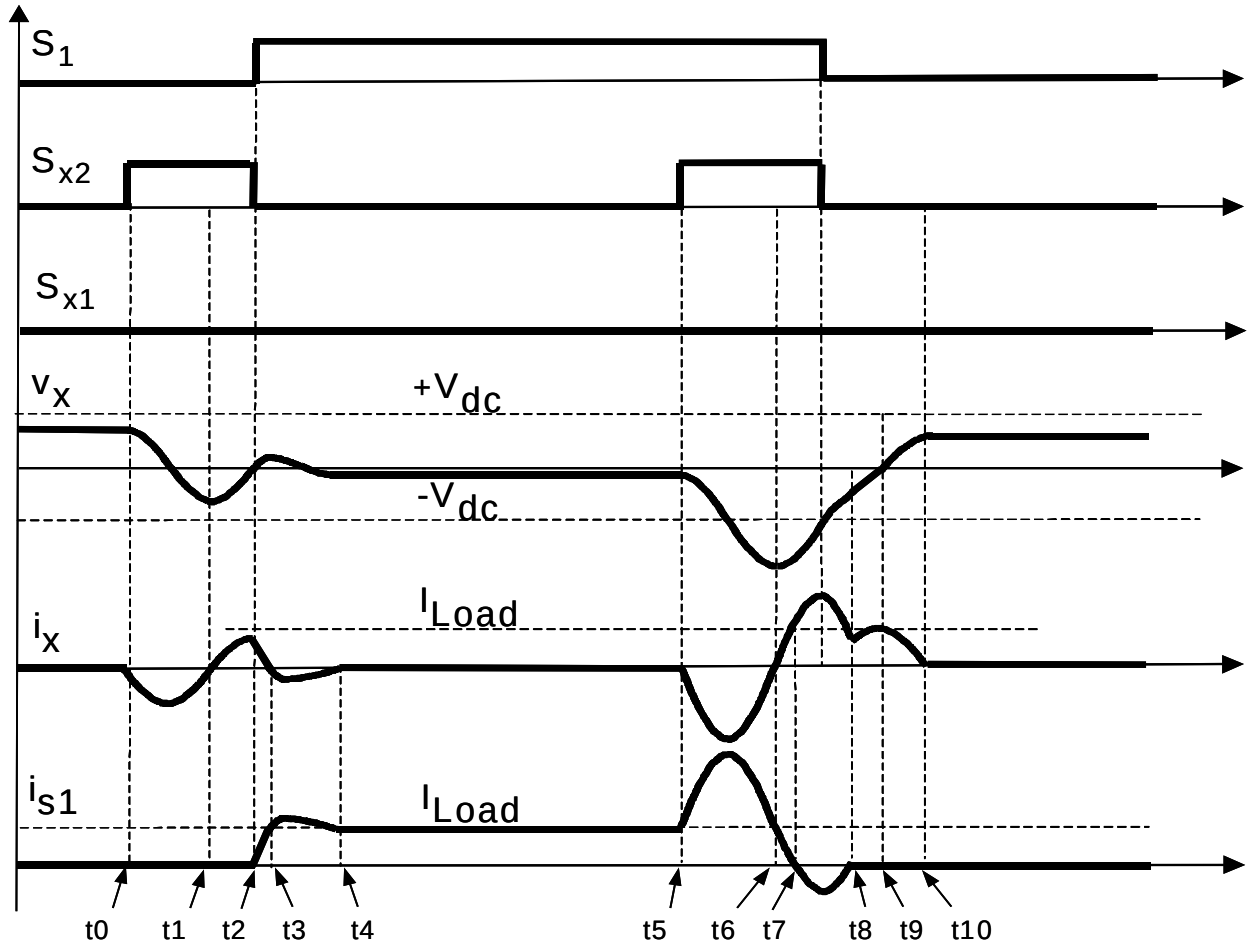

(b)

Figure 2.3. Operations of Mao's control scheme for the six-switch ZCT inverter:
(a) switching patterns; and
(b) waveforms (for I_{Load}>0 case, which are symmetrical to I_{Load}<0 case).

In addition, for DC/DC converter applications, a ZCT-type soft-switching topology was suggested that employs two auxiliary switches for each main switch and can achieve zero-current and zero-voltage switching when the converter operates under discontinuous conduction modes (DCM) [A7]. Because this topology requires that the number of auxiliary switches be twice the number of main switches, and its operation requires no current freewheeling in a main diode before the opposite main switch is turned on, both the topology and operation modes are not applicable to three-phase inverter applications.

2.2. A New Six-Switch ZCT Inverter Scheme for Zero-Current and Zero-Voltage Switching

2.2.1. Operational Principles

A new soft-transition control scheme is proposed for the six-switch ZCT inverter circuit shown in Figure 2.1. In the half-bridge-configured phase-leg circuit (Figure 2.2), the bi-directional load current I_{Load} is conducted in a "totem-pole" manner. Depending on the directions of I_{Load}, there are two cases for gating the switches, as shown in Figure 2.4.

- $I_{Load}>0$. When the top main switch S_1 is on and the bottom main switch S_2 is off complementarily, I_{Load} flows through IGBT S_1; when S_1 is off and S_2 is on complementarily, I_{Load} freewheels through diode D_2. During the half-positive cycle, only S_1 and D_2 need to be soft-switched. At the moment that S_1 is turned on (S_2 is turned off complementarily), the diagonally located auxiliary switch S_{x2} is activated for a short time; at the moment that S_1 is turned off (S_2 is turned on complementarily), the other auxiliary switch S_{x1} is activated for a short time.
- $I_{Load}<0$. When S_1 is on and S_2 is off complementarily, I_{Load} freewheels through diode D_1; when S_1 is off and S_2 is on, I_{Load} flows through IGBT S_2. During the half-negative cycle, only S_2

and D_1 need to be soft-switched. At the moment that S_2 is turned on, S_{x1} is activated for a short time; at the moment that S_2 is turned off, S_{x2} is activated for a short time.

The salient feature of the proposed scheme is that based on the load current information, the turn-on and turn-off transitions of each main switch are assisted alternately by the two auxiliary switches in the same phase leg. This alternating switching pattern automatically evens out the distribution of current and thermal stresses in the auxiliary devices in every switching cycle, enhancing the reliability of the inverter. More importantly, as will be explained in the following sections, sufficient energy can be built up in the resonant tank to establish a resonant current that completely diverts the current flowing through the main circuit prior to the switching transitions. Although the scheme needs the load current information, no additional sensor is required, because this information is already needed for other control functions in the three-phase inverter system.

The circuit operation for the cases of $I_{Load}>0$ and $I_{Load}<0$ are symmetrical; thus, the operating principle needs to be explained for one case only. Figure 2.5 illustrates the operational waveforms within one switching cycle for the $I_{Load}>0$ case. The operation description starts with the switch turn-on transition. To simplify the analysis, the circuit parasitics, such as the semiconductor junction capacitors and stray inductors, are ignored in the following description. I_{Load} and the DC bus voltage V_{dc} are assumed to be constant within one switching cycle. Initially, I_{Load} freewheels through the bottom main diode D_2. In the steady state, there is a positive voltage v_x across C_x, where $V_{dc}>v_x>0$. The v_x cannot exceed V_{dc}; otherwise, diode D_{x1} will conduct. The v_x cannot be negative; otherwise, diode D_{x2} will conduct. The circuit operation goes through eight topological stages, as shown in Figure 2.6. The bold lines represent the actual current path.

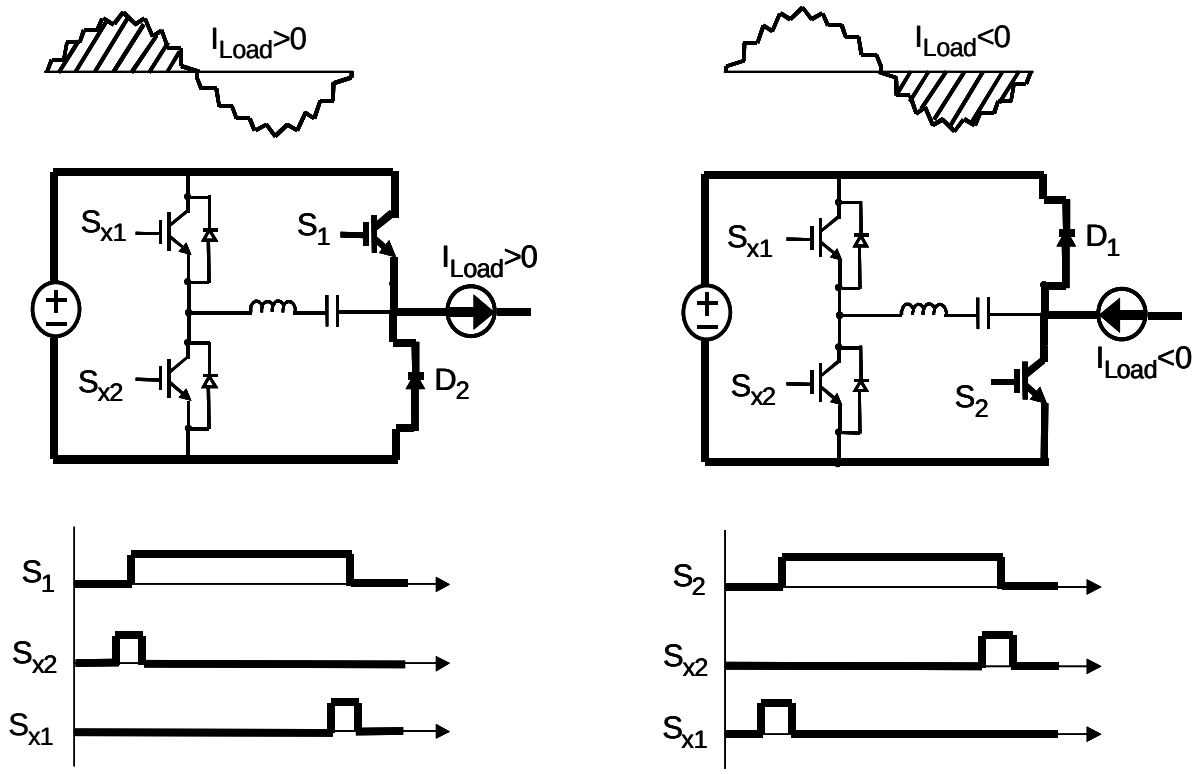

Figure 2.4. Switching pattern of the proposed six-switch ZV/ZCT scheme.

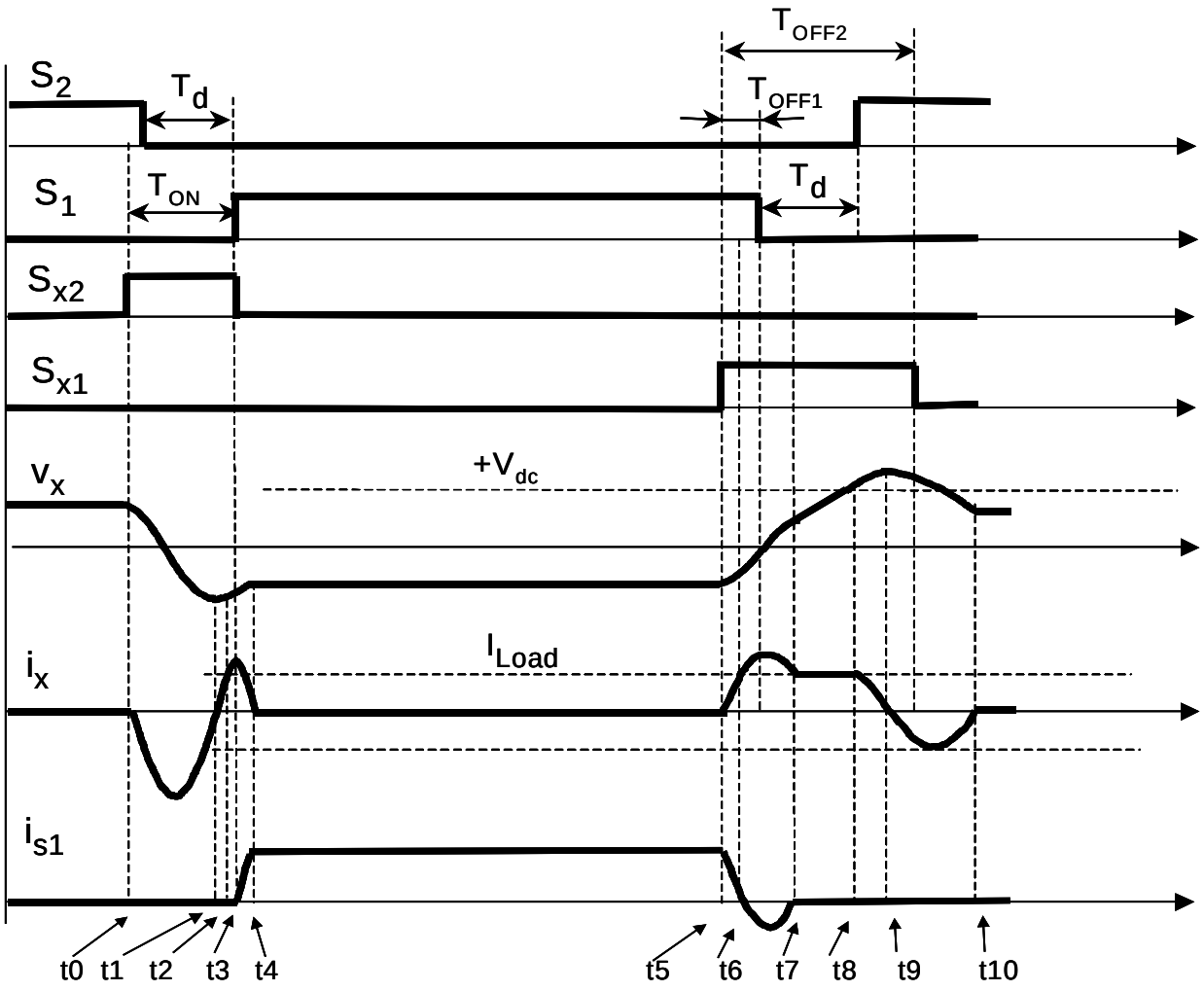

Figure 2.5. Operational waveforms of the proposed six-switch ZV/ZCT scheme.

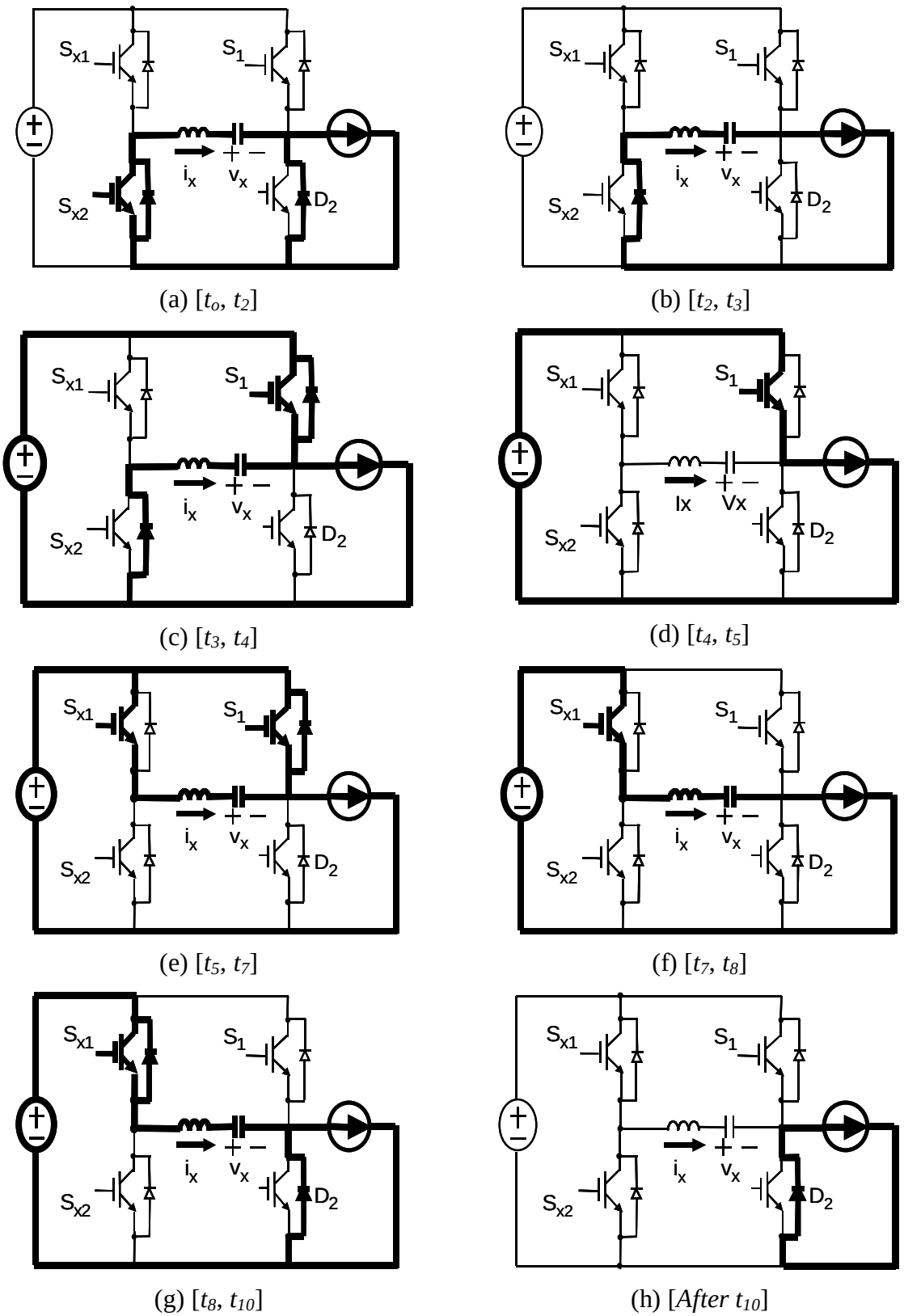

(a) [t_o, t_2] (b) [t_2, t_3]

(c) [t_3, t_4] (d) [t_4, t_5]

(e) [t_5, t_7] (f) [t_7, t_8]

(g) [t_8, t_{10}] (h) [*After* t_{10}]

Figure 2.6. Topological stages of the proposed six-switch ZV/ZCT commutation.

a) Turn-On Transition I [t_0, t_2]: Before S_1 is turned on, S_{x2} is turned on at t_0. L_x and C_x start to resonate, and the resonant current i_x increases in the negative direction to a peak, then decreases to zero at t_1. After t_1, i_x reverses its direction and is conducted by D_{x2}. S_{x2} turns off at the zero-current condition and its gate drive signal can be removed without causing switching loss. As i_x increases in the positive direction, the current in D_2 is diverted into the auxiliary circuit. The i_x reaches I_{Load} at t_2, and the current in D_2 drops to zero. The gate driver signal of the bottom main switch S_2 should be removed before t_2.

b) Turn-On Transition II [t_2, t_3]: Since D_2 has stopped conducting current and the top main switch S_1 is still off, I_{Load} can flow only through the resonant tank, charging C_x linearly. There is a voltage difference between V_{dc} and v_x. The voltage drop across S_1 equals this difference, and thus is less than V_{dc}.

In actual circuits, when the current through D_2 drops to zero at t_2, reverse-recovery current begins to flow, due to the removal of the remaining free carriers in the D_2 junction. As illustrated in Figure 2.7, this recovery will provide a path for i_x to continue increasing. After the reverse-recovery current in D_2 reaches its peak and begins to decrease, the difference between i_x and I_{Load} will force the top main diode D_1 into conduction and will clamp the voltage across S_1 to zero. This is an important property of the proposed scheme, because it provides an opportunity to achieve zero-voltage switching in the ZCT inverters, especially in those with high-power/high-voltage devices that require long reverse-recovery times. In addition, if the junction capacitors of S_1, D_1, S_2 and D_2 are not negligible or if small external capacitors are connected across the devices, these capacitors will resonate with L_x and C_x. The resonant period at this point is mainly determined by L_x and the junction or external capacitors. This resonance will also bring the voltage across S_1 to zero, in a manner similar to that of conventional ZVT inverters [A2].

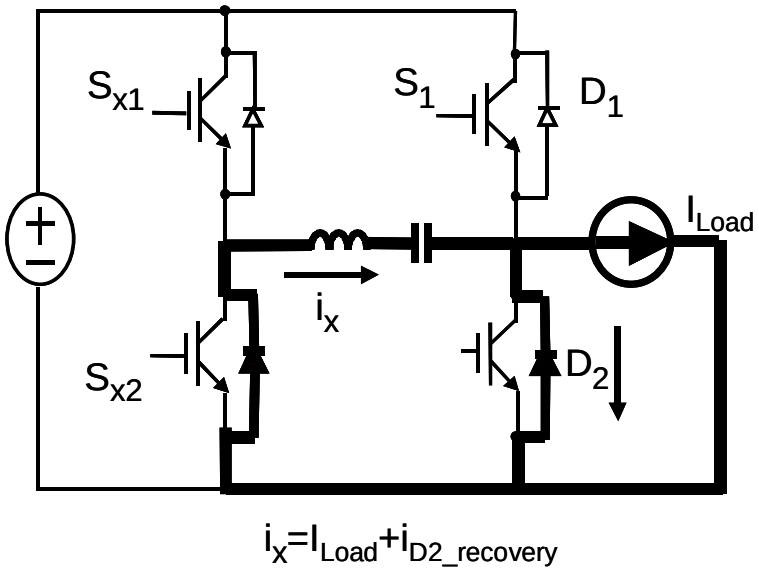

(a)

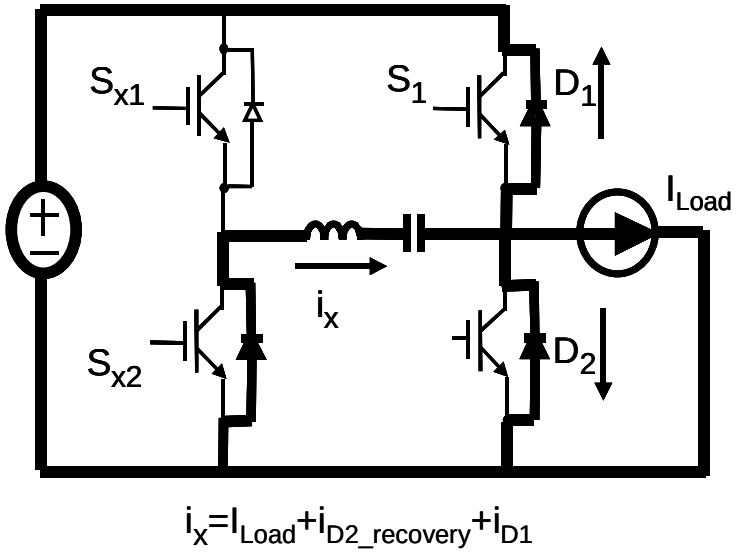

(b)

Figure 2.7. Reverse-recovery process of the main diode D_2:
(a) at t_2, D_2 reverse recoveries, and i_x keeps increasing, $i_x=I_{Load} + i_{D2\_recovery}$; and
(b) after the reverse-recovery current in D_2 peaks, D_1 conducts to carry the difference between i_x and ($I_{Load} + i_{D2\_recovery}$).

c) Turn-On Transition III [t_3, t_4]: S_1 is turned on at t_3 under the zero-voltage condition. The current in D_2 has been completely diverted to the auxiliary circuit since t_2, and the time within [t_2, t_3] allows the carrier in D_2 to be recombined appropriately. In addition, the resonant inductor

limits the rise rate of the switch current. Therefore, the diode reverse-recovery current and the switch turn-on loss are reduced significantly. After t_3, i_x decreases toward zero because now the negative V_{dc} is applied to the resonant tank.

d) Switch-On Stage [t_4, t_5]: At t_4, i_x drops to zero, and D_{x2} turns off naturally. The auxiliary circuit stops resonating and is functionally disconnected from the main circuit. I_{Load} flows through S_1, and the PWM operation resumes. C_x maintains a negative voltage during this period.

e) Turn-Off Transition I [t_5, t_7]: When it is time to turn off S_1, S_{x1} is turned on at t_5. L_x and C_x start to resonate again. As i_x increases in the positive direction, the current through S_1 decreases. After t_6, i_x exceeds I_{Load}, the current through S_1 drops to zero, and D_1 starts to conduct the surplus current. S_1 is turned off under the zero-current condition. The i_x increases to a peak, then drops to I_{Load} at t_7. The gate driver signal of S_1 is removed between t_6 and t_7 without causing turn-off loss.

f) Turn-Off Transition II [t_7, t_8]: After t_7, D_1 stops conducting. Since S_1 has been turned off and D_2 is still reverse-biased, I_{Load} can flow only through the resonant tank, charging C_x linearly.

g) Turn-Off Transition III [t_8, t_{10}]: At t_8, the voltage across C_x is charged to V_{dc}; thus, D_2 is forward-biased and starts to conduct current. V_{dc} is applied to the resonant tank, and L_x and C_x start to resonate again. The i_x decreases to zero and v_x reaches a peak at t_9. Since v_x is still greater than V_{dc}, the resonance continues, and i_x reverses its direction and is conducted by D_{x1}. S_{x1} is turned off under the zero-current condition. The gate driver signal of the bottom main switch S_2 can be applied after t_8.

h) Diode-On Stage [after t_{10}]: The i_x increases to a peak, then decreases to zero at t_{10}. D_{x1} turns off naturally. I_{Load} flows through D_2, and the PWM operation resumes.

2.2.2. State-Plane Analysis

One can analyze the circuit operation by solving the *LC* second-order differential equations, step by step through the topological stages. But this method is clearly too complicated. The state-plane technique is a simple visual tool to analyze resonant converters [F5]. It can also be used to analyze the proposed six-switch ZV/ZCT inverter operation because the key to the circuit operation is the *LC* resonant tank.

The basic concept of the state-plane technique can be explained by means of the *LC* resonant converter shown in Figure 2.8(a), where V_{Tank} is the external voltage applying to the resonant tank, and V_{xO} is the initial capacitor voltage. The state plane is created by plotting the inductor current i_x and the capacitor voltage v_x onto one graph, with i_x and v_x as the vertical and horizontal axes, respectively. After the switch S_x is turned on, the circuit starts to resonate, and these two variables change in sinusoidal waveforms. It is derived that

$$v_x = V_{Tank} - (V_{Tank} - V_{xO}) \cdot \cos(\omega_o t), \text{ and} \tag{2.1}$$

$$i_x = \frac{V_{Tank} - V_{xO}}{Z_o} \cdot \sin(\omega_o t), \tag{2.2}$$

where $\omega_o \triangleq 1/\sqrt{L_x C_x}$ is the resonant frequency (rad/s), and $Z_o \triangleq \sqrt{L_x/C_x}$ is the characteristic impedance of the resonant tank (Ω).

From Equations (2.1) and (2.2), the following equations for the state trajectory are derived:

$$(i_x Z_o)^2 + (v_x - V_{Tank})^2 = (V_{Tank} - V_{xO})^2 \triangleq \rho^2, \text{ and} \tag{2.3}$$

$$\omega_o t = \tan^{-1}\left(\frac{i_x Z_o}{V_{Tank} - V_x}\right). \tag{2.4}$$

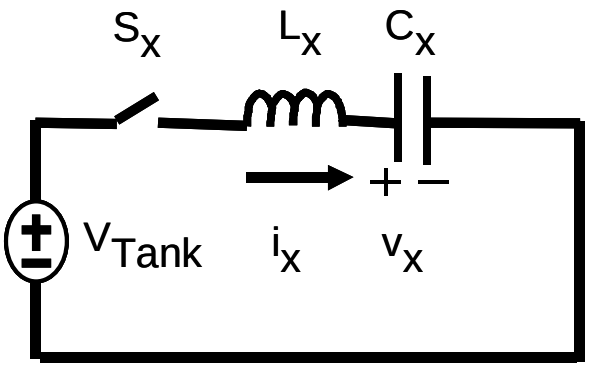

(a)

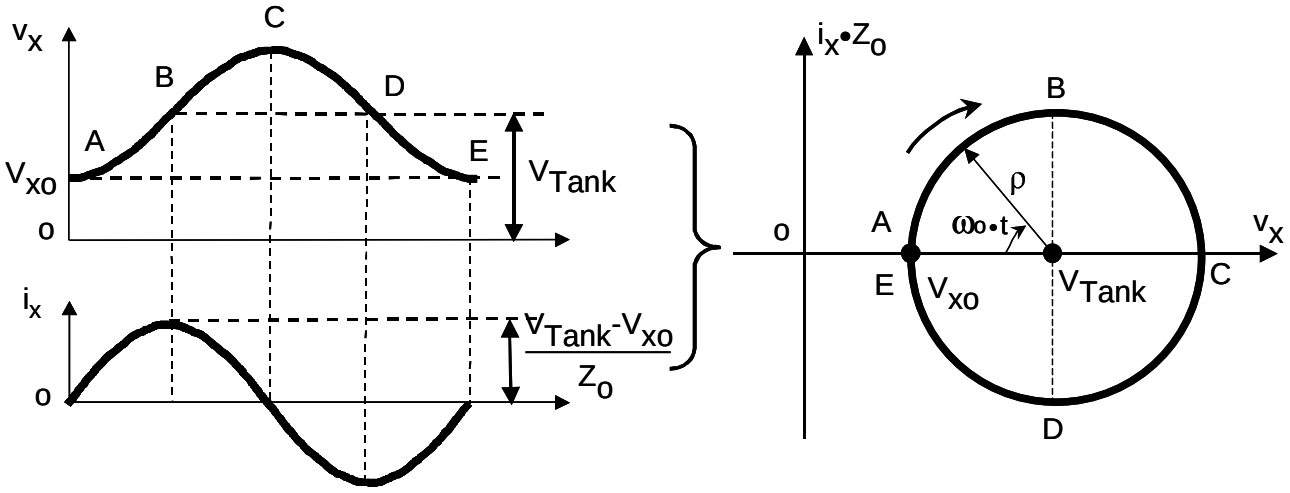

(b)

Figure 2.8. Basic concept of the state-plane technique:
(a) conceptual resonant converter; and
(b) mapping the time-domain waveforms into the state plane.

Equation (2.3) shows that the state trajectory is a circle with its center at (V_{Tank}, 0), and with radius ρ, where ρ is the difference between V_{Tank} and V_{xO}. Also, the initial state (V_{xO}, 0) is one point on this circle. Equation (2.4) shows that the time elapsed between two points on the circular trajectory is proportional to the angle subtended at the center. By mapping the time-domain waveforms into the state plane, the circular trajectory of this resonant converter is

obtained and is drawn in Figure 2.8(b). In the trajectory, the vertical axis is i_x scaled by factor Z_o, and time flows in a clockwise direction.

To apply the state-plane concept to the analysis of the proposed six-switch ZV/ZCT inverter operation, for each topological stage, the initial resonant capacitor voltage V_{xO} and the external voltage applied to the resonant tank V_{Tank} must be identified, because they determine the center and radius of the corresponding circular trajectory. There are eight topological stages for the proposed six-switch ZV/ZCT inverter (Figure 2.6), and their trajectories are continuous because of the continuation of circulating energy. Initially, before auxiliary switch S_{x2} is turned on at t_0, there is a positive voltage v_x across C_x, where $V_{dc}>v_x>0$. Correspondingly, on the state plane, the starting point at t_0 is located between the origin and ($+V_{dc}$, 0). In the intervals [t_0, t_2] and [t_5, t_7], V_{Tank}=0; in the interval [t_3, t_4], V_{Tank}= $-V_{dc}$; in the interval [t_8, t_{10}], V_{Tank}= $+V_{dc}$. The trajectories of these four intervals are circles with corresponding centers and radii. In the intervals [t_2, t_3] and [t_7, t_8], the resonant tank is linearly charged by the load current, and the trajectories are lines. In the intervals [t_4, t_5] and [*after* t_{10}], the resonant tank is functionally disconnected from the main circuit, and each trajectory remains one point until the next switching action. By connecting these trajectories step by step, the complete state-plane trajectory for one switching cycle of the proposed soft transition is obtained, as drawn in Figure 2.9.

State-plane diagrams reveal important information, such as voltage/current stresses and control timings. With the aid of the state-plane diagrams, the circuit operation and features can be easily identified and analyzed. For comparison purposes, referring to the waveforms shown in Figure 2.3, the state-plane trajectory of Mao's ZCT scheme is obtained using a similar approach and is drawn in Figure 2.10.

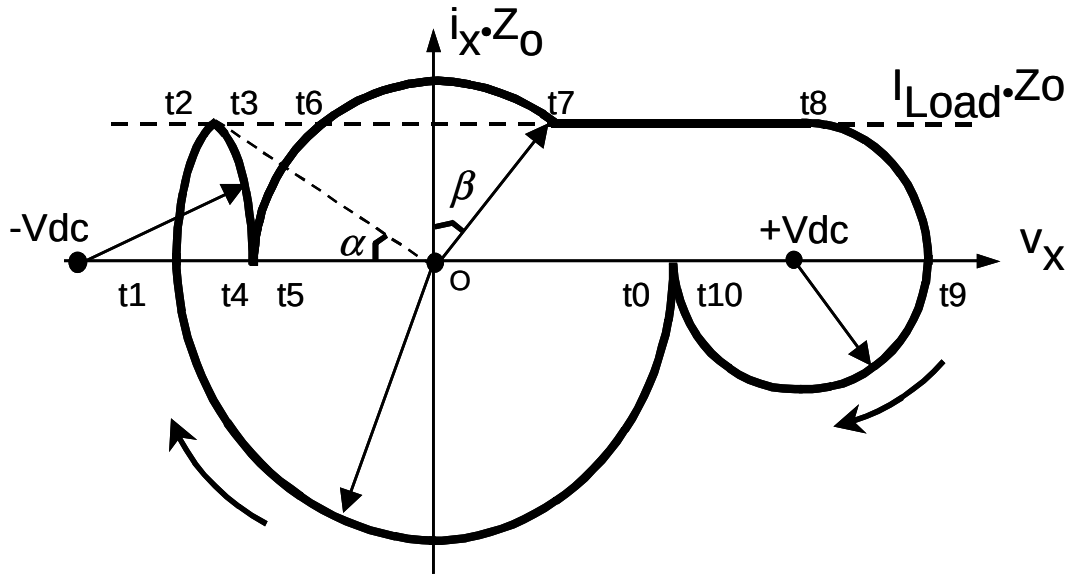

Figure 2.9. State-plane trajectory of the proposed six-switch ZV/ZCT scheme (t_0~t_4, turn-on; t_5~t_{10}, turn-off).

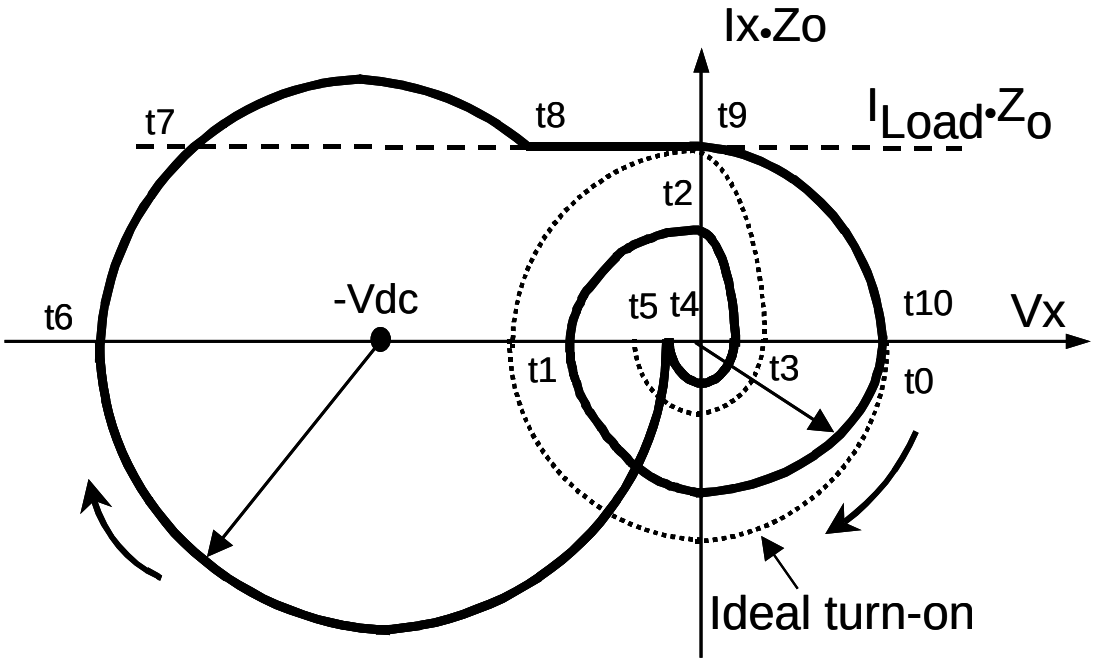

Figure 2.10. State-plane trajectory of the Mao's six-switch ZCT scheme (t_0~t_4, turn-on; t_5~t_{10}, turn-off).

- *The Turn-On Transitions [t_0, t_4]*. The main diode D_2 current is determined by $I_{Load} - i_x$. For both schemes, auxiliary switch S_{x2} is first turned on at t_0. With Mao's ZCT scheme (Figure 2.10), the opposite main switch S_1 is turned on at t_2 when i_x reaches a peak. The dashed line illustrates the trajectory of the ideal situation. Ideally, the circuit is lossless; thus, through ¾ of the resonant cycle, at t_2 the current in the main diode could drop to zero because the peak of i_x could equal I_{Load}. In a practical circuit, however, there are inevitable parasitic losses, which are caused by the equivalent series resistance (ESR) in L_x and C_x and the voltage drops across the devices. Consequently, this peak can not reach I_{Load} at t_2. The zero-current turn-on condition is lost, and a certain amount of diode reverse-recovery current still remains when S_1 is turned on under full V_{dc}. With the proposed ZV/ZCT scheme (Figure 2.9), the energy built-up in the resonant tank at t_0 is sufficient to ensure that D_2 will be turned off under zero-current after t_2. The i_x should reach a peak after ¾ of the resonant cycle, but it is actually clamped by I_{Load} at t_2. The time interval between [t_2, t_3], which is relatively short, is to ensure that the carriers in the main diode can be recombined appropriately before S_1. Meanwhile, the S_1 turn-on voltage is reduced from the DC bus voltage to zero. Therefore, both the diode reverse-recovery current and the switching turn-on loss are substantially reduced.

- *The Turn-Off Transitions [t_5, t_{10}]*. For both schemes, when i_x is greater than I_{Load}, the surplus current is conducted by the anti-parallel diode that is across the main switch, and zero-current turn-off is achieved. Yet, with Mao's ZCT scheme (Figure 2.10), the trajectory is biased on the left side of the vertical axis, and v_x reaches its peak V_{x_max} at t_6, which is around twice the DC bus voltage V_{dc}. With the proposed ZV/ZCT scheme (Figure 2.9), the trajectory is located evenly across the state plane. V_{x_max} occurs at t_9, which is clearly obtained from the trajectory as

$$V_{x\_max} = V_{dc} + I_{Load} \cdot Z_o . \tag{2.5}$$

Equation (2.5) shows that the V_{x_max} is influenced by the load current, and that it tends to become larger at heavier loads. Normally, the resonant tank is designed such that at the maximum load current condition, V_{x_max} is about 1.3~1.4 times the V_{dc}. As a result, the resonant capacitor voltage stress is reduced by about 30%.

2.3. Alternative to the New Six-Switch ZV/ZCT Scheme

In the proposed ZV/ZCT scheme, the *diagonal* auxiliary switch is to assist turn-*on*; and the other auxiliary switch is to assist turn-off. There should be an alternative approach in which the *diagonal* auxiliary switch is for turn-*off*, and the other auxiliary switch is for turn-on. When $I_{Load}>0$, S_1 is assisted by S_{x1} at turn-on, and by S_{x2} at turn-off. When $I_{Load}<0$, S_2 is assisted by S_{x2} at turn-on, and by S_{x1} at turn-off. Similarly, the current and thermal stresses in the auxiliary devices are evenly distributed throughout the line cycle. The operational waveforms and state-plane trajectory are shown in Figure 2.11. The operational principle of the alternative scheme is similar to that of the proposed ZV/ZCT scheme, and all main switches, diodes and auxiliary switches can still be turned on and turned off at zero current. However, as can be seen in Figure 2.11(b), the state-plane trajectory is biased on the left side of the vertical axis, and the resonant capacitor voltage reaches its peak value V_{x_max} at t_6, which reaches nearly twice the DC bus voltage V_{dc} under the light load condition. This drawback is similar to that of Mao's ZCT discussed in the preceding paragraph. In addition, at both turn-on and trun-off, additional resonant current portions are superimposed on top of the main device current waveform, increasing the device current stress. Therefore, the alternative scheme is not preferable.

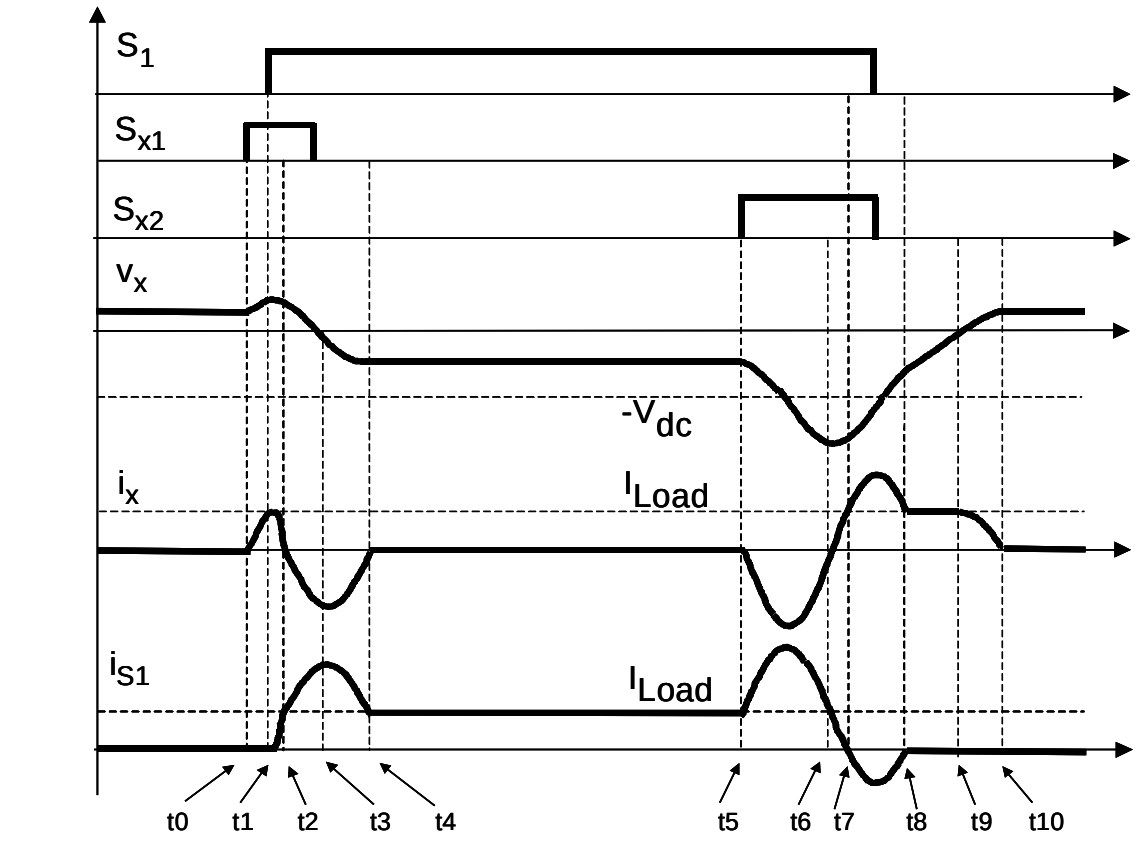

(a)

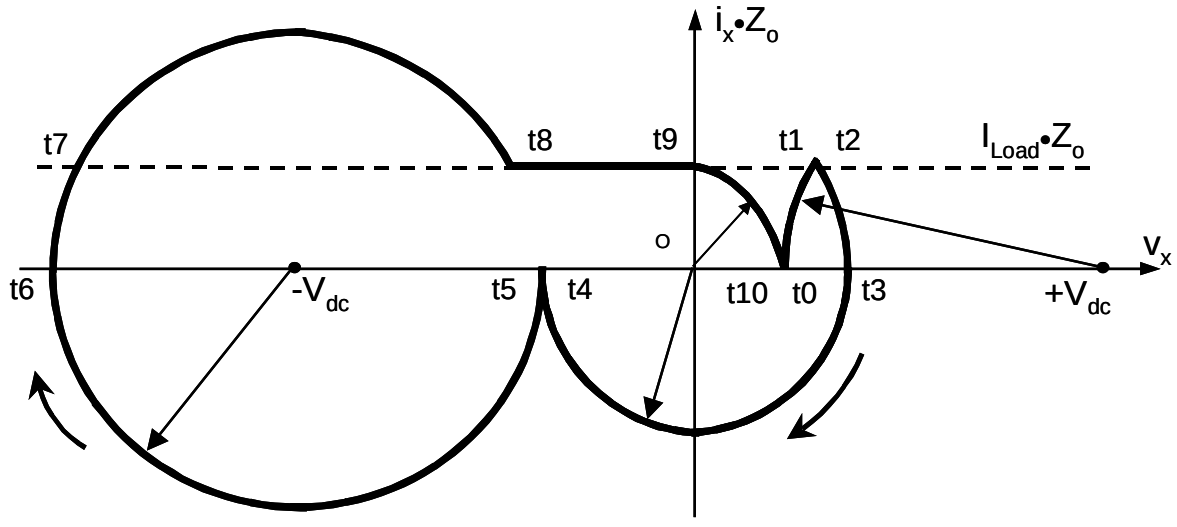

(b)

Figure 2.11. An alternative to the proposed ZV/ZCT scheme:
(a) operational waveforms; and
(b) state-plane trajectory.

2.4. General Design Criteria of the New Six-Switch ZV/ZCT Scheme

2.4.1. LC Resonant Tank Elements

As illustrated in the state-plane trajectory of the proposed ZV/ZCT scheme in Figure 2.9, without losing much accuracy, the resonant current peak at the turn-off transition, I_{xpk}, can be estimated as

$$I_{xpk} \approx \frac{V_{dc} - I_{Load} \cdot Z_o}{Z_o}. \tag{2.6}$$

Equation (2.6) implies that I_{xpk} tends to decrease as load current becomes heavier. The *LC* resonant tank should be designed based on the maximum load current subjected to the zero-current turn-off, I_m. When I_{Load} equals I_m, Equation (2.6) becomes

$$I_{xpk} = \frac{V_{dc}}{Z_o} - I_m. \tag{2.7}$$

To ascertain the zero-current turn-off, I_{xpk} must be greater than I_m. This leads to

$$\frac{V_{dc}}{Z_o} - I_m > I_m. \tag{2.8}$$

Correspondingly, one design variable k is defined as

$$k = \frac{I_{xpk}}{I_m}. \tag{2.9}$$

Combining Equations (2.7) and (2.9) yields

$$Z_o = \frac{V_{dc}}{(k+1) \cdot I_m}. \tag{2.10}$$

Obviously, k must be greater than 1. A detailed analysis of the design optimization will be addressed in Chapter 5, as will the description of two 55-kW ZCT prototype inverters for EV motor drives that are developed based on the proposed schemes. It is found that k can be selected

within a relatively large range around 1.5, which can result in a low additional conduction loss caused by the ZCT commutations in the main and auxiliary circuits.

The above discussion on determining Z_o is based on a rough approximation, as indicated by Equation (2.6), which is adequate and easy to use in most practical designs. A more accurate but complicated analysis on determining Z_o is provided in Appendix A.

Another variable to be considered is the resonant time period T_o. In order to reduce the switching losses, this period is related to the carrier lifetime in the semiconductor devices, such that the remaining free carriers will mostly recombine before voltage is reapplied to a switch or diode after turn-off. T_o also controls the di/dt of the diode current at the turn-off of the diodes. So a longer T_o is desirable. On the other hand, it should not be too long; otherwise, it will largely limit the duty cycle due to the time occupied by the resonant processes.

Once the k, Z_o and T_o are determined, the resonant tank parameters are designed as

$$L_x = Z_o \frac{T_o}{2\pi}, \tag{2.11}$$

and

$$C_x = \frac{L_x}{Z_o^{\,2}}. \tag{2.12}$$

2.4.2. Control Timings

Referring to the operational waveforms shown in Figure 2.5, at the turn-on transition, the bottom auxiliary switch S_{x2} is first turned on at t_0. At t_3, S_1 is turned on, and S_{x2} can be turned off under zero current at the same moment. At the turn-off transition, the other auxiliary switch S_{x1} is first turned on at t_5. S_1 is turned off under zero current between t_6 and t_7. S_{x1} is turned off between t_9 and t_{10} under zero current. In addition, the gate signal for S_2 should be removed before t_2 at the

turn-on, and can be applied after t_8 at the turn-off. A dead time T_d, which is around $(1/2)T_o$, is inserted between the complementary switching actions of S_1 and S_2. For the purpose of implementing the timing control, the delays between the main switch gate signals and the auxiliary switch gate signals need to be determined. These delays are: T_{ON}, the delay from S_{x2} turn-on to S_1 turn-on; T_{OFF1}, the delay from S_{x1} turn-on to S_1 turn-off; and T_{OFF2}, the delay from S_{x1} turn-on to S_{x1} turn-off.

2.4.2.1. The Turn-On Timing (T_{ON})

In order to guarantee zero-current turn-off of the main diode D_2 and to provide an opportunity for zero-voltage switching, S_1 should be turned on after t_2 so that i_x can be built up to a level higher than that of I_{Load}. The interval between t_2 and t_3 is to ensure sufficient time for D_2 to be completely "cleaned" in a practical circuit, which normally is relatively short. The turn-on timing T_{ON} should be varied based on the magnitude of load current I_{Load}. Referring to the state-plane trajectory shown in Figure 2.9, T_{ON} is derived as

$$T_{ON} = \frac{T_o}{2}(1+\frac{\alpha}{\pi}), \tag{2.13}$$

where

$$\alpha = sin^{-1}(\frac{IL_n}{1-IL_n}), \tag{2.14}$$

where IL_n is the normalized load current, given by

$$IL_n = \frac{I_{Load} \cdot Z_o}{V_{dc}}. \tag{2.15}$$

In Equation (2.13), T_o is the resonant time period. Against a changing IL_n, one curve for T_{ON}/T_o is plotted in Figure 2.12. In implementations with microprocessors, the curve and thus the control timing can be realized using a mapping table technique.

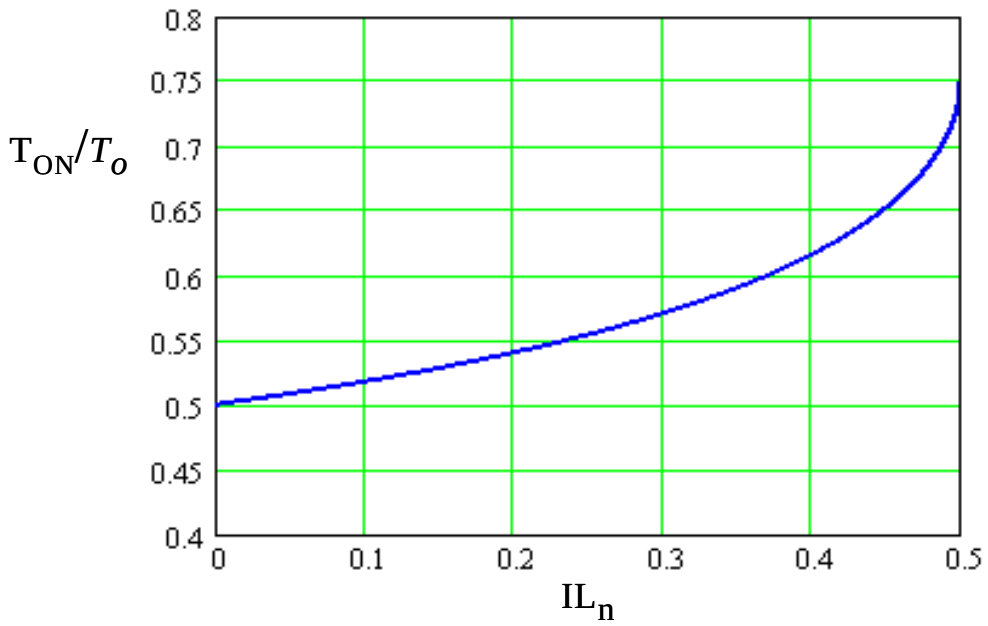

Figure. 2.12. A curve for the ZV/ZCT turn-on timing T_{ON}/T_o against the normalized load current IL_n (From Equation (2.8), a meaningful IL_n should be less than 0.5).

2.4.2.2. The Turn-Off Timings (T_{OFF1} and T_{OFF2})

S_1 is turned off between t_6 and t_7 under zero current, and clearly, T_{OFF1} can be fixed to $(1/4)T_o$. S_{x1} is turned off between t_9 and t_{10} under zero current. Referring to the state-plane trajectory in Figure 2.9, within t_7 and t_8, C_x is linearly charged by I_{Load}. Without losing much accuracy, the voltage variation across C_x, Δv_x, is estimated as

$$\Delta v_x \approx V_{dc} - \sqrt{(V_{dc} - I_{Load} \cdot Z_o)^2 - (I_{Load} \cdot Z_o)^2} \ . \tag{2.16}$$

With the normalization specified in Equation (2.15), the time interval $[t_7, t_8]$ is derived as

$$[t_7, t_8] = C_x \frac{\Delta v_x}{I_{Load}} = \frac{T_o}{2\pi} \cdot \frac{1 - \sqrt{1 - 2 \cdot IL_n}}{IL_n} . \tag{2.17}$$

The delay from t_5 to t_9 is obtained as

$$[t_5, t_9] = \frac{T_o}{2}(1 + \frac{\beta}{\pi}) + [t_7, t_8] , \tag{2.18}$$

where

$$\beta \approx \cos^{-1}\left(\frac{IL_n}{1-IL_n}\right). \tag{2.19}$$

The delay from t_5 to t_{10} is found to be

$$[t_5, t_{10}] = [t_5, t_9] + \frac{T_o}{2}. \tag{2.20}$$

Against a changing IL_n, Figure 2.13 plots two curves for the delays [t_5, t_9] and [t_5, t_{10}]. They provide a timing region in which S_{x1} is turned off between t_9 and t_{10} under zero current. It can be seen that T_{off2} can be fixed to a time located in this region over a changing IL_n, such as $1.1T_o$.

These control timings are explained based on the I_{Load}>0 case, and are symmetrical to those of I_{Load}<0. Although the scheme uses the load current information, no additional sensor is needed, since this information is already available from other control functions in the inverters. For modern three-phase inverters, which are normally controlled by digital signal processors (DSP), it is easy to implement the control timings, including the variable timing for the turn-on.

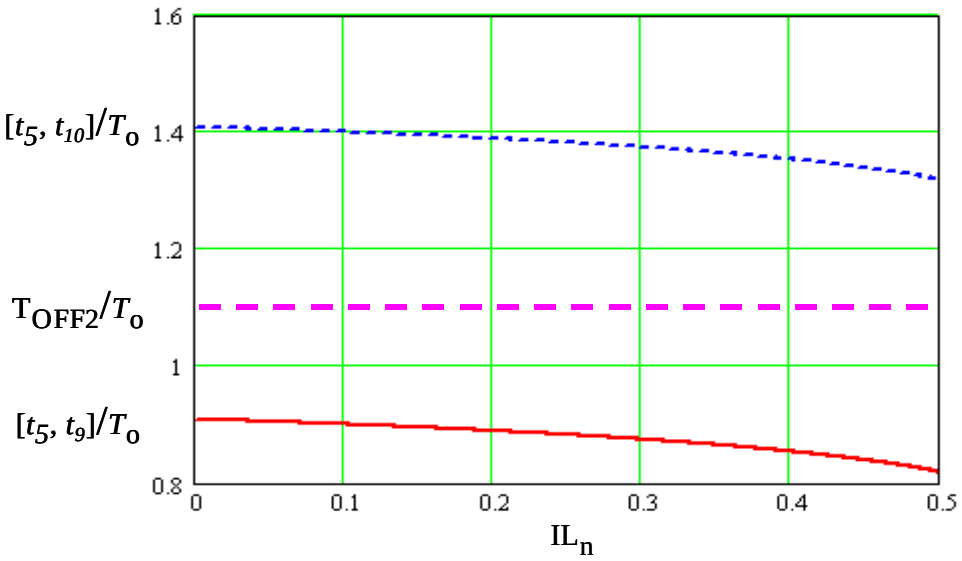

Figure 2.13. Curves for the ZV/ZCT turn-off timing T_{OFF2}/T_o against the normalized load current IL_n.

2.5. Experimental Verification on a 5-kW Prototype

To prove the proposed ZV/ZCT concept, a 5-kW single-phase prototype inverter is built and tested at a switching frequency of 20 kHz under a DC bus voltage of 320 V. The major inverter devices and components are listed as follows:

- Main device: Toshiba MG100J2YS50 half-bridge IGBT module (100-A/600-V);
- Auxiliary device: Toshiba MG50J2YS50 half-bridge IGBT module (50-A/600-V);
- Resonant capacitor: 0.2-μF/630-V (polypropylene film); and
- Resonant inductor: 2 μH (Magnetics MPP 55894 core).

The soft-transition experimental waveforms are shown in Figure 2.14, where i_x is the resonant inductor current, v_x is the resonant capacitor voltage, i_s is the main switch current, and v_{ce} is the main switch voltage. The experimental waveforms agree closely with the theoretical waveforms shown in Figure 2.5. It should be mentioned that in order to directly measure the switch current, no laminated bus bar is used in the prototype. This layout inevitably causes some parasitic ringing in the waveforms.

For comparison purposes, the 5-kW prototype is implemented with both a conventional hard-switching and the soft-transition functions, using a piggyback design. With the same set of hardware, the control circuit has an option of operating in the hard-switching mode by simply disabling the auxiliary switches. It also has another option of operating according to Mao's ZCT scheme, since both Mao's scheme and the proposed scheme are developed for the same circuit configuration, which is the six-switch ZCT inverter. Figure 2.15 compares the main switch oscillograms under the hard-switching, Mao's ZCT, and the proposed ZV/ZCT conditions.

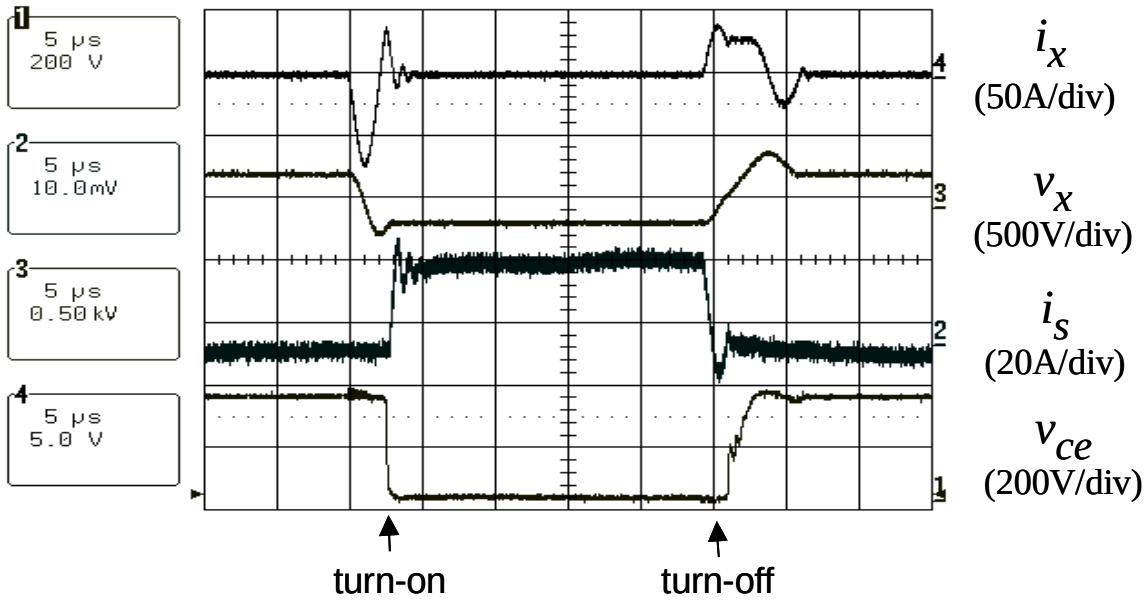

Figure 2.14. Waveforms of the six-switch ZV/ZCT scheme measured at a 5-kW prototype.

As shown in Fig. 2.15(a), there is a huge current spike in the hard-switching turn-on, which is caused by the diode reverse-recovery problem. In Mao's ZCT turn-on, as shown in Fig. 2.15(b), the current spike is indeed reduced as compared with the hard-switching turn-on, but a current spike is still observed when the switching current starts to rise, which indicates that a certain amount of reverse-recovery current still remains in the opposite diode when the switch is turned on. Meanwhile, it is found that the switch is still turned on under the full DC bus voltage. For the proposed ZV/ZCT turn-on shown in Figure 2.15(c), the switch voltage has decreased to zero before the switch current starts to rise, and there is virtually no overlap between the voltage and current waveforms at the turn-on transition. Moreover, the high-frequency ringing in both the hard-switching and Mao's ZCT turn-on current waveforms are basically eliminated in the proposed ZV/ZCT turn-on current waveform, which indicates that the opposite diode is turned off under a completely zero-current condition.

For the turn-off transitions, as shown in Figures 2.15(e) and (f), both ZCT schemes realize the zero-current turn-off (the negative portion of the switching current is conducted by the anti-parallel diode), and the voltage overshoot and high-frequency ringing in the hard-switching turn-off shown in Fig. 2.15(d) are basically eliminated. Yet a resonant current portion is superimposed on top of the switch current waveform in the Mao's ZCT, but there is no additional resonant current portion added on top of the switch current in the proposed ZV/ZCT. This difference is caused by the different circuit operations.

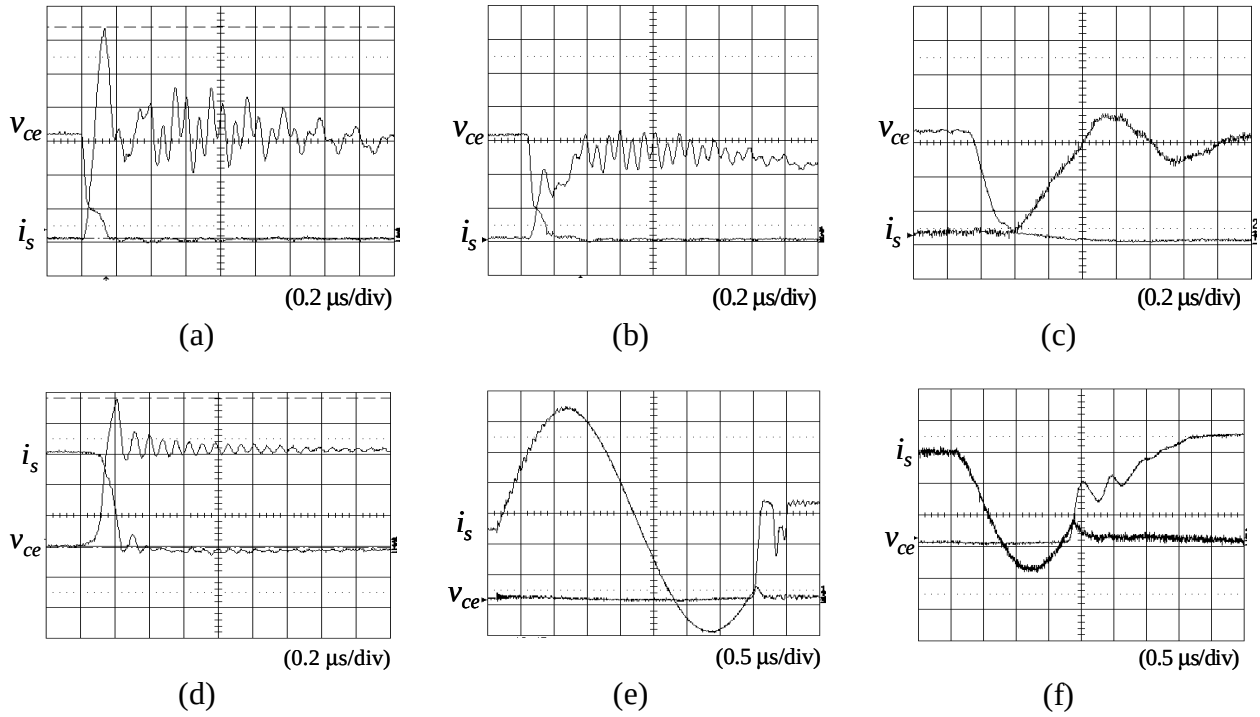

Figure 2.15. Comparison of switching waveforms measured at the 5-kW prototype (v_{ce}: 100 V/div, i_s: 10 A/div):

(a) hard-switching turn-on; (b) Mao's ZCT turn-on; (c) the proposed ZV/ZCT turn-on;

(d) hard-switching turn-off; (e) Mao's ZCT turn-off; and (f) the proposed ZV/ZCT turn-off.

Experimental results show that the switching loss reduction for this 5-kW prototype is also significant. The hard-switching turn-off energy is 1.7 mJ, and the turn-off energy for both ZCTs is about 0.3 mJ, which represents a reduction by nearly 85%. The hard-switching turn-on energy is 1.1 mJ, the Mao's ZCT turn-on energy is 0.6 mJ, and the proposed ZV/ZCT turn-on energy is 0.3 mJ. Compared to hard switching, the proposed ZV/ZCT reduces the turn-on loss by 70%, and reduces the total switching loss by about 80%. Compared to Mao's ZCT, the proposed ZV/ZCT reduces the turn-on loss by 50%, and reduces the total switching loss by about 35%.

For further comparison, by measuring i_x and v_x simultaneously at the X-Y display mode of the oscilloscope, the state-plane trajectories of the proposed ZV/ZCT and Mao's ZCT are obtained and shown in Figure 2.16. It can be seen that both agree with the theoretical trajectories shown in Figures 2.9 and 2.10. For the trajectory of the proposed ZV/ZCT (Figure 2.16(a)), during the turn-on transition (A->B->C), i_x reaches the load current level at point B, which visualizes that the current in the main diode has been totally diverted to the auxiliary circuit before the opposite main switch is turned on. During the turn-off transition (C->D->E->A), the maximum resonant capacitor voltage within one switching cycle occurs at point E, which is about 450V, or 1.4 times the DC bus voltage (320V). For the trajectory of Mao's ZCT (Figure 2.16(b)), during the turn-on transition (A->B->C), the peak of i_x can no longer reach the load current level at point B, indicating that a certain amount of current still remains in the main diode when the opposite main switch is turned on at this moment. The maximum resonant capacitor voltage occurs at point D during the turn-off transition (C->D->E->A), which is about 580 V, or close to twice the DC bus voltage. It is also observed that the circular trajectory is actually distorted; this is due to the parasitic losses in the circuit.

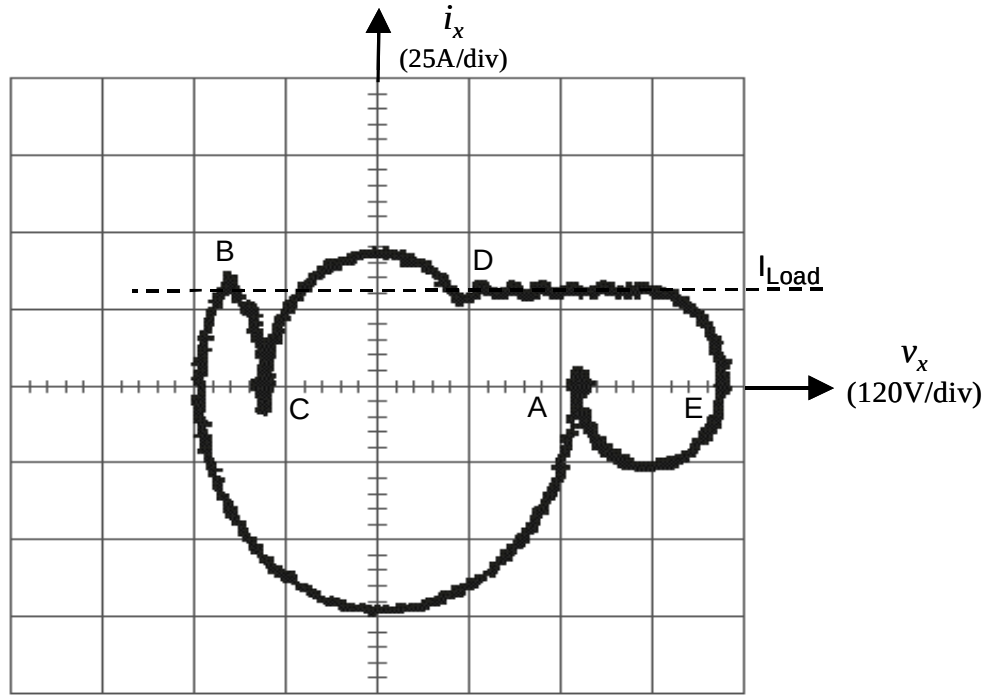

(a)

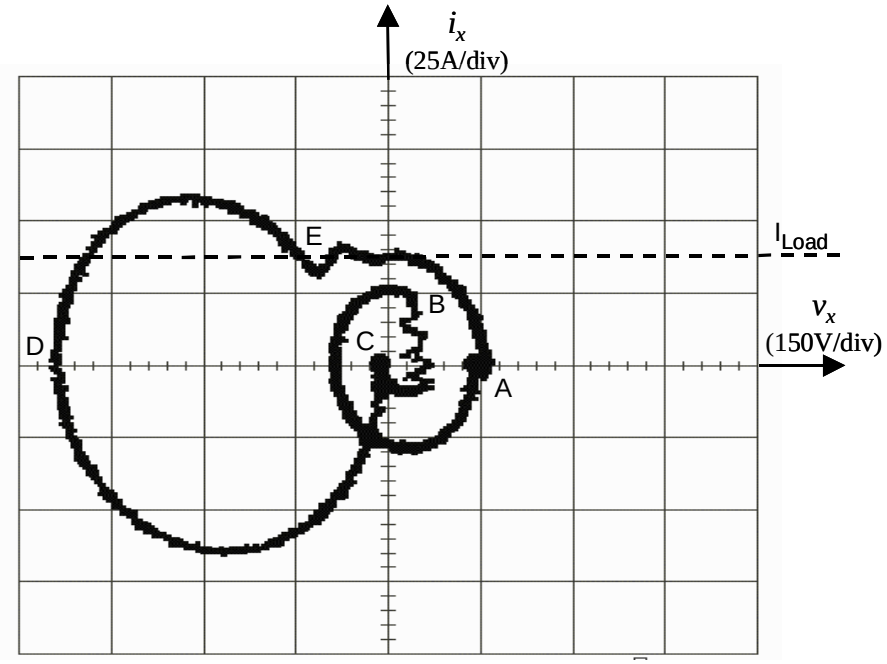

(b)

Figure 2.16. Comparison of state-plane trajectories measured at the 5-kW prototype:
(a) operated according to the proposed ZV/ZCT scheme; and
(b) operated according to Mao's ZCT scheme.
(A->B->C: Turn-on; C->D->E->A: Turn-off)

2.6. Summary

This chapter proposes a new soft-transition scheme for the six-switch ZCT inverter circuit that improves the performance by providing an opportunity to achieve zero-voltage turn-on for the main switches, and in the meantime enabling all main switches and auxiliary switches to be turned on and off under zero-current conditions. The significance of the proposed scheme is that it introduces a solution for minimizing the total inverter switching losses. The philosophy behind the proposed scheme is as follows: It fully utilizes the bi-directional property of the inverter load current and thus uses two auxiliary switches to alternately assist the turn-on and turn-off transitions of each main switch, without adding extra devices or components over the existing ZCT inverter circuit. As a result, the proposed scheme can generate sufficient resonant energy to build up a resonant current that completely diverts the currents in the main circuit at both turn-on and turn-off transitions. Since inverters are symmetrical rectifiers, the proposed scheme is suitable for three-phase power-factor-correction (PFC) rectifiers as well, such as those discussed in [C21].

Based on experimental results on a 5-kW prototype, the proposed ZV/ZCT scheme has demonstrated the following promising features.

- Compared with the hard-switching condition, the turn-on loss is reduced by about 70%, the turn-off loss is reduced by about 85%, and the total switching loss is reduced by about 80%. The voltage overshoot and high frequency ringing at the turn-off transition are basically eliminated.

- Compared with the existing ZCT scheme, the turn-on loss is reduced by about 50%, and the switch current at turn-on becomes much cleaner because the main diode is turned off under a complete zero-current condition. Meanwhile, the resonant capacitor voltage stress is reduced by

30%, and the current and thermal stresses are distributed evenly among the auxiliary devices over every switching cycle.

- The soft transition for each phase is executed independently from the main controller, and requires no modification to normal PWM algorithms.

Yet, as with the existing ZCT inverters, six auxiliary switches are still used in the proposed ZV/ZCT inverter, which are costly and complicated. Exploration of simple low-cost soft-switching topologies that maintain desirable soft-switching features will be conducted in the next chapter.

Chapter 3

A Simplified Three-Phase Zero-Current-Transition Inverter with Three Auxiliary Switches— The Three-Switch ZCT Inverter

Most existing three-phase soft-switching inverters with fewer than six auxiliary switches have fundamental drawbacks in performance. There are a few topologies with six auxiliary switches that can potentially achieve good performance, including the six-switch ZV/ZCT inverter proposed in Chapter 2, but the big disadvantage is the high complexity and cost associated with the auxiliary switches. It is a challenge to achieve the desirable soft-switching features with simple low-cost auxiliary circuits.

In an effort to seek simple low-cost soft-switching solutions, this chapter proposes a new ZCT inverter topology that requires only three auxiliary switches— the three-switch ZCT. With considerable reduction in device count, cost, and size, the proposed ZCT topology realizes zero-current turn-off for all main and auxiliary switches, and provides soft commutation for all diodes. Meanwhile, it still requires no modification to normal PWM algorithms. The operation principles and general design criteria are described. Experimental results on a 5-kW prototype are provided to verify the proposed concept.

3.1. Search for a Desirable Low-Cost Soft-Switching Inverter

A desirable low-cost soft-switching inverter topology should use a simple auxiliary circuit, in particular one with a minimum count of auxiliary switches. Meanwhile, it should be piggyback, meaning that it requires no modification to normal PWM algorithms. It should also realize soft commutation for all switches and diodes at every transition in all operational modes. Existing soft-switching inverter topologies with fewer than six auxiliary switches, however, cannot meet

the expectations. Those topologies cover both DC-side and AC-side topologies and include both zero-voltage switching and zero-current switching. They are reviewed in details in Chapter 1. For ease of addressing the issues, their major drawbacks are summarized briefly in this section.

Most of these topologies require modifications to normal SVM schemes or are incompatible with PWM control, causing system-level penalties. The RDCL inverters suffer from a high device voltage problem, and the DPM that is normally used causes an undesirable sub-harmonic problem [B1]-[B10]. The QRDCL inverters normally have high conduction and switching losses in the DC-rail auxiliary switches that are inserted into the main power flowing path [B11]-[B15]. Meanwhile, the modified PWM schemes typically cause extra switching events in the main switches, and increase the output current ripple.

The DC-rail ZVT inverter requires complicated implementations [B16]. Another version of the DC-rail ZVT topology changed the DC-rail switch into a diode [B17], which blocks the bi-directional power flow. The DC-rail zero-current-switching topology with two auxiliary switches has high conduction loss in the auxiliary switches that are placed in series with the main power path [B18]. Meanwhile, a resonant inductor is in series with each main switch, and can causes excessively high voltage stress if for any reason the zero-current switching is not achieved.

In the AC-side topologies, the simplified ZVT inverters with three auxiliary switches are not feasible in practical implementations because of the problems associated with turning off the auxiliary switches [C8] [C9]. For the simplified ZVT inverters with one or two auxiliary switches [C10]-[C13], additional hard turn-off events in the main switches are caused by the modified SVM schemes. The auxiliary circuit either has high conduction loss [C10][C11], or is turned off under a hard-switching condition with high current [C12]. An evaluation has shown that these low-cost ZVT inverters actually have worse efficiency than hard-switching inverters

[F4]. Implementations of the recently proposed ZVT inverters with two auxiliary switches requires complicated auxiliary circuits with additional SCR switches or saturable cores [C14]-[C16].

3.2. Derivation of the Three-Switch ZCT Inverter Topology

As discussed above, a lot of effort has been made to simplify the ZVT topologies, but the resultant topologies are still undesirable. From the other category of the soft-switching topology family, ZCT inverters are investigated in order to obtain a desirable low-cost soft-switching solution. For ease of illustration, the existing ZCT inverter circuit, which uses six auxiliary switches, is shown again in Figure 3.1. Originating from the McMurray inverters for the SCR forced-current commutations [C17], this topology has existed for about four decades. For soft-switching research with modern gate-turn-off devices, such as IGBTs, several ZCT schemes have been developed for this topology [C19] [C20]. In Chapter 2, a new ZV/ZCT scheme is proposed that realizes zero-current turn-off for all main switches, diodes, and auxiliary switches, and provides an opportunity for zero-voltage turn-on of the main switches.

The philosophy behind the six-switch ZCT circuit diagram, which is also behind most existing soft-switching inverters, is that in order to be able to piggyback (thus requiring no modification to normal PWM), each main switch should have its own auxiliary switch for zero-current turn-off; therefore, six auxiliary switches (S_{x1}~S_{x6}) are required. In one phase leg of the inverter (Figure 3.2), depending on the load current I_{Load} directions, there are two current commutation patterns: between the top switch S_1 and the bottom diode D_2, and between S_2 and D_1. For zero-current turn-off of S_1, a resonant current i_x flowing from terminal Ax to A must be generated in order to force the current through S_1 to zero before S_1 is turned off, and the required current path can be provided by the top auxiliary switch S_{x1}. For zero-current turn-off of S_2, the i_x

flowing from A to Ax must be generated in order to force the current through S_2 to zero, and the required current path can be provided by S_{x2}.

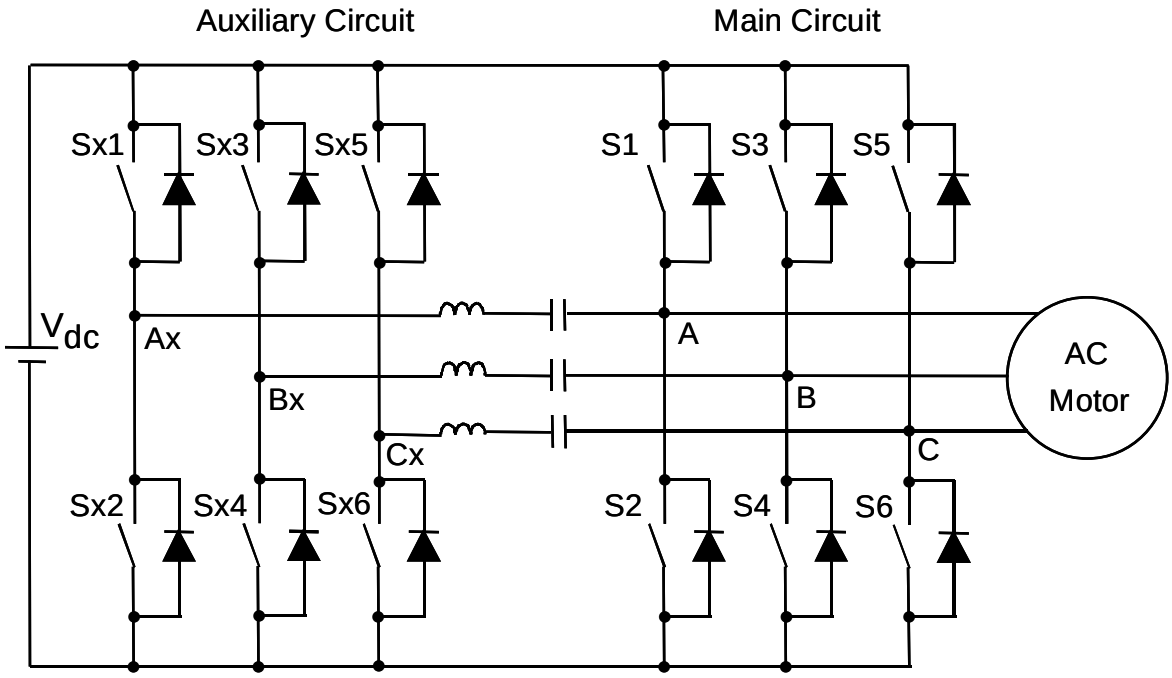

Figure 3.1. The existing ZCT inverter with six auxiliary switches.

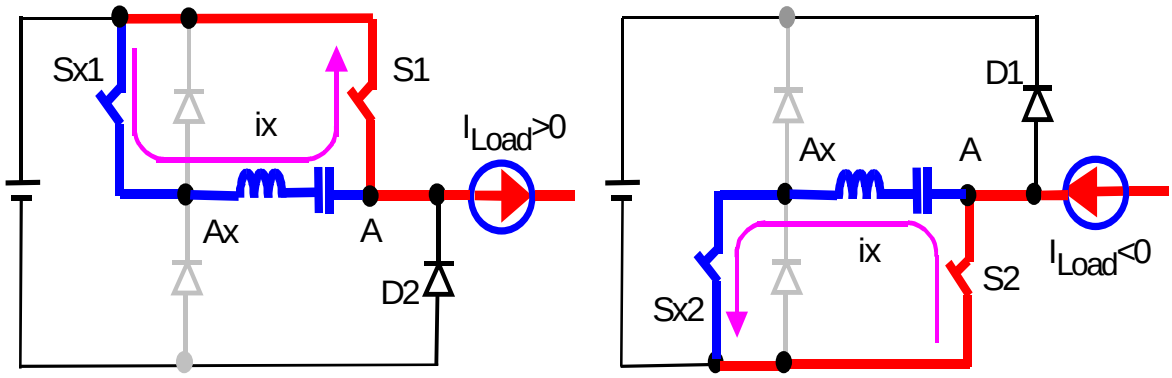

Figure 3.2. Turn-off commutations in one phase leg of the existing six-switch ZCT inverter: (a) $I_{Load}>0$; and (b) $I_{Load}<0$.

From the preceding discussion, one can realize that the basic requirement for ZCT is to inject a bi-directional resonant current that can divert the currents from both main switches to the auxiliary circuit prior to switching transitions. This was accomplished by using two auxiliary switches in each phase of the six-switch ZCT circuit. The issue then is how to use a minimum number of auxiliary switches to achieve soft commutation for all the main switches, auxiliary switches and diodes in all operational modes, and in the meantime to maintain normal PWM algorithms. Figure 3.3 shows the circuit diagram of the proposed ZCT inverter with three auxiliary switches— the three-switch ZCT. The philosophy behind this circuit diagram is that instead of assigning one auxiliary switch to each main switch, it employs only one auxiliary switch for each phase leg (for instance, S_{xa} for phase A). Clearly, this structure still allows independent ZCT commutation for each phase, and thus requires no modification to normal PWM algorithms.

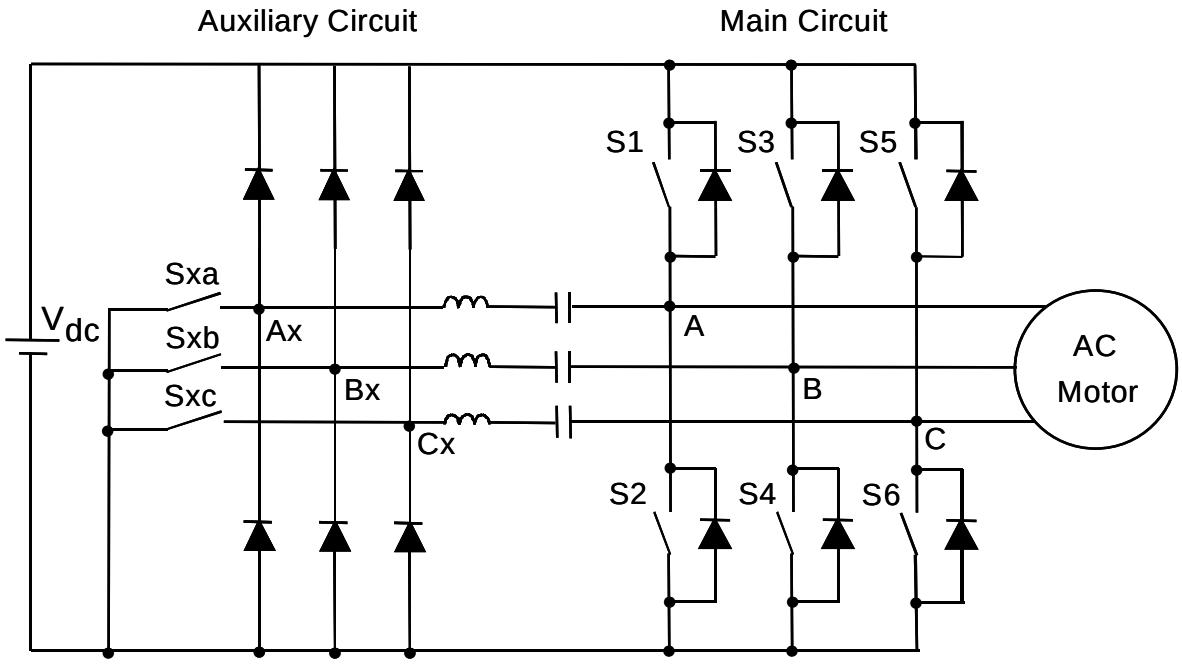

Figure 3.3. The proposed ZCT inverter topology with three auxiliary switches.

As can be seen, the central parts of the ZCT topologies are the series *LC* resonant tanks in the auxiliary circuits. The three-switch ZCT circuit is developed based on the fact that the *LC* resonance can create a bi-directional current; the role of the auxiliary switches is to start the required resonance and to provide flow paths for the resonant current at certain operational stages. As illustrated in Figures 3.4(a) and (b), when a resonance is started by the turn-on of S_{xa}, a resonant current i_x begins to build up in a sinusoidal waveform, flowing from A to Ax. After half a resonant cycle, i_x reverses its direction and flows from Ax to A. During $I_{Load}>0$, auxiliary diode D_{xa} can provide the resonant current path (from Ax to A) that is required for the zero-current turn-off of S_1. During $I_{Load}<0$, auxiliary switch S_{xa} can provide the resonant current path (from A to Ax) that is required for the zero-current turn-off of S_2. Therefore, using one auxiliary switch can achieve zero-current turn-off for both main switches.

Normally, ZCT refers to a reduction in the switching turn-off loss. However, using the same auxiliary switch can also reduce the turn-on loss of both main switches, which is mainly caused by the diode reverse recovery current. As illustrated in Figures 3.4(c) and (d), during $I_{Load}>0$, auxiliary diode D_{xa} provides a path (from Ax to A) for the resonant current that reduces the current through the bottom main diode D_2 before S_1 is turned on; during $I_{Load}<0$, auxiliary switch S_{xa} provides a path (from A to Ax) for the resonant current that reduces the current in the top main diode D_1 before S_2 is turned on.

Furthermore, the gate signal for S_{xa} can be removed at the moment when i_x flows through diode D_{xa}. Thus, the auxiliary switch is turned off under zero current. Since this event begins after the positive half-resonant cycle, and lasts through the negative half-resonant cycle, the zero-current turn-off for the auxiliary switch can be easily guaranteed in practical implementations.

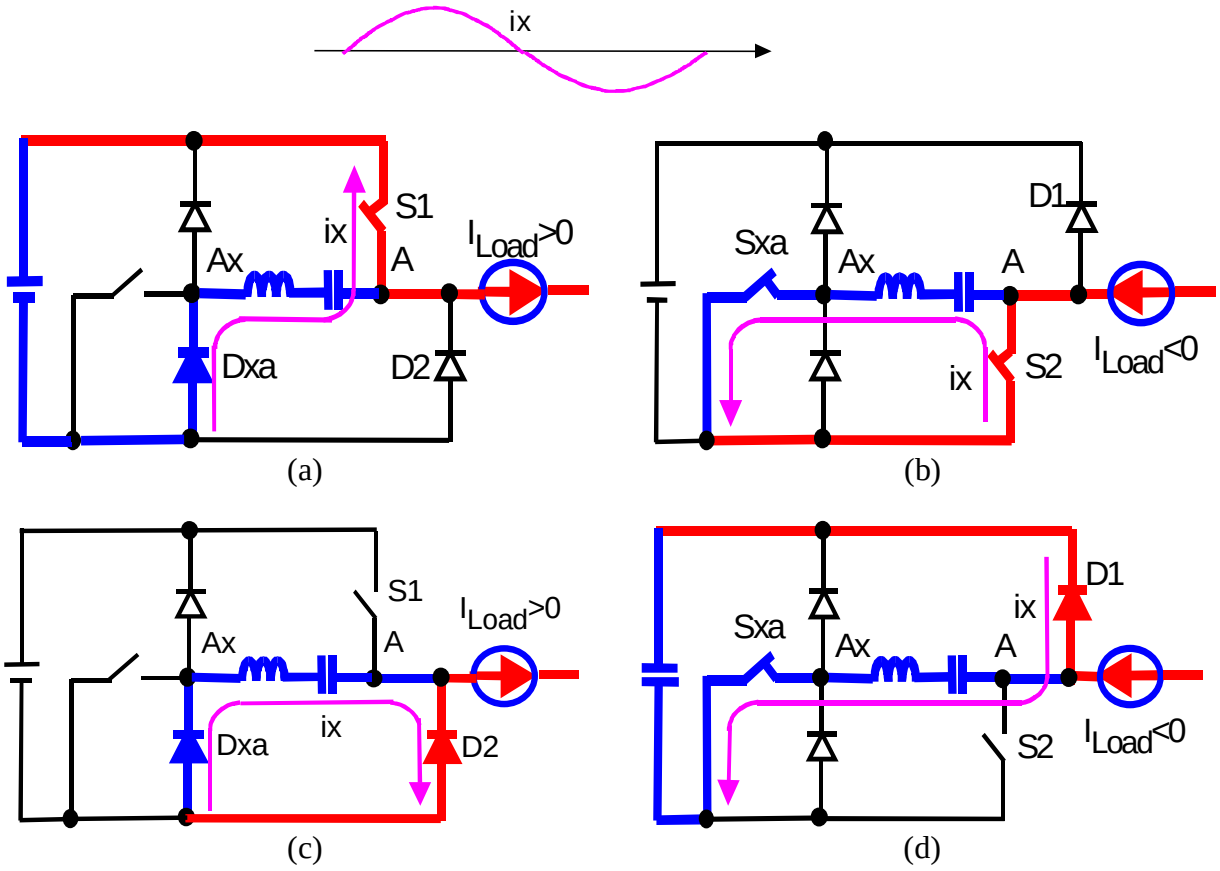

Figure 3.4. Using only one auxiliary switch can realize soft commutation for all switches and diodes in one phase leg:
(a) S_1 turn-off; (b) S_2 turn-off;
(c) S_1 turn-on; and (d) S_2 turn-on.

It is possible to simplify the existing six-switch ZCT topology. From the standpoint of circuitry, either the top or the bottom auxiliary switches can be removed. The number of auxiliary switches is thus reduced from six to three. With the bottom auxiliary switches commonly grounded, the electromagnetic interference (EMI) can be reduced and the circuit layout can be simplified. Therefore, it is preferable to remove the top three auxiliary switches and retain the bottom three. The final three-phase circuit obtained is shown in Figure 3.3, and the detailed phase-leg circuit is shown in Figure 3.5, in which the purpose of the top diode D_{ca} is to clamp voltage across the auxiliary switch.

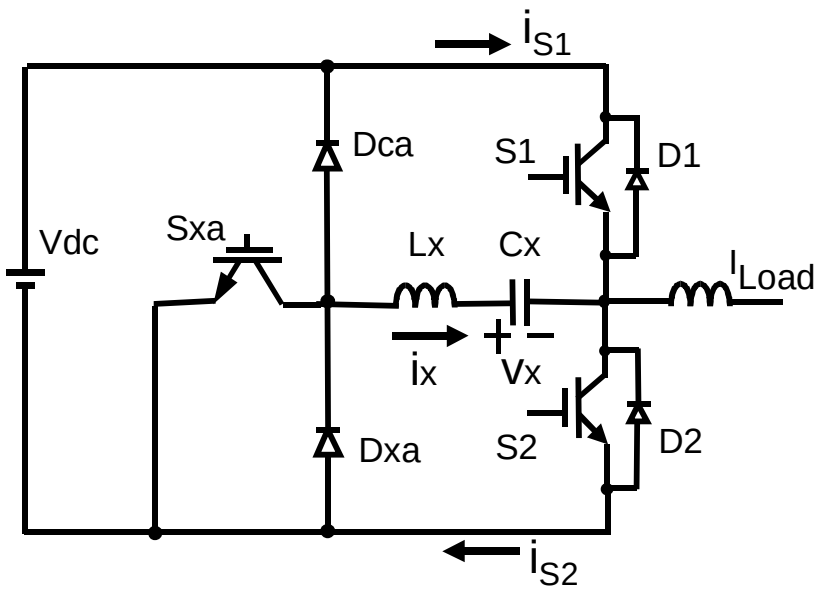

Figure 3.5. One phase leg of the proposed three-switch ZCT inverter.

3.3. Circuit Operations of the Three-Switch ZCT Inverter

Since the bi-directional inverter load current I_{Load} is conducted in a totem-pole manner, only one main switch needs to be soft-switched for each phase during each half-load-current-line cycle. Based on the I_{Load} directions, when a decision is made to turn on or turn off the main switch that needs to be soft-switched, the auxiliary switch is activated for a short time to assist the switching transition. In high-frequency DC/DC modes, the circuit operations during $I_{Load}>0$ and $I_{Load}<0$ are respectively equivalent to two ZCT schemes presented in [C20]. However, for three-phase inverters, those ZCT schemes in [C20] require *six* auxiliary switches. The originality of the proposed topology is that for three-phase inverters, only *three* auxiliary switches are needed in order to achieve the same soft-switching conditions. The circuit operation during $I_{Load}>0$ will be summarized briefly. The circuit operation during $I_{Load}<0$ is not symmetrical to that during $I_{Load}>0$, and will be described in detail. The operation description starts with the switch turn-on transition. To simplify the analysis, the circuit parasitics, such as the

semiconductor junction capacitors and stray inductors, are ignored. I_{Load} and the DC bus voltage V_{dc} are assumed to be constant among switching cycles.

3.3.1. I_{Load}>0, the Positive Half-Load-Current-Line Cycle

I_{Load} is conducted through S_1 and D_2. Figure 3.6 shows the one-phase operational waveforms within one switching cycle. The polarities of voltages and directions of currents are defined in Figure 3.5.

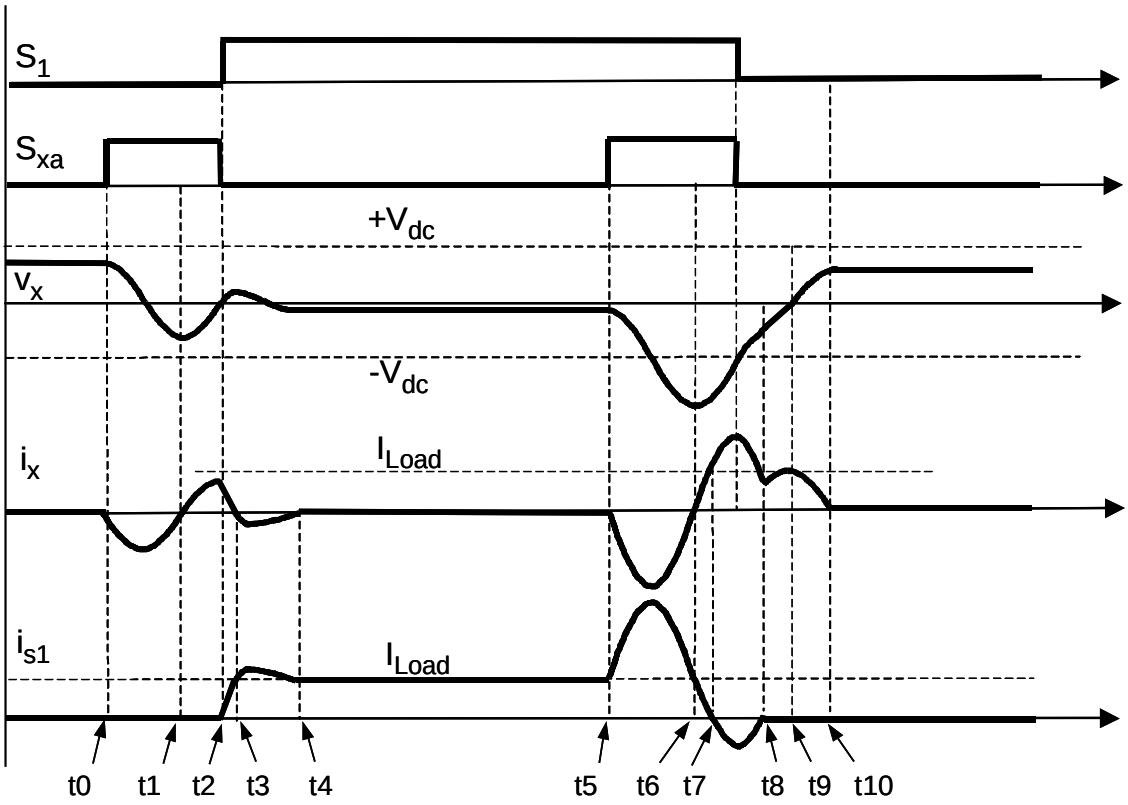

Figure 3.6. Operational waveforms of the three-switch ZCT inverter during I_{Load}>0.

Initially, I_{Load} freewheels through D_2. When it is time to turn on S_1, S_{xa} is first turned on at t_0, and then L_x and C_x begin to resonate. The resonant current i_x builds up and diverts the current through the main circuit. When i_x reaches its positive peak at t_2, the current through D_2 is reduced to near zero, at which point S_1 is turned on. The turn-on loss is reduced substantially because the

reverse recovery current in diode D_2 is reduced and the rise rate of the switch current is limited by L_x. Before S_1 is turned off, S_{xa} is turned on again at t_5. After t_7, i_x is greater than I_{Load}, the current through S_1 drops to zero, and its anti-parallel diode starts to conduct the surplus current. S_1 is turned off under zero current. In addition, S_{xa} is turned off at t_2 during the turn-on transition, and is turned off between t_7 and t_8 during the turn-off transition. Both turn-off events for S_{xa} occur under zero current, because D_{xa} conducts at these moments.

3.3.2. I_{Load}<0, the Negative Half-Load-Current-Line Cycle

I_{Load} is conducted through S_2 and D_1. The operation goes through eight topological stages, as shown in Figure 3.7. Operational waveforms within one switching cycle are shown in Figure 3.8. For ease of illustration, the polarity of v_x and direction of i_x are reversed from those shown in Figure 3.5. The initial stage is that I_{Load} freewheels through diode D_1. In the steady state, there is a positive voltage v_x across C_x, where $0<v_x<V_{dc}$. The v_x cannot be negative; otherwise, diode D_{ca} will conduct. The v_x cannot exceed V_{dc}; otherwise, diode D_{xa} will conduct.

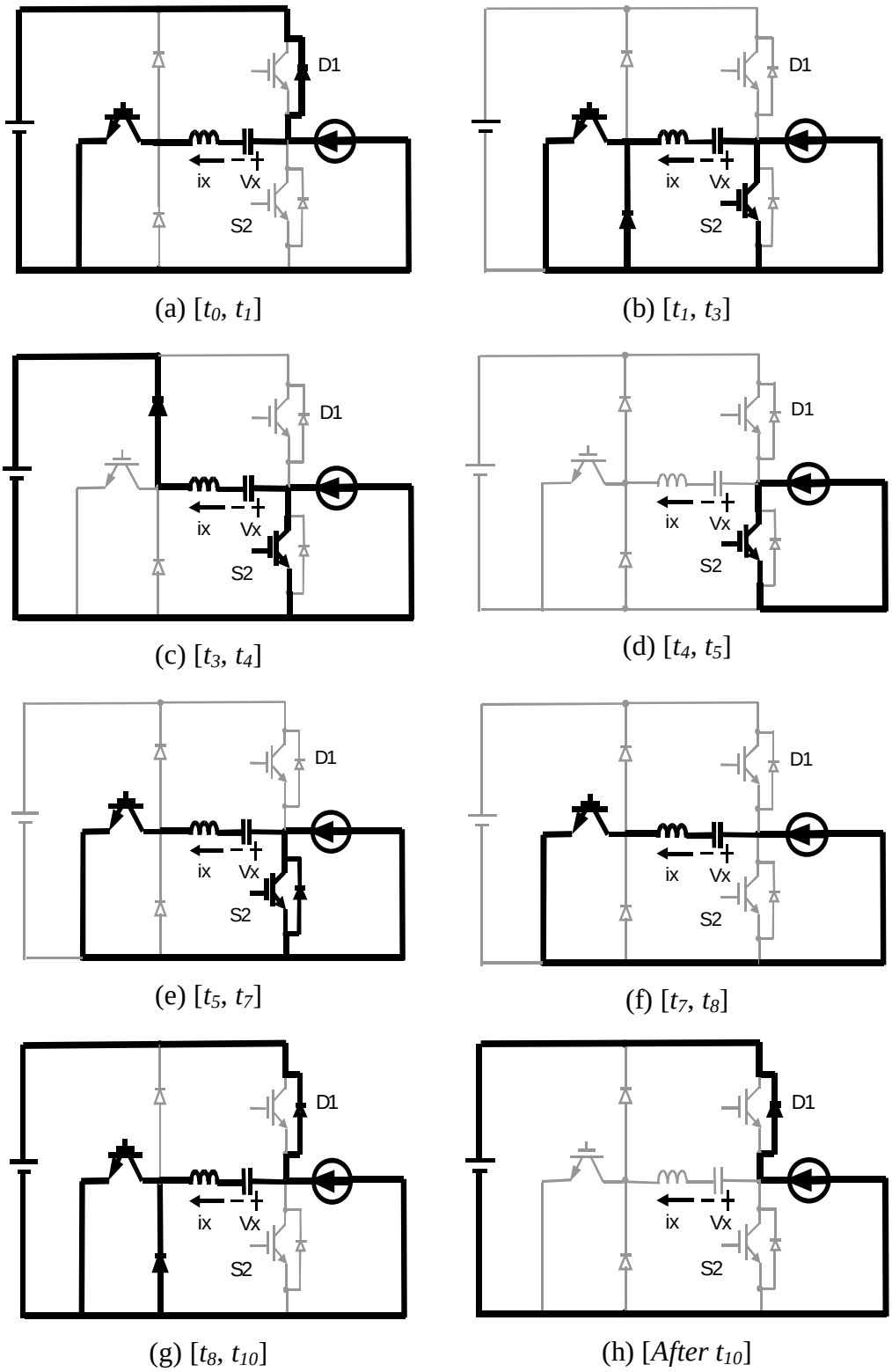

(a) [t_0, t_1] (b) [t_1, t_3]

(c) [t_3, t_4] (d) [t_4, t_5]

(e) [t_5, t_7] (f) [t_7, t_8]

(g) [t_8, t_{10}] (h) [*After* t_{10}]

Figure 3.7. Topological stages of the three-switch ZCT inverter during I_{Load}<0.

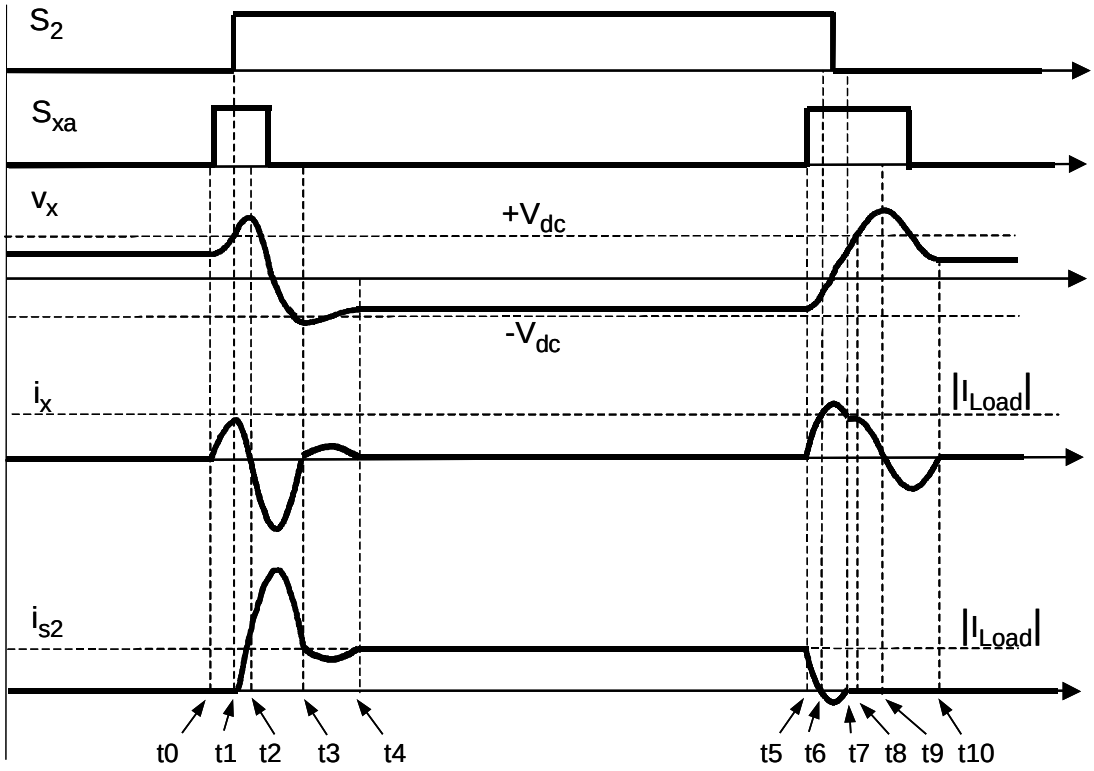

Figure 3.8. Operational waveforms of the three-switch ZCT inverter during $I_{Load}<0$ (direction of i_x and polarity of v_x are reversed from those in Figure 3.5).

a) Turn-On Transition I [t_0, t_1]: When a decision is made to turn on S_2, S_{xa} is first turned on at t_0, then L_x and C_x begin to resonate. When i_x reaches to its positive peak at t_1, the current through D_1 is reduced to near zero and S_2 is turned on with the reduced diode current and switching loss. The gate signal for the top main switch S_1 should be removed before t_1.

b) Turn-On Transition II [t_1, t_3]: After t_1, the resonant tank is short-circuited by S_2, and i_x decreases toward zero. At t_2, i_x drops to zero and v_x increases to a peak that is higher the V_{dc}. The resonance continues, and i_x is driven in the negative direction in which D_{xa} conducts. In this way, S_{xa} achieves zero-current turn-off.

c) Turn-On Transition III [t_3, t_4]: After half a resonant cycle, i_x returns to zero at t_3, and D_{xa} turns off naturally. At this point, since the magnitude of v_x is still greater than V_{dc}, the auxiliary

circuit continues to resonate. The i_x flows in the positive direction in which the clamping diode D_{ca} conducts.

d) Switch-On Stage [t_4, t_5]: At t_4, i_x again returns to zero, and D_{ca} turns off naturally. I_{Load} flows through switch S_2, and the PWM operation resumes.

e) Turn-Off Transition I [t_5, t_7]: Before S_2 is turned off, S_{xa} is turned on again at t_5. L_x and C_x begin to resonate. After t_6, i_x increases to I_{Load}, and the current through S_2 decreases to zero. As i_x continues to increase, the surplus current flows through the anti-parallel diode D_2. S_2 is turned off under zero current.

f) Turn-Off Transition II [t_7, t_8]: The resonance continues until t_7, at which point i_x falls to I_{Load}. D_2 turns off naturally. Since S_2 is off and D_1 is still reverse-biased, I_{Load} can flow only through the resonant tank, charging C_x linearly. At this point, the voltage across the resonant inductor is zero because the current is constant, so the voltage across D_1 equals the difference between V_{dc} and v_x.

g) Turn-Off Transition III [t_8, t_{10}]: At t_8, C_x is charged to V_{dc}, and D_1 starts to conduct. The resonant tank begins to resonate again. As i_x decreases, v_x continues to increase. At t_9, i_x returns to zero and v_x reaches a peak. The resonance continues, with the current now carried by diode D_{xa}. S_{xa} is turned off at zero current. In addition, the gate signal for the top main switch S_1 can be applied after t_8.

h) Diode-On Stage [after t_{10}]: The resonance continues until i_x returns to zero at t_{10}. I_{Load} is conducted by D_1, and the inverter resumes PWM operation until the next switching event for the main switch.

In summary, desirable soft-switching features are achieved with considerable reduction in device count, cost and size in the proposed three-switch ZCT inverter. It realizes zero-current

turn-off for all the main and auxiliary switches, and provides soft commutations for all the diodes. Meanwhile, it requires no modifications to normal PWM schemes.

3.4. General Design Criteria of the Three-Switch ZCT Inverter

To provide visual aids for design and control, the state-plane trajectories for both $I_{Load}>0$ and $I_{Load}<0$ cases are obtained and plotted in Figure 3.9. Referring to the waveforms in Figure 3.6 and 3.8, curves t_0-t_4 in Figure 3.9 depict the turn-on transitions, and curves t_5-t_{10} depict the turn-off transitions. In the circular trajectories, Z_o is the resonant tank impedance, and time flows in a clockwise direction. The time elapsed between two points is proportional to the angle subtended at the center, and the time elapsed for one circle equals the resonant time period T_o, given by

$$T_o = 2\pi\sqrt{L_x \cdot C_x} \,. \tag{3.1}$$

3.4.1. Requirements for Auxiliary Circuit Components

To ascertain the zero-current turn-off for both main switches, the resonant current peak at the turn-off transition I_{xpk} must be larger than the maximum load current subjected to the zero-current turn-off, I_m. As illustrated in Figure 3.9, without losing much accuracy, the magnitude of I_{xpk} for both $I_{Load}>0$ and $I_{Load}<0$ cases can be estimated as the same, which is about V_{dc}/Z_o. Thus, the requirements of the resonant tanks for both cases are the same. In other words, one set of *LC* tank elements, with two sets of control timings, can achieve ZCT commutations under two different I_{Load} directions.

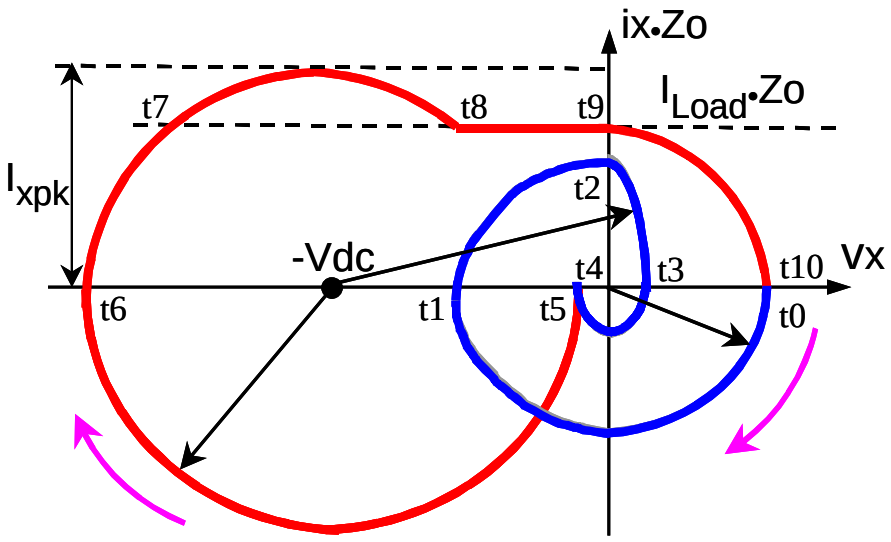

(a)

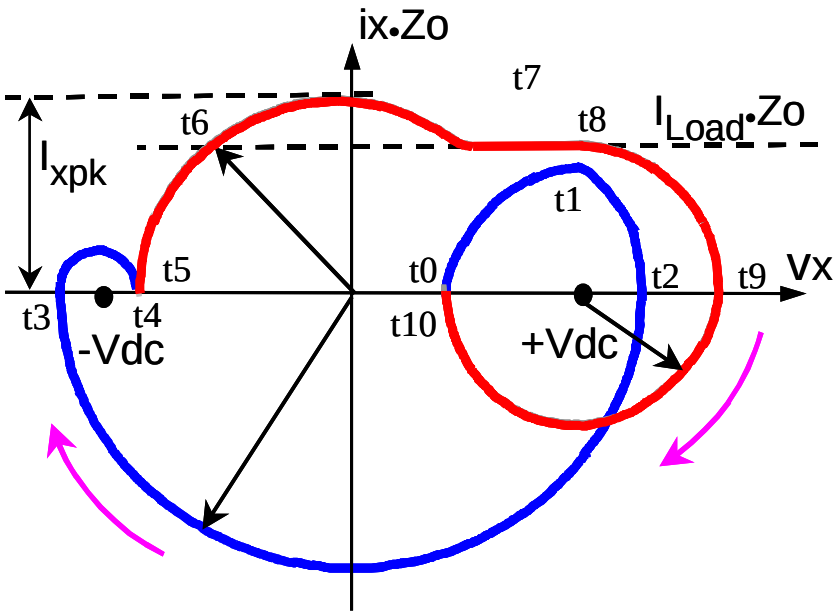

(b)

Figure 3.9. State-plane trajectories of the three-switch ZCT inverter under a bi-directional load current:
(a) $I_{Load}>0$ (direction of i_x and polarity of v_x follows Figure 3.5); and
(b) $I_{Load}<0$ (direction of i_x and polarity of v_x are reversed from Figure 3.5).

Once the I_{xpk} is identified, with a method similar to that for the six-switch ZV/ZCT inverter (see Section 2.4.1), it is obtained that

$$Z_o = \frac{V_{dc}}{k \cdot I_m}. \tag{3.2}$$

The choices of k and T_o are similar to the six-switch ZV/ZCT inverter, and the resonant tank parameters can also be calculated by Equations (2.11) and (2.12). In Chapter 5, with two 55-kW prototypes as design examples, comprehensive design considerations and trade-offs will be addressed.

Since the auxiliary switches are activated for only a short time at the main switch turn-on and turn-off transitions, the average current requirement is normally very low. Meanwhile, the auxiliary switch must conduct a high-peak resonant current of several microseconds pulse width (range of T_o), operating at a repetitive frequency of 10k~20 kHz (twice the switching frequencies). Thus, the device selection is based mainly on the peak current handling capability instead of on the DC current rating. The maximum resonant current peak in the proposed three-switch ZCT inverter is about V_{dc}/Z_o, which in fact is close to that in the six-switch ZCT inverters. Therefore, the proposed topology not only reduces the number of auxiliary switches from six to three, but also can retain the same switch power rating.

One unique advantage of the three-switch ZCT topology is that its auxiliary circuit is essentially immune to short-circuit failure. As can been seen in Figure 3.3, there is no path to allow current to directly shoot through the auxiliary switches from the DC bus. As a result, the conventional short-circuit protection functions, especially the de-saturation protection for IGBTs, are no longer needed in the gate drivers of the auxiliary switches. The simplification to the gate drivers further reduces the cost and increases the reliability.

3.4.2. Control Timings

3.4.2.1. I_{Load}>0

At the turn-on transition, S_{xa} is first turned on at t_0. Then, S_1 is turned on and S_{xa} is turned off at t_2. The delay from t_0 to t_2 can be found from Figure 3.9(a) to be $[t_0, t_2]=(3/4)T_o$. At the turn-off transition, S_{xa} is turned on again at t_5. S_1 is turned off between t_7 and t_8; meanwhile, S_{xa} is turned off at that same moment between t_7 and t_8, and the delay from t_5 is $(3/4)T_o$. In addition, the gate signal for S_2 is removed before t_1 at the turn-on, and can be applied after t_9 at the turn-off.

Referring to the control timings shown in Figure 3.10, which are delays from the auxiliary switch actions to the main switch actions, clearly $T_{ON}=(3/4)T_o$ and $T_{OFF}=(3/4)T_o$. A dead time T_d, which is around $(3/4)T_o$, is inserted between the complementary switching actions of S_1 and S_2.

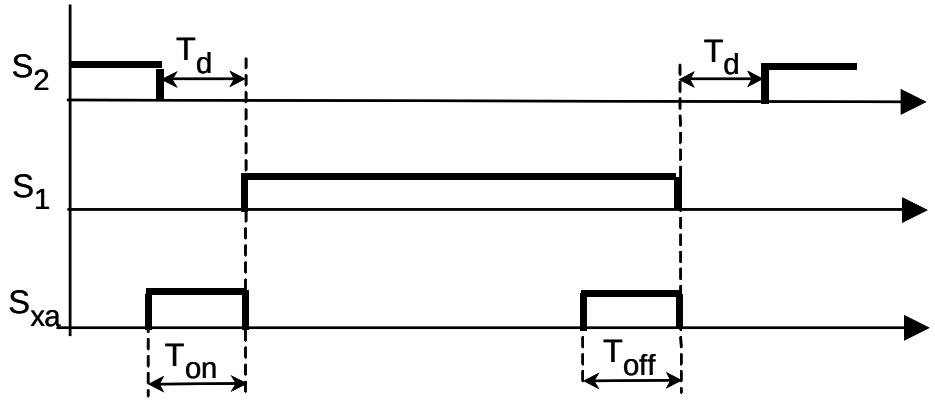

Figure 3.10. Control timings of the three-switch ZCT inverter during I_{Load}>0.

3.4.2.2. I_{Load}<0

At the turn-on transition, S_{xa} is first turned on at t_0. S_2 is turned on at t_1. The delay from t_0 to t_1 is found from Figure 3.9(b) to be $[t_0, t_1]=(1/4)T_o$. S_{xa} is turned off between t_2 and t_3, and the delay from t_0 is about $(1/2)T_o$. At the turn-off transition, S_{xa} is again turned on at t_5. S_2 is turned off between t_6 and t_7, and the delay from t_5 is around $(1/4)T_o$. S_{xa} is turned off between t_9 and t_{10},

and the delay from t_5 is around T_o. The gate signal for S_1 should be removed before t_1 at the turn-on, and can be applied after t_8 at the turn-off.

Referring to the control timings shown in Figure 3.11, clearly $T_{ON1}=(1/4)T_o$, and $T_{OFF1}=(1/4)T_o$. A dead time T_d is inserted between the switching actions of S_1 and S_2, which is around $(3/4)T_o$. The other two timing widths, T_{ON2} and T_{OFF2}, however, are not straightforward, and need further analysis.

For the turn-on, the timing delay from t_0 to t_2 is derived based on the state-plane trajectory as

$$[t_0, t_2] = \left(\frac{1}{4} + \frac{tan^{-1}(IL_n)}{2\pi}\right) T_o , \tag{3.3}$$

where IL_n is the normalized load current, given by

$$IL_n = \frac{I_{Load} \cdot Z_o}{V_{dc}} . \tag{3.4}$$

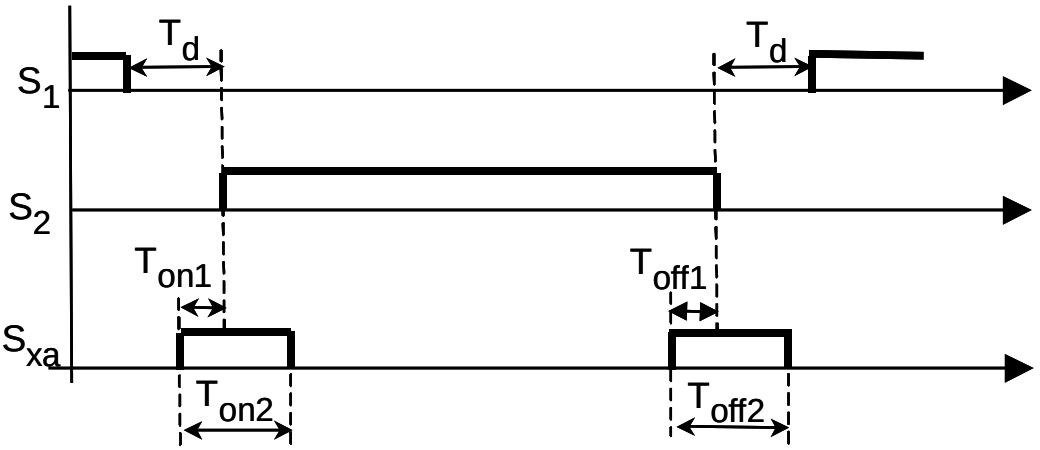

Figure 3.11. Control timings of the three-switch ZCT inverter during $I_{Load}<0$.

The timing delay from t_0 to t_3 is

$$[t_0, t_3] = [t_0, t_2] + T_o/2 . \tag{3.5}$$

Against a changing IL_n, two curves for the delays $[t_0, t_2]$ and $[t_0, t_3]$ are plotted in Figure 3.12. They provide a timing region in which S_{xa} is turned off between t_2 and t_3 under zero current. It can be seen that T_{ON2} can be fixed to a time located in this region under a changing IL_n, such as $0.5T_o$, which leads to a simple implementation.

For the turn-off, the timing delay from t_5 to t_9 is derived as

$$[t_5, t_9] = \left(\frac{1}{2} + \frac{\cos^{-1}(IL_n)}{2\pi} + \frac{1}{2\pi}\frac{1-\sqrt{1-IL_n^2}}{IL_n}\right)T_o. \tag{3.6}$$

The timing delay from t_5 to t_{10} is

$$[t_5, t_{10}] = [t_5, t_9] + T_o/2. \tag{3.7}$$

Two curves for the delays $[t_5, t_9]$ and $[t_5, t_{10}]$ are plotted against a changing IL_n in Figure 3.13. They provide a timing region in which S_{xa} is turned off between t_9 and t_{10} under zero current. It can be seen that T_{OFF2} can also be fixed to a time located in this region under a changing IL_n, such as T_o, which also leads to a simple implementation.

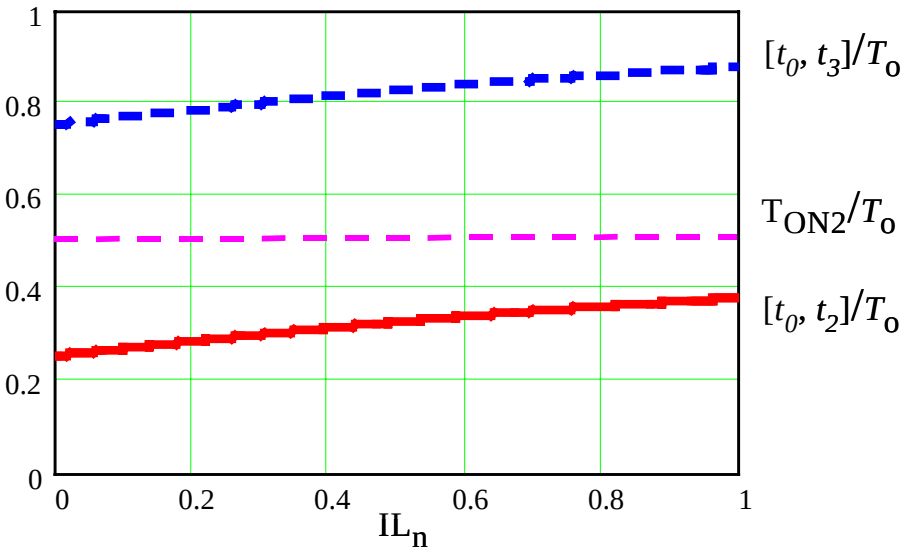

Figure 3.12. Curves for the three-switch ZCT turn-on timing T_{ON2}/T_o against the normalized load current IL_n during $I_{Load}<0$.

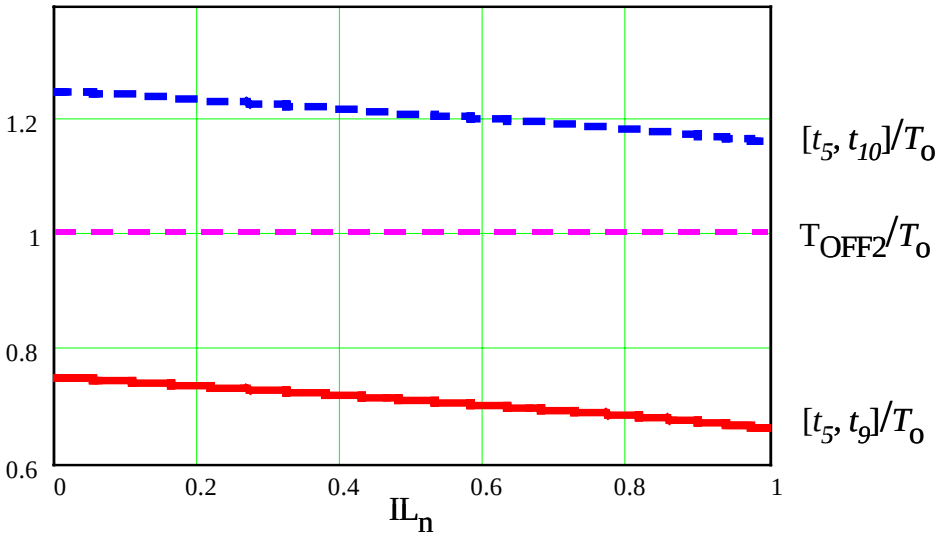

Figure 3.13. Curves for the three-switch ZCT turn-off timing T_{OFF2}/T_o against the normalized load current IL_n during $I_{Load}<0$.

In summary, although the three-switch ZCT control needs two sets of timings (both of which are based on the load current directions), the timings are fixed for each direction. Moreover, similar to the six-switch ZV/ZCT inverter proposed in Chapter2, the load current information is already available from other control functions in the three-phase inverter system, no additional sensors are needed.

3.5. Experimental Verification on a 5-kW Prototype

In order to verify the three-switch ZCT concept, a 5-kW single-phase prototype was built with the following major devices and components.

- Main switch: MG100J2YS50, 100-A/600-V, half-bridge IGBT module
- Auxiliary switch: IRGBC40U, 40-A/600-V, discrete IGBT
- Resonant inductor: 2 μH, built with Magnetics MPP 55894-A2 cores
- Resonant capacitor: 0.2-uF/630-V, polypropylene film

No saturable cores or snubbers to protect the auxiliary switches were used in this prototype. For comparison purposes, this prototype was implemented with both a conventional hard-switching and the proposed three-switch ZCT functions. The control circuit has the option of running in the hard-switching mode by simply disabling the auxiliary switch. In order to directly measure the switch current, no laminated bus bar was used for the hardware.

The prototype was tested first under the hard-switching condition with a DC bus voltage of 300 V. As shown in Figure 3.14, at the turn-on transition, the switch current (i_s) spike is up to twice the load current, which is mainly caused by the diode reverse-recovery current; at the turn-off transition, the switch voltage (v_{ce}) overshoot is up to 500 V. Due to the high voltage overshoot, the load current for the hard-switching test was limited to 35 A.

Next, with the same hardware and layout, the prototype was tested with the proposed three-switch ZCT operation under the same DC bus voltage at a switching frequency of 20 kHz. Because the ZCT operation eliminated the voltage overshoot at the turn-off transition, the load current was increased up to 50 A. The ZCT experimental waveforms for both $I_{Load}>0$ and $I_{Load}<0$ cases are shown in Figure 3.15. It can be seen that the experimental waveforms agree with the theoretical waveforms shown in Figures 3.6 and 3.8. In both the turn-on transitions, the peak of the resonant current (i_x) is built up close to the load current. Meanwhile, the spike in the switch current (i_s) is almost eliminated. In both the turn-off transitions, the switch current decreases to zero before the switch voltage rises to the DC bus voltage, and the negative part of the switching current waveform actually is conducted by the anti-parallel diode across this switch. Meanwhile, almost no overshoot is observed in the switch voltage waveforms.

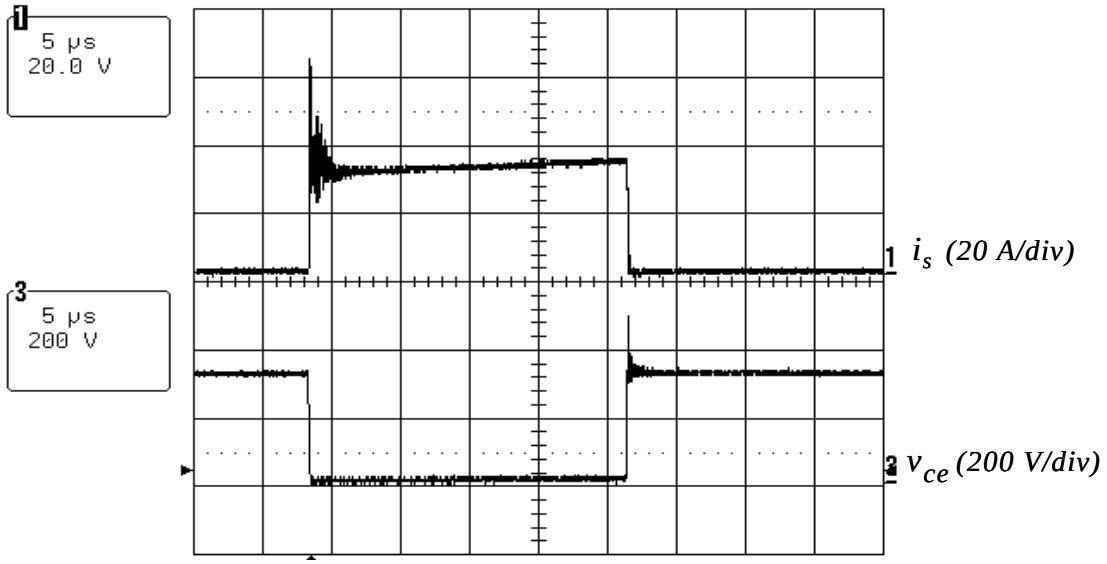

Figure 3.14. Hard-switching waveforms measured at the 5-kW prototype.

The experimental waveforms also show the different traits in the ZCT operations under different load current directions. When I_{Load}>0, a resonant current portion is superimposed on the top main switch current waveform (i_{s1}) at the turn-off; when I_{Load}<0, it is at the turn-on that a resonant current portion is superimposed on the bottom main switch current waveform (i_{s2}). This difference reflects the asymmetrical soft commutations and resonant current flow paths between different load current directions, which are unique in the proposed three-switch ZCT inverter. Since the soft transition occurs for only a very short time in the switch cycle, this asymmetry normally has no effect on the fundamental inverter operations. Despite the fact that the resonant current may somehow increase the conduction loss, the proposed low-cost ZCT inverter topology has demonstrated significant reduction in the switching losses and noises.

Figure 3.16 shows the measured state-plane trajectories of the 5-kW prototype under different I_{Load} directions. They agree well with the theoretical trajectories shown in Figure 3.9, which provide visual assistance to derive the design criteria of the proposed three-switch ZCT topology in Section 3.4.

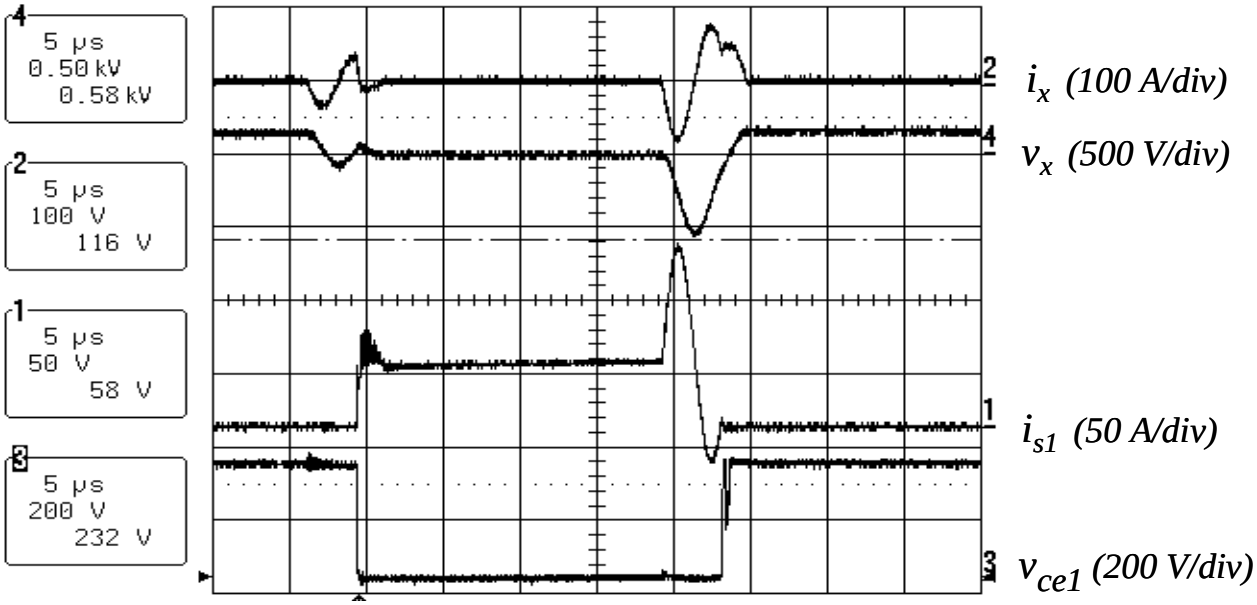

(a)

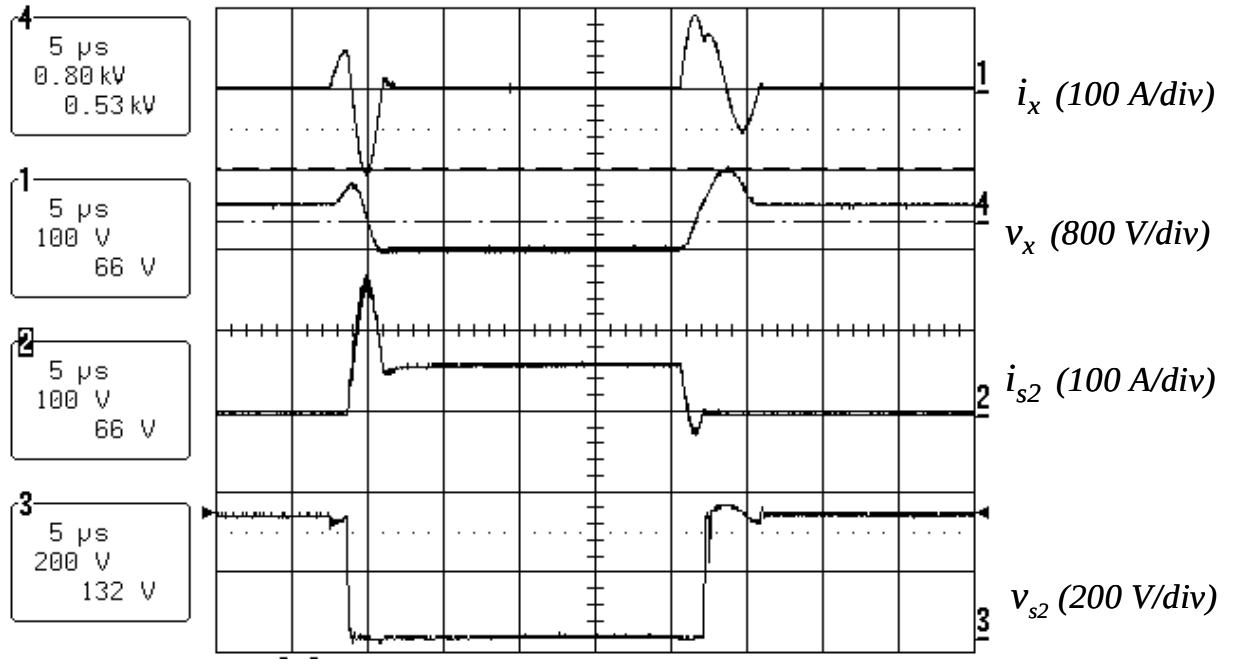

(b)

Figure 3.15. Three-switch ZCT waveforms measured at the 5-kW prototype: (a) $I_{Load}>0$; and (b) $I_{Load}<0$.

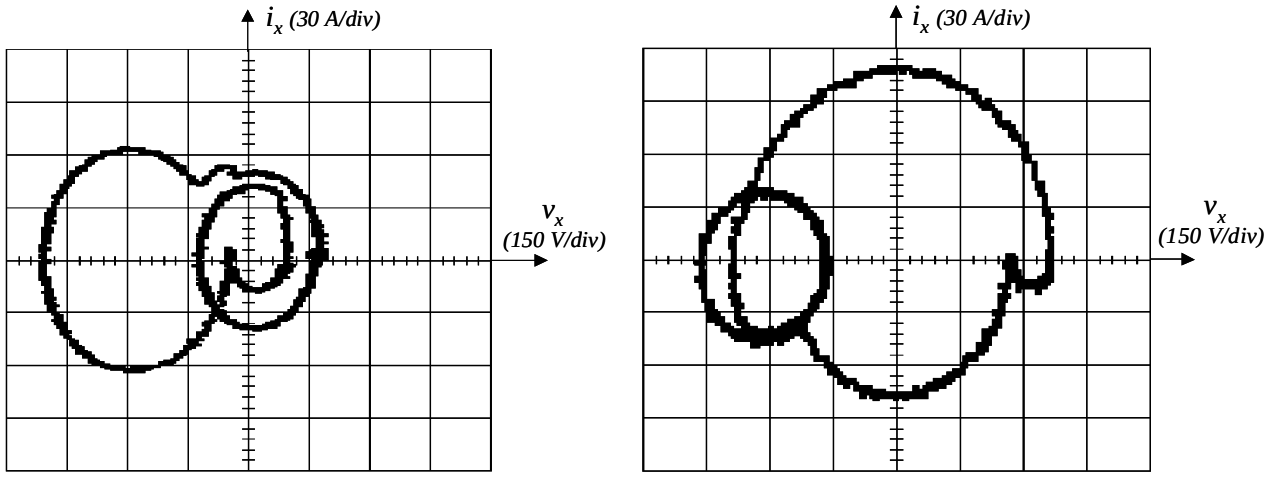

Figure 3.16. Three-switch ZCT state-plane trajectories measured at the 5-kW prototype under different load current directions:
(a) $I_{Load}>0$; and (b) $I_{Load}<0$.

3.6. Summary

This chapter proposes a simplified three-phase ZCT inverter topology that uses only three auxiliary switches. The philosophy of the proposed topology is as follows: It fully utilizes the bi-directional property of the *LC* resonant current, and thus instead of assigning one auxiliary switch to each main switch, it employs only one auxiliary switch to one phase leg to assist the soft transitions of all switches and diodes in this phase leg. As a result, it reduces the number of auxiliary switches by half from the existing ZCT inverters and still achieves similar soft-commutation features.

The theoretical analysis and experimental verifications have demonstrated the following promising features of the proposed three-switch ZCT topology.

- It still requires no modification to normal PWM algorithms.
- All main switches and auxiliary switches are turned off under zero-current conditions, and diodes are turned off under a near-zero-current condition.

- Since the selection of auxiliary switches is mainly determined by the peak current handling capability, not only is the number of auxiliary switches reduced by half, but also the same current rating can be retained. Moreover, the auxiliary switches are essentially immune to shoot-through failure.
- The ZCT control uses two sets of timings based on the load current directions, but each set of timings is fixed for each direction. No additional sensors are required, because the current information is already available from general inverter control functions.

The significance of the three-switch ZCT topology is that among three-phase soft-switching topologies developed so far, it is the only one that uses *fewer* than six auxiliary switches and still has the following three features: 1) soft commutation for all main switches, diodes and auxiliary switches in all operation modes; 2) no modification to normal PWM algorithms; and 3) in practical implementations, no need for extra resonant current sensing, saturable cores, or snubbers to protect the auxiliary switches. This topology is suitable for three-phase PFC rectifiers as well.

The proposed three-switch ZCT inverter satisfies the expectations for desirable low-cost soft-switching inverters. Since it is simplified from the six-switch ZCT inverter circuit, there are differences and connections compared to the new ZV/ZCT scheme proposed in Chapter 2 as well as to the existing six-switch ZCT schemes. A comparative study of the family of ZCT inverters will be presented in the next chapter.

Chapter 4

A Comparative Study of A Family of Three-Phase ZCT Inverters

The new six-switch ZV/ZCT scheme proposed in Chapter 2 and the simplified three-switch ZCT topology proposed in Chapter 3, together with existing schemes for the six-switch ZCT inverter circuit, constitute a family of three-phase ZCT inverters. It is necessary to clarify the difference and connections between these inverters, and to explore the essentiality of ZCT commutations. For this purpose, this chapter presents a comparative study of the family of ZCT inverters. A simplified equivalent circuit is presented to unify the common traits of ZCT commutations. With the visual aid of state planes, evolution of the ZCT inverter technique is examined, and behaviors of individual inverters, including switching conditions, circulating energy, and device/component stresses, are compared. Suggestions for practical applications are provided.

4.1. The Family of Three-Phase ZCT Inverters

ZCT is accomplished by the addition of an auxiliary circuit that provides a resonant current to divert the current through the main circuit prior to switching transitions. Using the same ZCT concept, there are a variety of circuit configurations and control schemes that have different operational behaviors and soft-switching features.

Figure 4.1 illustrates five ZCT control schemes developed for the six-switch ZCT inverter circuit: Hua's ZCT [C19], the modified Hua's ZCT [C20], Mao's ZCT [C20], the new ZV/ZCT proposed in Chapter 2, and its alternative. In the phase-leg circuit, there are two main switches (S_1 and S_2), two auxiliary switches (S_{x1} and S_{x2}), and one LC resonant tank. The switching

patterns during $I_{Load}>0$ and $I_{Load}<0$ are symmetrical, and those during $I_{Load}>0$ will be discussed to explain the differences, in which S_1 and D_2 need to be soft-switched. For Hua's ZCT scheme, the auxiliary circuit assists only the turn-off of S_1, while for the other schemes, it assists both the turn-on and the turn-off. With flipped switching patterns, for the modified Hua's ZCT and Mao's ZCT, one auxiliary switch is activated twice to assist both turn-on and turn-off, while the other auxiliary switch idles. Also with flipped switching patterns, for the proposed ZV/ZCT scheme and its alternative, the two auxiliary switches alternately assists the turn-on and turn-off. The connections between the switching patterns are clear. The turn-on pattern of the proposed ZV/ZCT is similar to the turn-on pattern of the Mao's ZCT, in which S_{x2} is activated. The turn-off pattern of the proposed ZV/ZCT is similar to the turn-off pattern of the modified Hua's ZCT, in which S_{x1} is activated. In terms of switching patterns, the proposed ZV/ZCT combines the turn-on of the Mao's ZCT with the turn-off of the modified Hua's ZCT. It should be mentioned that the switching pattern of the Hua's ZCT is similar to that of the McMurray inverter [C17]; the difference is that SCRs are replaced by modern gate-controlled devices, such as IGBTs, with different circuit operations.

Figure 4.2 illustrates the scheme of the three-switch ZCT inverter proposed in Chapter 3. There is only one auxiliary switch S_{xa} in each phase leg. During both $I_{Load}>0$ and $I_{Load}<0$, S_{xa} is activated twice at every switching cycle to assist both the turn-on and the turn-off transitions of the main switch that needs to be soft-switched. As discussed in Chapter 3, the timings and circuit operations between $I_{Load}>0$ and $I_{Load}<0$ are asymmetrical.

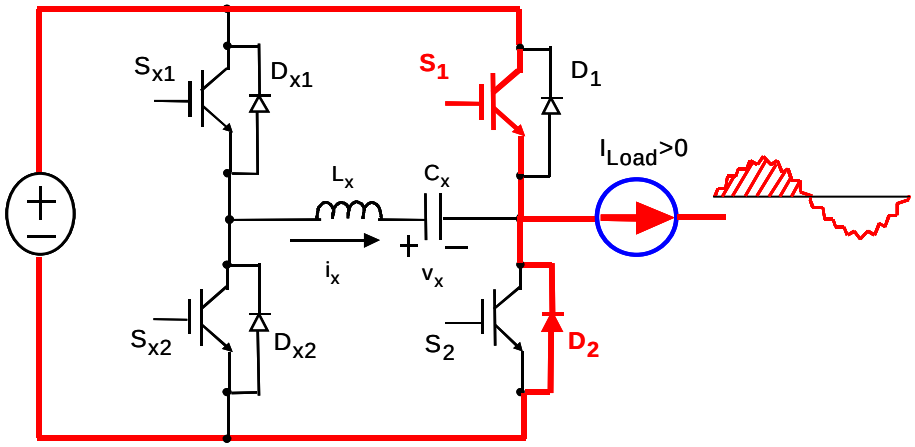

(a)

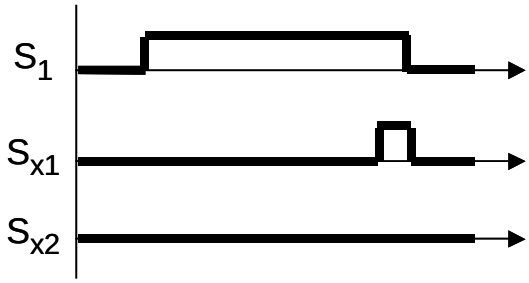

(i) Hua's ZCT

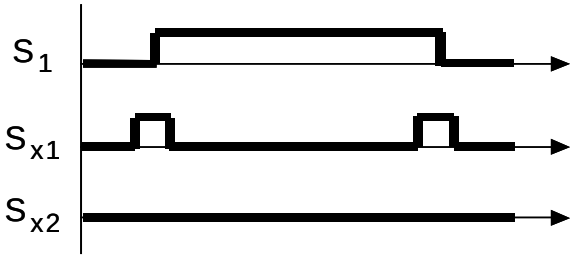

(ii) The modified Hua's ZCT

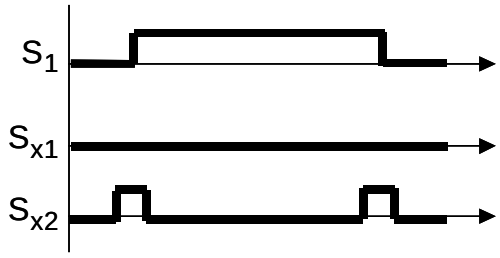

(iii) Mao's ZCT

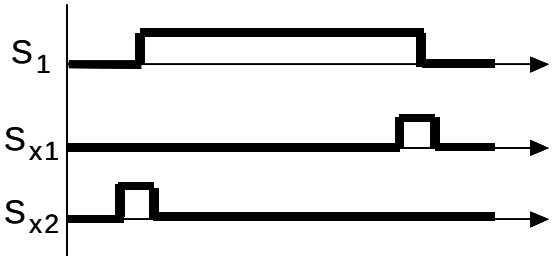

(iv) The proposed ZV/ZCT

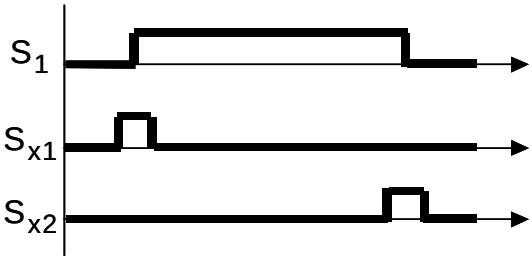

(v) Alternative to the ZV/ZCT

(b)

Figure 4.1. Five control schemes for the six-switch ZCT inverter circuit:
(a) phase-leg circuit; and
(b) switching patterns for the I_{Load}>0 cases.

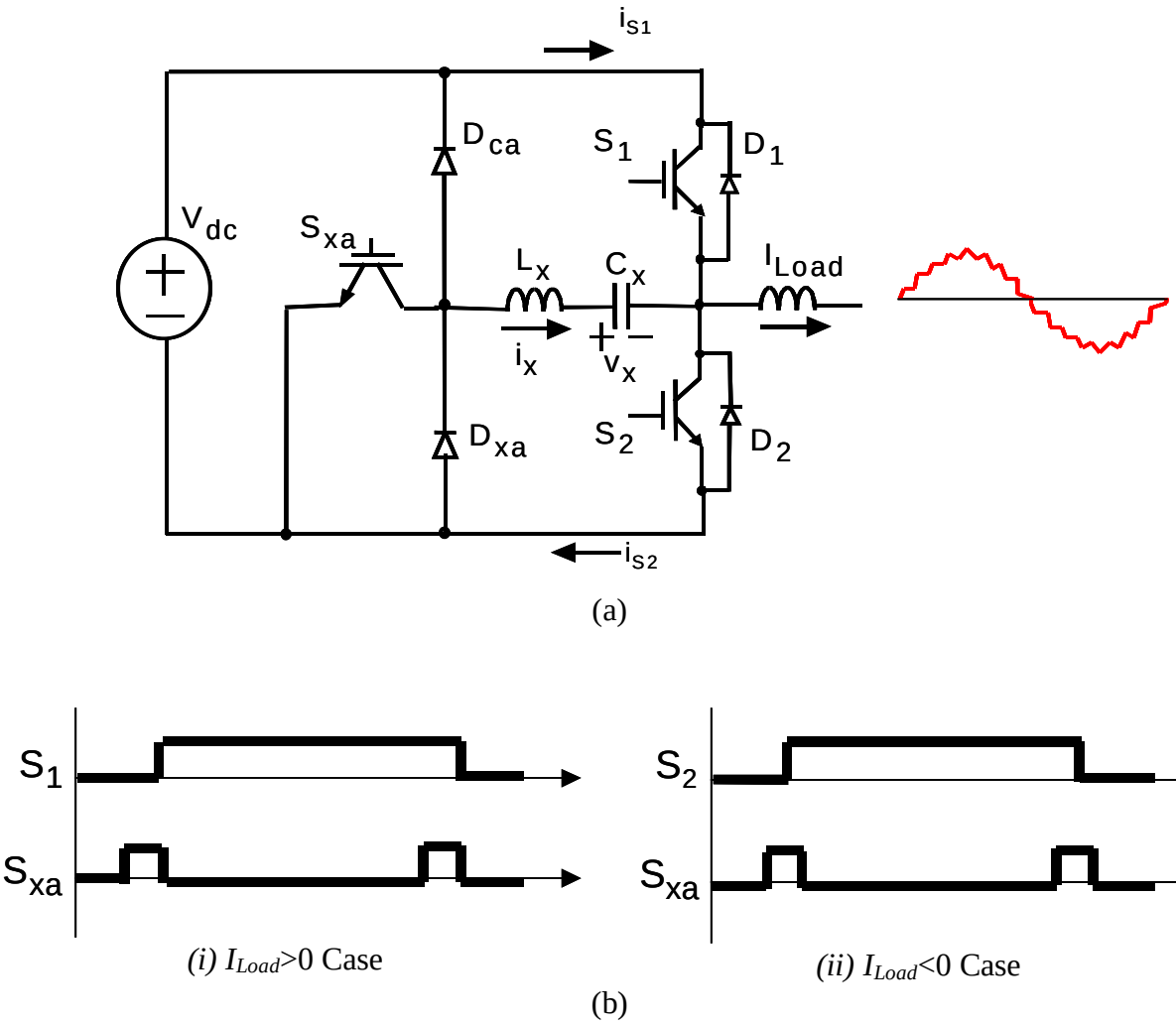

Figure 4.2. The scheme for the three-switch ZCT inverter:
(a) phase-leg circuit; and
(b) switching patterns under a bi-directional load current.

There are also connections between the three-switch ZCT and the six-switch ZCT schemes. In high-frequency DC/DC modes, the switching pattern of the three-switch ZCT during I_{Load}>0 is equivalent to the switching pattern of the Mao's ZCT, in which the *diagonal* auxiliary switch is activated; the switching pattern of the three-switch ZCT during I_{Load}<0 is equivalent to the switching pattern of the modified Hua's ZCT, in which the *adjacent* auxiliary switch is activated. However, the originality of the three-switch ZCT topology is that only three auxiliary switches

are needed in a three-phase inverter to achieve the same soft-switching conditions. Meanwhile, it still requires no modification to normal PWM algorithms.

Besides the difference in switching patterns, which determines the auxiliary switches that should be triggered and how and when to trigger them, there are more important differences regarding the behaviors of individual inverters, such as soft-switching conditions, circulating energy, and device/component stresses. The purpose of this chapter is to use a systematic and comparative approach to explore the fundamental properties of the family of ZCT inverters. It is not a repeat of the description of circuit operations for each ZCT scheme. Rather, it is an effort to bring together the members of this family as a whole, to unify the common traits of ZCT commutations, and to compare the soft-switching behaviors of different inverters.

4.2. Common Traits of ZCT Commutations

Although the detailed operational principles may be different, it is found that the various ZCT inverters share the basic soft-commutation principle, which can be illustrated by a simplified equivalent circuit shown in Figure 4.3. In the circuit, S_x represents the equivalent actions of auxiliary switches: Depending on schemes, it may be S_{x1} or S_{x2} in the six-switch ZCT inverter, S_{xa} in the three-switch ZCT inverter, or their equivalent combinations. The purpose of S_x in ZCT commutations is to start an *LC* resonance and to provide a path for the flow of bi-directional sinusoidal resonant current i_x.

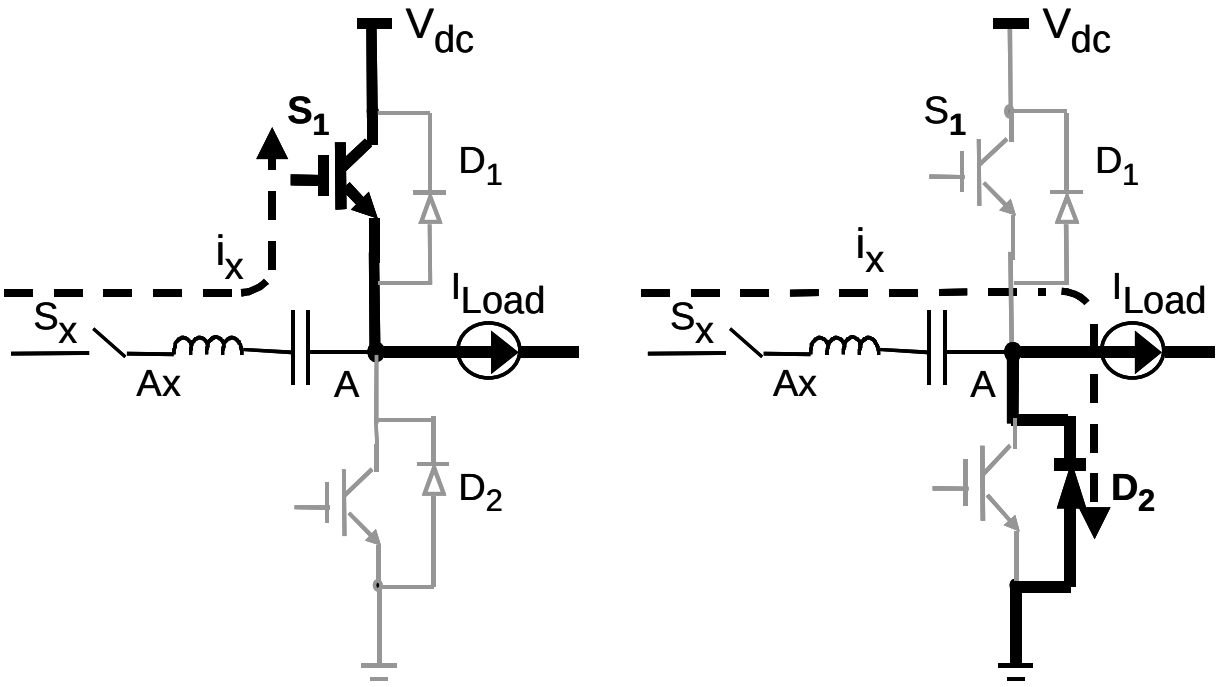

Figure 4.3. A simplified equivalent circuit for ZCT commutations: (a) turn-off of S_1; and (b) turn-on of S_1.

As illustrated in Figure 4.3(a), to assist the turn-off of main switch S_1, S_x is turned on first. Immediately (or after half of a resonant cycle, depending on operational stages), i_x flows from Ax to A, and the current through S_1 is forced to decrease. When i_x exceeds I_{Load}, the current through S_1 drops to zero and its anti-parallel diode conducts the surplus current. S_1 is turned off under zero current and its gate signal is removed without causing switching loss.

The resonant current i_x is driven by an excitation voltage V_{exc}. It is clear that the necessary condition for zero-current turn-off is that the peak of i_x must be greater than I_{Load}. With given L_x and C_x, this peak is proportional to V_{exc}. For different ZCT inverters, V_{exc} is determined by different topological stages and control timings. Equivalently, V_{exc} can be formed in one of the following three operational modes, as shown in Figure 4.4:

a) The initial voltage across the resonant capacitor, $V_{x(IC)}$, which is built up through previous switching actions;

b) The DC bus voltage, V_{dc}; or

c) The difference between V_{dc} and $V_{x(IC)}$.

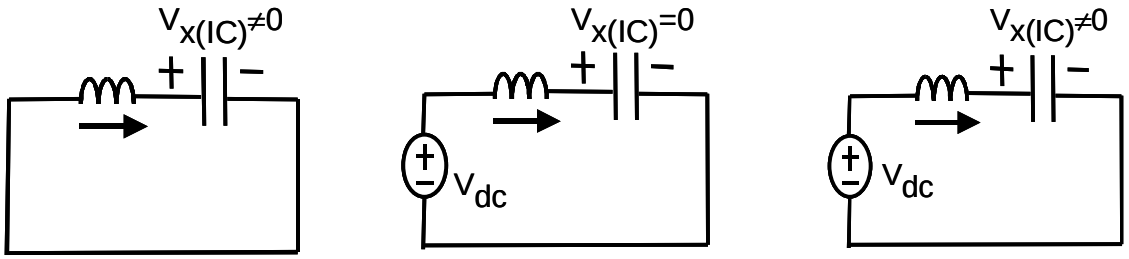

(a) (b) (c)

Figure 4.4. Three operational modes to form the excitation voltage of the *LC* resonance, V_{exc}.

ZCT normally refers to a reduction in the switching turn-off loss, but it can also reduce the turn-on loss, which is mainly caused by the diode reverse-recovery current. As illustrated in Figure 4.3(b), to assist the turn-on of S_1, S_x is turned on first. Immediately (or after half a resonant cycle, depending on operational stages), i_x will be built up in the direction from Ax to A, which forces the current through D_2 to decrease. After that, there are two possible scenarios for the remaining operations of turn-on commutations.

- *Resonant Current Peak* $I_{xpk} < I_{Load}$

If the excitation voltage for the resonance, V_{exc}, is not high enough, then the resonant current peak I_{xpk} cannot reach I_{Load}. When i_x peaks, the current through D_2 drops to its lowest level, but not to zero. S_1 is turned on at this moment, with reduced diode reverse-recovery current. A certain amount of reverse-recovery current still remains, and S_1 is turned on under the full DC bus voltage. This is the soft turn-on transition that occurs in the modified Hua's ZCT, Mao's ZCT, and the proposed three-switch ZCT.

- $I_{xpk} >= I_{Load}$

If the V_{exc} is high enough, then the peak of i_x will be built up higher than I_{Load}. The current in D_2 completely drops to zero before S_1 is turned on. Moreover, after the turn-off process of D_2 is completed, the difference between i_x and I_{Load} will force the top diode D_1 into conduction. This will offer an opportunity to achieve zero-voltage turn-on for S_1. This is the turn-on transition that occurs in the proposed six-switch ZV/ZCT inverter, for which the detailed operational principles are explained in Section 2.2.1.

From the above discussion, it can be seen that the necessary condition for the ZCT circuits to achieve zero-voltage switching is that the V_{exc} must be high enough so that the peak of i_x can exceed the load current. This requires ZCT control schemes to generate sufficient resonant energy for both the turn-on and turn-off transitions.

4.3. Evolution, Differences, and Connections of the ZCT Inverters

4.3.1. The Hua's Six-Switch ZCT Scheme

The excitation voltage for the turn-off resonance in Hua's ZCT scheme is formed in the mode shown in Figure 4.4(a). The operational waveforms and state-plane trajectory are illustrated in Figure 4.5(a). Initially, there is a positive voltage across the resonant capacitor C_x. S_1 is turned on at t_0. After half a resonant cycle, at t_1, the polarity of v_x is reversed, which serves as the excitation voltage for the turn-off resonance. At the turn-off transition, S_{x1} is first turned on at t_2, then S_1 is turned off under zero current at t_3, at which point i_x is greater than I_{Load}. When i_x falls to I_{Load} at t_4, S_{x1} is turned off with I_{Load} under the hard-switching condition. The state-plane trajectory is a circle with V_R as the radius, and the maximum v_x equals V_R, which is less than V_{dc}. The V_R is given by

$$V_R = I_{Load} \cdot Z_o / \cos\alpha, \tag{4.1}$$

where α corresponds to the time delay from the main switch turn-off to the auxiliary switch turn-off, T_{d2}, given by

$$\alpha = 2\pi \cdot T_{d2} / T_o. \tag{4.2}$$

The instantaneous resonant tank energy E_T is given by

$$E_T = (C_x \cdot v_x^2 + L_x \cdot i_x^2)/2 = \frac{C_x}{2} \cdot d^2, \tag{4.3}$$

where d is defined as

$$d = \sqrt{v_x^2 + (Z_o \cdot i_x)^2}. \tag{4.4}$$

In state-plane trajectories, d is the distance between the current state of the system and the origin. Equation (4.3) shows that E_T is proportional to d^2. Within one switching cycle, the E_T of the Hua's ZCT maintains a constant value, $\frac{1}{2} C_x V_R^2$. Therefore, E_T is determined by the load current and control timing, and is adaptive to load variation.

4.3.2. The Modified Hua's Six-Switch ZCT Scheme

In Hua's ZCT scheme discussed in the preceding paragraphs, the main diodes and the auxiliary switches are not subjected to soft commutation. The diode reverse-recovery and auxiliary switch hard-turn-off losses are serious problems.

As illustrated in Figure 4.5(b), in order to solve the hard-switching-turn-off problem of the auxiliary switch S_{x1}, the gate signal of S_{x1} is extended until i_x reverses its direction and flows through the diode that is anti-paralleled with S_{x1}. In this way, S_{x1} is turned off under zero current between t_6 and t_7. During [t_4, t_5], C_x is linearly charged by I_{Load}; during [t_5, t_7], a positive DC bus

voltage is applied to the resonant tank. Due to these additional stages, the resonant process requires a longer time, and the state-plane trajectory is no longer a circle. At t_6, the tank energy E_T and v_x reach their peaks. It is found that

$$v_{x\_max} = V_{dc} + I_{Load} \cdot Z_o \,. \tag{4.5}$$

Equation (4.5) shows that v_{x_max} is influenced by the load current, and that it tends to become larger at heavier loads. The resonant tank is usually designed such that v_{x_max} is 1.3~1.4 times V_{dc} at the maximum load. Correspondingly, referring to Equation (4.3), it follows that

$$E_{T\_max} \approx (0.85 \sim 1) \cdot C_x \cdot V_{dc}^{\,2} \,. \tag{4.6}$$

The scheme in Figure 4.5(b) does not solve the hard-switching-turn-on problem of the main switch. Furthermore, as illustrated in Figure 4.5(c), the auxiliary switch S_{x1} is activated again at the turn-on transition. A resonant current is provided to divert the current freewheeling through diode D_2 into the auxiliary circuit before S_1 is turned on, so the diode reverse-recovery problem is alleviated. This is the modified Hua's scheme, as discussed in [C20]. The E_{T_max} and v_{x_max} are the same as those of the scheme illustrated in Figure 4.5(b). However, the time occupied by the resonant process becomes even longer because of the soft turn-on transition, and the resonant current can cause more conduction loss.

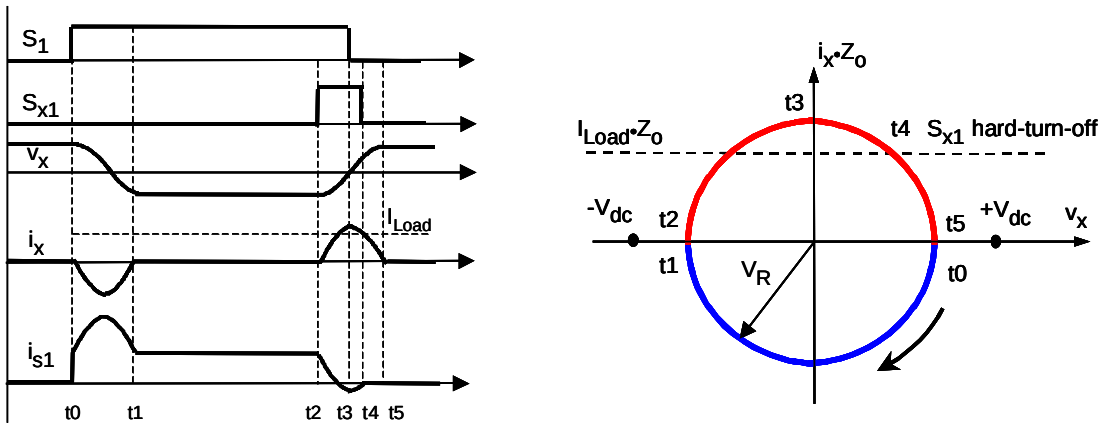

(a) The original Hua's ZCT: hard-switching turn-on of S_1, and hard-switching turn-off of S_{x1}.

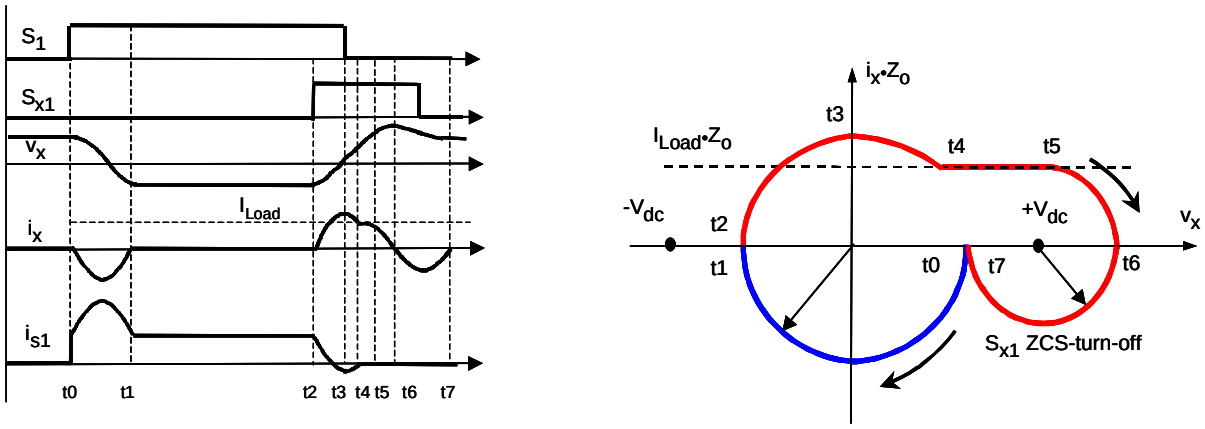

(b) The S_{x1} gate signal is extended for ZCS turn-off, but S_1 is still hard-switching turn-on.

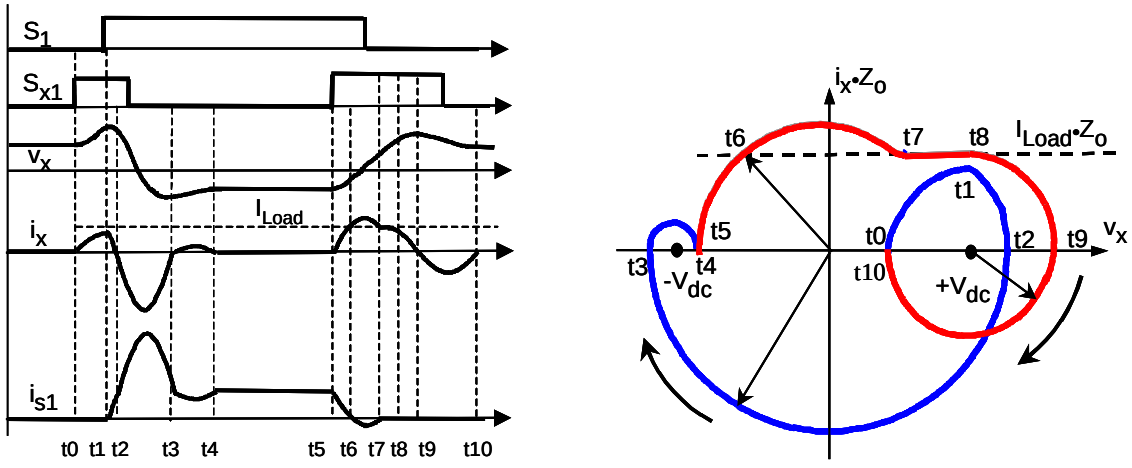

(c) The modified Hua's ZCT: It also achieves soft turn-on of S_1.

Figure 4.5. Evolutions based on Hua's ZCT schemes.

4.3.3. The Mao's Six-Switch ZCT Scheme

Mao's scheme uses a concept similar to that of the modified Hua's scheme, which is to activate one auxiliary switch twice to assist both the turn-on and turn-off transitions of the main switch. But their switching patterns are flipped, as illustrated in Figure 4.1. The operational waveforms and state-plane trajectory have already been shown in Figures 2.3 and 2.10 in Chapter 2. Similar to the modified Hua's ZCT, the Mao's ZCT also realizes zero-current turn-off for the main and auxiliary switches and soft turn-on for main switches. Compared to the modified Hua's ZCT, the Mao's ZCT has lower resonant current peak at turn-on, but higher resonant capacitor voltage stress. The excitation voltage for the turn-off resonance in the Mao's ZCT is formed in the mode shown in Figure 4.4(c); i.e., it is the difference between V_{dc} and $V_{x(IC)}$. Normally, the $V_{x(IC)}$ is near zero, thus v_x peaks at about twice V_{dc}. Correspondingly, the maximum instantaneous resonant tank energy is given by

$$E_{T\_max} = \frac{C_x}{2} \cdot V_{x\_pk}^{\ 2} \approx 2C_x \cdot V_{dc}^{\ 2}. \tag{4.7}$$

4.3.4. The Proposed Six-Switch ZV/ZCT Scheme and Its Alternative

For both the Mao's ZCT and the modified Hua's ZCT, the main diodes cannot be turned off under a complete zero-current condition, and the main switches are still turned on under full DC bus voltage. This is because there is insufficient resonant energy at turn-on to completely divert the current through the main diode into the auxiliary circuit. A discussion of the soft turn-on transition for the Mao's ZCT is in Section 2.2.2, which is also applicable to the modified Hua's ZCT. On the other hand, the ZV/ZCT scheme proposed in Chapter 2 realizes complete zero-current turn-off of the diodes and provides an opportunity for zero-voltage turn-on of the main switches. This is accomplished by using two auxiliary switches to alternately assist the turn-on

and turn-off transitions of each main switch such that the initial energy stored in the resonant capacitor is sufficient to build up the resonant current to a level higher than I_{Load} prior to the turn-on of the main switch. The corresponding operational waveforms and state-plane trajectory are shown in Figures 2.5 and 2.8.

With the visual aids of state-plane trajectories, Figure 4.6 illustrates the inherent connections between the proposed ZV/ZCT scheme and the existing ZCT schemes. The Mao's ZCT has lower resonant current peak at turn-on, but higher resonant capacitor voltage stress at turn-off ($2V_{dc}$). In contrast, the modified Hua's ZCT has a higher resonant current peak at turn-on, but lower resonant capacitor voltage stress at turn-off (1.3~1.4 times V_{dc}). The basic idea is to combine the advantages of these two existing ZCT schemes and to inject more resonant energy for zero-voltage switching. Therefore, the turn-on trajectory of the Mao's ZCT is used by the proposed ZV/ZCT scheme, with more energy in the resonant tank; the turn-off trajectory of the modified Hua's ZCT is directly used by the proposed ZV/ZCT scheme. Then, combining these two sub-trajectories results in the complete trajectory of the ZV/ZCT scheme. As a result, the ZV/ZCT scheme has an opportunity to achieve zero-voltage turn-on with low resonant capacitor voltage stress. Because there is more resonant energy for the turn-on, the turn-on trajectory virtually expands, and the resonant current peak becomes higher. The proposed ZV/ZCT scheme requires two auxiliary switches to assist the soft transitions of one main switch, which is unacceptable for conventional PWM DC/DC converters. However, fully utilizing the property of bi-directional load current, the ZV/ZCT scheme is realized for the six-switch ZCT inverter circuit, without requiring additional devices or components over the existing schemes.

On the other hand, the alternative to the proposed ZV/ZCT scheme, which flips the switching patterns, as shown in Figures 2.11 and 4.1, actually combines the turn-off of the Mao's ZCT with

the turn-on of the modified Hua's ZCT. Therefore, it has higher resonant capacitor voltage stress and higher resonant current peak, and thus is not advantageous.

4.3.5. The Proposed Three-Switch ZCT Topology

The three-switch ZCT inverter topology proposed in Chapter 3 is simplified from the six-switch ZCT inverter circuit. Figure 4.6 also visualizes the difference and connections between the three-switch ZCT and the proposed six-switch ZV/ZCT. The major compromises of the three-switch ZCT appear in the switch turn-on conditions. It cannot achieve complete zero-current turn-off for the diodes, and the main switches are turned on under full DC bus voltage. This feature is the same in the Mao's and the modified Hua's schemes, which are developed for the six-switch ZCT inverter circuit. In fact, in high-frequency DC/DC modes, during $I_{Load}>0$, the circuit operation of the three-switch ZCT inverter is equivalent to that of the Mao's ZCT; during $I_{Load}<0$, it is equivalent to that of the modified Hua's ZCT. Again, the originality of the three-switch ZCT is that only three auxiliary switches are needed to achieve the same soft-switching conditions in a three-phase inverter.

In addition, the three-switch ZCT has higher resonant capacitor voltage stress, which occurs during $I_{Load}>0$, and higher resonant current peak, which occurs during $I_{Load}<0$. Equivalently, the six-switch ZV/ZCT combines the advantages of the three-switch ZCT under different load current commutation patterns. However, the six-switch ZV/ZCT doubles the auxiliary switch count. In other words, the three-switch ZCT can serve as a low-cost solution for soft-switching inverters.

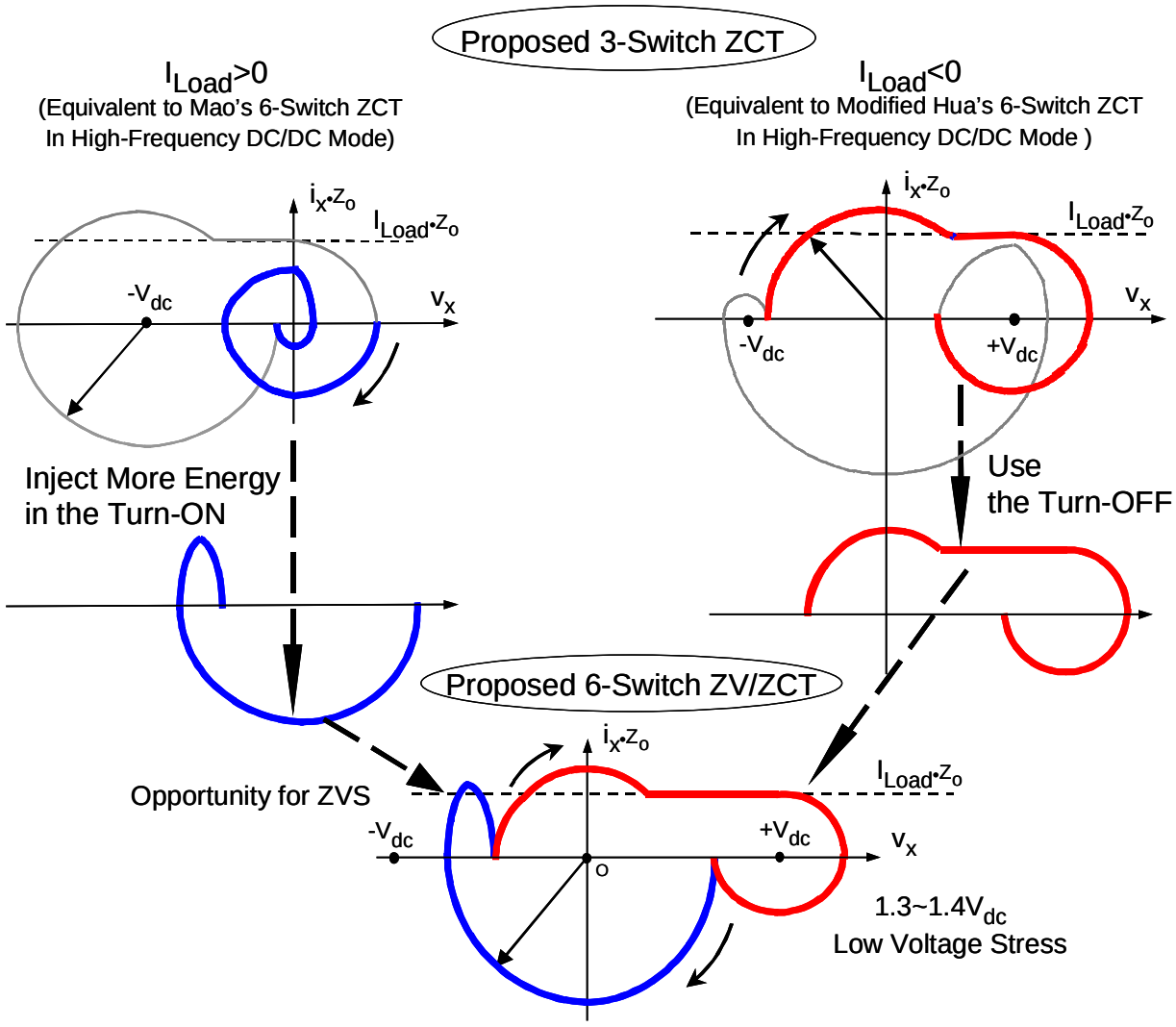

Figure 4.6. Connections between the family of three-phase ZCT inverters:
The six-switch ZV/ZCT combines the advantages of the three-switch ZCT under different current commutation patters.

4.4. Comparison and Suggestion

A comparative study of the family of ZCT inverters, including five schemes for the six-switch ZCT inverter circuit and the three-switch ZCT topology, has been conducted. These inverters share basic operating principles but with different behaviors. Their major differences in soft-switching conditions and voltage/current stresses are summarized in Table 4.1. The state-plane-based analysis confirms that there are inherent connections between these inverters. The

evolution of the ZCT technique also indicates that the step-by-step improvements of switching conditions, i.e., from hard switching to soft switching, from soft turn-on to zero-voltage turn-on, etc., are normally associated with compromises, in such aspects as the time occupied by the resonant process, circulating energy, voltage/current stresses, and/or auxiliary switch counts.

This comparative study can serve as a reference for practical three-phase soft-switching inverter applications. It suggests that the proposed six-switch ZV/ZCT has the best overall soft-switching features, and that the proposed three-switch ZCT can be a simple low-cost soft-switching solution. Based on these two proposed ZCT techniques, two 55-kW inverter prototypes have been developed for EV motor drive applications. The next two chapters will present the design considerations, implementations, experimentation, and evaluation.

Table 4.1.
Comparison of the Family of Three-Phase ZCT Inverters

	Six-Switch ZCT Inverter Circuit					**Three-Switch ZCT Inverter**
	Hua's ZCT	Modified Hua's ZCT	Mao's ZCT	Proposed ZV/ZCT	Alternative to ZV/ZCT	Proposed
Piggyback	Yes	Yes	Yes	Yes	Yes	Yes
Main Switch Turn-Off	ZCS	ZCS	ZCS	ZCS	ZCS	ZCS
Main Switch Turn-On	Hard	Soft, V_{dc}	Soft, V_{dc}	ZVS	ZVS	Soft, V_{dc}
Main Diode Turn-Off	Hard	Near ZCS	Near ZCS	ZCS	ZCS	Near ZCS
Auxiliary Switch Turn-Off	Hard	ZCS	ZCS	ZCS	ZCS	ZCS
Resonant Cap. Voltage Stress	V_{dc}	$1.3V_{dc}$	$2V_{dc}$	$1.3V_{dc}$	$2V_{dc}$	$2V_{dc}$
Resonant Current Peak	Load Adapt	High	Medium	High	High	High
Distribution of Auxiliary Device Current Stress	Uneven	Uneven	Uneven	Even	Even	N/A

Chapter 5

Two 55-kW ZCT Inverter Prototypes for EV Motor Drives — Design Considerations

According to the proposed six-switch ZV/ZCT scheme and the three-switch ZCT topology, two three-phase inverter prototypes have been developed for EV traction motor drives in the Partnership for a New Generation of Vehicles (PNGV). The inverters are required to provide peak output power of 55 kW and continuous output power of 30 kW, and to operate at switching frequency of 10 kHz. The nominal DC input voltage is 325 V. Based on the DC bus voltage and power requirements, Toshiba MG300J2YS50, 300-A/600-V half-bridge IGBT modules are selected as the main switches. These two 55-kW inverters have been completely implemented and tested to the full power level with a closed-loop controlled induction motor dynamometer. This chapter presents in detail the design considerations, and compares the design aspects of these two ZCT inverters. The hardware implementations, experimentation and evaluation will be presented in Chapter 6.

First, this chapter presents an experimental characterization of the main IGBT under the ZCT soft-switching conditions. Second, it addresses aspects of the design of auxiliary circuits. The resonant tank parameters are determined in such as way to optimize the total inverter losses over the entire speed/torque range of EV drives. Generalized equations of auxiliary circuit current stresses are developed, which provide assistance in the selection of resonant capacitors. The resonant inductor core losses, which are caused by discontinuous nonsinusoidal flux excitations, are modeled and calculated. Based on the core loss model, design optimization of the resonant inductors is performed to achieve low loss and small size. The non-conventional operation conditions of the auxiliary switches are analyzed, and it is found that the current ratings specified

for commercial IGBT devices cannot meet the requirements for the auxiliary switches. Methods to select and test the suitable auxiliary devices, as well as to characterize the devices under the non-conventional operation conditions, are proposed. Thirdly, ZCT inverter loss models are developed and methods for minimizing the inverter losses are numerically analyzed. Fourth, some aspects of system-level operation are investigated, including duty-cycle differences between the ideal and actual PWM control signals, pulse-width limits caused by soft switching, and transient behaviors. Finally, layout and parasitic issues are discussed.

5.1. Experimental Characterization of the Main IGBT under ZCT Conditions

The motivation for the use of soft-switching techniques stems from a desire to alleviate some of the problems associated with the non-ideal switching characteristics of power devices. The first step of design, therefore, is to experimentally characterize the switching losses and behaviors of the IGBT (MG300J2YS50) that is selected as the main switches under hard-switching, three-switch ZCT and six-switch ZV/ZCT conditions. An IGBT soft-switching tester is developed. Both turn-on and turn-off losses are measured and compared under variable switch current conditions. The switching loss reduction is quantified, and switching behavior differences between the two ZCT conditions under different *LC* resonant tank designs are compared and analyzed.

5.1.1. Test Setup

The circuit diagram of the IGBT tester is shown in Figure 5.1(a). S_1 and S_2 are the main switches, and they as a whole are implemented by one piece of MG300J2YS50 half-bridge IGBT module. S_{x1} and S_{x2} are the auxiliary switches. Since the purpose of the tester is to characterize

the main IGBT switching losses and behaviors, S_{x1} and S_{x2} are also implemented by one piece of MG300J2YS50. Figure 5.1(b) is a photo of the tester. It has a convenient re-connection capability for achieving either hard-switching, three-switch ZCT, or six-switch ZV/ZCT operations. When the auxiliary circuit is removed, the main switches are tested under hard-switching conditions. As illustrated in Figure 5.2, with S_2 and S_{x1} disabled, S_1 is tested under the three-switch ZV/ZCT for $I_{Load}>0$— it is assisted by S_{x2} at both turn-on and turn-off. With S_1 and S_{x1} disabled, S_2 is tested under the three-switch ZV/ZCT for $I_{Load}<0$— it is assisted by S_{x2} at both turn-on and turn-off. Furthermore, with S_2 disabled, S_1 is tested under the six-switch ZV/ZCT— it is assisted by S_{x2} at turn-on, and by S_{x1} at turn-off. The resonant tank components (L_x and C_x) can be changed easily, which facilitates the study of ZCT switching behaviors under different resonant tank designs.

In the tester, the load inductor is 0.6 mH, the gate drivers used are HP316, and the gate resistance is set to 7.6 Ω. To reduce parasitic inductance, a laminated bus bar is used to connect the DC power supply and the switches. The device tests are performed in a "double-pulse" sequence, as illustrated in Figure 5.3. At T_0, the main device under test (DUT) is turned on, and the load inductor is built up. At T_1, the DUT is turned off, and the turn-off loss is measured. At T_2, the DUT is turned on again, and the turn-on loss is measured. When the DUT is switched, the corresponding auxiliary switches are activated for a short time. The ZCT circuit operations are presented in Chapters 2 and 3, and the detailed timings can been seen in Figures 2.5, 3.6 and 3.8. [T_0, T_1] determines the value of inductor current at which the switching losses are measured, and it is relatively long. [T_1, T_2] should ensure that before the DUT is turned on at T_2, the turn-off transition is completed. During [T_1, T_3], the load inductor current remains almost constant.

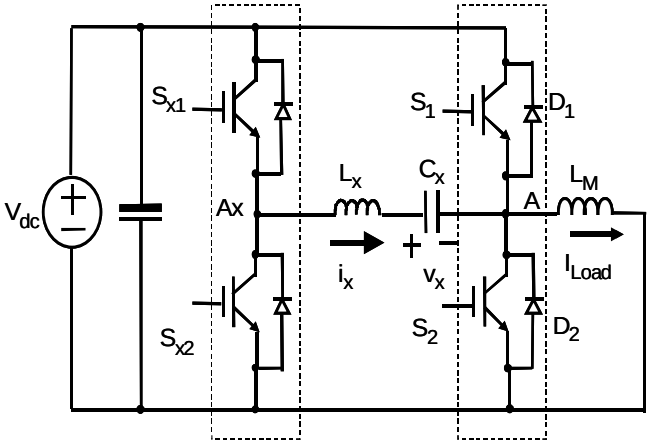

(a)

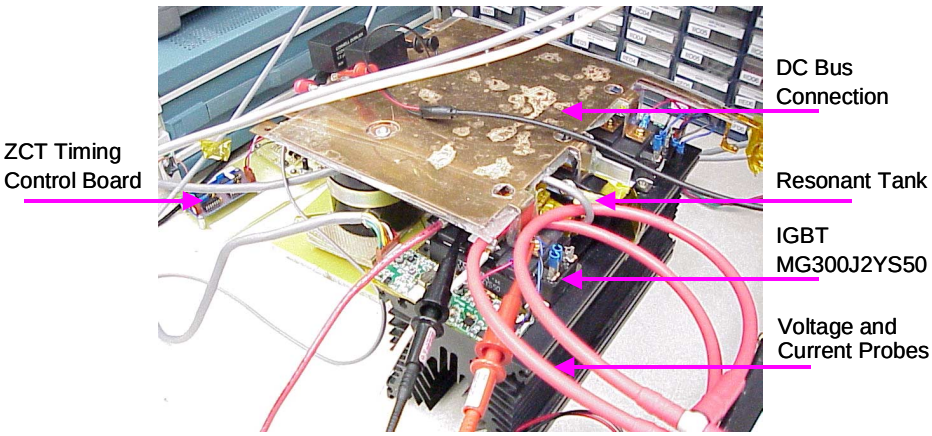

(b)

Figure. 5.1. A device tester to characterize the main IGBT under ZCT conditions: (a) circuit diagram; and (b) a photo of the hardware.

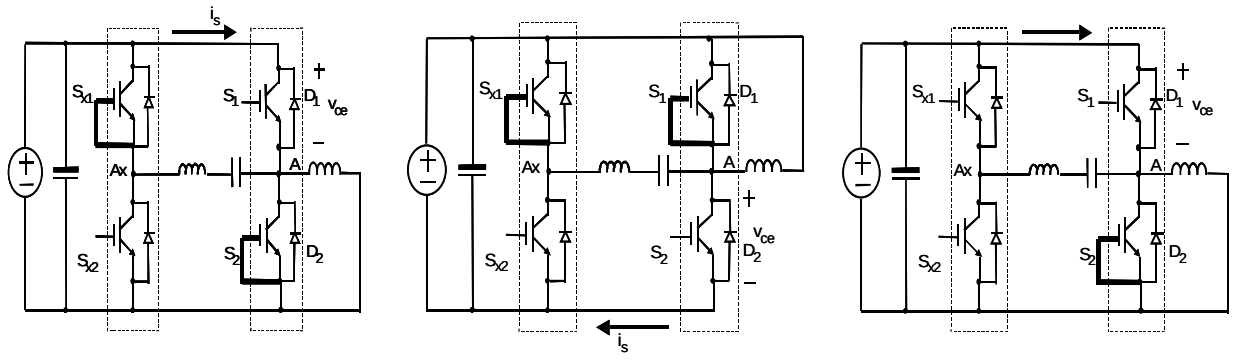

(a) (b) (c)

Figure 5.2. Testing setup for different ZCT operations:
(a) three-switch ZCT during I_{Load}>0;
(b) three-switch ZCT during I_{Load}<0; and
(c) six-switch ZV/ZCT;

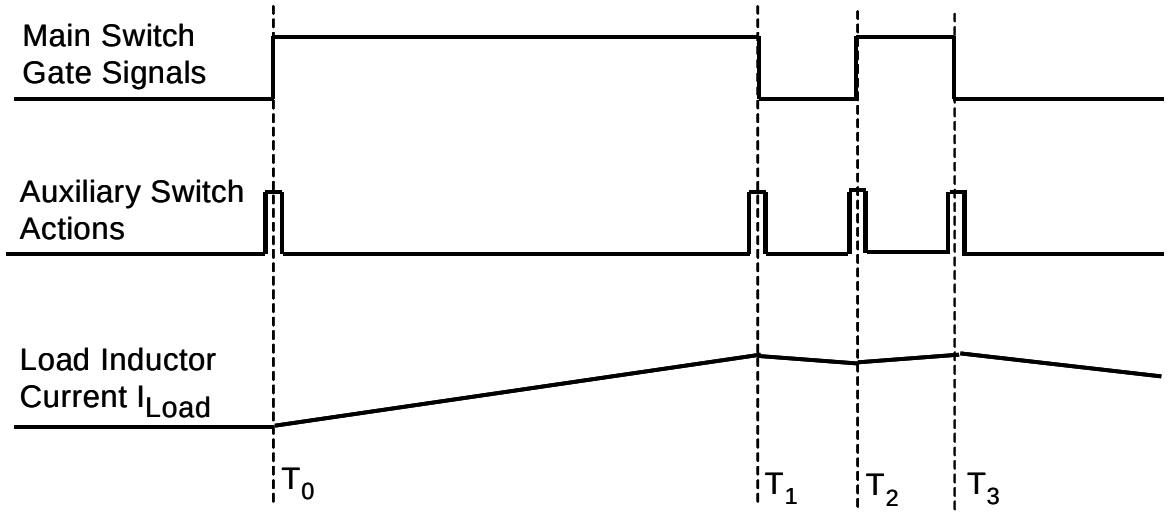

Figure 5.3. The "double-pulse" device test sequence.

The switch currents are measured using Rogoski current probes, which have small physical dimensions and can provide relatively accurate measurements given the compact layout of the tester. The switch voltages are measured using Tektronix voltage probes. The switching losses are obtained by direct integration of the product of the current and voltage waveforms on the Lecroy 9401 oscilloscope.

5.1.2. Test Results and Analysis

The main IGBT MG300J2YS50 has been tested under hard-switching, the three-switch ZCT and the six-switch ZV/ZCT conditions with the above setup. All tests are performed under a DC bus voltage of 320 V, with different current levels. For both ZCT conditions, tests under different *LC* resonant tank designs are also conducted. The test results of switching losses are listed in Tables 5.1, 5.2, and 5.3, and the loss curves are plotted in Figures 5.7, 5.8, and 5.9.

Table 5.1.
Measured Switching Losses of the Main IGBT under the Hard-Switching Condition

Is (A)	E_on (mJ)	E_off (mJ)	Total (mJ)
16	0.6	0.4	1
35	1.2	1	2.2
55	2.4	1.7	4.1
75	3.3	2.8	6.1
100	4.2	3.6	7.8
125	5.7	4.5	10.2
145	7.1	5.7	12.8
170	8.4	6.8	15.2
190	9.7	7.8	17.5

Table 5.2.
Measured Switching Losses of the Main IGBT under the Three-Switch ZCT Condition with Different Resonant Tank Designs

L_x=1 µH, C_x=1 µF, T_o=6.3 µs				L_x=0.58 µH, C_x=1 µF, T_o=4.8 µs				L_x=1.6 µH, C_x=0.625 µF, T_o=6.3 µs			
Is (A)	E_on (mJ)	E_off (mJ)	Total (mJ)	Is (A)	E_on (mJ)	E_off (mJ)	Total (mJ)	Is (A)	E_on (mJ)	E_off (mJ)	Total (mJ)
55	1.7	0.1	1.8	50	2.8	0.2	3.0	50	1.4	0.1	1.5
75	2.3	0.1	2.4	75	3.3	0.2	3.4	75	1.7	0.1	1.8
100	2.8	0.1	2.9	100	4	0.2	4.2	100	1.9	0.1	2.0
123	3.2	0.1	3.3	120	4.7	0.2	4.9	120	2.6	0.1	2.7
140	3.5	0.1	3.6	145	5.2	0.2	5.4	140	2.7	0.1	2.8
160	4	0.1	4.1	160	6	0.2	6.2				
173	4.9	0.1	5.0	170	6.6	0.2	6.8				

Table 5.3.
Measured Switching Losses of the Main IGBT under the Six-Switch ZV/ZCT Condition with Different Resonant Tank Designs

L_x=1 µH, C_x=1 µF, T_o=6.3 µs				L_x=0.58 µH, C_x=1 µF, T_o=4.8 µs			
Is (A)	E_on (mJ)	E_off (mJ)	Total (mJ)	Is (A)	E_on (mJ)	E_off (mJ)	Total (mJ)
50	0.1	0.2	0.3	50	0.4	0.2	0.6
75	0.3	0.1	0.4	75	0.6	0.2	0.8
100	0.6	0.1	0.7	100	1	0.2	1.2
120	1.1	0.1	1.2	123	1.6	0.2	1.8
140	1.5	0.1	1.6	145	1.9	0.2	2.1
155	2.2	0.1	2.3	160	2.4	0.2	2.6
165	2.6	0.1	2.7	170	2.7	0.2	2.9

5.1.2.1. Switching Loss Reduction by the ZCT Operations

Figure 5.4 shows the measured hard-switching waveforms. During the turn-on process of the IGBT, there is a large overlap between switch current (I_s) and voltage (V_{ce}). This is mainly caused by the establishment of the conductivity modulation of the IGBT and the reverse recovery of the opposite main diode. Consequently, high turn-on loss occurs. During the turn-off process, the loss is mainly caused by the overlap between the rising voltage and falling current in the initial phase, and the dissipation caused by the tail current in the subsequent phase. Meanwhile, high voltage overshoot can occur. The voltage overshoot of the tested IGBT increases approximately linearly with the current level, while the peak diode reverse-recovery current is about 50A under all tested current levels.

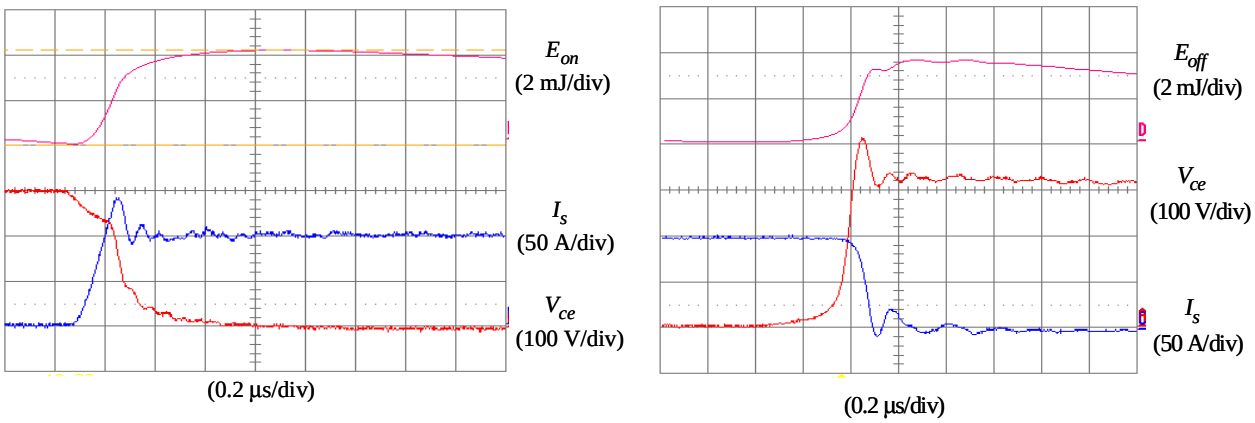

Figure 5.4. Switching waveforms of the main IGBT under the hard-switching condition: (a) turn-on; and (b) turn-off.

Figures 5.5 shows the measured three-switch ZCT waveforms, with resonant tank elements of L_x=1 µH and C_x=1 µF. As discussed in Chapter 3, the three-switch ZCT operates asymmetrically between different load current directions. For I_{Load}>0, a resonant current portion is superimposed on the switch current at turn-off; for I_{Load}<0, a resonant current portion is

superimposed on the switch current at turn-on. With the assumption that the superimposed resonant current attributes only to the increase in the conduction losses, the switching losses in both directions are the same. Experimentally, it is also not easy to differentiate the switching loss from the conduction loss at the soft transitions. During the turn-on process, the peak of reverse-recovery current is indeed significantly reduced from that obtained by the hard switching. However, at the moment when the switch voltage begins to decrease, a current spike still exists; this is caused by the reverse-recovery current that remains in the opposite main diode. The three-switch ZCT cannot generate sufficient energy to completely divert the main diode current into the auxiliary circuit. It realizes soft commutation, but the IGBT is still turned on under the full DC bus voltage. Following the reverse-recovery current spike, there is an overlap between the rising current and falling voltage tail, which causes turn-on loss. During the turn-off process, the overlap between the switch voltage and current is eliminated, and the zero-current duration, which is the interval during which the switch current becomes negative and is conducted by the anti-parallel diode, is long enough to ensure that the remaining carriers in the IGBT can be appropriately recombined. Therefore, the turn-off loss is almost eliminated. Meanwhile, since the energy stored in the parasitic inductance is pre-discharged and diverted to the resonant capacitor, the IGBT does not exhibit a turn-off voltage overshoot.

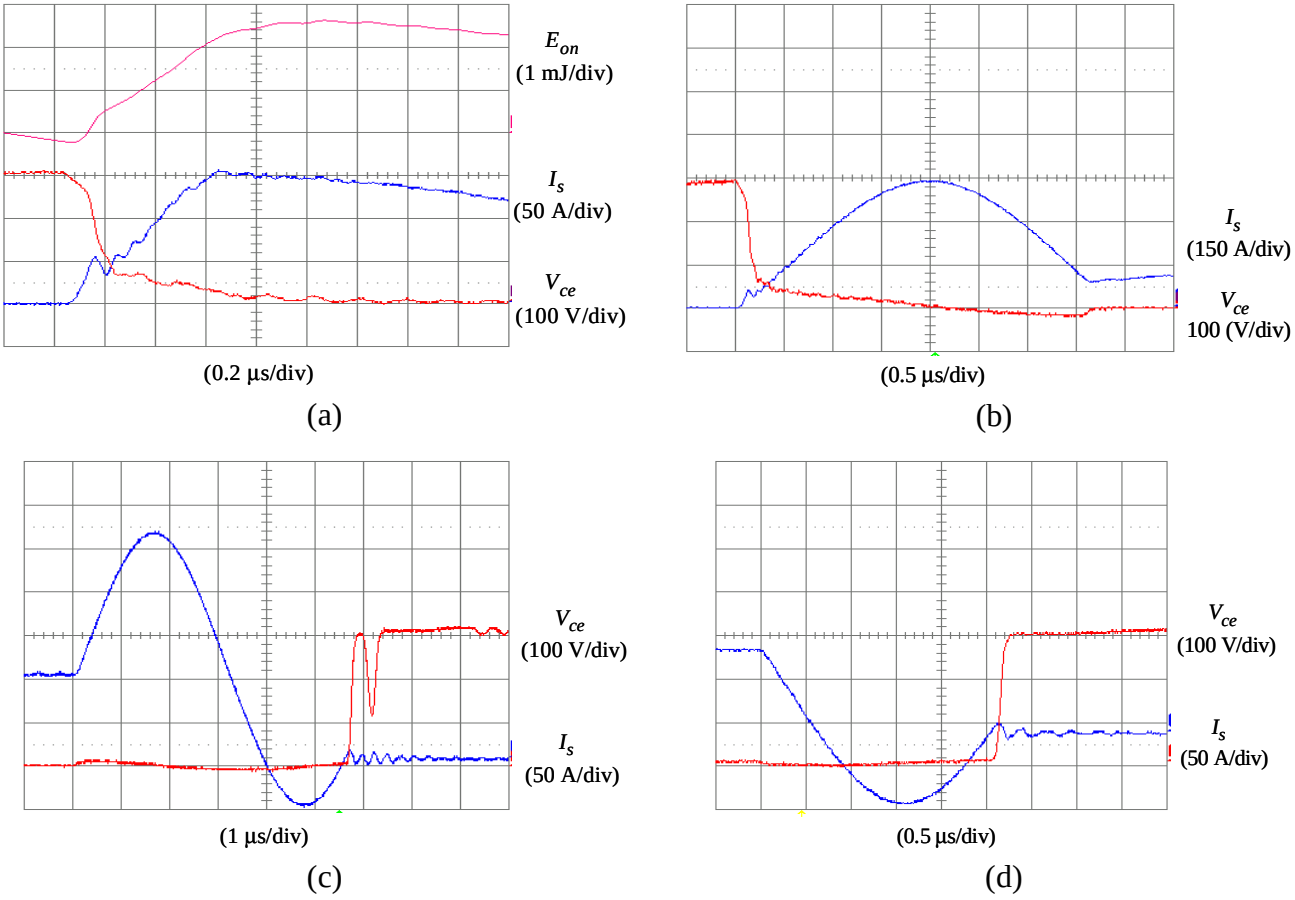

Figure 5.5. Switching waveforms of the main IGBT under the three-switch ZCT condition: (a) turn-on for I_{Load}>0; (b) turn-on for I_{Load}<0; (c) turn-off for I_{Load}>0; and (d) turn-off for I_{Load}<0.

Figure 5.6 shows the measured six-switch ZV/ZCT waveforms, with resonant tank elements of L_x=1 µH and C_x=1 µF. As discussed in Chapter 2, an important feature of the ZV/ZCT scheme is that it introduces sufficient resonant energy to completely divert the main diode current into the auxiliary circuit prior to the turn-on of the opposite main switch. Therefore, it realizes a complete zero-current turn-off for the diode, and provides an opportunity to achieve zero-voltage turn-on for the switch. As can be seen in Figure 5.6(a), the switch voltage has reduced to zero before the current starts to rise, and the main diode reverse-recovery current is almost eliminated. Therefore, the turn-on loss is further reduced from that of the three-switch ZCT.

From Figure 5.6(a), it can be also seen that a dynamic saturation voltage drop exists across the IGBT when the current is ramping up, and this voltage drop is around 10~20 V. It is caused by the "conductivity modulation lag," which produces an inductor-like behavior. It occurs because the initial conductivity in the IGBT drift region is low, and the IGBT current rises faster than that can be accommodated by the rate at which the charge carriers within the device are generated to support the current. As the injected carrier concentration increases, the voltage drop across the IGBT decreases to the normal value. This phenomenon has been observed in ZVS converters [E1]-[E3], and it has also been observed in P-i-N diodes and labeled as diode forward recovery [E4]. However, this is the first time this phenomenon is observed to occur in ZCS converters. As a consequence, a certain amount of turn-on loss exists. The turn-off process of the six-switch ZV/ZCT is similar to that of the three-switch ZCT for $I_{Load}<0$, in which the turn-off loss is almost eliminated.

Figure 5.7 plots the switching loss curves. Under the hard-switching condition, both the turn-on and turn-off losses of the tested IGBT increase approximately linearly with the current level. With L_x=1 μH and C_x=1 μF, the turn-off losses under both ZCT conditions are almost negligible (around 0.2 mJ) under different current levels. This means the higher the current, the more significant the effect of turn-off-loss reduction. The difference is found in the turn-on losses. Both the turn-on losses increase with the current level; however, compared to the three-switch ZCT, the six-switch ZV/ZCT reduces the turn-on loss by about 50%, and the total loss by about 50%. Compared to hard switching, the three-switch ZCT reduces the turn-on loss by about 40%, and the total loss by about 70%; the six-switch ZV/ZCT reduces the turn-on loss by about 75%, and the total loss by about 90%.

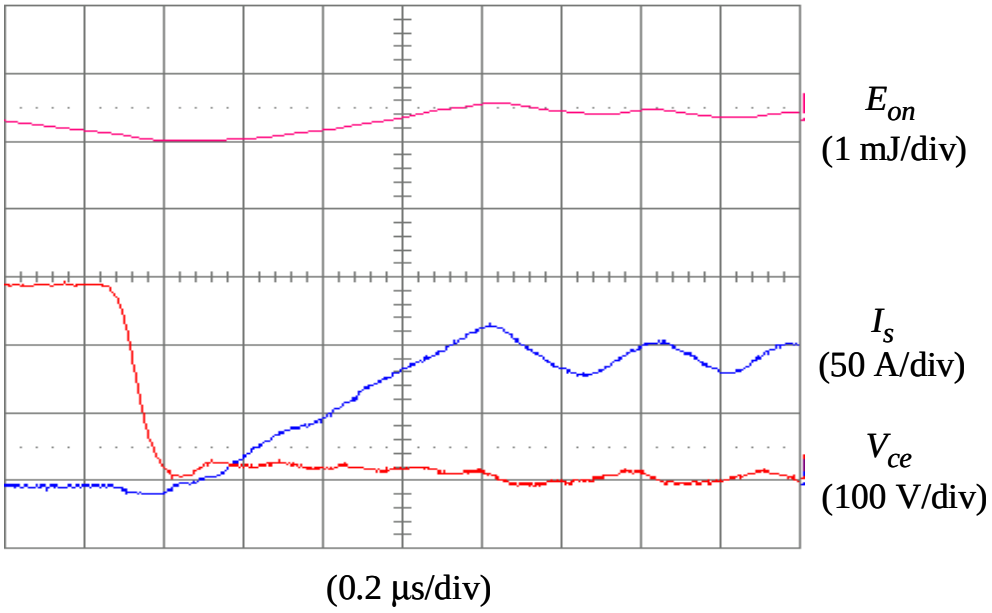

(a)

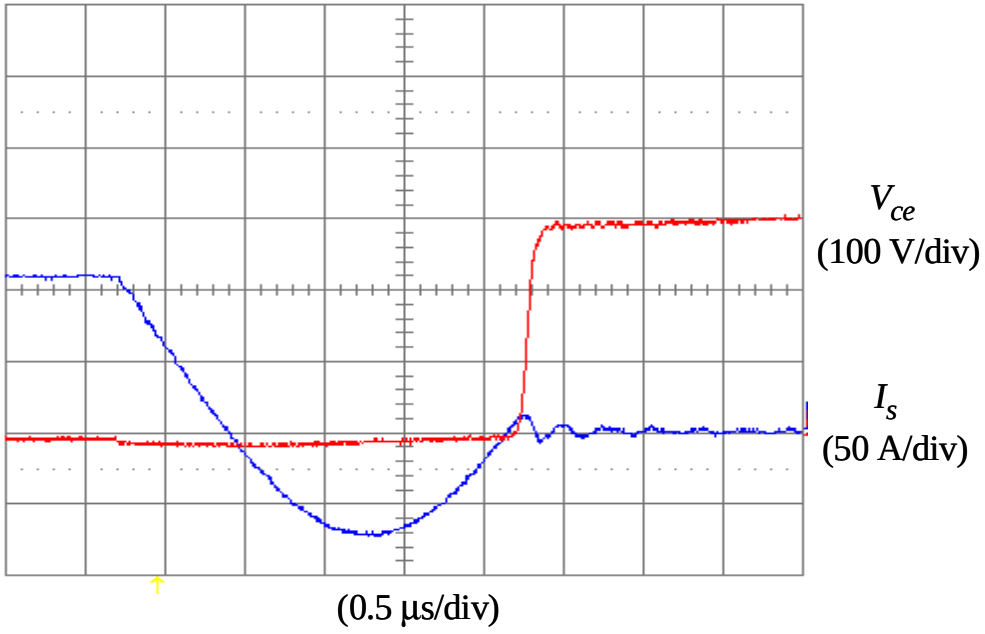

(b)

Figure 5.6. Switching waveforms of the main IGBT under the six-switch ZV/ZCT condition:
(a) turn-on; and
(b) turn-off.

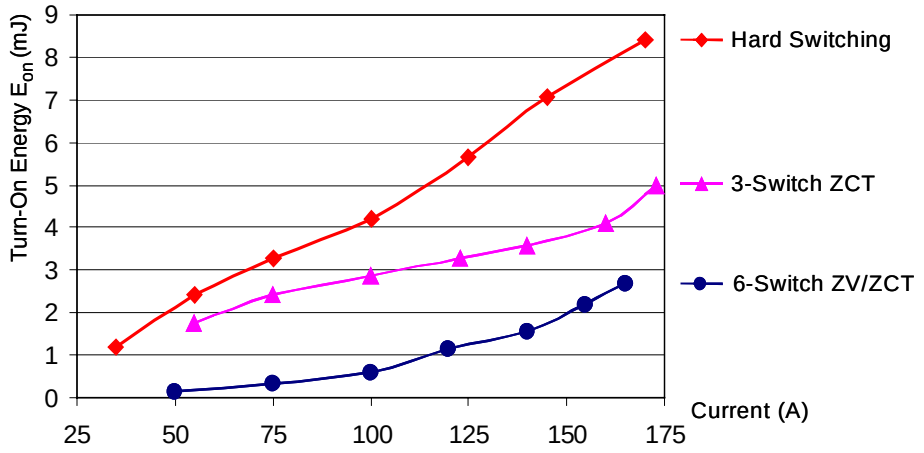

(a)

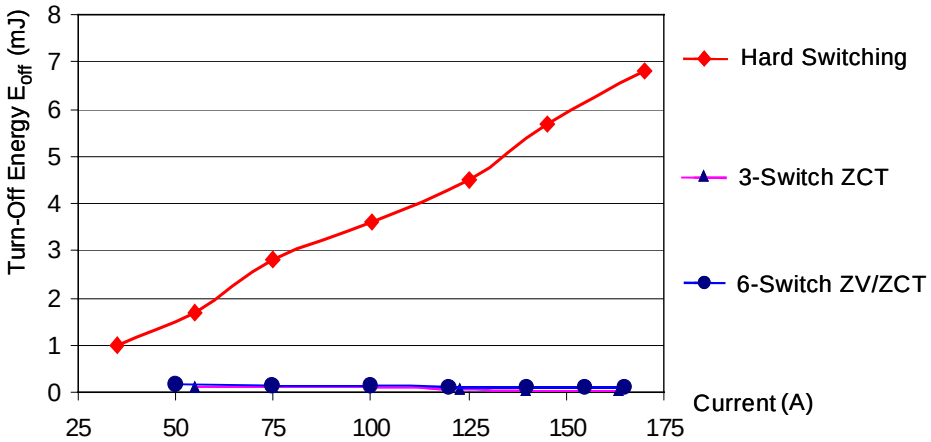

(b)

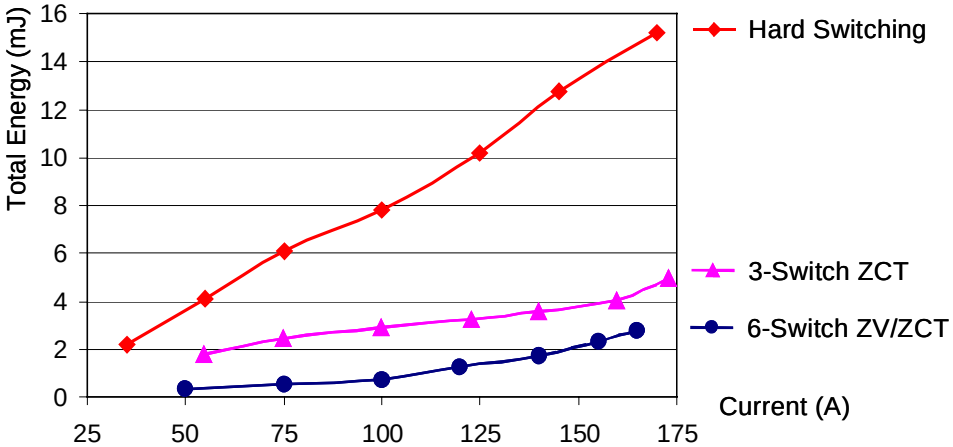

(c)

Figure 5.7. Switching loss curves of the main IGBT under the hard-switching, three-switch ZCT and six-switch ZV/ZCT conditions (in both ZCTs, L_x=1 μH and C_x=1 μF): (a) turn-*on* energy loss; (b) turn-*off* energy loss; and (c) *total* energy loss.

5.1.2.2. Variation of ZCT Switching Behaviors with Different Resonant Tank Designs

The comparison of switching losses in the preceding section is under a resonant tank of L_x=1 μH and C_x=1 μF for both ZCT conditions. It is necessary to study the variation of ZCT switching behaviors with different resonant tank designs.

Figure 5.8. plots the turn-off loss curves of both ZCT conditions with two sets of resonant tank elements: 1) L_x=1 μH, C_x=1 μF, and T_o=6.3 μs; and 2) L_x=0.58 μH, C_x=1 μF, and T_o=4.8 μs. It is found that changing the resonant tank elements does not affect the turn-off loss. This is understandable: As long as the zero-current turn-off is achieved, which means that the overlap between voltage and current at turn-off is eliminated, and the zero-current duration is long enough to ensure that the remaining carriers in the IGBT can be appropriately recombined, then the turn-off loss can be almost eliminated [E5].

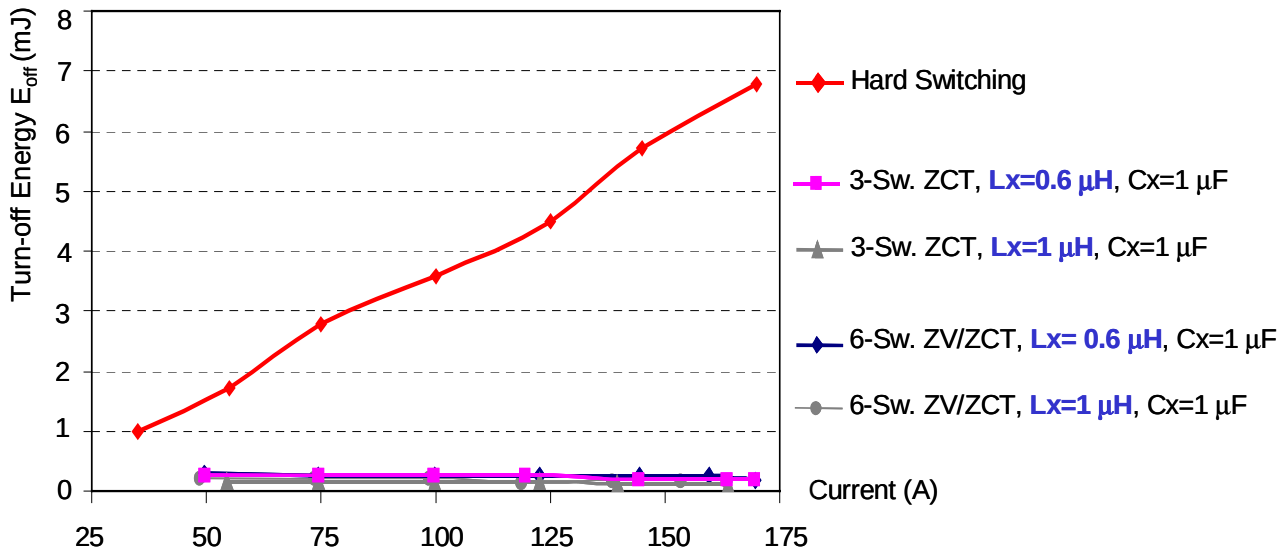

Figure 5.8. Variation of turn-*OFF* energy losses of the main IGBT under the ZCT conditions with different resonant tank designs.

Figure 5.9 plots the turn-on loss curves of both ZCT conditions using different resonant tank elements. Unlike the turn-off loss, the turn-on loss and behaviors vary quite substantially between the two ZCT operations. When L_x decreases from 1 µH to 0.58 µH (and C_x remains the same), the turn-on loss of the three-switch ZCT is increased by about 40% at most of the testing points, while that of the six-switch ZV/ZCT remains almost unchanged, especially at higher current levels. On the other hand, when L_x increases from 1 µH to 1.6 µH (and C_x is reduced to 0.625 µF or else T_o would be too long), the turn-on loss of the three-switch ZCT is indeed reduced, but the reduction is by only about 20%, and so is not as significant as the change when L_x decreases. Meanwhile, the ZCT range is reduced because the resonant current peak decreases with the increased tank impedance Zo(=$\sqrt{L_x/C_x}$).

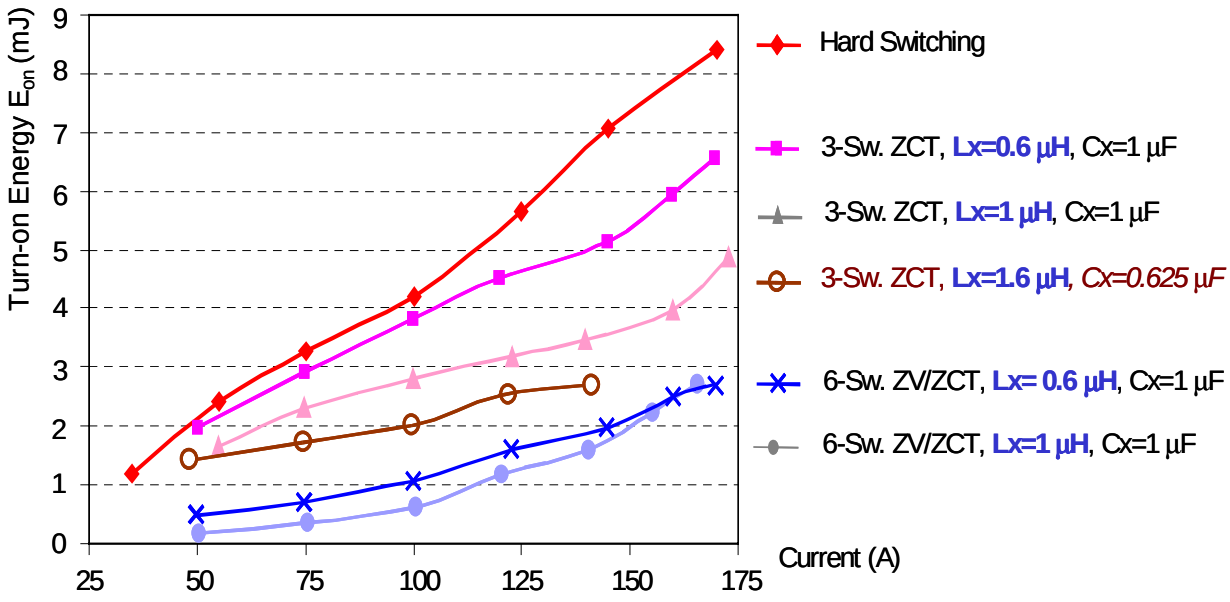

Figure 5.9. Variation of turn-*ON* energy losses of the main IGBT under the ZCT conditions with different resonant tank designs.

To explain why reducing the L_x can significantly increase the turn-on loss in the three-switch ZCT, Figure 5.10 shows the operational stages and measured waveforms of the turn-on transition in the three-switch ZCT during $I_{Load}>0$, which are similar to those during $I_{Load}<0$ in terms of the mechanism of switching losses. Initially, diode D_2 conducts the load current, and S_x is turned on first at t_0. A resonant current i_x is generated to force the current through D_2 to decrease. At t_1, i_x peaks, the current through D_2 is reduced to its lowest level, and S_1 is turned on under the full DC bus voltage. One of the major sources of turn-on loss is the overlap between switch voltage V_{ce} and current I_s that occurs after the reverse recovery of D_2 is completed. L_x determines the rising rate of I_s, and thus the overlap. Therefore, a smaller L_x contributes to a larger turn-on loss. Meanwhile, during [t_1, t_2], the *LC* resonance continues through S_1-C_x-L_x-D_c. If I_s rises too quickly, the resonant current i_x can be added to the switch current before the switch voltage completely falls to zero. Consequently, additional turn-on loss can be caused.

On the other hand, increasing the L_x has a limited impact on reducing the turn-on loss of the three-switch ZCT. This is because another source of the turn-on loss is the reverse-recovery current that remains in D_2 at the moment S_1 is turned on at t_1, which is almost independent of L_x. Figure 5.11 shows the turn-on waveforms of the three-switch ZCT under three different resonant tank designs. When L_x is increased, the rising rate of the switch current is reduced, so the turn-on loss that can be controlled by L_x is reduced. However, the turn-on loss that is caused by the diode reverse recovery is almost unaffected by L_x; thus, it becomes a dominant portion in the total turn-on loss.

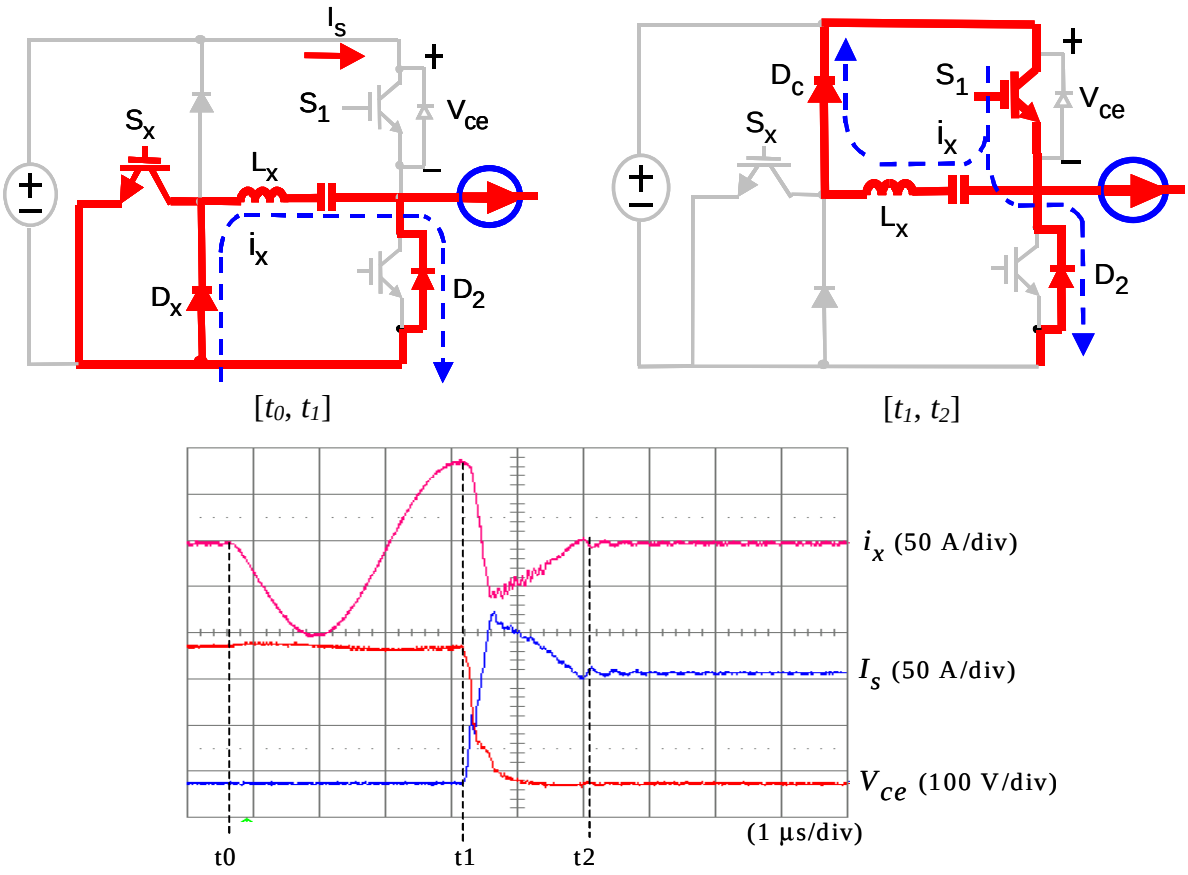

Figure 5.10. Operational stages and measured waveforms of the main IGBT turn-*ON* transition under the three-switch ZCT condition.

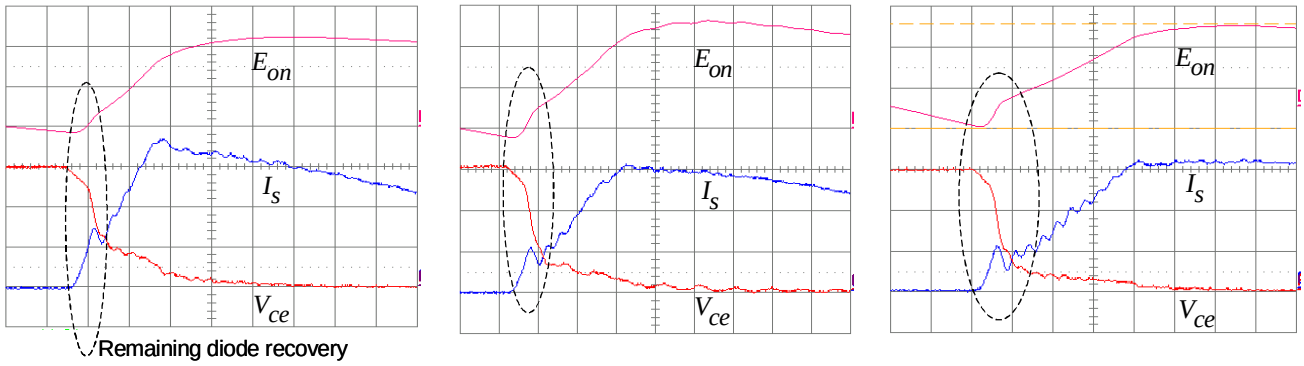

Figure 5.11. Comparison of the main IGBT turn-*ON* waveforms under the three-switch ZCT condition with different resonant tank designs:
(a) L_x=0.58 µH, C_x=1 µF, T_o=4.8 µs;
(b) L_x=1 µH, C_x=1 µF, T_o=6.3 µs; and
(c) L_x=1.6 µH, C_x=0.625 µF, T_o=6.3 µs
(0.2 µs/div; I_s: 50 A/div; V_{ce}: 100 V/div; E_{on}: 2 mJ/div in (a), and 1 mJ/div in (b) and (c)).

For the six-switch ZV/ZCT, because the switch voltage has decreased to zero before the current starts to rise, the overlap between the switch voltage and current is almost unaffected by the rising rate of the switch current, and is therefore unaffected by L_x. Although the rising rate of the switch current has some influence on the dynamic saturation voltage drop that is caused by the conductivity modulation lag effect, changing L_x does not significantly affect the turn-on loss. However, L_x does affect the reverse recovery in the auxiliary diodes. This can be explained via the operational stages shown in Figure 5.12. At t_0, S_{x2} is turned on, and then i_x is built up to a level higher than I_{Load}. After t_3, D_2 turns off under zero current, and S_1 is turned on under zero voltage. Then, i_x decreases, since V_{dc} is applied to the resonant tank through S_1 and D_{x2}, and the decreasing rate is determined by L_x. When i_x falls to zero, reverse-recovery current begins to flow in D_{x2}, which is reflected to the main switch current I_s waveform. Figure 5.13 compares the turn-on waveforms of the six-switch ZV/ZCT under two different resonant tank designs. Clearly, with a larger L_x, the switch current rises more slowly, and the reflected auxiliary diode reverse-recovery effect is less severe. Because the main switch is fully on by the time this recovery occurs, it only slightly increases the conduction loss in the main switch, and does not change the switching loss.

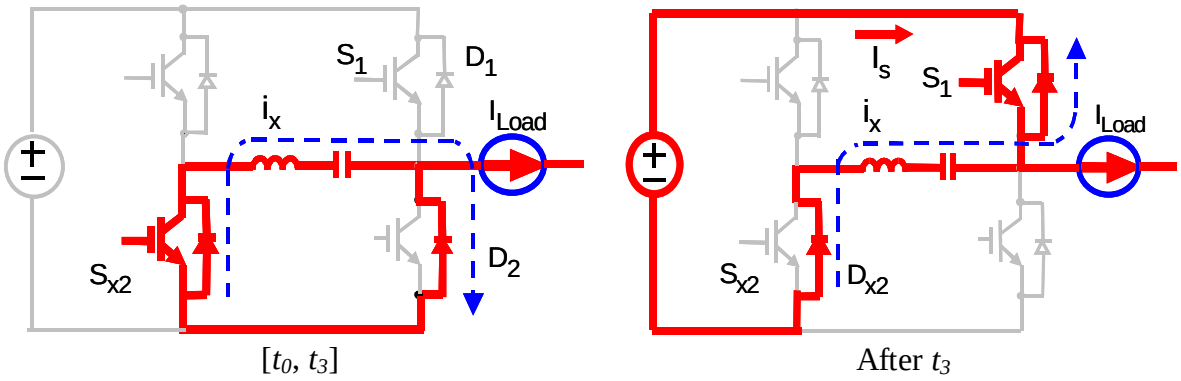

Figure 5.12. Reverse-recovery effect of auxiliary diode D_{x2} in the turn-on transition of the six-switch ZV/ZCT.

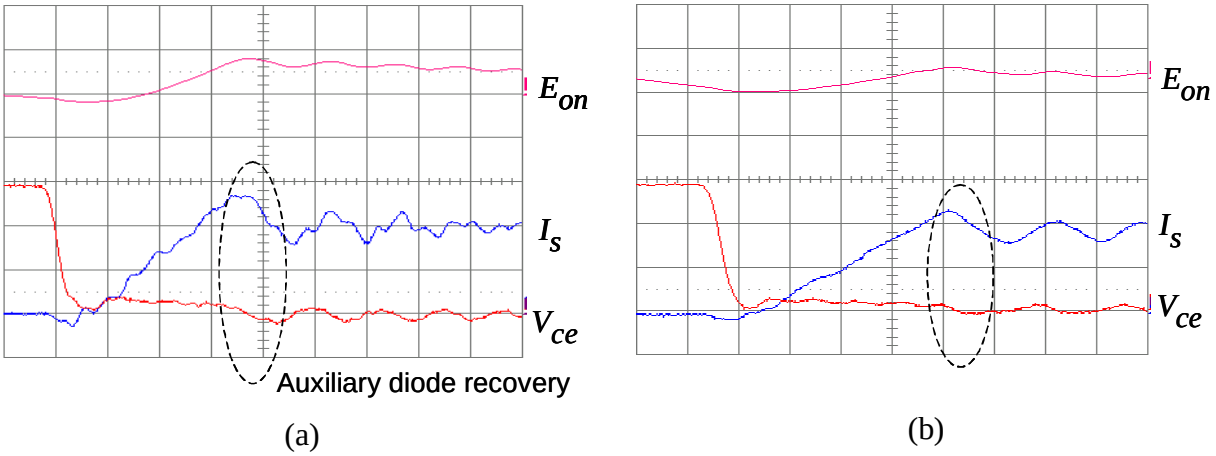

Figure 5.13. Comparison of the main IGBT turn-on waveforms under the six-switch ZV/ZCT condition with different resonant tank designs:
(a) L_x=0.58 μH, C_x=1 μF, T_o=4.8 μs; and
(b) L_x=1 μH, C_x=1 μF, T_o=6.3 μs;
(0.2 μs/div, I_s: 50 A/div, V_{ce}: 100 V/div, E_{on}: 1 mJ/div).

5.1.2.3. Other Factors Affecting Switching Losses

In theoretical analysis, the amplitude of load current I_{Load} is assumed to be constant among switching cycles; also, in the device tests described in the preceding sections, the amplitude of switch current at the instants of turn-on and turn-off are almost the same. In actual applications such as motor drives, however, the amplitude of I_{Load} is normally smaller at turn-on than at turn-off, because of the current ripple that occurs due to the finite inductance of the motor stator winding. As a result, the three-switch ZCT inverter may nearly achieve zero-current turn-off of the main diodes, which further reduces the turn-on loss.

The gate driver is another important influence on the IGBT switching loss. The lower the gate drive resistance, the faster the switch turn-on speed, and the smaller the turn-on loss, but the more severe the diode reverse recovery. It has much less influence on the turn-off loss. So with a larger gate drive resistance, the effect of switching loss reduction by the ZCT operations, especially for the six-switch ZV/ZCT, will be more significant.

5.1.3. Summary

This section has presented an experimental comparative study of the switching behaviors and losses of the main IGBT (MG300J2YS50, 300-A/600-V, half-bridge) under the hard-switching, three-switch ZCT and six-switch ZV/ZCT conditions. To facilitate the comparison, a high-power soft-switching tester has been developed. Turn-on and turn-off losses of the IGBT under different current levels and resonant tank designs are measured and compared. Both ZCT operations almost eliminate the turn-off loss, and the difference is mainly found in the turn-on losses. Under resonant tank elements of L_x=1 μH and C_x=1 μF, compared to hard switching, three-switch ZCT reduces the turn-on loss by about 40%, and the total switching loss by about 70%; the six-switch ZV/ZCT reduces the turn-on loss by about 75%, and the total switching loss by about 90%. The effect of the conductivity modulation lag is observed in the six-switch ZV/ZCT inverter. This effect is common to the turn-on processes of most ZVS converters, but this is the first time to observe this effect in ZCS converters. Moreover, with different resonant tank designs, the ZCT turn-off loss is basically unchanged, but the turn-on loss and behaviors vary quite substantially between the two ZCT operations. For the three-switch ZCT, reducing L_x can significantly increase the turn-on loss; on the other hand, increasing L_x has a limited effect in reducing the turn-on loss. For the six-switch ZV/ZCT, reducing L_x does not significantly increase the turn-on loss. L_x and C_x also affect the diode reverse recovery and the range of ZCT operations.

Knowledge of the switching characteristics of the main IGBTs is important to the design of the 55-kW inverters. Moreover, the methods used for the study and the soft-switching mechanisms obtained from the study are applicable to other IGBT devices with similar power ratings.

5.2. Considerations for Determining Resonant Tank Parameters

Since EV drives cover wide torque and speed ranges with changing power factors, it is important to investigate the soft-switching operation over a variable instantaneous switch current *I(t)*. For ZVT inverters, such as the ARCP inverter, snubber capacitors are directly connected across the main switches, so the zero-voltage turn-on condition must be satisfied for every switching event; otherwise, the energy remaining in the snubber capacitors will "dump" directly into the switches, causing excessive turn-on losses. For the ZCT inverters, the resonant current peak I_{xpk} is largely determined by the DC bus voltage V_{dc} and the resonant tank impedance Z_o. The necessary condition for the zero-current turn-off is that I_{xpk} exceeds *I(t)*. If I_{xpk} is less than *I(t)* in heavy load or transient situations, the zero-current turn-off can not be realized completely. Unlike the case for ZVT inverters, however, if the zero-current turn-off condition is lost, the main switch can still be safely turned off with a substantially reduced switching loss. Meanwhile, voltage overshoots across the switches are still reduced. On the other hand, under light load conditions, the switching loss is relatively small. If I_{xpk} is too high compared with the load current, unnecessary circulating energy and conduction loss will be caused by the ZCT commutations.

The design of resonant tanks aims to optimize the total inverter losses over the entire torque and speed ranges of EV drives, with an appropriate trade-off between switching losses and conduction losses. The resonant tank parameters are determined based on the maximum switch current subjected to the zero-current turn-off, I_m, at which level the zero-current turn-off is completely realized. There are several factors involved in choosing the I_m: the power rating of the inverter, the power factor, and the SVM scheme.

The required peak output power is 55 kW, and the continuous output power is 30 kW. The 30-kW continuous power is used to determine the I_m. The output power is given by

$$P_{out} = \sqrt{3} \cdot I_{rms} \cdot \frac{V_{dc} \cdot M}{\sqrt{2}} \cdot pf \,, \tag{5.1}$$

where I_{rms} is the RMS value of the motor phase current, pf is the power factor of the load induction motor, and M is the modulation index, defined as

$$M = \frac{V_{line\_line\_peak}}{V_{dc}}. \tag{5.2}$$

According to data for typical motor drives with hard-switching inverters, it is reasonable to assume that M=0.7 and pf=0.85. From Equation (5.1), I_{rms} is determined to be 128 A, and the peak value of the phase current I_{L_pk} is 180 A.

The six-step space vector modulation (SVM) will be employed for inverter control. This method keeps the main switch of one phase closed within each 60^o sector and modulates the duty cycles of the other two phases to regulate the output voltage. Assuming the power factor is high enough, within one sector, the phase with the highest current is the one that is left *on* to avoid high switching losses. Therefore, I_m is obtained as

$$I_m = I_{L\_pk} \cdot \sin(60^\circ) = 156\,A\,. \tag{5.3}$$

With these considerations, I_m is determined to be 160 A for the design case.

To achieve zero-current turn-off, the resonant current peak I_{xpk} must exceed the I_m. Meanwhile, to effectively reduce the IGBT turn-off loss under I_m, the zero-current interval T_{tran}, in which the surplus current is conducted by the anti-parallel diode across the IGBT, should be long enough that the remaining free carriers in the IGBT will be mostly recombined. For the six-switch ZV/ZCT, the T_{tran} is [t_6, t_7] in Figure 2.5. For the three-switch ZCT, the T_{tran} is [t_7, t_8] in Figure 3.6 under I_{Load}>0, and is [t_6, t_7] in Figure 3.8 under I_{Load}<0. The choice of T_{tran} is device-

independent. Normally, T_{tran} should be longer than the turn-off time of the IGBT. As illustrated in Figure 5.14, for a given T_{tran} and I_m, there are various combinations of L_x and C_x that can achieve zero-current turn-off. Under the premise of achieving the ZCT soft commutations, the design objective is to search for the optimal L_x and C_x that can minimize the additional conduction loss caused by the soft-switching action for the given T_{tran}.

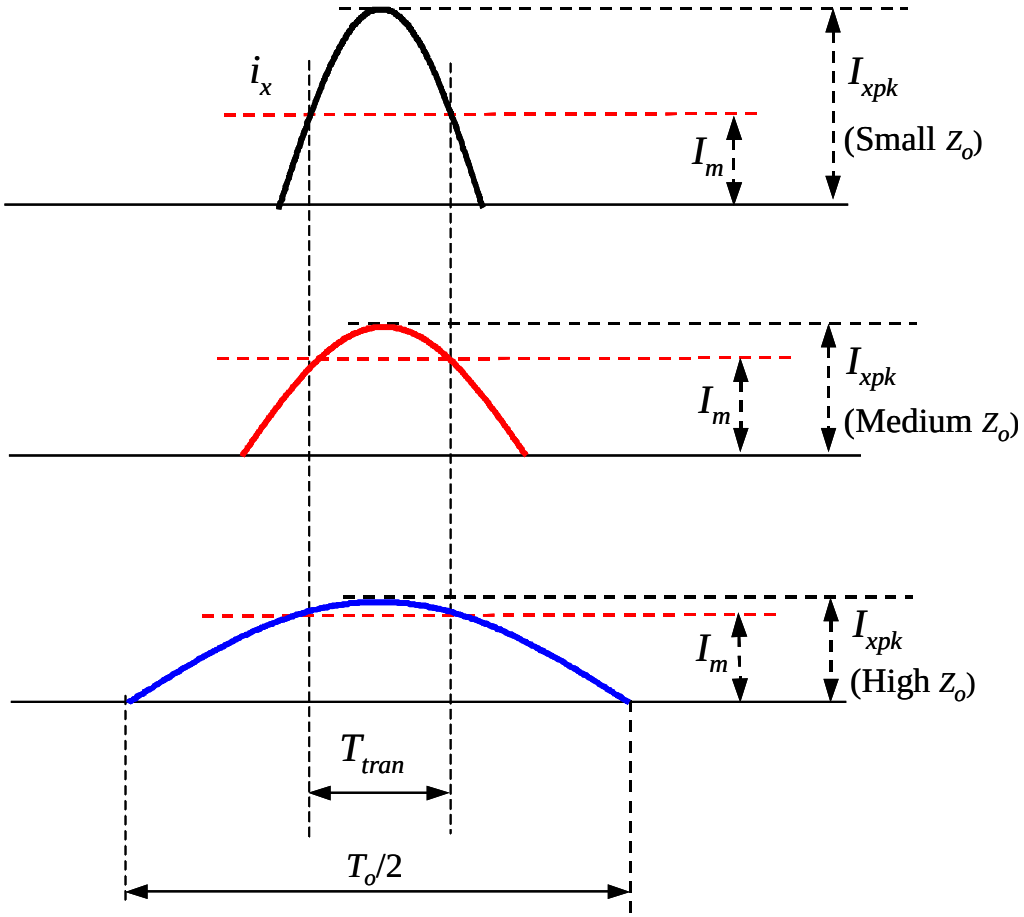

Figure 5.14. Zero-current-turn-off commutation current pulses under different Z_o and T_o.

One design variable k is defined as

$$k = \frac{I_{xpk}}{I_m}. \tag{5.4}$$

It is derived for both ZCT inverters that

$$T_{tran} = T_o \cos^{-1}(1/k)/\pi . \tag{5.5}$$

To simplify the analysis, it is assumed that the auxiliary switches and diodes have equal conduction voltage drops, and that the conduction loss in the auxiliary circuits is proportional to the resonant current i_x. This power loss is represented by a constant conduction voltage drop with i_x flowing through, and is denoted as V_c. In the main circuits, the ZCT commutations also cause additional conduction loss. The conduction loss in the main circuits is increased when both the resonant current and load current flow in the same direction, i.e., both flow into the main circuit or vice versa. The loss is reduced when the two currents flow in the opposite directions. It is also assumed that the main switches and diodes have equal voltage drops, and that this voltage drop remains constant under changing device currents, and is *1/h* of the voltage drop in the auxiliary circuit, i.e., V_c/h.

Using a method similar to that used in [C20], based on the physical understanding that the charge variation of the resonant capacitor equals the integral of i_x, expressions for the total additional conduction energy loss caused by soft switching in one switching cycle, E_{total}, are derived. It turns out that the expressions for both the six-switch ZV/ZCT and the three-switch ZCT inverters are the same, as given by

$$E_{total} = 2V_c\left(1 + k + \frac{\sqrt{k^2 - 1} - \cos^{-1}(1/k)}{h}\right) \cdot I_m \cdot T_o / \pi . \tag{5.6}$$

In the design with given V_c, T_{tran} and I_m, the objective then becomes to minimize the normalized energy loss caused by soft switching, as follows:

$$E_n = E_{total} / (2V_c I_m T_{tran}) = \frac{1 + k + (\sqrt{k^2 - 1} - \cos^{-1}(1/k))/h}{\cos^{-1}(1/k)} . \tag{5.7}$$

Figure 5.15 plots the E_n as a function of k. It can be seen that k should be in the range of 1.5~1.7 in order to minimize the E_n. However, Figure 5.15 also indicates that the optimum E_n is not very sensitive to the variation of k, so k can be selected within a relatively wide range around its optimal value without significantly increasing power loss. This feature allows freedom to control the di/dt of the switch and diode currents and to reduce the turn-on losses, as discussed in Section 5.1.

Although both ZCT inverters use the same criteria for selecting the value of k, the resonant elements are calculated based on different equations. For the six-switch ZV/ZCT inverter, referring to Section 2.4.1, combining Equation (2.10) with (5.4) and (5.5), L_x and C_x are calculated as

$$L_{x\_6Sw} = \frac{V_{dc} T_{tran}}{2(k+1) I_m \cos^{-1}(1/k)}, \text{ and} \tag{5.8}$$

$$C_{x\_6Sw} = \frac{(k+1) T_{tran} I_m}{2V_{dc} \cos^{-1}(1/k)}. \tag{5.9}$$

On the other hand, for the three-switch ZCT inverter, referring to Section 3.4.1, combining Equation (3.2) with (5.4) and (5.5) yields

$$L_{x\_3Sw} = \frac{V_{dc} T_{tran}}{2k \cdot I_m \cos^{-1}(1/k)}, \text{ and} \tag{5.10}$$

$$C_{x\_3Sw} = \frac{k \cdot T_{tran} I_m}{2V_{dc} \cos^{-1}(1/k)}. \tag{5.11}$$

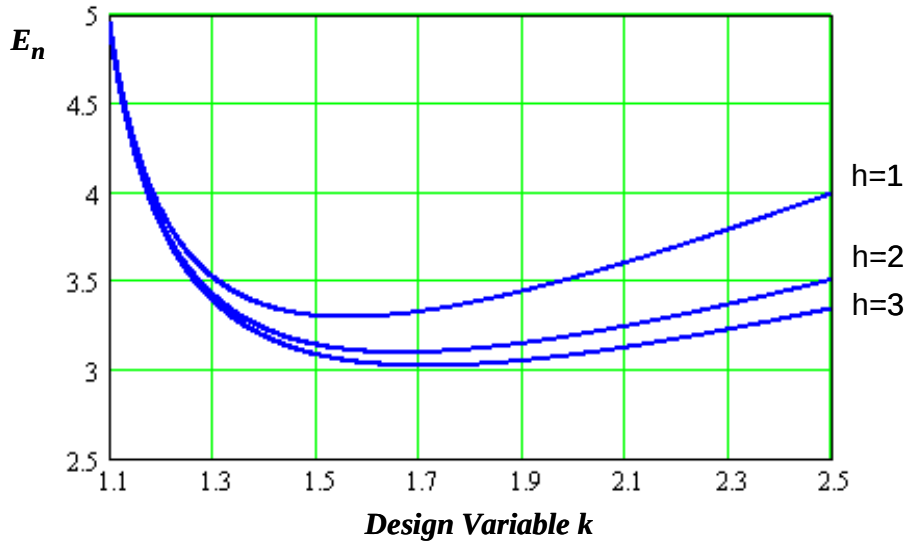

Figure. 5.15. The normalized additional conduction energy loss caused by ZCT commutations E_n as a function of the design variable k.

The MG300J2YS50 IGBT is chosen as the main switch. Its typical turn-off time is around 0.5~1 μs [E6], so T_{tran} can be selected to be around 1.2~1.5 μs. This T_{tran} can ensure proper ZCT commutations; meanwhile, it will not make resonant time period T_o be too long. Following Equations (5.8)~(5.11), by plotting the values of L_x and C_x onto one graph, with L_x and C_x as the horizontal and vertical axes respectively, the trajectories of the resonant elements of both ZCT inverters against a changing k are obtained, as shown in Figure 5.16. With the same operation conditions and device characteristics, the six-switch ZV/ZCT is generally designed with smaller L_x but larger C_x.

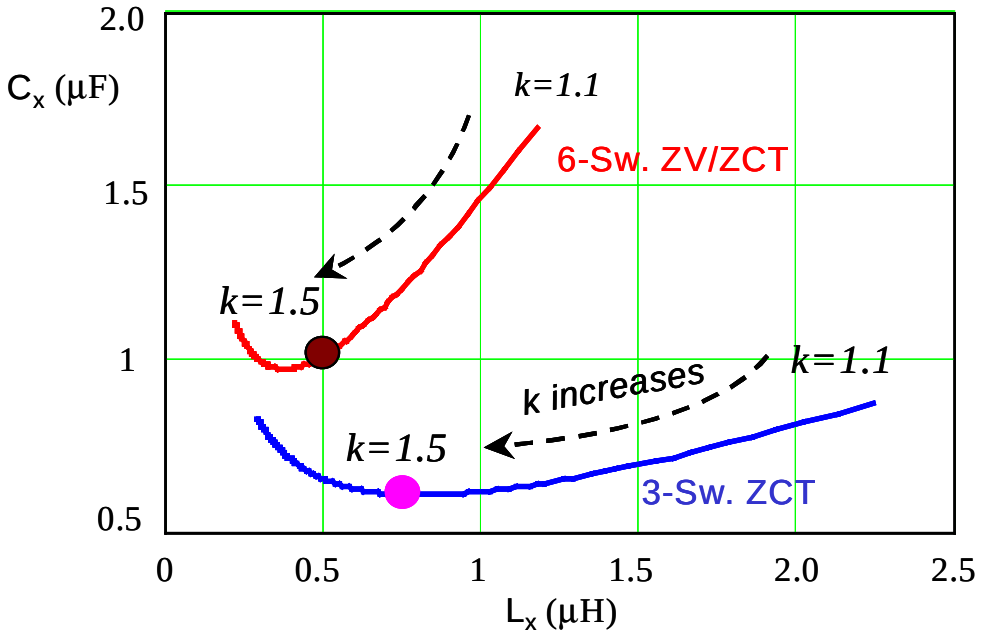

Figure 5.16. Trajectories of the *LC* resonant elements of the two ZCT inverters against a changing *k* (conditions: V_{dc}=325 V, I_m=160 A, and T_{tran}=1.2 μs)

Given these considerations, for the 55-kW six-switch ZV/ZCT inverter, the resonant tank parameters are designed as L_x=600 nH and C_x=1 μF, which creates T_o of 4.9 μs and Z_o of 0.77 Ω; for the 55-kW three-switch ZCT inverter, these parameters are designed as L_x=820 nH and C_x=0.625 μF, which creates T_o of 4.5 μs and Z_o of 1.15 Ω.

The preceding analysis of conduction losses can provide some insight and serve as a starting point for the design. However, they are based on the much-simplified loss models of the devices and components, and are relatively rough. In Section 5.6, improved loss models of the devices and components as well as the entire ZCT inverters will be developed, from which further design optimization will proceed.

5.3. Selection of Resonant Capacitors

5.3.1. Expressions of the Auxiliary Circuit Current Stresses

The knowledge of the auxiliary circuit currents is critical to the selection of the resonant capacitors, as well as to the design of resonant inductors and the selection of auxiliary devices. For ease of illustration, the resonant current waveforms of both ZCT inverters are repeated in Figures 5.17 and 5.18, which also show control timings that will be used for the discussions in Sections 5.6 and 5.7. Using the waveforms' properties and the state-plane trajectories (Figures 2.9 and 3.9) as visual aids, the expressions of the peak currents in the auxiliary switches and diodes are estimated and given in Tables 5.4 and 5.5, where *I(t)* is the instantaneous load current at a switching cycle, given by

$$I(t) = I_{L\_pk} \sin(\frac{2\pi}{T} t). \tag{5.12}$$

(Note: the instantaneous load current was labeled as I_{Load} in Figures 2.5, 3.6 and 3.8; in order to simplify the appearance of the equations that will be described in this chapter and to reflect the time-dependent property of the sinusoidal line current, unless specially indicated, the instantaneous load current is denoted as *I(t)* in this chapter.)

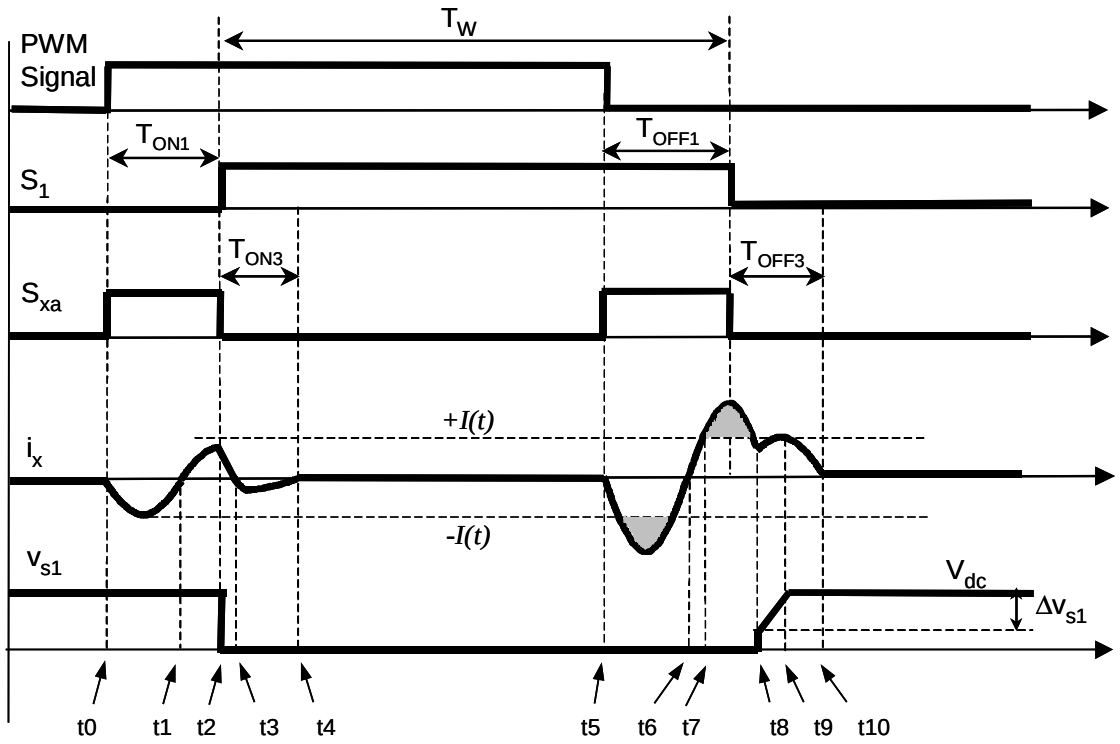

(a)

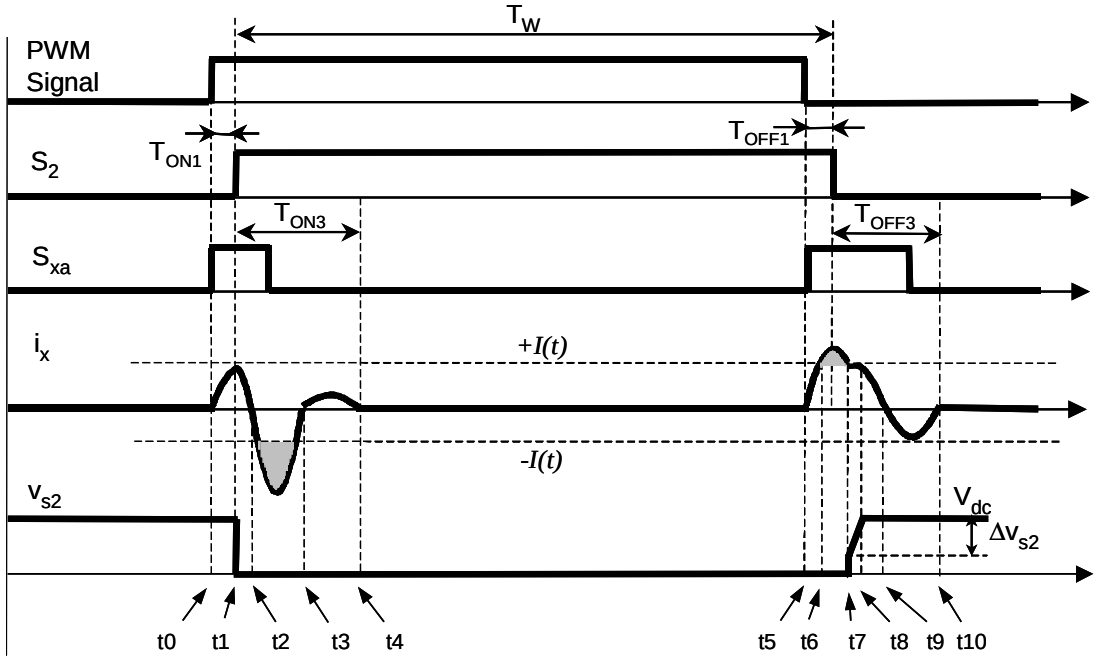

(b)

Figure 5.17. Operational waveforms and control timings of the three-switch ZCT inverter: (a) I_{Load}>0; and (b) I_{Load}<0.

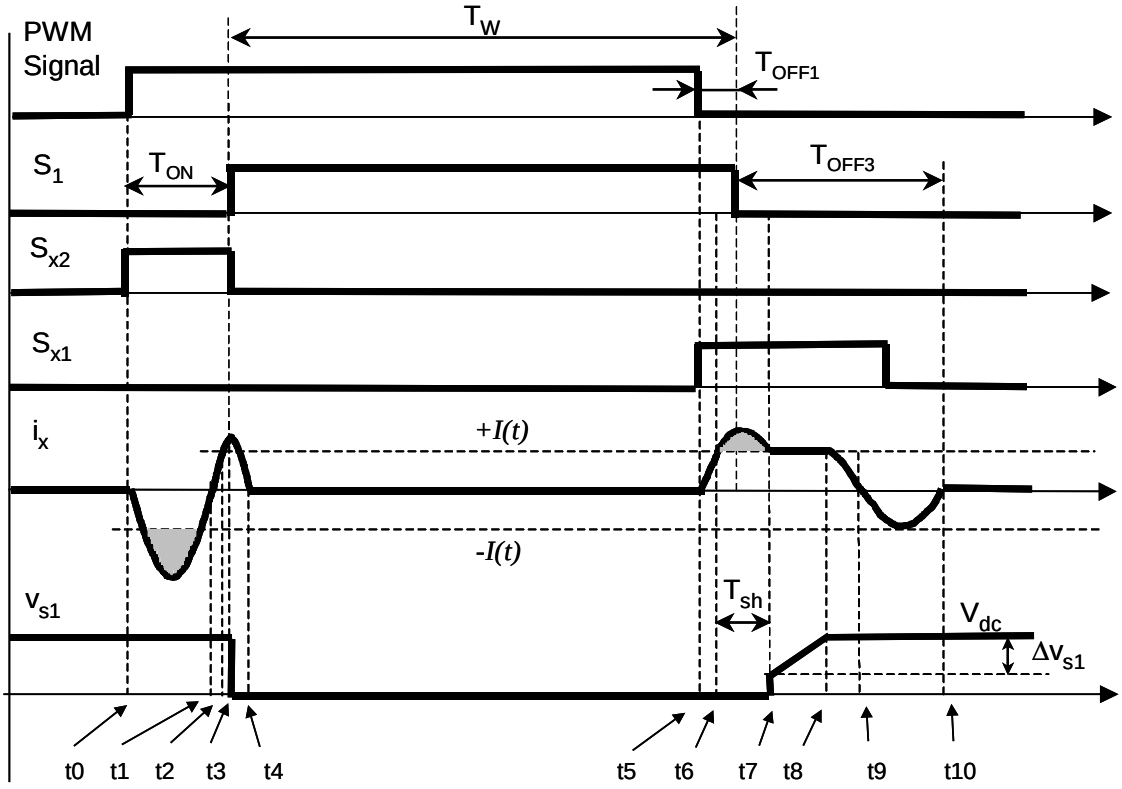

Figure 5.18. Operational waveforms and control timings of the six-switch ZV/ZCT inverter.

Table 5.4
Expressions of the Peak Auxiliary *Switch* Currents

	Actual Peak Currents	Normalized by V_{dc}/Z_o
6-Switch ZV/ZCT $I_{x\_pk\_6sw}(t)$	$\frac{V_{dc}}{Z_{o\_6sw}} - I(t)$	$1 - IL_n$
3-Switch ZCT @ $I_{Load}>0$ $I_{x\_pk\_off\_3sw}(t)$	$\frac{V_{dc}}{Z_{o\_3sw}}\left(2 - \sqrt{1 + \frac{(I(t)Z_{o\_3sw})^2}{{V_{dc}}^2}}\right)$ $\approx \frac{V_{dc}}{Z_{o\_3sw}}$	$2 - \sqrt{1 + {IL_n}^2} \approx 1$
3-Switch ZCT @ $I_{Load}<0$ $I_{x\_pk\_off\_3sw}(t)$	$\frac{V_{dc}}{Z_{o\_3sw}}\left(2 - \sqrt{1 + \frac{(I(t)Z_{o\_3sw})^2}{{V_{dc}}^2}}\right)$ $\approx \frac{V_{dc}}{Z_{o\_3sw}}$	$2 - \sqrt{1 + {IL_n}^2} \approx 1$

Table 5.5
Expressions of the Peak Auxiliary *Diode* Currents

	Actual Peak Currents	Normalized by V_{dc}/Z_o
6-Switch ZV/ZCT	$I(t)$	IL_n
3-Switch ZCT @ $I_{Load}>0$ $I_{x\_pk\_off\_3sw}(t)$	$\frac{V_{dc}}{Z_{o\_3sw}}(2-\sqrt{1+\frac{(I(t)Z_{o\_3sw})^2}{{V_{dc}}^2}}$ $\approx \frac{V_{dc}}{Z_{o\_3sw}}$	$2-\sqrt{1+{IL_n}^2} \approx 1$
3-Switch ZCT @ $I_{Load}<0$ $I_{x\_pk\_on\_n\_3sw}(t)$	$\frac{\sqrt{{V_{dc}}^2+(I(t)Z_{o\_3sw})^2}}{Z_{o\_3sw}}$	$\sqrt{1+{IL_n}^2}$

The average and RMS currents of the six-switch ZV/ZCT inverter are derived as follows. First, the turn-on transition is considered. One auxiliary switch conducts during [t_0, t_1], and its average and RMS currents within the switching cycle are obtained by

$$I_{avg\_s\_on\_6sw}(t) = I_{x\_pk\_6sw}(t)\cdot T_o f_s/\pi, \text{ and} \tag{5.13}$$

$$I_{rms\_s\_on\_6sw}(t) = I_{x\_pk\_6sw}(t)\cdot \sqrt{T_o f_s}/2, \tag{5.14}$$

where f_s is the inverter switching frequency. The anti-parallel diode across the auxiliary switch conducts during [t_1, t_4], and its average and RMS currents are approximated as

$$I_{avg\_d\_on\_6sw}(t) = I_{avg\_s\_on\_6sw}(t)/4, \text{ and} \tag{5.15}$$

$$I_{rms\_d\_on\_6sw}(t) = I_{rms\_s\_on\_6sw}(t)/2. \tag{5.16}$$

Second, the turn-off transition is considered. The other auxiliary switch conducts during [t_5, t_9]. For simplicity, this interval is estimated as half of a resonant cycle, with the peak current as $I_{x\_pk\_6sw}(t)$. The auxiliary switch currents are given by

$$I_{avg\_s\_off\_6sw}(t) = I_{x\_pk\_6sw}(t)\cdot T_o f_s/\pi, \text{ and} \tag{5.17}$$

$$I_{rms\_s\_off\_6sw}(t) = I_{x\_pk\_6sw}(t)\cdot \sqrt{T_o f_s}/2. \tag{5.18}$$

The other auxiliary diode conducts during [t_9, t_{10}] with the peak current as $I(t)$, and its currents are given by

$$I_{avg\_d\_off\_6sw}(t) = I(t) \cdot T_o f_s / \pi, \text{ and} \tag{5.19}$$

$$I_{rms\_d\_off\_6sw}(t) = I(t) \cdot \sqrt{T_o f_s} / 2. \tag{5.20}$$

Over the fundamental line cycle, with the six-step SVM, the average and RMS currents of the auxiliary switch and diode are obtained respectively as

$$\begin{cases} I_{avg\_s\_6sw} = \int_0^{T/6} (I_{avg\_s\_on\_6sw}(t) + I_{avg\_s\_off\_6sw}(t)) dt \cdot 2/T \\ I_{rms\_s\_6sw} = \sqrt{\int_0^{T/6} (I^2_{rms\_s\_on\_6sw}(t) + I^2_{rms\_s\_off\_6sw}(t)) dt \cdot 2/T} \end{cases}, \tag{5.21}$$

and

$$\begin{cases} I_{avg\_d\_6sw} = \int_0^{T/6} (I_{avg\_d\_on\_6sw}(t) + I_{avg\_d\_off\_6sw}(t)) dt \cdot 2/T \\ I_{rms\_d\_6sw} = \sqrt{\int_0^{T/6} (I^2_{rms\_d\_on\_6sw}(t) + I^2_{rms\_d\_off\_6sw}(t)) dt \cdot 2/T} \end{cases}. \tag{5.22}$$

Thus, the RMS current flowing through the resonant capacitor is obtained as

$$I_{x\_rms\_6sw} = \sqrt{2(I^2_{rms\_d\_6sw} + I^2_{rms\_s\_6sw})}. \tag{5.23}$$

In a similar way, the average and RMS currents of the three-switch ZCT inverter are derived, and the expressions are listed in Appendix B.

5.3.2. Threshold Control to Reduce the RMS Currents in Resonant Capacitors

Following the derived auxiliary circuit current expressions, Figure 5.19 plots the resonant capacitor RMS current as a function of the peak load current IL_{pk} under different switching frequencies f_s. As implied by Equations (5.14), (5.18) and (5.20), and also as shown in Figure 5.19, the RMS current is proportional to $\sqrt{f_s}$. The RMS current is almost constant under

different levels of IL_{pk} in the three-switch ZCT, and even slightly increases under smaller levels of IL_{pk} in the six-switch ZV/ZCT inverter. This will cause relatively high conduction losses in the auxiliary circuit under light load currents, at which conditions the switching losses are relatively small. To have a proper trade-off between the conduction and switching losses, a method is proposed to control the ZCT inverters— the auxiliary switches should be disabled when the instantaneous current *I(t)* becomes less than a certain threshold value I_{th}. This method is called "threshold control," and is illustrated in Figure 5.20, in which the T_{th} is a time interval corresponding to I_{th}, given by

$$T_{th} = \frac{\sin^{-1}\left(\frac{I_{th}}{IL_{pk}}\right)}{2\pi} T \,. \tag{5.24}$$

Clearly, the I_{th} should be chosen such that when *I(t)* is above I_{th}, the switching loss saved by soft switching is greater than the additional conduction loss caused by soft switching. The determination of the value of I_{th} involves device, component and inverter loss models, and will be calculated in Section 5.6. Normally, it is around 50 A in the 55-kW ZCT inverters. To calculate the RMS current with threshold control, the integration in Equations (5.21) and (5.22) should start from T_{th}. For instance, Equation (5.21) becomes

$$\begin{cases} I_{avg\_s\_6sw} = \int_{T_{th}}^{T/6} (I_{avg\_s\_on\_6sw}(t) + I_{avg\_s\_off\_6sw}(t))dt \cdot 2/T \\ I_{rms\_s\_6sw} = \sqrt{\int_{T_{th}}^{T/6} (I^2_{rms\_s\_on\_6sw}(t) + I^2_{rms\_s\_off\_6sw}(t))dt \cdot 2/T} \end{cases}. \tag{5.25}$$

As shown in Figure 5.21, with threshold control, the RMS current becomes adaptive to the change of IL_{pk}. Under 10-kHz switching frequency, the maximum RMS current is reduced from about 60 A to below 40 A in the six-switch ZV/ZCT inverter. For the three-switch ZCT inverter, the maximum RMS current, which occurs at the heaviest load condition, is almost unchanged,

but the RMS current at lighter loads is significantly reduced. The ESR loss in the resonant capacitors, which is proportional to the square of the RMS current, is substantially reduced. More importantly, the capacitors will have less severe thermal management requirements.

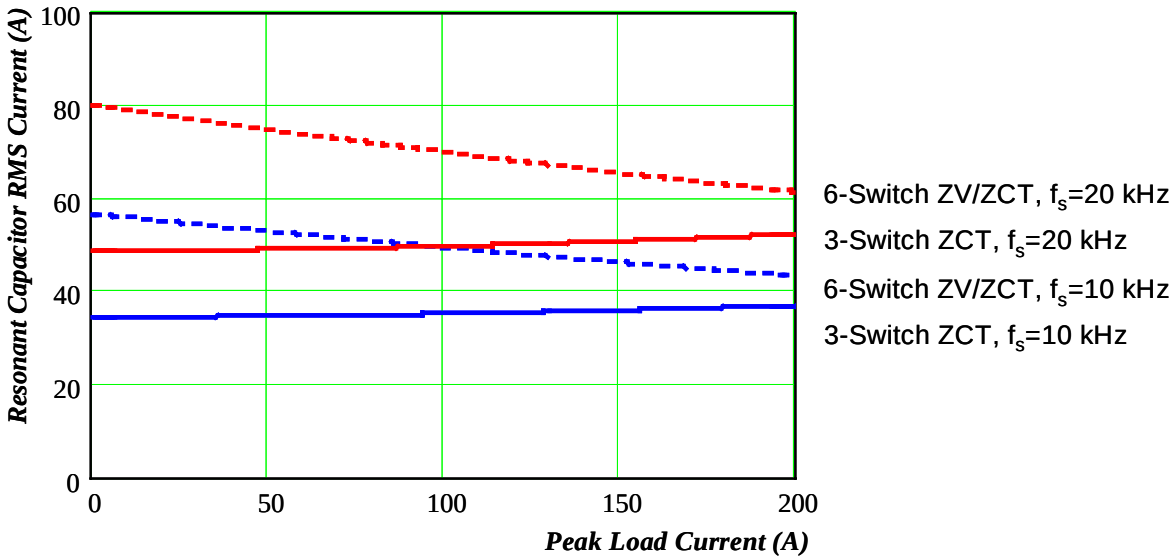

Figure 5.19. Resonant capacitor RMS current as a function of the peak load current IL_{pk} *without* threshold control.

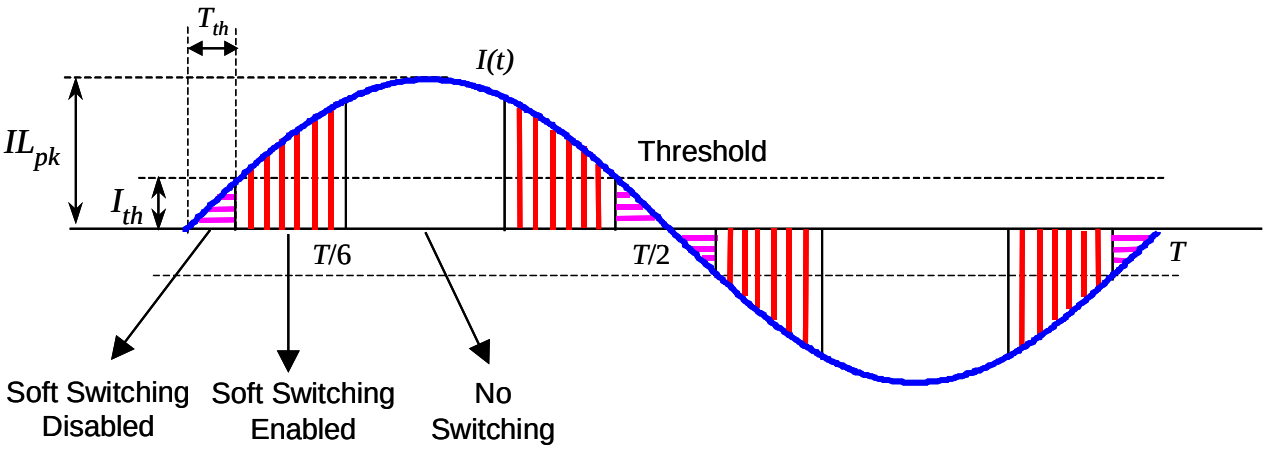

Figure 5.20. Concept of the threshold control with the six-step SVM (assuming the power factor angle is less than 30 degrees).

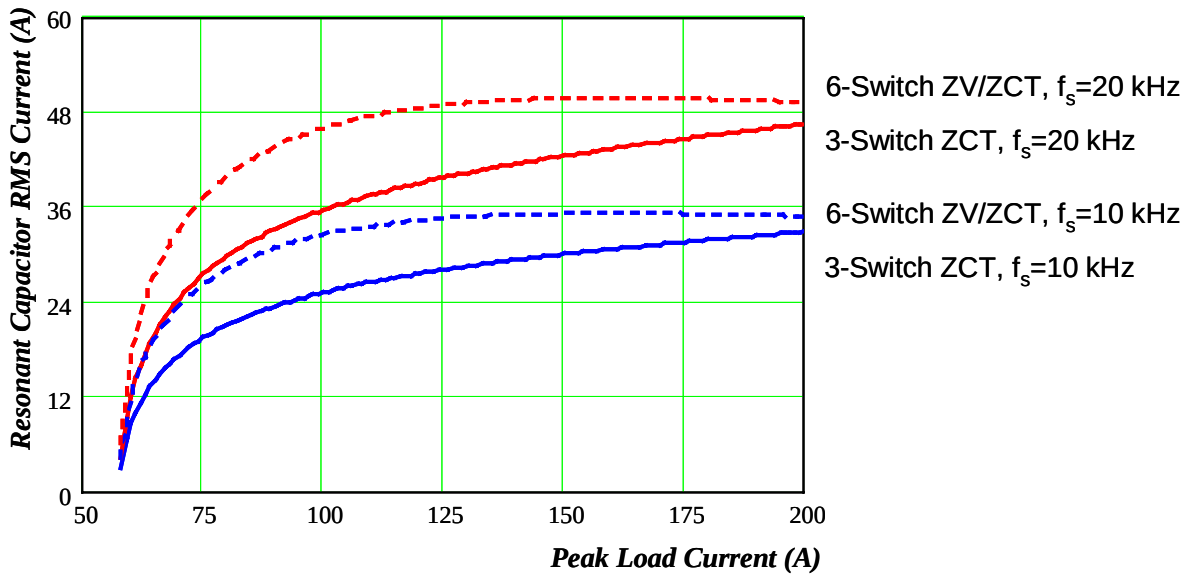

Figure 5.21. Resonant capacitor RMS current as a function of the peak load current *with* threshold control under different switching frequencies (I_{th}=50 A).

5.3.3. The Selected Capacitors

Polypropylene film capacitors are a good choice for minimizing the power loss under high-frequency high-current operations. For the 55-kW six-switch ZV/ZCT inverter, the SBE 78PC105K6-100, 1-μF/630-V polypropylene metalized film capacitor is chosen; for the 55-kW three-switch ZCT inverter, the SBE 716P series 0.625-μF/1000-V polypropylene metalized film capacitor is chosen. Both have an RMS current rating of 50 A, a dissipation factor of approximately 0.08% at 100 kHz, and an ESR of about 1.4 mΩ at 50 kHz [E7].

5.4. Design of Resonant Inductors

Molypermalloy powder (MPP) cores are suitable for the resonant inductors, because they typically saturate at 0.8 T and offer low losses at high frequencies. With all other things being equal, at typical power frequencies, MPP shows the lowest core losses among powder cores,

followed by Kool Mμ, then high flux, and then iron powder [E8]. The Magnetics MPP core with permeability of μ=60 is selected, which yields inductance by

$$L_x = \frac{0.4\pi\mu N^2}{L_p} A_c , \tag{5.26}$$

where L_p is the magnetic path length, A_c is the cross-section area, and N is the turns number.

The design objective is to minimize the inductor losses, or with some trade-offs, to achieve low losses with small size; the size is represented by the product of L_pA_c. With the conductor losses being negligible, the core losses are the major source of inductor losses. However, the core loss calculation, which is critical to the design task, is different from those of conventional applications, because the cores are exposed to discontinuous nonsinusoidal flux waveforms, as shown in Figures 5.17 and 5.18 (assuming the cores operate in the linear region, the flux waveforms are in the same shape as the resonant current i_x waveforms). Since the core losses with magnetic materials are highly nonlinear, the Fourier analysis and superposition method cannot be used. In instead, the modified Steinmetz equation (MSE), which was proposed recently [E9]-[E11], is used to analyze the core losses and to assist the design optimization.

5.4.1. Design Optimization Based on the Modified Steinmetz Equation

5.4.1.1. The Modified Steinmetz Equation (MSE)

One well-known empirical equation for calculating core losses can be traced back more than a century ago to the original work of Steinmetz, and is formulated by means of an empirical equation [E12], as follows:

$$p_v = C_m f^{\alpha} \left(\frac{\Delta B}{2}\right)^{\beta} . \tag{5.27}$$

It states that the power losses per volume p_v are dependent on power functions of the excitation frequency f and the flux swing ΔB (the peak-to-peak flux density amplitude), using three empirical parameters C_m, α and β, which are usually published by the core manufacturers. The Steinmetz equation, however, cannot be used for the resonant inductor design and analysis, because this equation is only valid for sinusoidal flux excitation.

The MSE is useful for this application due to its simplicity and because it requires no additional material parameters beyond those used in the Steinmetz equation. The MSE is based on the physical understanding that the core losses are proportional to the changing rate of flux density, *dB/dt*. It determines an equivalent frequency f_{eq} for a nonsinusoidal excitation. The core loss of a sinusoidal excitation under the same f_{eq} is considered equal to the core loss of the nonsinusoidal excitation. With the same ΔB, both excitations have the same $\langle dB/dt \rangle_w$, which is the averaged *dB/dt* over an excitation cycle, given by

$$\langle dB/dt \rangle_w = \frac{1}{\Delta B} \int_0^{T_m} (\frac{dB}{dt})^2 dt, \tag{5.28}$$

where T_m is the period of the flux waveform. Therefore, the f_{eq} is defined by

$$f_{eq} = \frac{2}{\Delta B^2 \pi^2} \int_0^{T_m} (\frac{dB}{dt})^2 dt. \tag{5.29}$$

In a format similar to that of the original Steinmetz equation, the core energy loss per volume of one excitation cycle, e_v, is calculated by the MSE as

$$e_v = C_m f_{eq}^{\alpha-1} (\frac{\Delta B}{2})^{\beta}. \tag{5.30}$$

If the nonsinusoidal flux waveform is repeated with f_r, the power loss per volume is

$$p_v = (C_m f_{eq}^{\alpha-1} (\frac{\Delta B}{2})^{\beta}) f_r. \tag{5.31}$$

5.4.1.2. Analysis and Design of the Resonant Inductors

To use the MSE for the analysis and design of the resonant inductors, the critical step is to identify the equivalent frequency f_{eq} for the flux waveforms shown in Figures 5.17 and 5.18. Assuming the cores operate in the linear region, Equation (5.29) can be rewritten as

$$f_{eq} = \frac{2}{\Delta i_x{}^2 \pi^2} \int_0^{T_m} \left(\frac{di_x}{dt}\right)^2 dt, \tag{5.32}$$

where Δi_x is the peak-to-peak resonant current amplitude.

The turn-on transition of the three-switch ZCT for $I_{Load}>0$ (Figure 5.17(a)) is analyzed first. As shown in Figure 5.22, the resonant current i_x waveform at this transition can be approximated as ¾ of a resonant cycle T_o at [t_1, t_2], followed by a straight line at [t_2, t_3]. Assuming the width during [t_2, t_3] is T_o/6, the slope turns out to be $6I/T_o$. Following Equation (5.32), the equivalent frequency is estimated by

$$\begin{aligned} f_{eq\_3sw} &= \frac{2}{(2I)^2 \pi^2}\left(\int_0^{\frac{3}{4}T_o} \left(\frac{d(-I\cdot\sin(\frac{2\pi}{T_o}\gamma))}{d\gamma}\right)^2 d\gamma + \int_{t_2}^{t_3} \left(\frac{6I}{T_o}\right)^2 d\gamma\right) \\ &= \left(\frac{3}{4}+\frac{3}{\pi^2}\right)\frac{1}{T_o} \\ &\approx \frac{1}{T_o} \end{aligned} \quad . \tag{5.33}$$

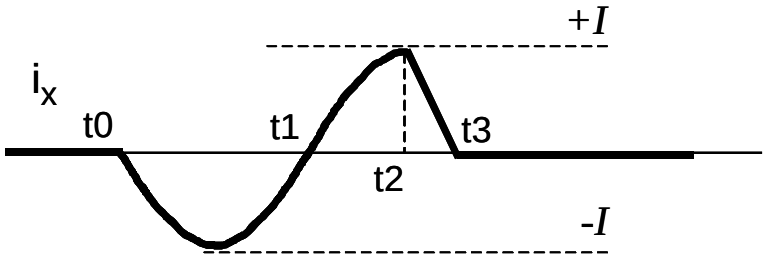

Figure 5.22. Approximated resonant current waveform at turn-on of the three-switch ZCT for $I_{Load}>0$.

In a similar way, the equivalent frequencies f_{eq} are estimated for every turn-on and turn-off transitions in both ZCT inverters, and they turn out to be the same: The resonant frequency $1/T_o$. According to Equation (5.30), the relationship between the variation of core energy loss per volume e_v and the variation of f_{eq} is found to be

$$\frac{\Delta e_v}{e_v} = (1 + \frac{\Delta f_{eq}}{f_{eq}})^{\alpha - 1} - 1. \tag{5.34}$$

For the μ=60 MPP core, α=1.41. Thus, Equation (5.34) means that the variation of f_{eq} does not significantly change the e_v. In other words, the uncertainty and approximation in the estimation of f_{eq} has negligible influence on the core loss calculation. This relationship is also shown as a curve in Figure 5.23.

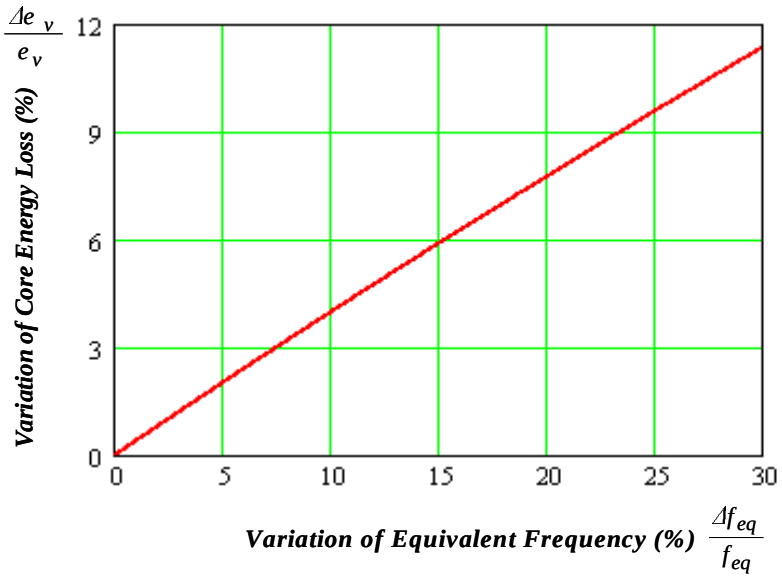

Figure 5.23. Variation of core energy loss $\frac{\Delta e_v}{e_v}$ as a function of $\frac{\Delta f_{eq}}{f_{eq}}$.

The flux swing ΔB in a switching transition can be obtained based on the peak-to-peak resonant current Δi_x as

$$\Delta B = \frac{0.4\pi\mu N}{L_p}\Delta i_x . \tag{5.35}$$

For the μ=60 MPP core, C_m=0.0365, and β=2.24. They are provided in the data sheet for W/Lb, and the core weight per volume is 0.019 Lb/cm^3 [E13]. Thus, the actual core energy loss of a particular inductor in a switching transition, e_c, is calculated by

$$e_c = 0.019 C_m \left(\frac{1}{T_o}\right)^{\alpha-1}\left(\frac{\Delta B}{2}\right)^{\beta} L_p A_c . \tag{5.36}$$

Equation (5.35) implies that a larger L_p or smaller N is preferred in order to reduce ΔB and thus e_c. However, Equation (5.26) implies that for a given inductance, a larger L_p or smaller N requires a larger A_c, which tends to increase the core volume L_pA_c and thus the e_c. Therefore, the design objective becomes to search for a reasonable L_p and N that can result in an acceptably low e_c under I_m, which is the maximum switch current subjected to the zero-current turn-off and which is the design point for the resonant tanks. Figure 5.24 shows the design curves. In these curves, the core energy loss per switching cycle for the six-switch ZV/ZCT is calculated by

$$e_{c\_6sw} = e_{c\_on\_6sw} + e_{c\_off\_6sw}, \tag{5.37}$$

where $e_{c\_on\_6sw}$ and $e_{c\_off\_6sw}$ are respectively the core energy losses at the turn-on and turn-off transitions. For the three-switch ZCT, the core energy loss per switching cycle is calculated by

$$\begin{aligned} e_{c\_3sw} = &(e_{c\_on\_p\_3sw} + e_{c\_off\_p\_3sw})/2 \\ &+ (e_{c\_on\_n\_3sw} + e_{c\_off\_n\_3sw})/2 \end{aligned}, \tag{5.38}$$

where $e_{c\_on\_p\_3sw}$ and $e_{c\_off\_p\_3sw}$ are respectively the core energy losses of turn-on and turn-off transitions for I_{Load}>0, and $e_{c\_on\_n\_3sw}$ and $e_{c\_off\_n\_3sw}$ are those for I_{Load}<0.

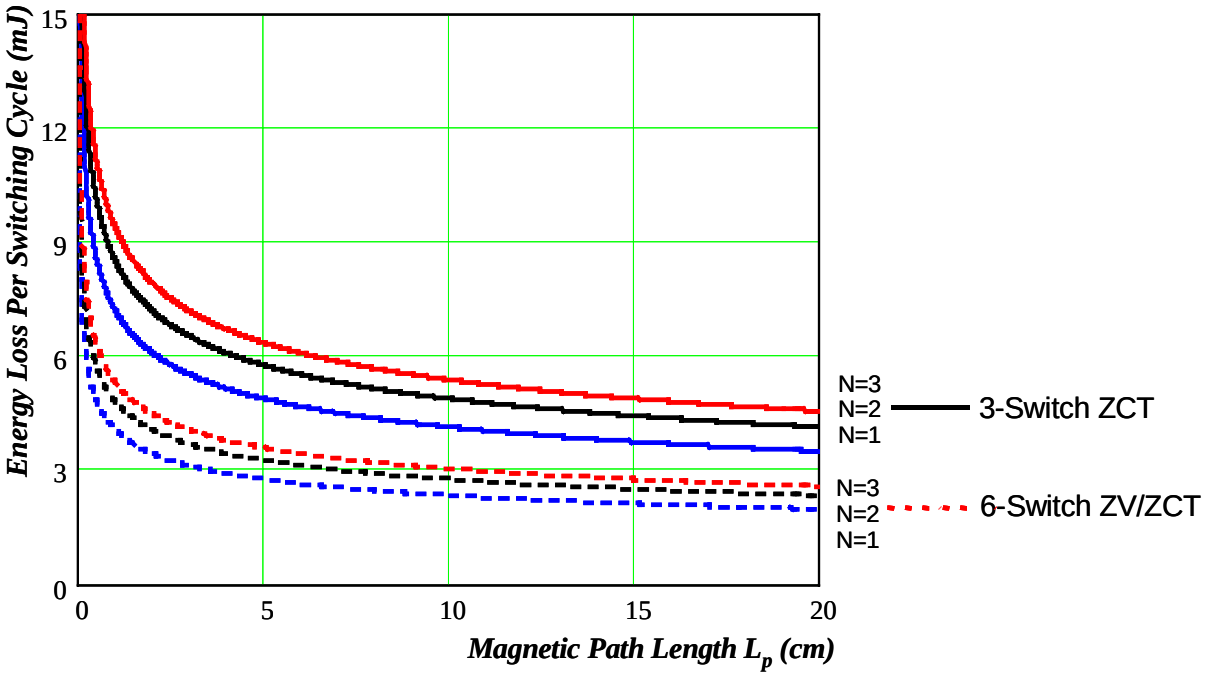

(a)

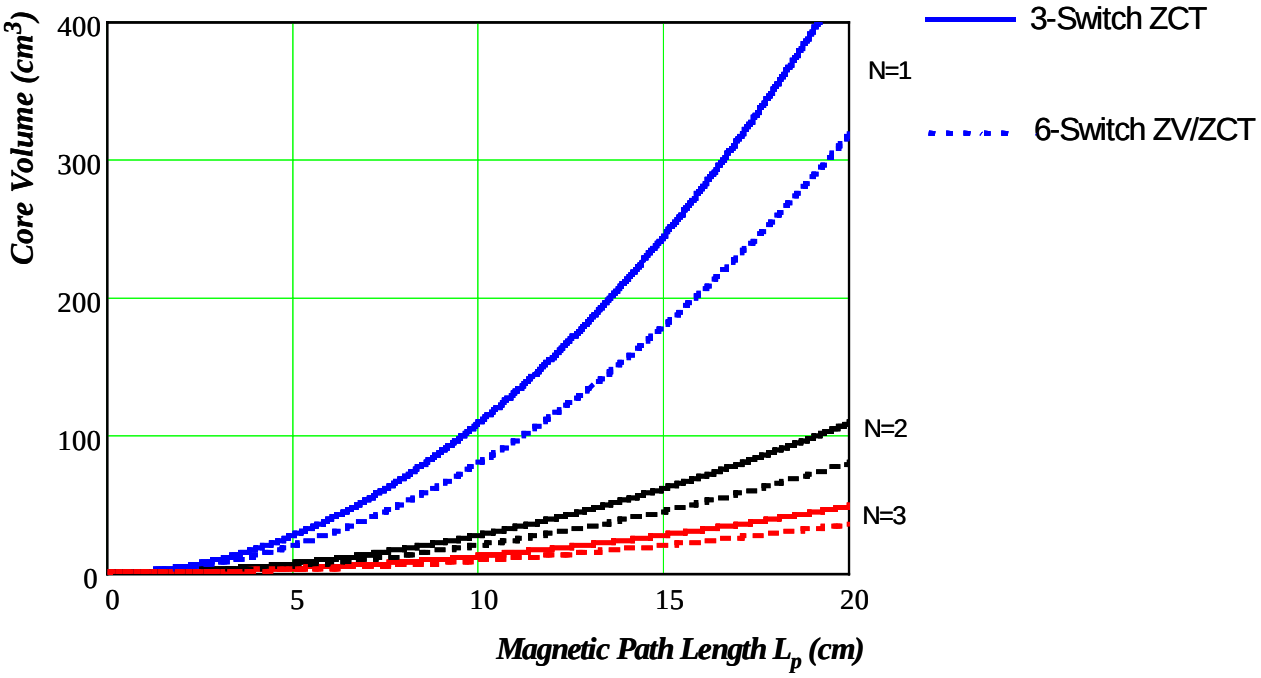

(b)

Figure 5.24. Design curves for the resonant inductors:
(a) core energy loss per switching cycle as a function of L_p and N under I_m=160 A; and
(b) core volume as a function of L_p and N.

The design curves lead to several observations. First, Figure 5.24(a) indicates that the core energy losses per switching cycle for both ZCT inverters decrease as L_p increases; however, after L_p is increased beyond 5~6 cm, the loss decreasing rate becomes much slower, and the curves are almost saturated. On the other hand, as shown in Figure 5.24(b), the core volume increases exponentially as L_p increases. Thus, a good design should choose L_p to be around 5~6 cm. Second, Figure 5.24(a) indicates that a smaller turns number N results in a lower core loss. Although on the other hand a smaller N requires larger core volumes, Figure 5.24(b) shows that if L_p is around 5~6 cm the difference in core volumes between different N is not significant. So N=1 should be chosen. There is another consideration in choosing N=1. In the loss calculation, the cores are assumed to operate in the linear region, and N=1 can prevent the core from being saturated under high-peak resonant current. Third, with the same L_p and N, the three-switch ZCT has higher core volume and loss. There are two major reasons: 1) The three-switch ZCT has a larger inductance (820 nH) than the six-switch ZV/ZCT (600 nH); and 2) at its turn-off transition for $I_{Load}>0$, the i_x peak swings approximately between $+V_{dc}/Z_o$ and $-V_{dc}/Z_o$, which causes the highest ΔB, while the core loss increases exponentially with higher ΔB by the power of β=2.24.

Based on the above discussions, the Magnetics μ=60 MPP 55894-A2 core is selected. Its major parameters are as follows: L_p=6.35 cm, inner dimension of 1.41 cm, and cross-section area of 0.654 cm^2. With N=1, the inductance generated by one 55894-A2 core is about 80 nH. Several cores need to be stacked in order to achieve the desired inductance.

Since the inductance required is less than 1 μH, the stray inductance caused by the inverter layout is counted into the total inductance. Both theoretical analysis and experimental measurements show that the inductance of a one-inch-long AWG 20 wire is about 20 nH; and that of a one-inch-long, 0.3-inch-wide, 32-mil-thick copper foil is about 15 nH within a high

frequency range (100~500 kHz). The difference is caused by the high-frequency parasitic capacitor effect. In the designed inverter power stage, the distance from the main devices to the resonant inductors is about 10~15 inches, which causes about 150~220 nH of stray inductance. Including the stray inductance caused by the laminated bus bar, about 280 nH of stray inductance is counted into the total resonant inductance.

With the stray inductance counted and one turn of conductor going through, the resonant inductor of the six-switch ZV/ZCT inverter is designed using four 55894-A2 cores in stack, and that of the three-switch ZCT inverter is designed using seven 55894-A2 cores in stack. The maximum flux density is around 4000~5000 Gauss in the six-switch ZV/ZCT inverter, and is around 3000 Gauss in the three-switch ZCT inverter. Both are in the core linear region. It should be mentioned that the stray inductance is just an estimated value at the design stage. After the construction of the inverter power stage is completed, a resonant test is performed to verify the actual inductance by measuring the actual resonant time period.

5.4.2. Resonant Inductor Loss Calculation

For the designed resonant inductors, the losses are generated in the four 55894-A2 cores in the six-switch ZV/ZCT inverter, and in the seven 55894-A2 cores in the three-switch ZCT inverter. The core energy losses per switching cycle for both inverters, e_{c_6sw} and e_{c_3sw}, are plotted as functions of the variable instantaneous load current $I(t)$, as shown in Figure 5.25. The e_{c_6sw} is smaller than the e_{c_3sw} within the entire $I(t)$ range. As discussed earlier, this is mainly because the three-switch ZCT uses more cores and has the highest ΔB at the turn-off for $I_{Load}>0$. The important observation is that both e_{c_6sw} and e_{c_3sw} are quite large when $I(t)$ is small. This

result justifies the use of threshold control proposed in Section 5.3 that allows a proper trade-off between the conduction loss and switching loss.

With threshold control, for the two ZCT inverters, the resonant inductor power losses with six-step SVM in line cycles are calculated by

$$p_{c\_6sw} = 4(\sum_{n=N_{th}}^{N_S} e_{c\_6sw}(\frac{n}{f_s}))/T\,, \tag{5.39}$$

$$p_{c\_3sw} = 4(\sum_{n=N_{th}}^{N_S} e_{c\_3sw}(\frac{n}{f_s}))/T\,, \tag{5.40}$$

where N_S is the number of switching cycles within a 60° sector, given by

$$N_S = \frac{T}{6} f_s\,, \tag{5.41}$$

and N_{th} is a number corresponding to the threshold value I_{th}, given by

$$N_{th} = \frac{\sin^{-1}(\frac{I_{th}}{IL_{pk}})}{2\pi} T f_s\,. \tag{5.42}$$

The resonant inductor power losses in line cycles are calculated under a threshold value of I_{th}=50 A, and the curves are plotted using the peak load current IL_{pk} as a running parameter, as shown in Figure 5.26. It can be seen that due to the threshold control, the power losses are adaptive to the load current variation, and no power losses are generated when IL_{pk} is below around 60 A. Under a switching frequency of 10 kHz, the maximum power loss of one inductor is about 7 W in the six-switch ZV/ZCT, and is around 13 W in the three-switch ZCT inverter. The results also indicate that the power losses are basically proportional to the switching frequency.

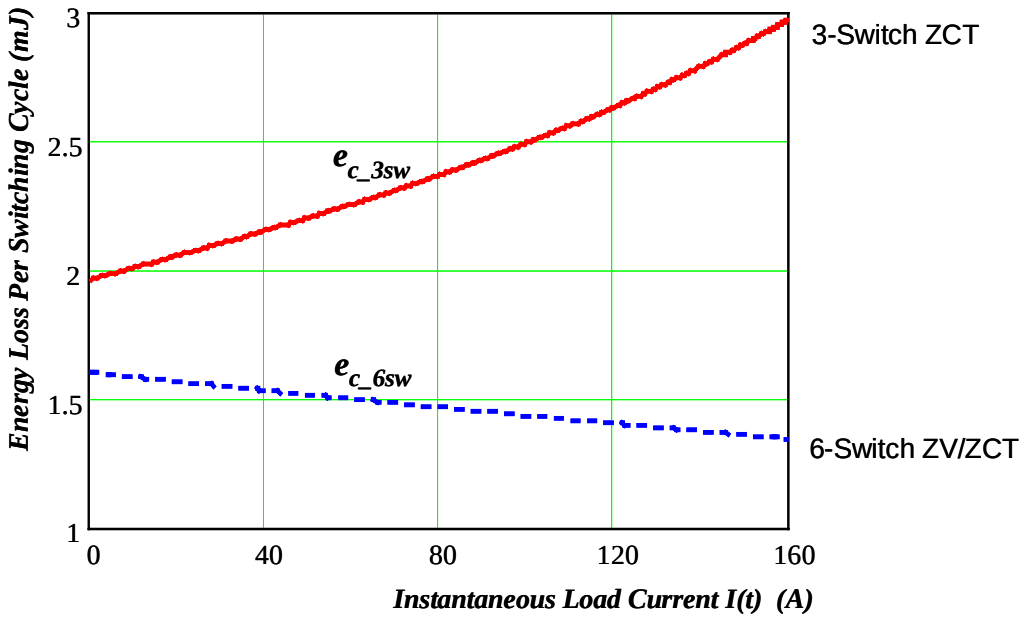

Figure 5.25. Resonant inductor *energy* losses per switching cycle as a function of variable instantaneous load current *I(t)*.

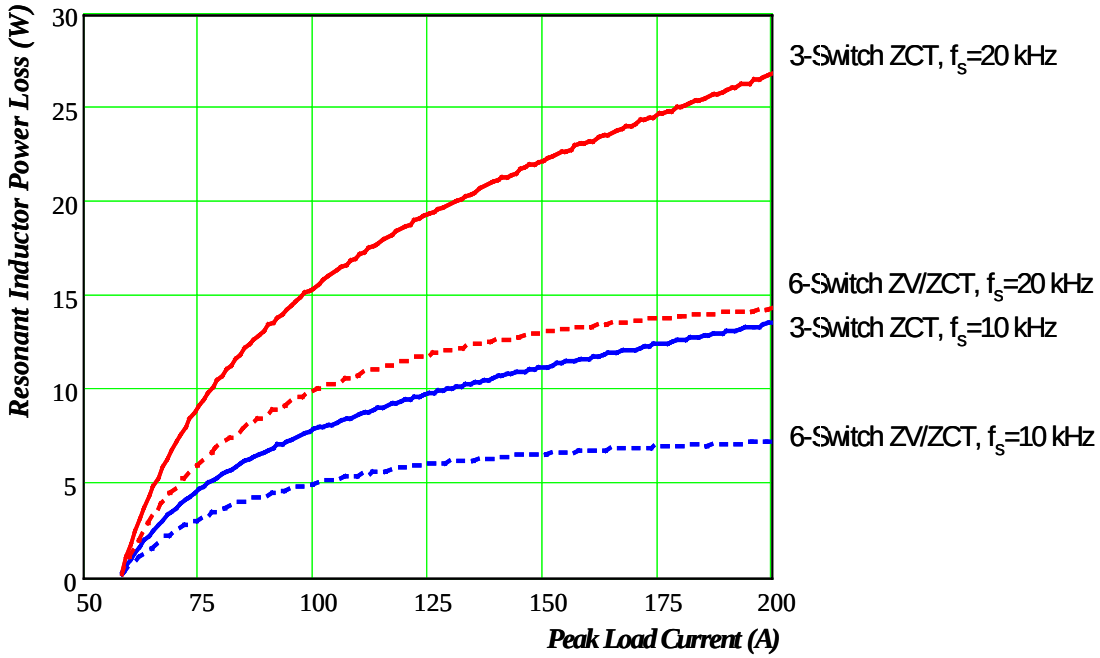

Figure 5.26. Resonant inductor *power* losses as a function of peak load current IL_{pk} under different switching frequencies (threshold control I_{th}=50 A).

Referring to the resonant inductor RMS current I_{x_rms} (derived in Section 5.3 and shown in Figure 5.21), the ratio of the inductor loss over the square of the RMS current can be calculated, i.e., $P/I_{x\_rms}^2$, which represents the power consumption characteristics of the inductors, and is the ESR of the inductors. The preceding analysis has shown that both the core losses and $I_{x\_rms}^2$ are proportional to the switching frequency, so the ESR is independent of the switching frequency. As shown by the curves in Figure 5.27, the ESR is around 4~6 mΩ in the six-switch ZV/ZCT, and around 12 mΩ in the three-switch ZCT. This information is important for the design of inductors, as well as for the loss analysis conducted for the entire ZCT inverters.

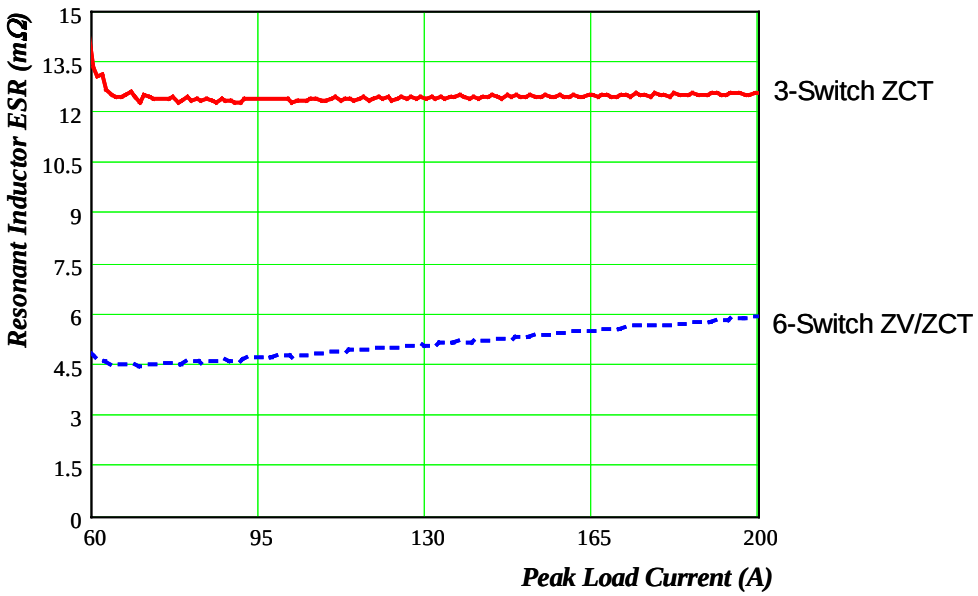

Figure 5.27. Estimated ESR of the resonant inductors.

The core temperature rise depends heavily on environmental factors such as ambient temperature, air flow, geometry, and the thermal conductivity of all the materials involved. It is difficult to precisely predict, but for the purpose of design, it can be approximated by an equation given by [E8], as the following:

$$\text{Rise (°C)} = \left[\frac{\text{Power Loss (mW)}}{\text{Surface Area (cm}^2\text{)}} \right]^{0.833} . \tag{5.43}$$

As shown in Figure 5.28, the predicted core temperature rises (ΔT) for the two ZCT inverters are quite close. Although the three-switch ZCT has more power loss in its resonant inductors, this loss is consumed by more cores. As a result, the core material thermal stresses for both inverters are almost the same. The maximum ΔT is below 40°C at 10-kHz switching frequency, and below 70°C at the 20-kHz switching frequency. The core temperatures are therefore far below 200°C, which is the limit of the MPP cores.

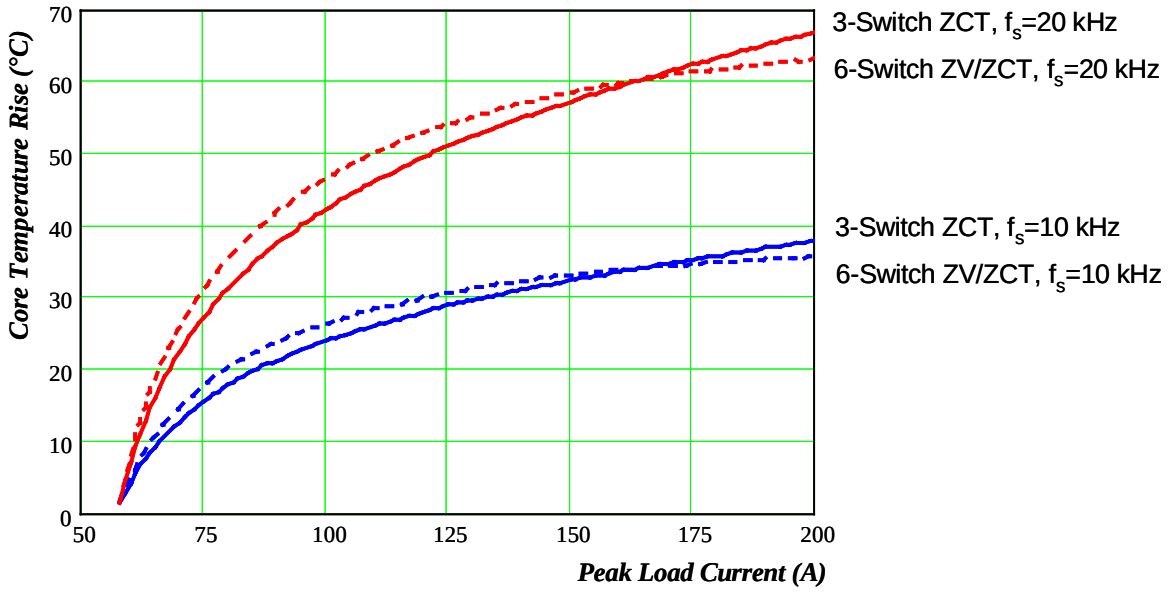

Figure 5.28. Predicted core temperature rise as a function of peak load current IL_{pk} under different switching frequencies (threshold control I_{th}=50 A).

5.4.3. Summary

In order to achieve low loss and small size, the MSE is used to calculate the core loss and to assist the design optimization of the resonant inductors, which are exposed to discontinuous nonsinusoidal flux excitations. With the stray inductance counted and one turn of conductor going through, the resonant inductor of the six-switch ZV/ZCT inverter is designed using four 55894-A2 cores in stack, and that of the three-switch ZCT inverter is designed using seven 55894-A2 cores in stack. Figure 5.29 shows a photo of the designed resonant tank of the six-switch ZV/ZCT inverter, the configuration of which is similar to that in the three-switch ZCT inverter. The inductor power losses, core temperature rises and ESR are estimated. Experimental results, which will be presented in Chapter 6, show that the predicted core temperatures are close to the measured ones. This verifies the inductor design.

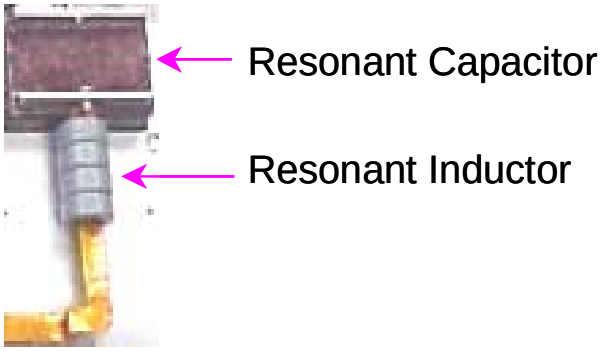

Figure 5.29. One photo of the designed resonant tank in the six-switch ZV/ZCT inverter.

5.5. Selection and Characterization of Auxiliary Devices

5.5.1. Current Ratings for Commercial Devices Do Not Match Requirements for the Auxiliary Switches

Since the auxiliary switches are activated for only a very short time (several microseconds) at the main switch turn-on and turn-off transitions, the average current requirement is very low. On the other hand, the auxiliary switches must conduct a narrow, high-peak resonant current. As a consequence, the auxiliary device selection is quite different from those of conventional applications, and is mainly determined by the peak current handling capability.

Power MOSFETs are not suitable for use as the auxiliary switches because of their high conduction losses, so the device selection focuses on 600-V IGBTs. As summarized in Table 5.6, the auxiliary switches must meet the following current requirements: low average (10~20 A), high peak (up to 400 A), sinewave of 3~6 μs pulse width (range of T_o), and repetitive frequency of 10~20 kHz (same as the switching frequency f_s in the six-switch ZV/ZCT and $2f_s$ in the three-switch ZCT). Current ratings specified in data sheets of commercial IGBT devices, however, cannot match these requirements. Some of them specify twice or four times the repetitive peak current handling capability over the DC current rating I_{DC}, but this is for a pulse width of 1 ms, or is just limited by the maximum junction temperature *Tj* [E14]-[E19]. The data sheets do not provide information for the value of peak current that can be repetitively handled within pulse widths down to 3~6 μs, either for the waveform of pulse current, or for the repetitive frequency. In addition, current ratings of commercial IGBTs are specified for hard-switching turn-off with clamped inductive loads, but the auxiliary switches in the ZCT inverters are turned off under zero current, with much lower device stress. Some IGBTs have a 10 times short circuit safe operation area (SCSOA) over I_{DC}. To protect the device from destruction when a shoot-through occurs, the IGBT current is cut off with a high value under hard switching, normally within less

than 10 μs. But the SCSOA is a non-repetitive capability, and generally an IGBT module can survive no more than 100 short-circuit events on a non-repetitive basis over its entire life. Thus, the SCSOA is not applicable for the peak current handling requirements of the auxiliary switches.

Therefore, it is necessary to develop a method to select suitable devices for the auxiliary switches, and more importantly to characterize devices under this non-conventional application.

Table 5.6.
Current Ratings for Commercial IGBTs
Do Not Match Requirements of Auxiliary Switches

		Required in the 55-kW ZCT Inverters	Specified in Data Sheets
Average Current		10~20 A	Rated by DC Current I_{DC}
Peak Current	Value	400A (20X Average)	2X or 4X I_{DC}
	Pulse Width	3~6 μs (Range of T_o)	1 ms or Limited by Max. T_j
	Waveform	Sine	Not Specified
	Repetitive Rate	10~20 kHz (Range of f_s)	Limited by Max. T_j
Operation Conditions		Zero-Current Turn-Off	Hard Switching with Clamped Inductive Load

5.5.2. Single-Shot Resonant Tests to Determine Peak Current Handling Capability

As a minority-carrier device, when the IGBT collector current I_C exceeds the maximum allowable peak current, the device will be de-saturated, and the on-state collector-emitter voltage V_{CE} tends to increase dramatically and uncontrollably, which will prevent I_C from increasing further. If this effect occurs in a resonant circuit, the conduction loss in the circuit will increase dramatically, the resonance will become highly nonlinear, and the resonant current will be

distorted. Based on this property, a series resonant converter (SRC) is designed to mimic the zero-current commutation and to test the devices. As shown by the simplified conceptual circuit diagram in Figure 5.30, initially, the DC capacitor is charged to a certain voltage. Then, the DUT is turned on. L_x and C_x start to resonate. After half of a resonant period, the device current I_C reverses and is carried by its anti-parallel diode. Thus, the device is turned off under zero current and its gate-drive signal V_{GE} is removed without causing much voltage overshoot or stress. The purpose of the test is to verify the device's peak current handling capability and is therefore a "single-shot" test. Devices can be safely tested up to a very high level of peak current without raising thermal management concerns.

The resonant time period set for the device tester is about 7 μs, which is close to the one designed for the inverters. This period is so short that the internal packaging inductance from the module terminals to the silicon die and the parasitic inductance in the voltage probes can cause significant voltage drops, which occurs because of the high *di/dt*. Because these voltage drops add to the measured device voltage waveform V_{CE}, it is impossible to tell if the IGBT is de-saturated by directly observing the V_{CE} waveform. Fortunately, the switch current waveform is a good indicator**.** As the DC voltage is gradually increased, the peak of the switch current will increase correspondingly. If the IGBT can handle the peak current, the current waveform should be close to sinusoidal. Otherwise, the current waveform will be distorted and the measured resonant time period will become abnormally longer.

Several types of IGBT modules have been chosen and tested. Figure 5.31 compares the results of two types of 150-A/600-V "six-pack" IGBT modules: the Eupec BSM150GD60 DLC and the Powerex CM150TF-12H. Both have the same current ratings, but the testing results show that they have quite different peak current handling capabilities. For the Eupec device shown in

Figure 31(a), even when the switch current peak is increased over 700 A, the current waveform is still close to sinusoidal, demonstrating a superior peak current handling capability. For the Powerex device shown in Figure 31(b), however, when the current peak is increased to 380 A, the measured current waveform becomes largely distorted, indicating that this device is not suitable for the high peak current requirement.

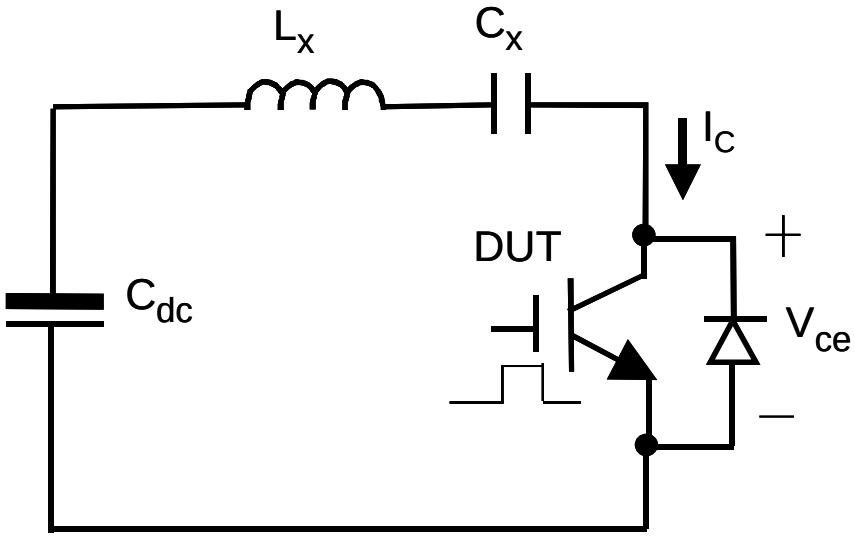

Figure 5.30. The simplified conceptual series resonant converter for testing the IGBT peak current handling capability.

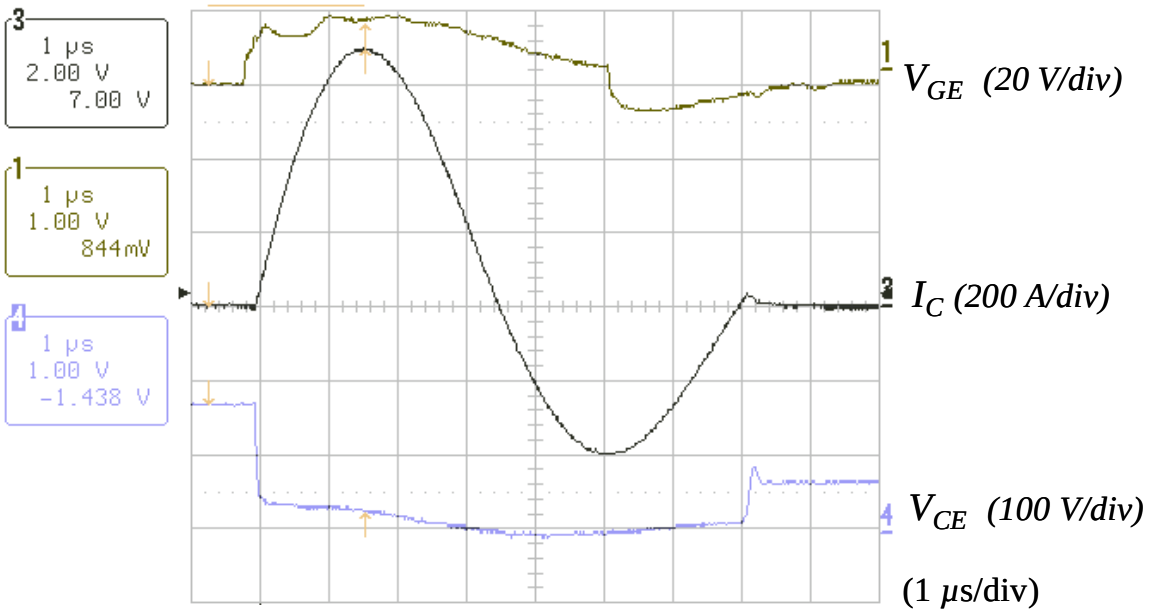

(a)

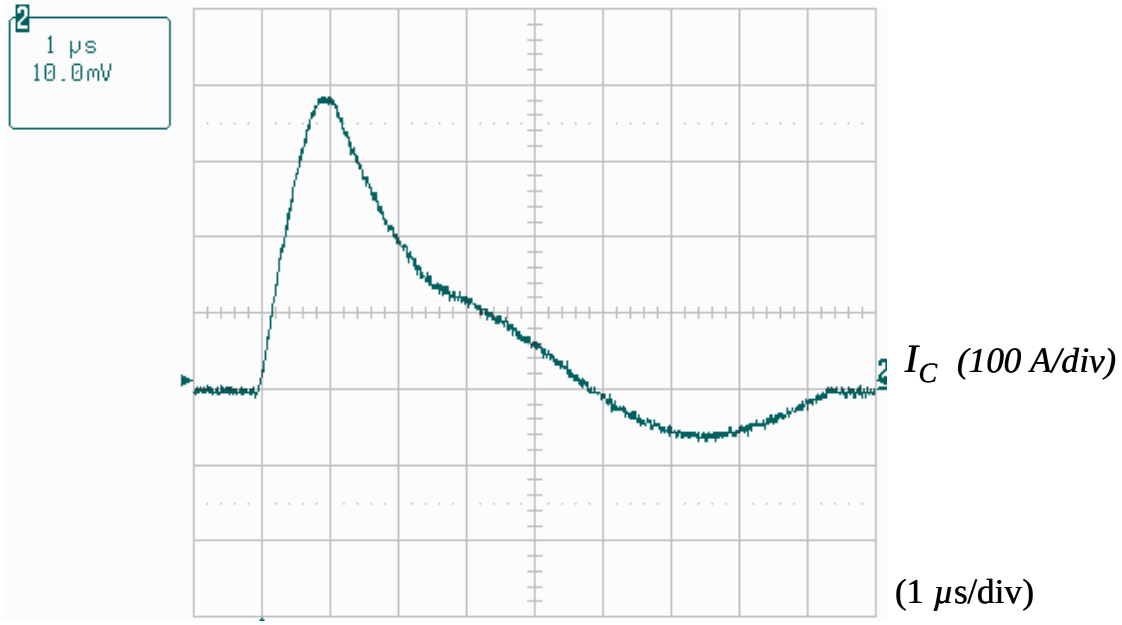

(b)

Figure 5.31. Switch current waveforms of two different 150-A/600-V IGBT modules produced during the single-shot resonant device testing:
(a) the Eupec BSM150GD60DLC; and
(b) the Powerex CM150TF-12H .

5.5.3. Estimating the IGBT Peak Current Handling Capability from Data Sheets

The single-shot test demonstrates that IGBT modules from different manufacturers can have quite different peak current handling capabilities even though they have the same DC current ratings. As shown in the equivalent circuit of Figure 5.32, one IGBT consists of a PNP driven by an N-channel MOSFET in a pseudo-Darlington configuration. From the standpoint of *device* design, the IGBT peak current handling capability is related to both the on-resistance of the MOSFET and the gain of the PNP. From the standpoint of *circuit* design, however, it is more meaningful to explore ways to estimate the peak current capability from device data sheets.

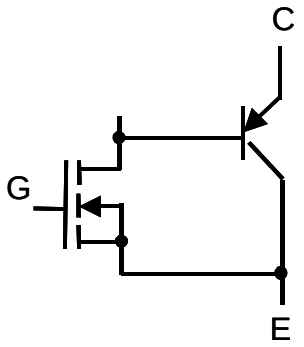

Figure 5.32. An equivalent circuit of the IGBT.

The output characteristic curves in data sheets define the value of V_{CE} that an IGBT will have when conducting a given I_C for a given value of gate voltage V_{GE}, but it is not convenient to directly use these curves to estimate the peak current handling capability. As can be seen in Figure 5.33, the values of I_C in these curves are limited to only twice the DC current ratings, which is far below the required peak current for the auxiliary switches. Also, a V_{GE} of 15 V will be used in the inverter design; this allows sufficient device current, while also leaving margin from the maximum gate voltage rating (+/- 20 V). However, the output characteristic curves under V_{GE}=15 V are limited only within the saturation region. It is impossible to tell at what current level the IGBT will be de-saturated. For some IGBTs, the curves that are for lower levels

of V_{GE}, such as 11~12 V, are still limited within the saturation region (Figure 5.33(b)). Since the value of V_{CE} is sensitive to the variation of I_C within the saturation region, it is inaccurate to compare the saturation voltage drops of different IGBTs by directly observing the output characteristic curves.

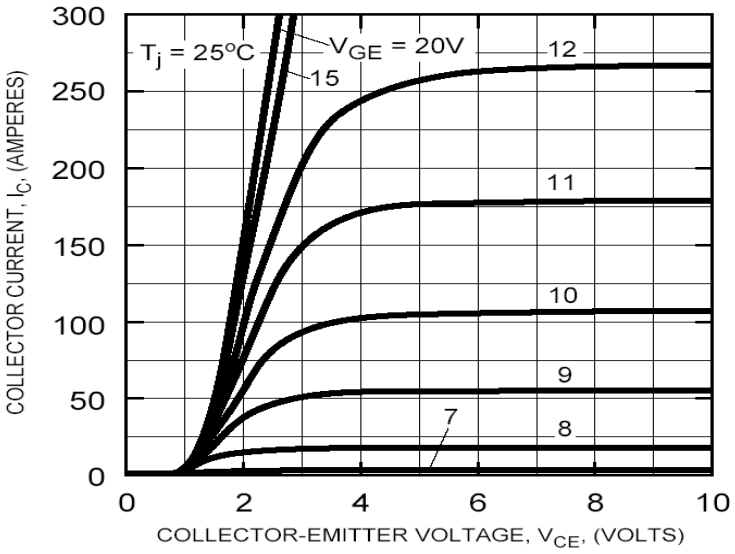

(a)

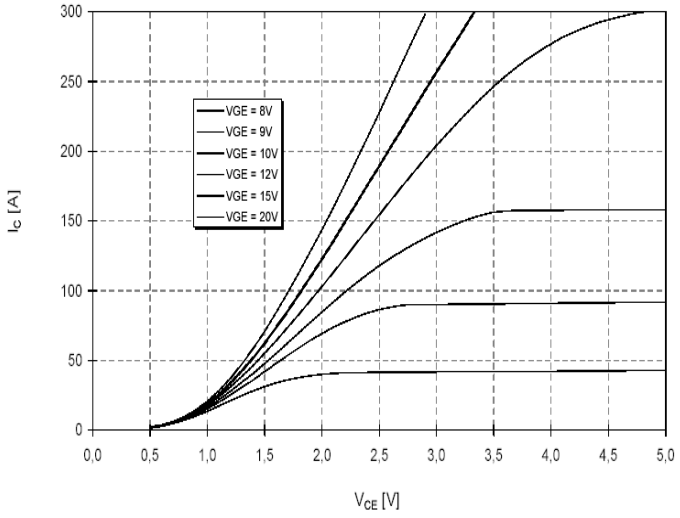

(b)

Figure 5.33. Output characteristic curves of two 150-A/600-V IGBT modules — it is inaccurate to use these curves to compare the peak current handling capabilities: (a) the Eupec BSM 150GD 60 DLC; and (b) the Powerex CM150TF-12H .

On the other hand, the transfer characteristic curves are useful for estimating the peak current-handling capability. Using the Eupec BSM150GD60DLC and the Powerex CM150TF-12H IGBT modules as examples, Figure 5.34 illustrates this estimation approach. The transfer characteristic curves define the value of I_C that can flow through an IGBT under a given V_{GE} in the linear region, within which the V_{CE} is much larger than the saturation voltage drops. The testing condition in the data sheets is V_{CE}=10 V for the Eupec device, and is V_{CE}=20 V for the Powerex device. For both conditions the devices are deeply de-saturated. As presented in the preceding section, the Eupec device can handle much higher peak current than the Powerex device, although they have the same DC current rating of 150 A. Correspondingly, a clear difference is observed between their transfer characteristic curves: Under V_{GE}=11 V, the I_C is about 230 A for the Eupec device, and is only 150 A for the Powerex device. Starting from the points of (I_C=230 A, V_{CE}=20 V) and (I_C=150 A, V_{CE}=10 V) for these two devices, respectively, according to conventional device technology, the output characteristic curves that span from the linear region down to the saturation region can be approximately drawn. By putting the resulting two curves together onto one graph, it is found that the Eupec device has a lower V_{CE} at the saturation region, i.e., a lower saturation voltage drop. Normally, the values of V_{GE} in the transfer characteristic curves given in the data sheets are lower than 15 V. This is probably because the device conduction loss in the linear region under V_{GE} =15 V would be too high. However, by shifting the obtained output characteristic curves under V_{GE}=11 V to higher levels, it becomes reasonable to estimate the output characteristic curves under V_{GE}=15 V, which again indicates that the Eupec device has a lower saturation voltage drop and thus higher peak current handling capability.

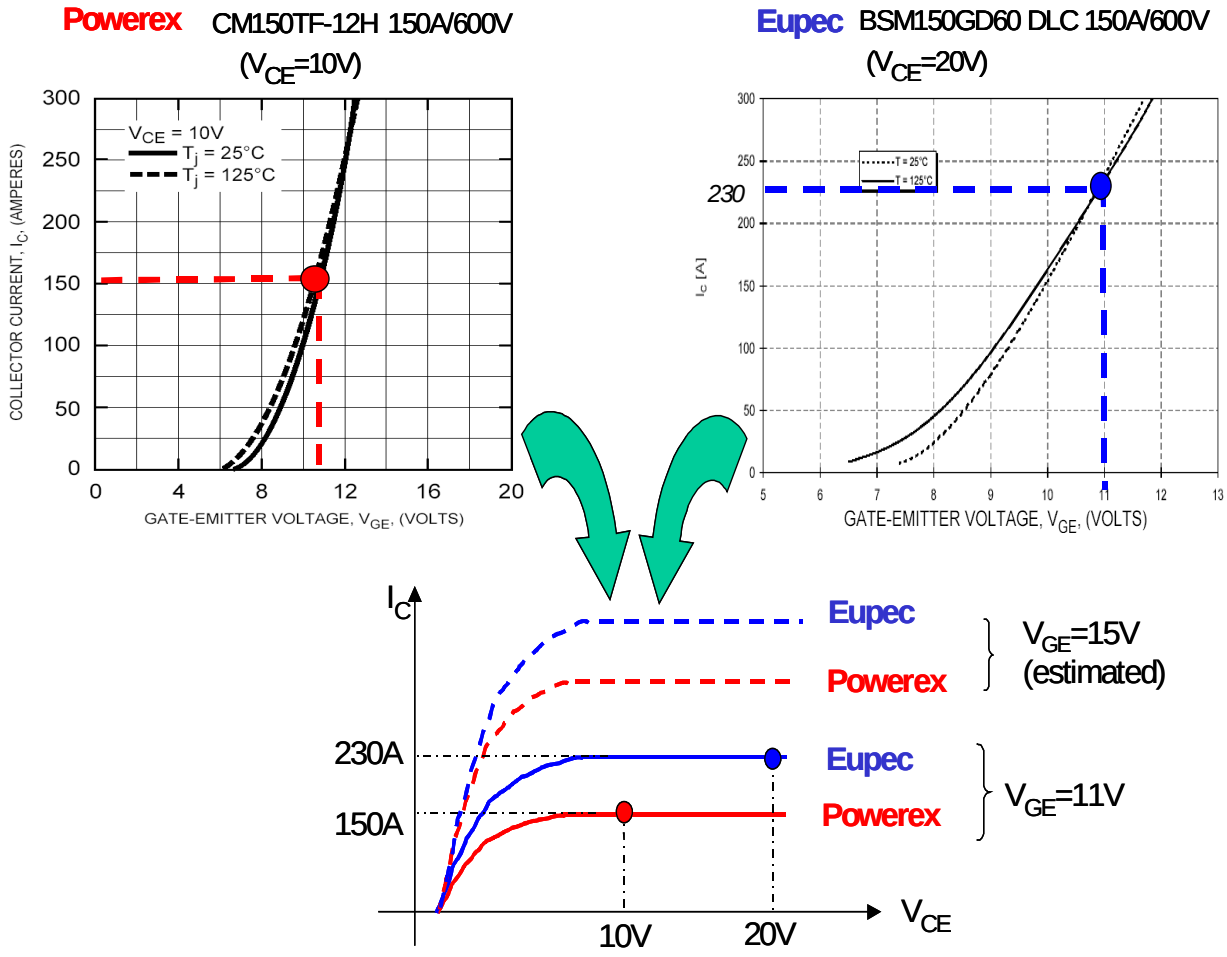

Figure 5.34. Using the transfer characteristic curves
to estimate the IGBT peak current handling capability.

The above discussion allows a parameter to be defined as follows: the DC transconductance G_{DC}, as the I_C to V_{GE} ratio in the IGBT linear region; i.e., $G_{DC} = \frac{I_C}{V_{GE}}$. It is found that G_{DC} equals 13 for the Powerex device, and 20 for the Eupec device. So the difference between the transfer characteristics, and quantitatively between the two values of G_{DC}, makes these two devices behave differently in terms of peak current handling capability. It should be mentioned that a so-called small-signal transconductance is conventionally defined as the ratio of the change in I_C to the change in V_{GE}. For conventional hard-switching operations, the

transconductance is often an ignored parameter. For the purpose of selecting the auxiliary devices in the ZCT inverters, the DC transconductance is defined to characterize the IGBT peak current handling capability.

A group of 600-V IGBTs have been tested using the proposed single-shot tester. As listed in Table 5.7, these devices are from different manufacturers, and have different current ratings and packaging. The test results indicate that from the standpoint of applications, the IGBT peak current handling capabilities suitable for the auxiliary switches largely depend on manufacturers. For example, the Powerex CM150TF-12H IGBT can handle only 2.3X peak current, while the IRG4PC50FD IGBT can handle up to 11X peak current. Moreover, the G_{DC} of the tested devices are estimated from their transfer characteristic curves using the method illustrated in Figure 5.34. It is found that most of the tested devices follow the same trend: The higher the G_{DC}, the higher the peak current handling capability. For instance, the peak current of the CM150TF-12H is tested to be the lowest (340 A), and its G_{DC} is also the lowest (13); the peak current of the IRG4ZC70UD is tested to be the highest (800 A), and its G_{DC} is also the highest (50). One exception is that the Eupec BSM150GD60DLC 150-A IGBT has a lower G_{DC} but a higher peak current I_{PEAK} than both the HGTG30N60B3D 60-A and the IRG4PC50FD 39-A IGBTs. Certainly it should be more accurate to compare the curves of those devices with similar current ratings and under similar V_{CE} test conditions. In general, the test results suggest that the transfer characteristics given in the data sheets can be used to estimate and compare the peak current handling capabilities of different IGBTs, which are not directly specified.

Table 5.7.
Single-Shot Resonant Test Results of a Group of IGBTs and Their Estimated G_{DC}

Tested IGBTs	DC Rating I_{DC}	Peak Specified I_{CM}	**Peak Tested** I_{PEAK}	I_{PEAK} / I_{CM}	G_{DC} Estimated from data sheets @V_{GE}=11V
Powerex CM150TF-12H 6-Pack	150 A	300 A	340 A	2.3	13, under V_{CE}=10V
Eupec BSM150GD60DLC 6-Pack	150 A	300 A	700 A	4.6	20, under V_{CE}=20V
Harris HGTG30N60B3D Discrete	60 A	220 A	360 A	6	22, under V_{CE}=10V
IR IRG4PC50FD Discrete	39 A	280 A	450 A	11	25, under V_{CE}=50V
IR IRG4ZC70UD Discrete	100 A	400 A	800 A	8	50, under V_{CE}=50V

5.5.4. Continuous Resonant Tests to Verify Long-Term Electrical and Thermal Capabilities

From the single-shot tests, three IGBTs (BSM150GD60DLC, IRG4ZC70UD and IRG4PC50FD) are found to be capable of handling peak current higher than 400 A, which is the required peak current of the auxiliary switches in the 55-kW ZCT inverters. In particular, the IRG4PC50FD 39-A IGBT can handle peak current of up to 450 A. It would be highly desirable if this 39-A IGBT could be used as the auxiliary switches. Since the device will operate in a non-conventional way that is not specified or intended by the manufacturers, a continuous resonant test is necessary to verify whether it can stand the long-term electrical and thermal stresses.

The basic concept of the continuous resonant tester follows that of the series resonant converter shown in Figure 5.30. In the tester, L_x=650 nH and C_x=1 μF, which creates To=5 μs. However, in order to continuously generate a 400-A peak current with a 200-kHz resonant

frequency under a repetitive frequency of 10~20 kHz, there are some practical issues. One issue is how to use a conventional low-current, slow-response DC power supply to facilitate the test. The solution is shown as the practical testing circuit in Figure 5.35: The resonant current is provided by the discharge of a film capacitor C_{dc} when the DUT is turned on, and when the DUT is off, the C_{dc} is charged by the DC power supply through D_1, T_1 and R_1. The other issue is that the resonant capacitor C_x voltage must be reset to zero after every resonant event, or else this voltage will be accumulated and the desirable peak values of the resonant current cannot be reached. This is solved by the addition of D_2, T_2 and R_2 that discharge C_x after the DUT is turned off. In addition, D_c is used to clamp the device voltage spikes that may occur due to parasitic effects. A photo of the device tester is shown in Figure 5.36. The devices and components are mounted on a heatsink, a laminated bus bar is used to connect the DC power supply to the C_{dc}, and two fans are used for cooling.

The IRG4PC50FD IGBT has been tested using the tester shown in Figure 5.36. As the experimental waveforms shown in Figure 5.37, indeed this 39-A IGBT can operate up to 400-A peak current with a 200-kHz resonant frequency under a repetitive frequency F_{repeat} of 10 kHz ! After continuously operating for half an hour, no abnormality was found in the device, and the device case temperature T_{case} was measured as 72°C, from which the junction temperature T_j can be estimated. The equivalent switching duty cycle D=10 kHz/200 kHz=0.05; at this condition, the transient thermal impedance Z_{th} given in the data sheet is about 0.05 °C/W. With the sine current waveform being approximated by a rectangular waveforms with a peak I_{pk} of 400 A, and the device on-state voltage drop V_{ce_on} is assumed to be 2.5 V, the T_j is estimated as

$$T_j = V_{ce\_on} \cdot I_{pk} \cdot Z_{th} + T_{case} = 122^\circ C, \tag{5.44}$$

which is below 150°C, the maximum allowable device junction temperature.

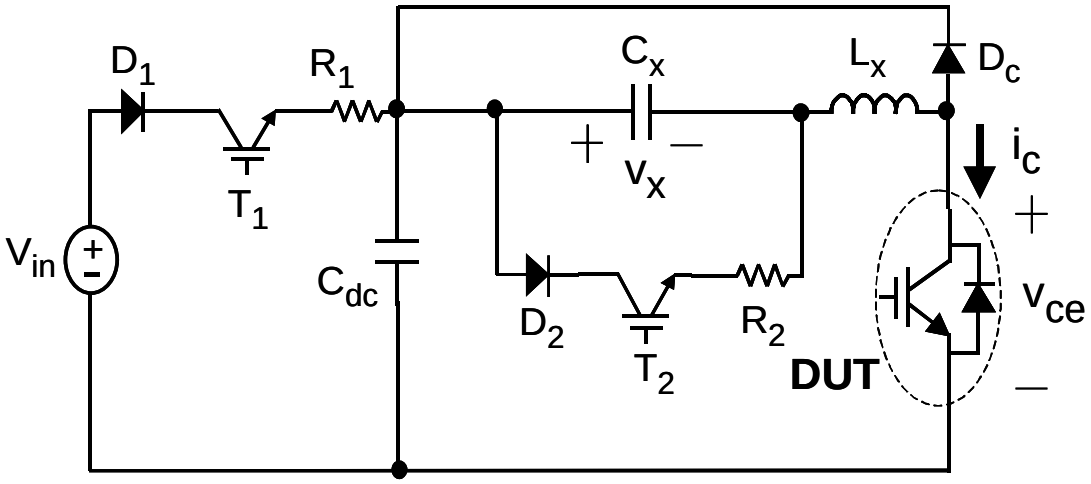

(a)

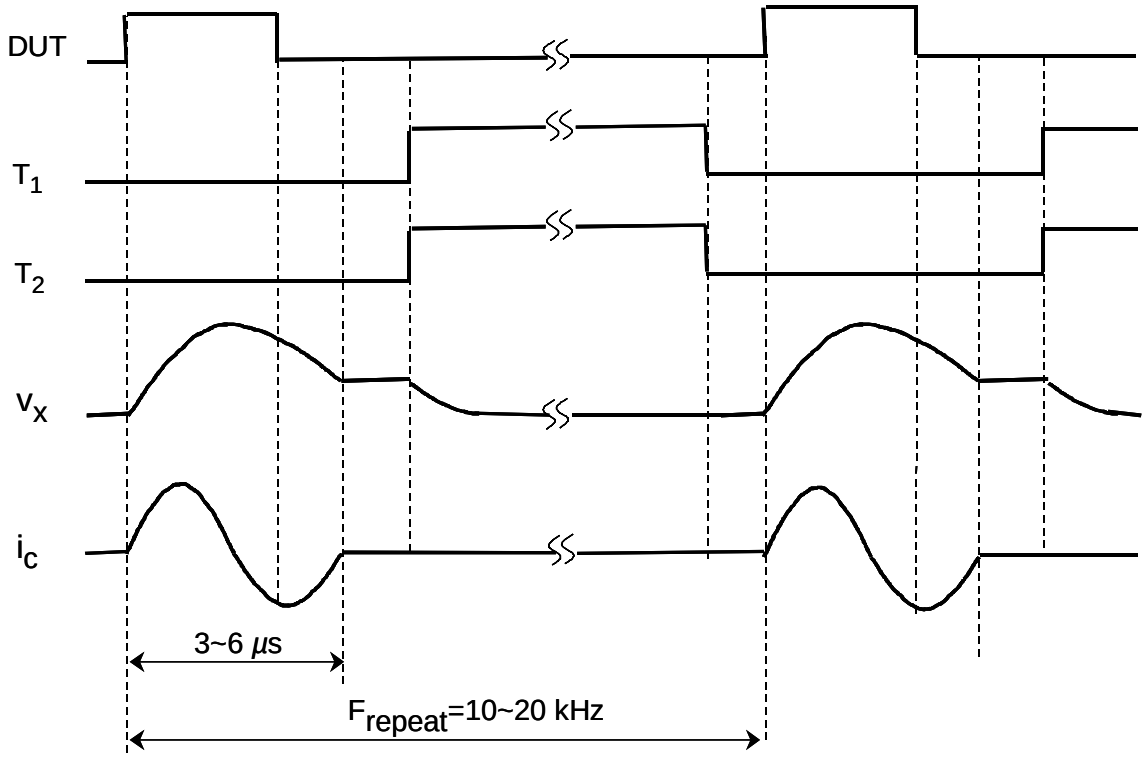

(b)

Figure 5.35. The continuous resonant device tester:
(a) practical circuit diagram; and (b) operational waveforms

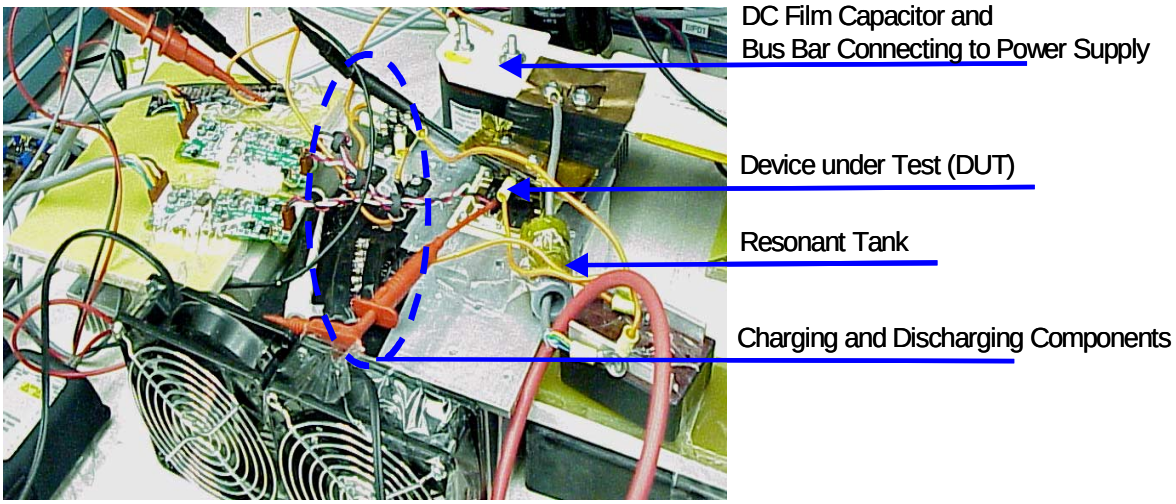

Figure 5.36. A photo of the continuous resonant device tester.

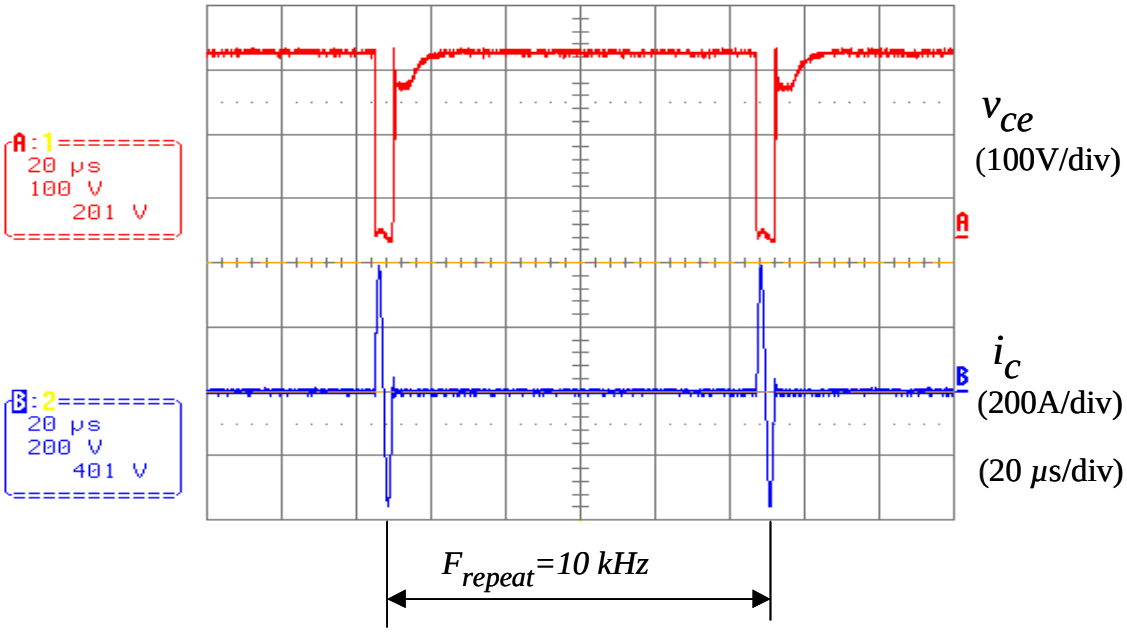

Figure 5.37. Testing waveforms of the IRG4PC50FD 39-A IGBT operating with a 400-A peak current and a 200-kHz resonant frequency under a repetitive frequency of 10 kHz.

In addition to the tests under F_{repeat}=10 kHz, this 39-A IGBT is also tested under an F_{repeat} of 15 kHz and 20 kHz, with the same 200-kHz resonant frequency. Figure 5.38 shows the measured device case temperature T_{case} under different peak resonant current I_{pk}, where the device

continuously operated for half an hour at each testing point. Since the device conduction loss is basically proportional to the repetitive frequency F_{repeat}, the T_{case} becomes higher with higher F_{repeat}. The test was stopped at I_{pk}=325 A for F_{repeat}=15 kHz, and at I_{pk}=280 A for F_{repeat}=20 kHz.

For the purpose of comparison, the IRG4ZC70UD 100-A IGBT was also tested using the continuous resonant device tester. Under an F_{repeat} of 20 kHz, this 100-A IGBT device can operate to 400-A peak current with 200-kHz resonant frequency, while the IRG4PC50FD 39-A IGBT can operate only to 280-A peak current. As can be seen from the comparison curves shown in Figure 5.39, the 100-A IGBT reduces the case temperature rise by almost half from the 39-A IGBT, which indicates a reduction of conduction loss and better thermal handling capability.

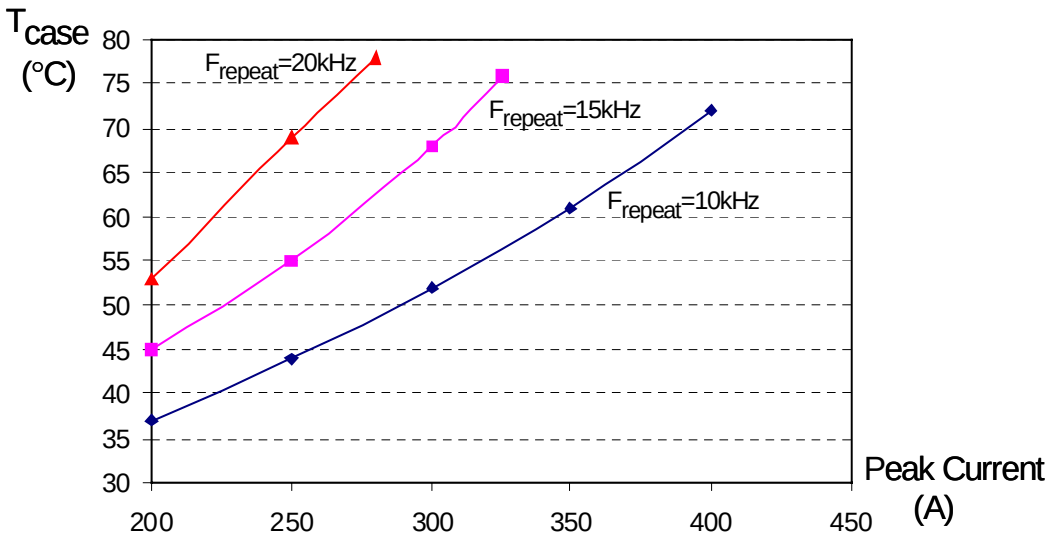

Figure 5.38. Case temperatures of the IRG4PC50FD 39-A IGBT measured at the continuous resonant test under different peak current and repetitive frequency F_{repeat}.
(conditions: each point operated for half an hour, $T_{ambient}$=23°C, and forced air cooling.)

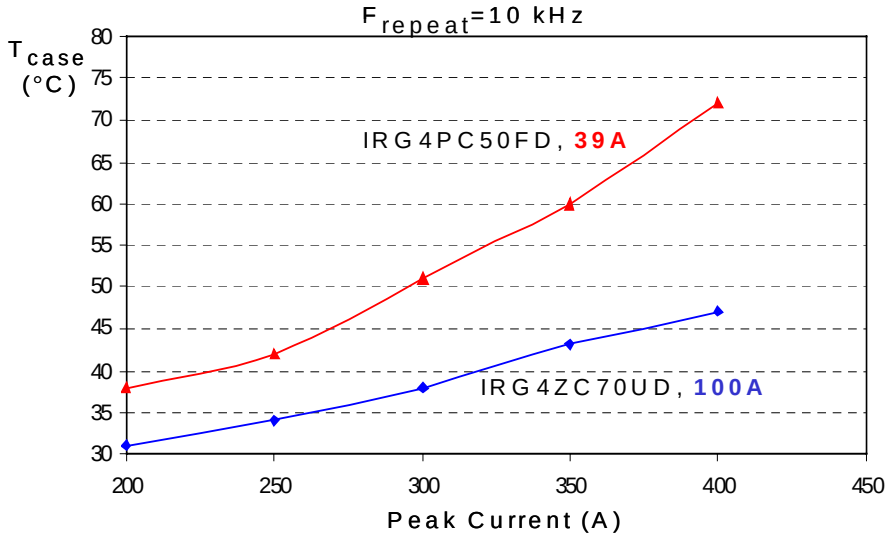

(a)

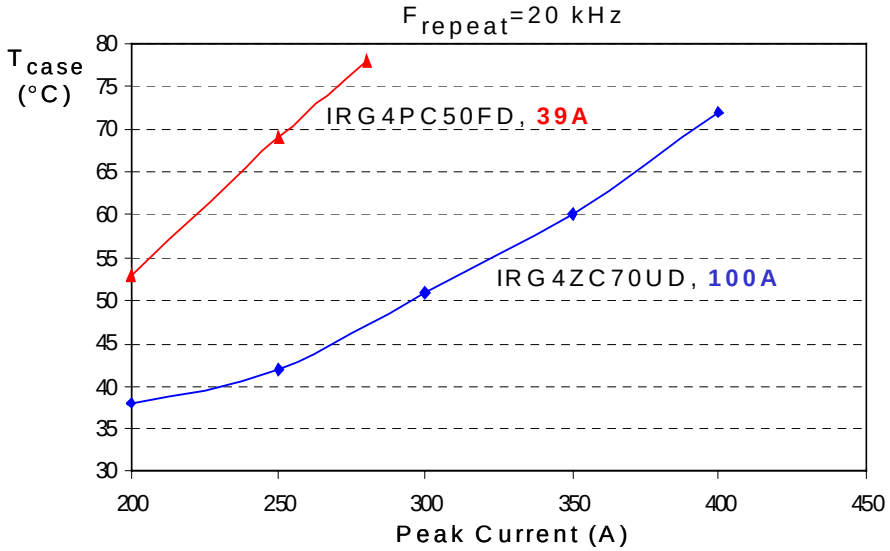

(b)

Figure 5.39. Comparison of the case temperatures between the IRG4PC50FD 39-A IGBT and the IRG4ZC70UD 100-A IGBT measured at the continuous resonant test: (a) F_{repeat}=10 kHz; and (b) F_{repeat}=20 kHz (same conditions as those given for Figure 5.38).

From these continuous resonant tests, it is suggested that the IRG4PC50FD 39-A IGBT is capable of becoming the auxiliary switch in the 55-kW ZCT inverters, especially in the six-switch ZV/ZCT inverter, in which one auxiliary switch is activated only once at each main

switch transition. This suggestion is more reasonable considering the fact that the six-step SVM will be used for the inverter control and the auxiliary switches are normally disabled under lighter load conditions due to the threshold control. However, the tests also suggest that the IRG4PC50FD 39-A IGBT can cause too much conduction loss and has poor thermal handling capability, so the IRG4ZC70UD 100-A IGBT is a better choice.

5.5.5. Conclusion of the Auxiliary Device Selection

The selection of the auxiliary switches is mainly determined by the peak current handling capability, and is quite different from conventional applications. A method has been developed to select suitable auxiliary devices. For the 55-kW six-switch ZV/ZCT inverter, one piece of the Eupec BSM150GD60DLC six-pack 150-A/600-V IGBT module is finally selected. Within this module, six IGBT switches and their anti-parallel diodes are integrated into one package, which simplifies the inverter layout. This 150-A module may not be the optimal choice; however, no other types of six-pack IGBT modules were found during the project that could meet the auxiliary switch requirements. A compact laminated bus bar is designed using a two-layer six-ounce Cu printed circuit board (PCB) to connect this six-pack module to the DC source, resonant tanks, and gate drivers. For the 55-kW three-switch ZCT inverter, three pieces of IRG4ZC70UD 100-A/600-V IGBT, which is a surface-mounted discrete device with anti-parallel diode, are selected as the auxiliary switches, and the IR60EPF06 60A/600V fast-recovery diode is selected as the clamping diode D_c. These devices are directly surface-mounted on a two-inch by two-inch isolated–metal-substract (IMS)/aluminum board. Figure 5.40 shows photos of both auxiliary switch packages.

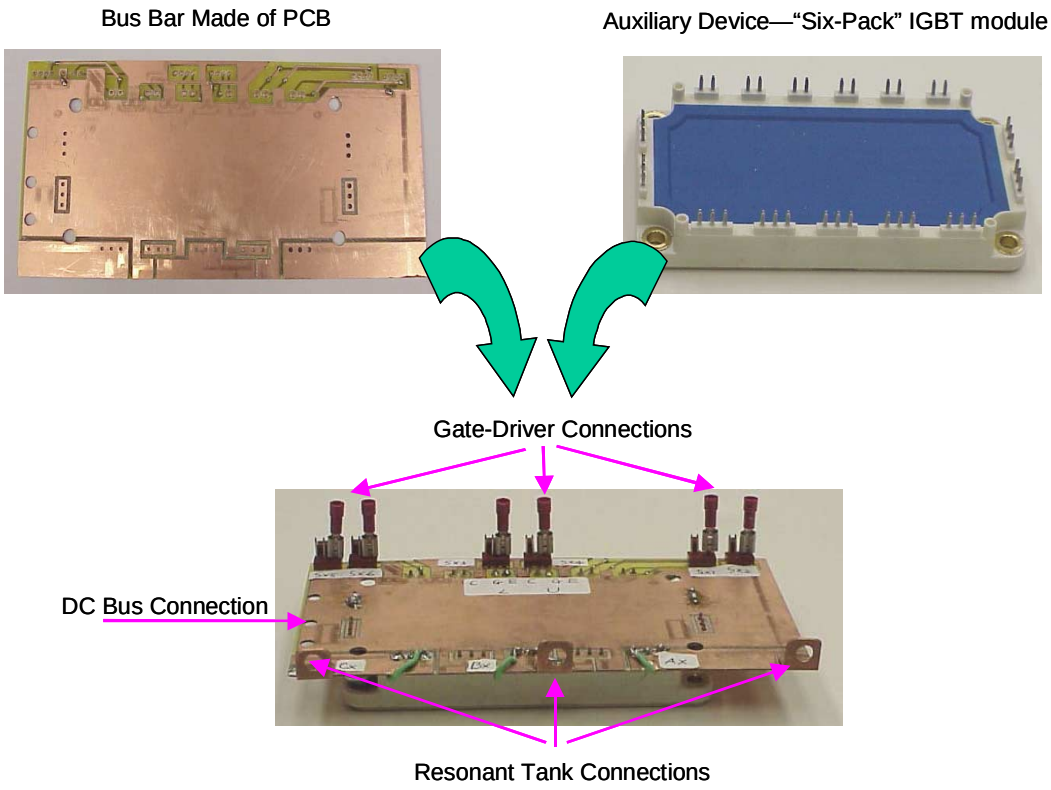

(a)

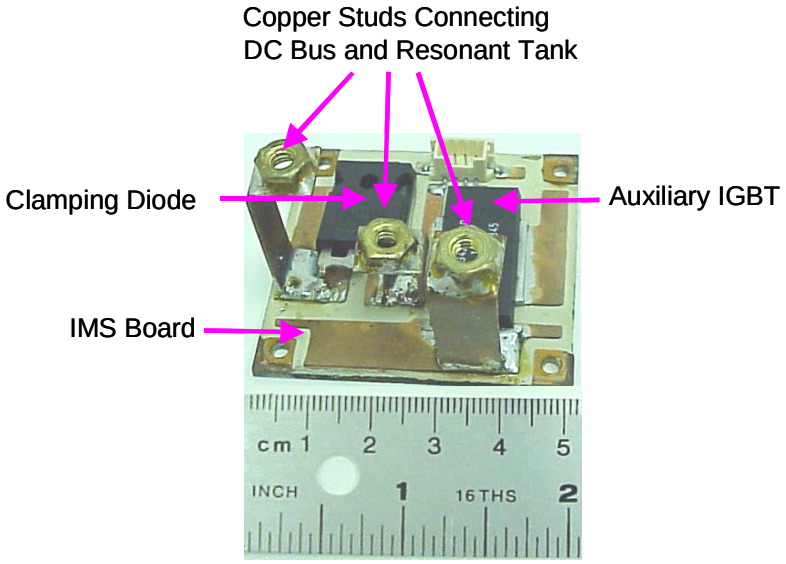

(b)

Figure 5.40. Photos of the selected auxiliary switches and their packaging:
(a) for the six-switch ZV/ZCT inverter; and
(b) for the three-switch ZCT inverter.

More importantly, a method has been developed to characterize IGBTs under the non-conventional conditions in auxiliary circuits: low average (10~20 A), high peak (400 A), sinewave of 3~6 μs pulse width, repetitive frequency of 10~20 kHz, and zero-current turn-off. These conditions are not specified or intended in commercial IGBT data sheets; therefore, it is proposed that both a single-shot resonant tester and a continuous resonant tester be used for device characterization. The device tests demonstrate that a sample 39-A IGBT can continuously operate to 400-A peak current with 200-kHz resonant frequency under a repetitive frequency of 10 kHz, and that the IGBT peak current handling capability suitable for the auxiliary switches is largely dependent on manufacturers. A method, which estimates this current capability from data sheets, is recommended; it utilizes the transfer characteristic curves as a comparison index. A new parameter, namely the DC transconductance G_{DC}, is defined to quantify the difference in the peak current handling capabilities. It is suggested that IGBTs with higher G_{DC} tend to have higher peak current handling capability.

5.6. Loss Modeling and Analysis of the ZCT Inverters

As illustrated in Figure 5.41, the total ZCT inverter power losses consist of the device switching losses, conduction losses, and passive component losses. The effect of soft switching on inverter loss reduction is basically a trade-off between the switching losses saved by soft switching and the additional conduction losses in the main and auxiliary circuits caused by soft switching. This effect is ultimately dependent on the device and component characteristics, and is affected by the operational conditions and control schemes. The complex trade-offs involved often make the process counterintuitive at first glance. Intuitively, the threshold control discussed in the preceding sections should be helpful in achieving a proper trade-off; however, further rigorous investigation of this method is needed. In addition, it is important to investigate the differences in loss mechanisms and distributions between the six-switch ZV/ZCT and the three-switch ZCT inverters. In an effort to provide a design methodology, an analytical ZCT inverter loss model is developed. Then, the developed model is used to numerically analyze the losses in the two 55-kW ZCT inverters and to investigate the effect of threshold control on the optimization of the inverter losses.

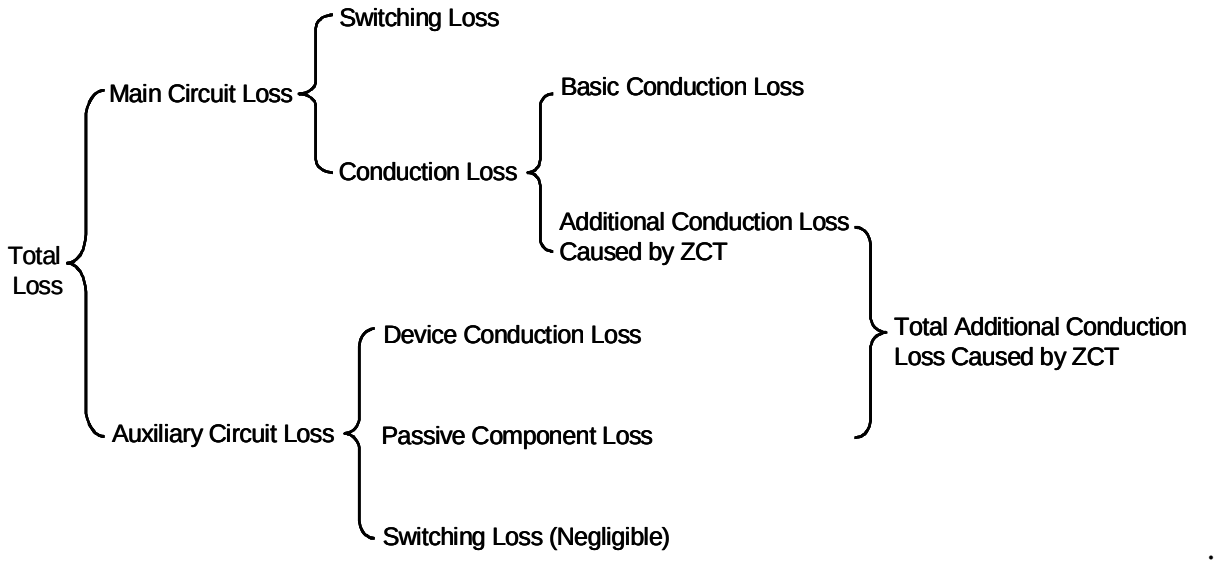

Figure 5.41. Major loss components of the ZCT inverters.

5.6.1. Device Loss Models

5.6.1.1. Switching Loss Models

The switching characterization presented in Section 5.1 suggests that the IGBT switching energy loss increases approximately linearly along with the switched current. A simplified straight-fitting curve is made to obtain the switching loss model. Given a fixed DC bus voltage, the switching energy losses under hard-switching conditions are given by

$$E_{on} = K_{on} I \text{, and} \tag{5.45}$$

$$E_{off} = K_{off} I \text{.} \tag{5.46}$$

The switching characterization also shows that both ZCT inverters can almost eliminate the turn-off loss, and that this small amount of ZCT turn-off loss is nearly constant under a variable switching current. In the meantime, both ZCT inverters reduce the switching turn-on losses from hard switching, and the six-switch ZV/ZCT has substantially smaller turn-on loss than the three-switch ZCT. Correspondingly, the turn-off energy losses in both ZCT inverters are approximated

as a constant, represented by E_{off_ZCT}. The turn-on energy losses in the six-switch ZV/ZCT and the three-switch ZCT inverters are approximated by

$$E_{on\_6Sw} = K_{6Sw}K_{on}I \text{, and} \tag{5.47}$$

$$E_{on\_3Sw} = K_{3Sw}K_{on}I \text{ .} \tag{5.48}$$

5.6.1.2. Conduction Loss Models

A simplified conduction loss model is employed for the IGBTs and diodes [F8] [F9]. This model assumes that the voltage drop across the device can be represented as a constant voltage source in series with a constant resistor during conduction. The models for the IGBTs and diodes are expressed in (5.49) and (5.50), respectively:

$$V_{ce} = V_t + R_{ce}I \text{, and} \tag{5.49}$$

$$V_{ak} = V_f + R_{ak}I \text{ .} \tag{5.50}$$

where V_{ce} and V_{ak} represent the on-state voltage drops of IGBT and diode, V_t and V_f are IGBT and diode voltage drops at zero current condition, R_{ce} and R_{ak} are the resistive elements, and I is the device current. Parameters V_{ce}, V_{ak}, R_{ce}, and R_{ak} can be estimated from the data sheets.

5.6.2. ZCT Inverter Loss Models

5.6.2.1. Main Circuit Switching Losses

Since Equations (5.45) and (5.46) suggest that the switching energy loss is proportional to the switched current, averaging the switched phase current within the fundamental line cycle will obtain the switching power loss for one phase. Considering that the six-step SVM will be used for inverter control, and assuming the load power factor angle be less than 30 degrees, the average phase current when the switching actions are actually occurring is found to be

$$I_{avg} = \frac{4}{T}\int_{0}^{T/6} IL_{pk}\sin(\frac{2\pi}{T}t)dt = IL_{pk}/\pi . \quad (5.51)$$

Under the hard-switching condition, the turn-on and turn-off power losses in one phase are

$$P_{on\_ph} = E_{on} f_s = K_{on} I_{avg} f_s , \text{ and} \quad (5.52)$$

$$P_{off\_ph} = E_{off} f_s = K_{off} I_{avg} f_s , \quad (5.53)$$

where f_s is the switching frequency.

For the six-switch ZV/ZCT and three-switch ZCT inverters, without threshold control, the turn-on and turn-off power losses in one phase are

$$P_{on\_ph\_6sw} = K_{6sw} K_{on} I_{avg} f_s , \quad (5.54)$$

$$P_{on\_ph\_3sw} = K_{3sw} K_{on} I_{avg} f_s , \text{ and} \quad (5.55)$$

$$P_{off\_ph\_6sw} = P_{off\_ph\_3sw} = \frac{2}{3} E_{off} f_s . \quad (5.56)$$

Under threshold control, which disables the auxiliary circuits when the instantaneous switch current is below a threshold value I_{th} (see Figure 5.20), the average current within the interval when the auxiliary circuits are disabled is

$$I_{avg\_hs} = \frac{4}{T}\int_{0}^{T_{th}} IL_{pk}\sin(\frac{2\pi}{T}t)dt , \quad (5.57)$$

and the average current within the interval when the auxiliary circuits are enabled is

$$I_{avg\_ZCT} = \frac{4}{T}\int_{T_{th}}^{T/6} IL_{pk}\sin(\frac{2\pi}{T}t)dt , \quad (5.58)$$

where T_{th} is a time instant related to the I_{th}, given by Equation (5.24). Therefore, the turn-on and turn-off power losses with threshold control in one phase become

$$P_{on\_ph\_6sw\_TH} = K_{on} I_{avg\_hs} f_s + K_{6sw} K_{on} I_{avg\_ZCT} f_s , \quad (5.59)$$

$$P_{on\_ph\_3sw\_TH} = K_{on} I_{avg\_hs} f_s + K_{3sw} K_{on} I_{avg\_ZCT} f_s, \text{ and} \tag{5.60}$$

$$\begin{aligned} P_{off\_ph\_6sw\_TH} &= P_{off\_ph\_3sw\_TH} \\ &= K_{off} I_{avg\_hs} f_s + \frac{4}{T} E_{off\_ZCT} (N_s - N_{th}) \end{aligned}, \tag{5.61}$$

where N_S is the number of switching cycles within a 60° sector, given by Equation (5.41), and N_{th} is a number corresponding to the I_{th}, given by Equation (5.42). Therefore, total switching losses in the ZCT inverters are

$$P_{s\_main\_6sw} = 3(P_{on\_ph\_6sw\_TH} + P_{off\_ph\_6sw\_TH}), \text{ and} \tag{5.62}$$

$$P_{s\_main\_3sw} = 3(P_{on\_ph\_3sw\_TH} + P_{off\_ph\_3sw\_TH}). \tag{5.63}$$

5.6.2.2. Basic Conduction Loss in the Main Circuits

The basic conduction loss in the main circuits is equal to that in a hard-switching inverter. The difference in conduction losses between SVM and SPWM controls is only marginal under the same fundamental output voltage [F10]. Therefore, the expressions that are valid for SPWM can be used to evaluate the basic conduction loss. Following the discussions in [F8] [F9], the conduction losses of one IGBT and its anti-parallel diode are calculated respectively by

$$P_{cs\_main} = \frac{1}{2} IL_{pk} V_t \left(\frac{1}{\pi} + \frac{M}{2\sqrt{3}} \cos\varphi\right) + IL^2{}_{pk} R_{ce} \left(\frac{1}{8} + \frac{2M}{3\sqrt{3}\pi} \cos\varphi\right), \text{ and} \tag{5.64}$$

$$P_{cd\_main} = \frac{1}{2} IL_{pk} V_f \left(\frac{1}{\pi} - \frac{M}{2\sqrt{3}} \cos\varphi\right) + IL^2{}_{pk} R_{ak} \left(\frac{1}{8} - \frac{2M}{3\sqrt{3}\pi} \cos\varphi\right), \tag{5.65}$$

where M is the modulation index of SVM and cosφ is the power factor. The total basic conduction loss is

$$P_{c\_main\_basic} = 6(P_{cs\_main} + P_{cd\_main}). \tag{5.66}$$

5.6.2.3. Additional Main Circuit Conduction Losses Caused by ZCT Commutations

The current in either the main switch or the main diode is the difference between the instantaneous load current and the resonant current, i.e., $I(t)$-i_x. Since i_x resonates between negative and positive, its net effect on the main circuit conduction loss can be considered nullified for the portion $|i_x| \le I(t)$. So, the additional main circuit conduction loss caused by soft switching is determined only by the portion of i_x for which i_x is higher in magnitude than $I(t)$, as shown in the shaded areas in Figures 5.17 and 5.18.

The six-switch ZV/ZCT inverter is discussed first. At the turn-on transition, i_x is superimposed on the current through the outgoing main diode; at the turn-off, when i_x is greater than $I(t)$, the surplus current flows through the anti-parallel diode across the outgoing main switch. So additional conduction losses occur only in the main diodes. The time intervals of both shaded areas at turn-on and turn-off in Figure 5.18 are approximately equal, as calculated by

$$T_{sh} = 2\cos^{-1}\left(\frac{I(t)}{I_{x\_pk\_6sw}(t)}\right)\cdot\frac{T_o}{2\pi}. \tag{5.67}$$

The additional conduction energy loss at the turn-on is calculated by

$$E_{add\_on\_6sw}(t) = 2\cdot\int_{\frac{T_o}{4}-\frac{T_{sh}}{2}}^{\frac{T_o}{4}} \left(V_{ak\_6sw\_on}\left(I_{x\_pk\_6sw}(t)\sin\left(\frac{2\pi}{T_o}\gamma\right)+I(t)\right)\right. \\ \left.-(V_f + R_{ak}I(t))\cdot I(t)\right)\cdot d\gamma, \tag{5.68}$$

where

$$V_{ak\_6sw\_on} = V_f + R_{ak}\left(I_{x\_pk\_6sw}(t)\sin\left(\frac{2\pi}{T_o}\gamma\right)+I(t)\right). \tag{5.69}$$

The additional conduction energy loss at the turn-off is

$$E_{add\_off\_6sw}(t) = 2 \cdot \int_{\frac{T_o}{4}-\frac{T_{sh}}{2}}^{\frac{T_o}{4}} (V_{ak\_6sw\_off}(I_{x\_pk\_6sw}(t)\sin(\frac{2\pi}{T_o}\gamma) - I(t))d\gamma, \quad (5.70)$$

where

$$V_{ak\_6sw\_off} = V_f + R_{ak}(I_{x\_pk}(t)\sin(\frac{2\pi}{T_o}\gamma) - I(t)). \quad (5.71)$$

Under threshold control, the main circuit additional conduction power loss in the three phases is calculated by

$$p_{add\_6sw} = 12(\sum_{n=N_{th}}^{N_S}(E_{add\_on\_6sw}(\frac{n}{f_s}) + E_{add\_off\_6sw}(\frac{n}{f_s}))/T. \quad (5.72)$$

Unlike the six-switch ZV/ZCT, the additional conduction losses in the main circuit of the three-switch ZCT inverter occur in both the main switches and the main diodes. These losses can be calculated using a similar method, and the expressions are listed in Appendix C.

5.6.2.4. Auxiliary Circuit Switching Losses

The turn-on of an auxiliary switch is not accompanied by the turn-off of an opposite diode, and the current rising rate is limited by the resonant inductor. Meanwhile, the auxiliary switches are turned off under zero current. Therefore, the auxiliary circuit switching losses are negligible.

5.6.2.5. Auxiliary Circuit Conduction Losses

The expressions of the average and RMS auxiliary currents for both ZCT inverters are derived in Section 5.3.1. The conduction power losses in the auxiliary devices (including switches and diodes) are obtained respectively as

$$\begin{aligned} P_{c\_aux\_6sw} &= 3(V_t I_{avg\_s\_6sw} + V_f I_{avg\_d\_6sw}) \\ &\quad + 3(I^2_{rms\_s\_6sw} R_{ce} + I^2_{rms\_d\_6sw} R_{ak}) \end{aligned}, \text{ and} \tag{5.73}$$

$$\begin{aligned} P_{c\_aux\_3sw} &= 3(V_t I_{avg\_s\_3sw} + V_f I_{avg\_d\_3sw}) \\ &\quad + 3(I^2_{rms\_s\_3sw} R_{ce} + I^2_{rms\_d\_3sw} R_{ak}) \end{aligned}. \tag{5.74}$$

The ESR losses in the resonant capacitors are

$$P_{ESR\_6sw} = 3 I_{aux\_rms\_6sw}{}^2 R_{ESR}, \text{ and} \tag{5.75}$$

$$P_{ESR\_3sw} = 3 I_{aux\_rms\_3sw}{}^2 R_{ESR}. \tag{5.76}$$

The resonant inductor loss models are provided in Section 5.4.

5.6.3. Numerical Analysis of ZCT Inverter Losses

Based on the loss models, a numerical analysis of the ZCT inverter losses are performed. The loss model parameters used are as follows: For main device conduction losses, V_t=1.25 V, R_{ce}=0.00333 Ω, V_f=0.7 V, and R_{ak}=0.004 Ω; for auxiliary device conduction losses, V_t=1.125 V, R_{ce}=0.0075 Ω, V_f=0.7 V, and R_{ak}=0.0075 Ω; for switching losses, K_{6sw}=0.25, K_{3sw}=0.5, K_{on}=0.12 mJ/A, K_{off}=0.1 mJ/A, and E_{off_ZCT}=0.2 mJ. These parameters are only approximations, and the calculation results are more meaningful in revealing the design essence and loss mechanisms rather than for comparing exact numbers.

Use of threshold control is important for achieving a proper trade-off between switching losses and conduction losses in the ZCT inverters, for which the instantaneous load current *I(t)* changes in sinusoidal waveform and the peak of the sinusoidal line current IL_{pk} also changes with operation conditions (output power, modulation index and power factor). The developed inverter loss models are useful for determining the threshold current I_{th}. When *I(t)* is below the I_{th}, the auxiliary circuits are disabled. As shown in Figure 5.42, in one switching cycle, the switching energy losses saved by soft switching, which are the difference between the switching energy losses under hard switching and those under soft switching, increase linearly with *I(t)*. On the other hand, the additional conduction energy loss in the main and auxiliary circuits caused by soft switching is almost constant in the three-switch ZCT, and slightly decreases with *I(t)* in the six-switch ZV/ZCT. Clearly, the crossover points between the curves of the switching loss saved by soft switching and the curves of the additional conduction loss caused by soft switching determine the value of I_{th}. Based on these curves, for both 55-kW ZCT inverters, the I_{th} is determined to be 50 A.

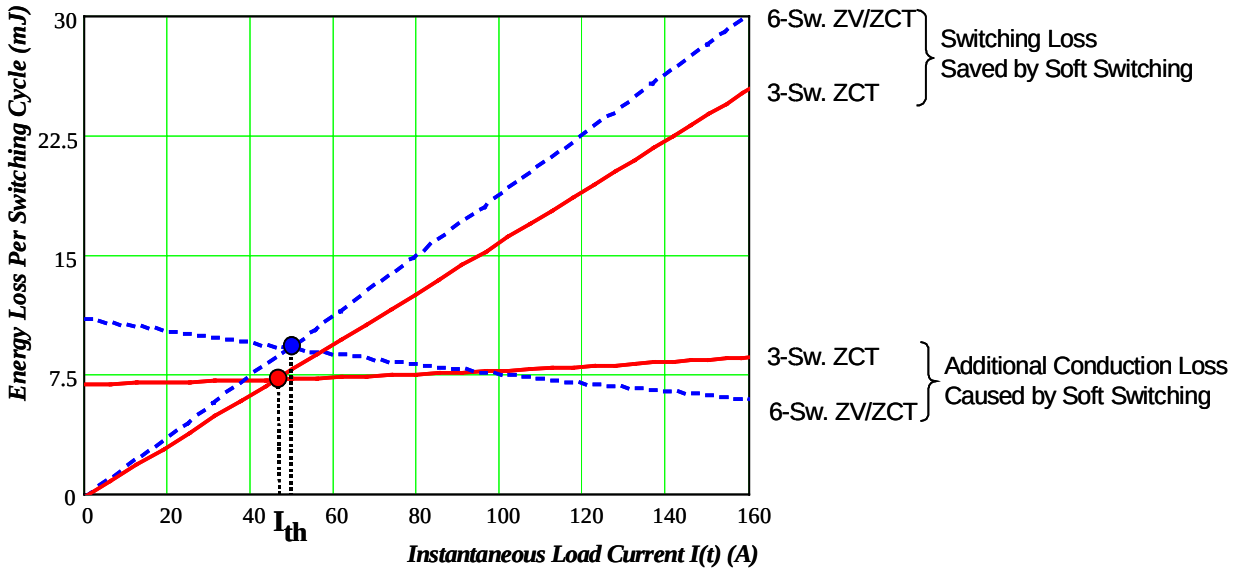

Figure 5.42. Determining the threshold current I_{th} by comparing the switching *energy* loss saved by soft switching and the additional conduction *energy* loss caused by soft switching.

Figure 5.43 shows the effects of threshold control on the additional conduction power losses and the switching power losses in line cycles. Without threshold control, the additional conduction losses are almost constant in the three-switch ZCT, regardless of the change in peak load current IL_{pk}; and those losses even increase under a smaller IL_{pk} in the six-switch ZV/ZCT. With threshold control, however, these losses become adaptive to the change of IL_{pk} and are significantly reduced. In particular, the reduction is more remarkable under lighter load conditions. On the other hand, since the main devices operate under hard switching when $I(t)$ is below I_{th}, the switching losses increase with threshold control. As implied by Equation (5.24), under a smaller IL_{pk}, the time interval T_{th} during which the auxiliary circuits are disabled becomes relatively longer for a given I_{th}; thus, the switching losses actually tend to slightly increase when IL_{pk} decreases. Yet, comparing Figure 5.43(a) to Figure 5.43(b), it is apparent that with threshold control, the increase in switching losses is much smaller than the decrease in

additional conduction losses. As a result, in regards to the net effect of soft switching, the total inverter power losses can be reduced from those in the hard-switching inverter.

This net effect is also shown in Figure 5.44. Without threshold control, the total power losses of ZCT inverters can be even higher than that of the hard-switching inverter under light load conditions. For this calculation, only after IL_{pk} is greater than about 100 A do the total ZCT inverter losses start to become less than the total loss of the hard-switching inverter. With threshold control, however, the total ZCT inverter losses are lower than the hard-switching inverter loss within the entire load current range. The results also show that the six-switch ZV/ZCT inverter has less loss than the three-switch ZCT inverter, and that the difference is more considerable under heavy load conditions.

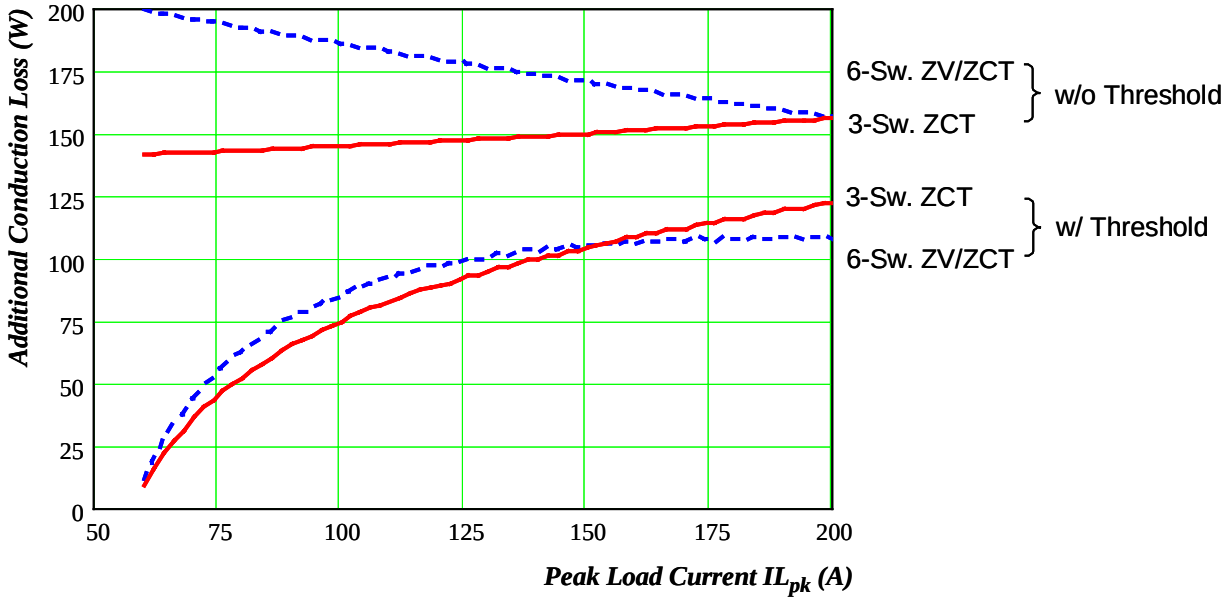

(a)

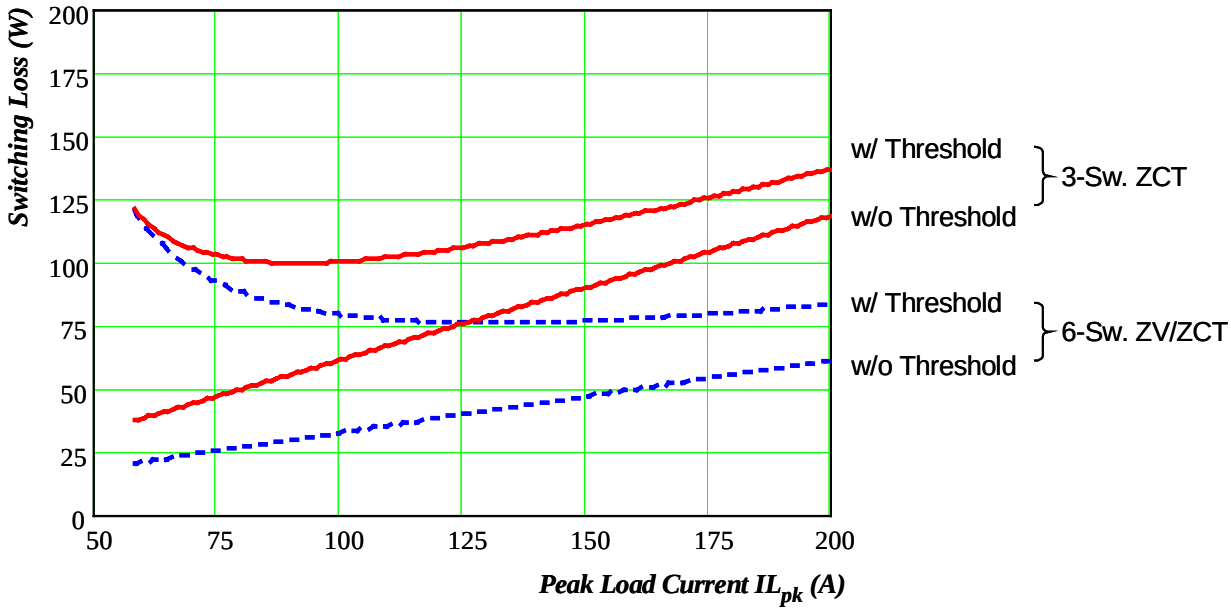

(b)

Figure 5.43. Effects of threshold control on the additional conduction loss and the switching loss (f_s=10 kHz):
(a) additional conduction power losses with (w/) and without (w/o) threshold control; and
(b) switching power losses w/ and w/o threshold control.

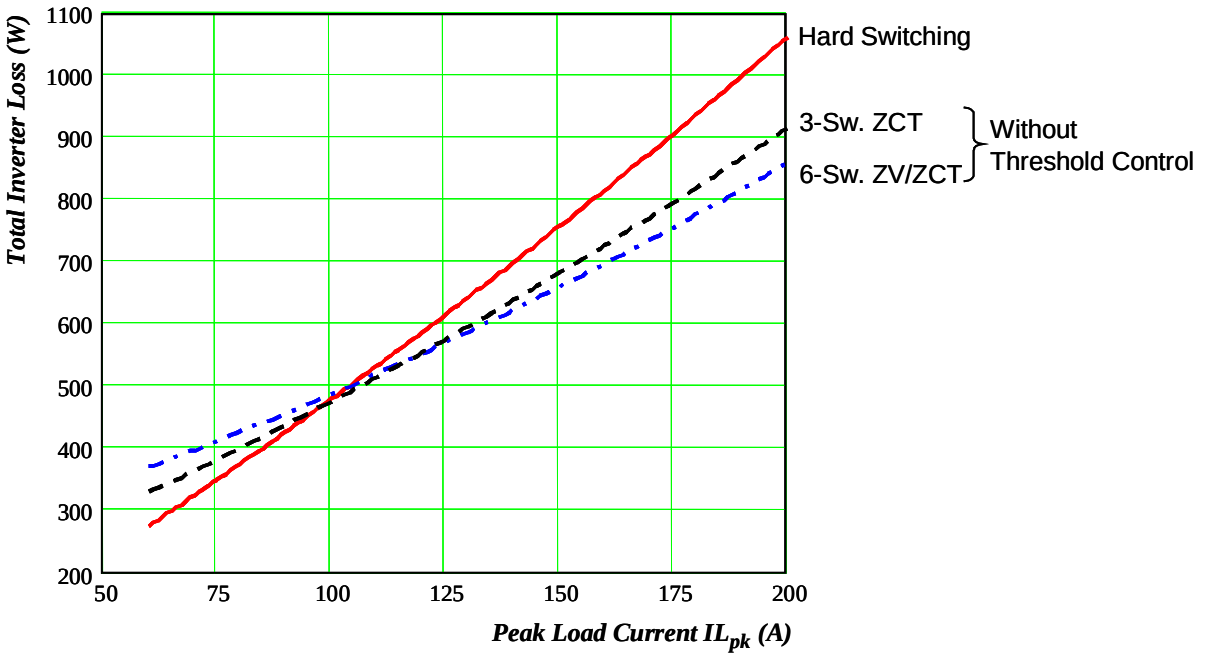

(a)

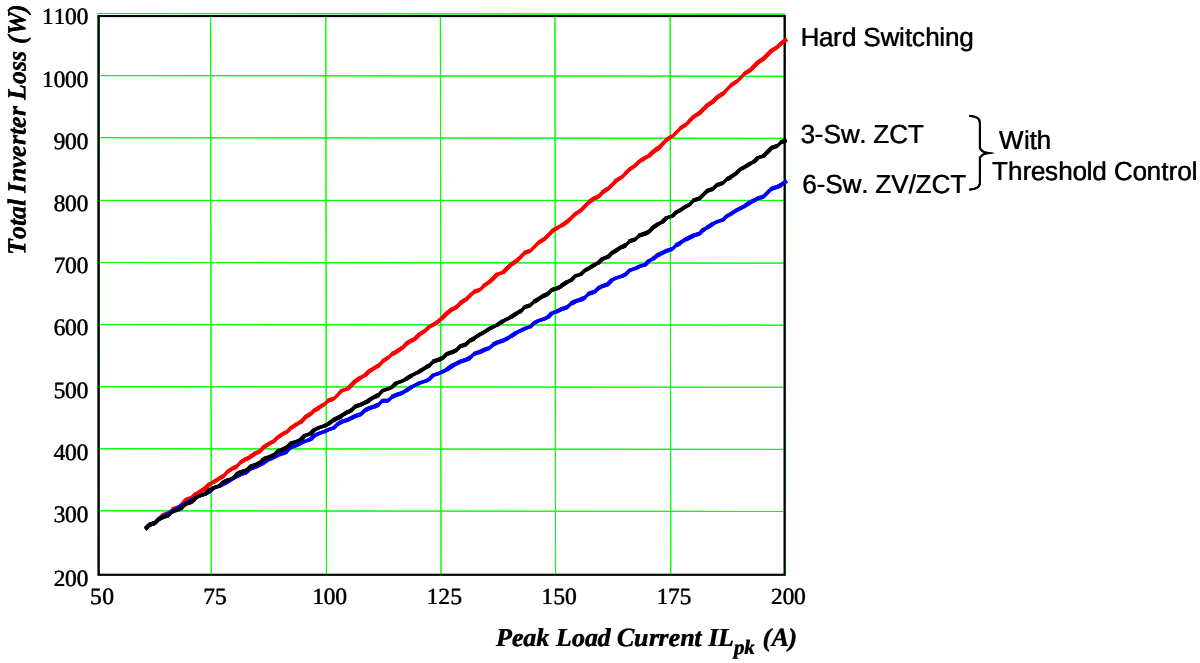

(b)

Figure 5.44. *Net* effect of threshold control on the total inverter power losses (f_s=10 kHz; conduction losses are for M=0.66 and pf=0.96):
(a) ZCT inverters *without* threshold control; and
(b) ZCT inverters *with* threshold control.

Although Figure 5.43(a) shows that the additional conduction losses in both ZCT inverters are almost the same within the entire load current range under threshold control, they do have different distributions, which are illustrated in Figure 5.45. In the six-switch ZV/ZCT, there is no additional conduction loss in the main IGBTs; meanwhile, in the three-switch ZCT, most of the conduction losses in the main circuit occur in the main IGBTs. In terms of the passive component losses, most of them occur in the resonant inductors, and the three-switch ZCT has higher inductor loss than the six-switch ZV/ZCT. The conduction losses in the auxiliary devices are basically evenly shared by IGBTs and diodes in the three-switch ZCT. However, they are mostly handled by IGBTs in the six-switch ZV/ZCT. These losses are further divided in six auxiliary IGBTs, so the burden for the individual IGBT is almost the same as that in the three-switch ZCT. This variation in loss distributions reflects the different soft-commutation operations and resonant current flowing paths of the two inverters.

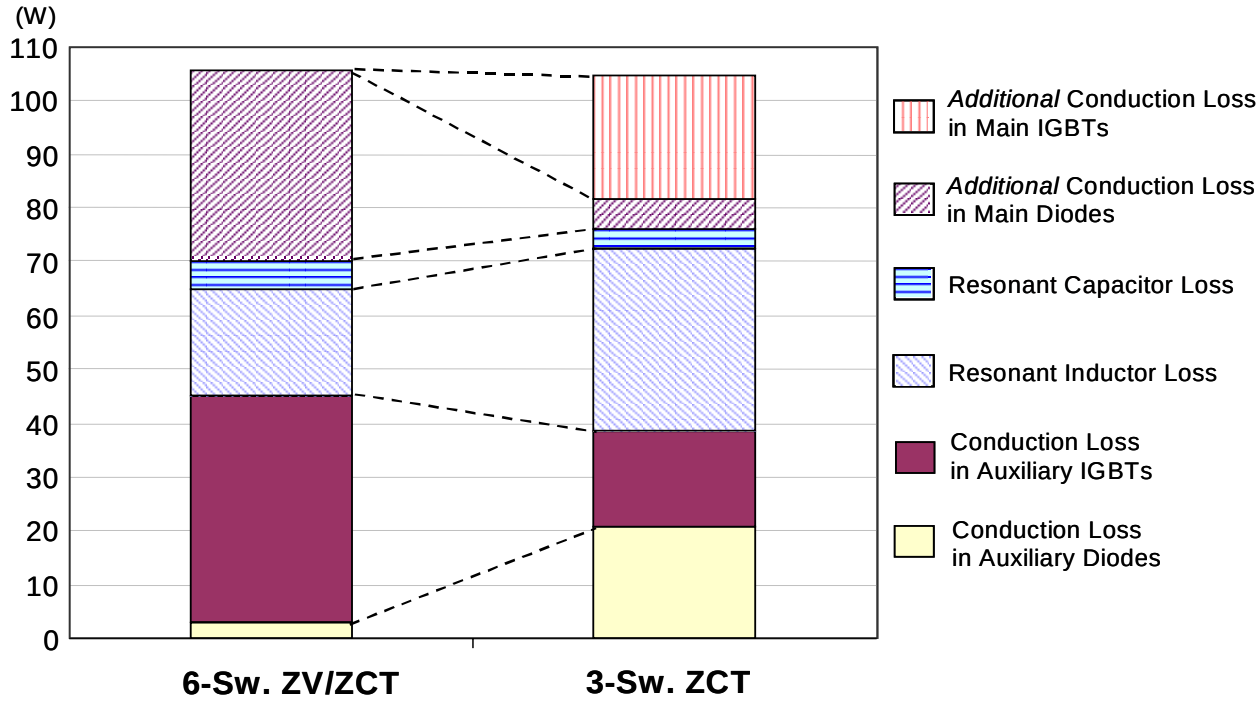

Figure 5.45. Distribution of the additional conduction power losses caused by soft switching for one operation point (IL_{pk}=150 A, f_s=10 kHz, and with threshold control).

Figure 5.46 depicts the inverter switching and conduction losses as a function of the peak load current IL_{pk}. Figure 5.47 is a breakdown of the total inverter losses for one operation point: IL_{pk}=150 A, M=0.66, and pf=0.96, for which detailed calculation results are listed in Table 5.8. As will be discussed in Chapter 6, the No. 9 point of the dynamometer test has the same operation condition.

One important feature revealed by the loss breakdown is that the hard-switching inverter itself has much smaller switching loss than conduction loss; this conduction loss is also equal to the basic conduction loss in the ZCT inverters. As a consequence, although the switching losses are significantly reduced and the additional conduction losses are optimized by the design, the effect on the total inverter loss reduction can still be limited because of this dominant conduction loss. This indicates that besides proper design and control of the auxiliary circuits, it is the device characteristics that ultimately determine the efficiency benefit of using soft-switching inverters. In addition, the operation conditions have an important impact on the effect of soft switching. The six-step SVM results in low switching losses in the hard-switching inverter, but on the other hand it offsets the effect of soft switching. With higher switching frequency f_s, the switching loss will increase but the basic conduction loss will be the same; thus, the ZCT inverters will have greater reduction of the total power losses. For this calculation case, under f_s=10 kHz, the total inverter loss is reduced by about 20% in the three-switch ZCT, and by about 25% in the six-switch ZV/ZCT; under f_s=20 kHz, the total inverter loss is reduced by about 30% in the three-switch ZCT, and by about 35% in the six-switch ZV/ZCT.

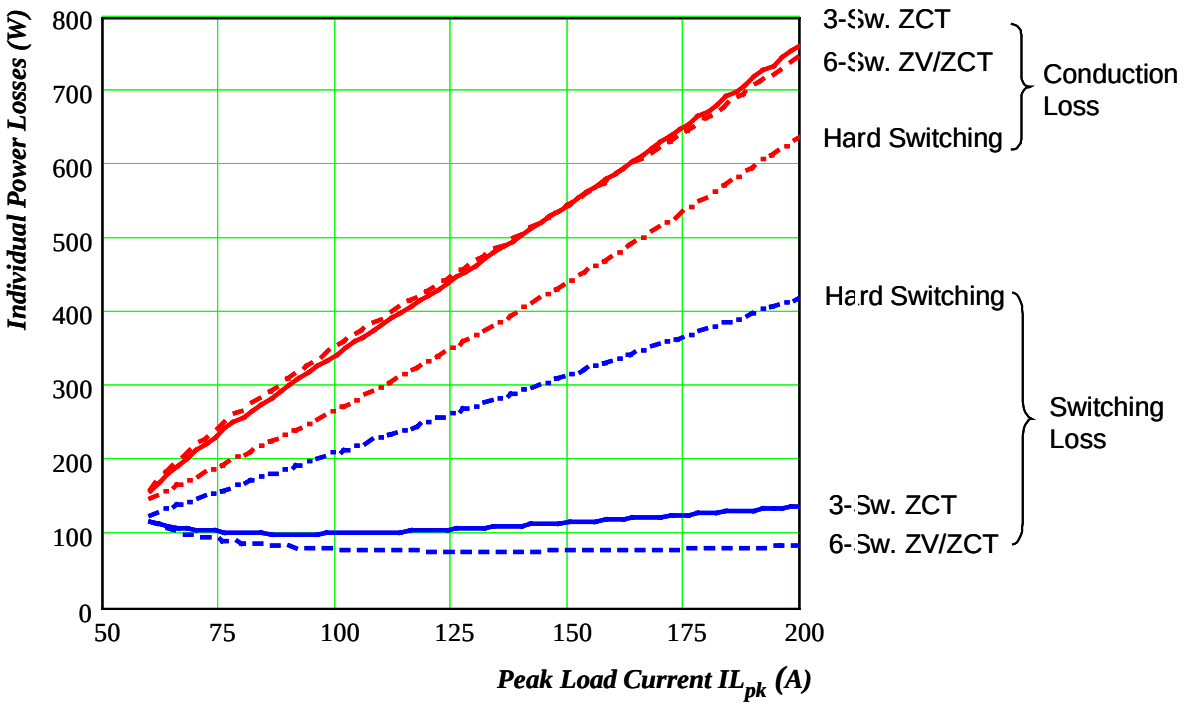

Figure 5.46. Individual inverter power losses as a function of the peak load current (f_s=10 kHz, with threshold control, and conduction losses are for M=0.66 and pf=0.96).

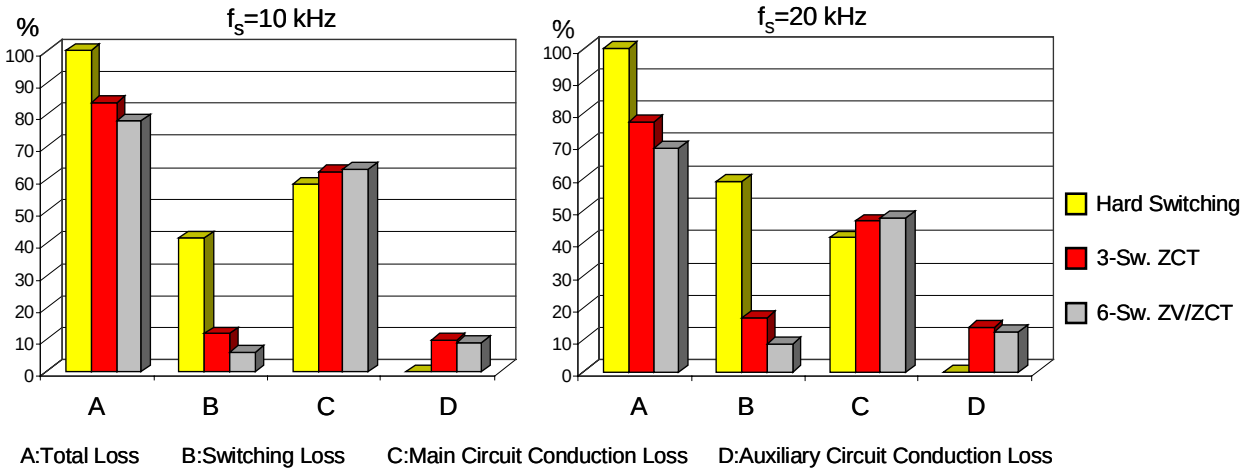

Figure 5.47. Breakdown of inverter losses under different switching frequencies. (For each f_s, losses are normalized by the corresponding total loss of the hard-switching inverter. Conditions: M=0.66, pf=0.96, IL_{pk}=155 A, the same as the No. 9 point of the dynamometer test.)

Table 5.8.
Inverter Loss Calculation Results
(Same Conditions as Figure 5.47)

Output Power		27154 W									
Switching Conditions		Hard Switching		3-Switch ZCT				6-Switch ZV/ZCT			
				w/o Threshold Control		w/ Threshold Control		w/o Threshold Control		w/ Threshold Control	
		10k	20k	10k	20k	10k	20k	10k	20k	10k	20k
Switching Loss (W)	Turn On	171.9	343.8	85.9	171.8	95.8	191.6	42.9	85.8	57.7	115.4
	Turn Off	143.2	286.4	4	8	19.5	39.0	4	8	19.5	39.0
	Subtotal	315.1	630.2	89.9	179.8	115.3	230.6	46.9	93.8	77.2	154.4
Main Circuit Conduction Loss (W)	Basic	441.3	441.3	441.3	441.3	441.3	441.3	441.3	441.3	441.3	441.3
	Additional	0	0	41.9	83.8	28.5	57.0	59.4	118.8	35.6	71.2
	Subtotal	441.3	441.3	483.2	525.1	469.8	498.3	500.7	560.1	476.9	512.5
Auxiliary Circuit Conduction Loss (W)	Auxiliary Switch	0	0	25.4	50.8	17.8	35.6	69.6	139.2	42.2	84.4
	Auxiliary Diode			30.2	60.4	20.8	41.6	3.0	6.0	2.8	5.6
	Cap. Loss			5.4	10.8	3.8	7.6	8.7	17.4	5.2	10.4
	Inductor Loss			47.1	94.2	33.7	67.4	29.9	59.8	19.8	39.6
	Subtotal			108.1	216.2	76.1	152.2	111.2	222.4	70.0	140.0
Total Loss (W)		756.4	1072	681.2	921.1	661.2	881.1	658.8	876.3	624.1	806.9
Efficiency (%)		97.29	96.20	97.55	96.72	97.62	96.86	97.63	96.87	97.75	97.12

5.6.4. Summary

An analytical ZCT inverter loss model is developed. Numerical analysis based on the model shows that the proposed threshold control is effective in achieving a proper trade-off between the switching losses and additional conduction loss, and thus minimizing the total inverter losses. The different loss mechanisms and distributions between the two ZCT inverters are

characterized. The calculation results for the two 55-kW ZCT inverters suggest that both can reduce the total losses from the hard-switching inverter; however, the efficiency benefit can be limited because the conduction losses in the main circuits are dominant in the total inverter loss. The loss modeling and calculation is meaningful in assisting the design optimization and predicting the trend in loss reductions. Measurement results for the 55-kW prototype inverter losses and efficiencies will be presented in Chapter 6.

5.7. System-Level Operation Aspects of the ZCT Inverters

5.7.1. Duty-Cycle Difference Between Ideal and Actual PWM Signals

In soft-switching inverters, when the controller sends out a command to start a transition, an auxiliary switch is turned on first, and the PWM signal generated from the controller is delayed for an interval before it is passed to the corresponding main switch gate driver. For ZVT inverters operating under a sufficient load current, the auxiliary circuits are activated only at turn-on; this causes a significant difference between the actual phase duty cycle and the ideal phase duty cycle that is demanded by the controller, and can cause undesirable variations in the inverter output voltage [F11] [F14]. For the proposed ZCT inverters, however, soft transitions occur not only at turn-on, but also at turn-off, so both the rising and falling edges of the main bridge pole voltages are delayed. As a result, the net effect on the phase duty-cycle difference, and thus the variation of output voltage, is much smaller.

For the six-switch ZV/ZCT, referring to the timings shown in Figure 5.18, the falling edge of the main switch voltage v_{s1} is delayed by $[t_0, t_3]$ at the turn-on, and its rising edge is delayed by $[t_5, t_8]$ at the turn-off. During $[t_7, t_8]$, without considering parasitic effects, C_x is linearly charged by i_x, so approximately v_{s1} increases by Δv_{s1} in a straight line until reaching V_{dc} at t_8.

The phase duty-cycle difference between ideal and actual PWM signals is derived as

$$\begin{aligned}\Delta d_{6sw} &= f_s \cdot ([t_0, t_3] - [t_5, t_7] - \frac{\Delta V_{s1}}{V_{dc}}[t_7, t_8]) \\ &= \frac{f_s \cdot T_o}{2\pi}\left(\frac{\pi}{2} + \sin^{-1}\frac{IL_n}{1-IL_n} - \cos^{-1}\frac{IL_n}{1-IL_n} - \frac{(1-\sqrt{1-2IL_n})^2}{2IL_n}\right)\end{aligned}, \quad (5.77)$$

where IL_n is the normalized instantaneous load current, given in Equation (2.15).

Similarly, for the three-switch ZCT, referring to the timings shown in Figures 5.17, during $I_{Load}>0$, v_{s1} is delayed by [t_0, t_3] at the turn-on, and by [t_5, t_9] at the turn-off; during $I_{Load}<0$, v_{s2} is delayed by [t_0, t_1] at the turn-on, and by [t_5, t_8] at the turn-off. The phase duty-cycle difference for both load current directions are found to be equal, as given by

$$\Delta d_{3sw} = -\frac{f_s \cdot T_o}{2\pi}\left(\cos^{-1} L_n + \frac{(1-\sqrt{1-IL_n{}^2})^2}{2IL_n}\right). \quad (5.78)$$

The negative sign in Equation (5.78) means that the actual phase duty cycle is larger than the ideal one. Figure 5.48 plots curves of the duty-cycle differences as functions of IL_n and f_sT_o. For the designed 55-kW ZCT inverters, the T_o is 4~5 μs. Under f_s=10 kHz, the duty-cycle difference is found to be around 0.01, which is negligible and will have almost no impact on the control performance.

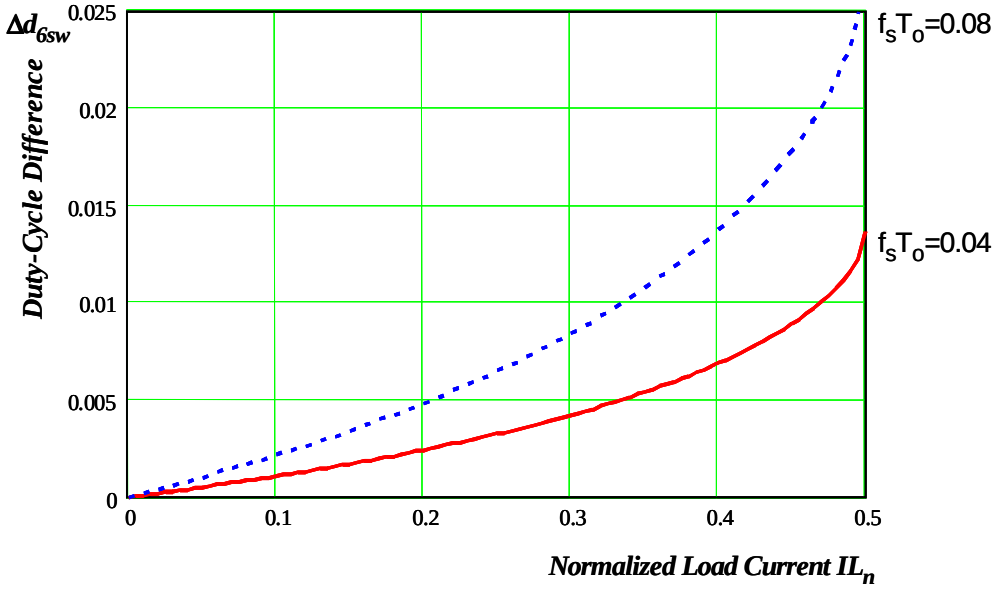

(a)

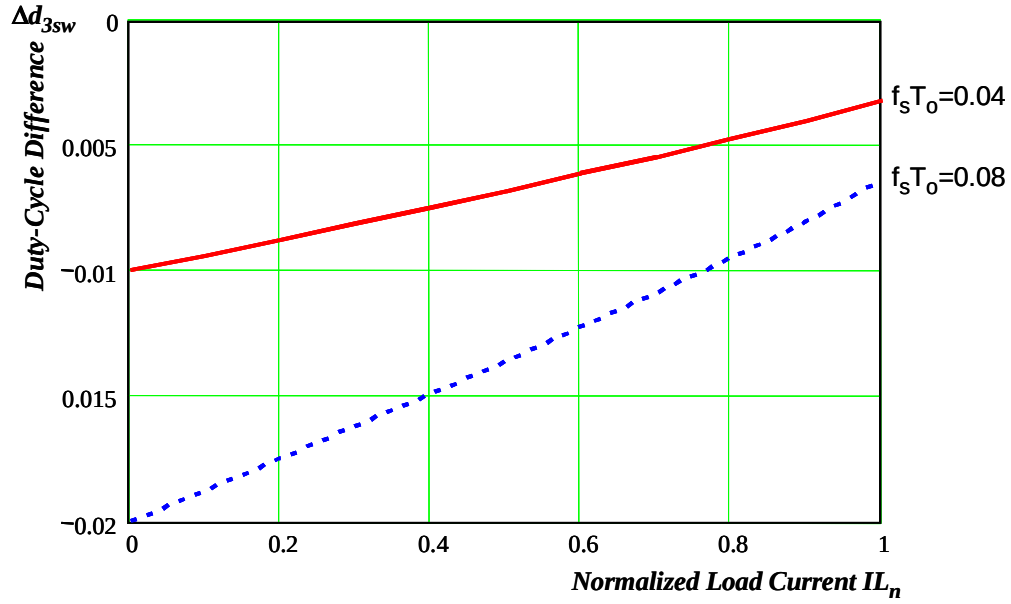

(b)

Figure 5.48. Duty-cycle differences between ideal and actual PWM signals as functions of IL_n and f_sT_o:
(a) six-switch ZV/ZCT inverter (from Equation (2.8), the meaningful IL_n is less than o.5); and
(b) three-switch ZCT inverter.

5.7.2. Pulse-Width Limits

A soft commutation can start only after the previous commutation is completed. Consequently, the resonant process imposes a limitation on the pulse widths, and thus, the phase duty cycle. The impact of the pulse-width limits on soft-switching converter control performance was discussed in [F12] [F14]; but for ZCT inverters, no mathematically based analysis of the pulse-width limits themselves was performed. This section will derive the generalized equations of these limits in ZCT inverters, which can give insight into this aspect and provide knowledge for further modeling and control.

The pulse width of the main switch gate signals, T_w, must be limited by a minimal pulse width T_{min}, as expressed in (5.79)

$$T_{min} \le T_w \le 1/f_s - T_{min} . \tag{5.79}$$

For the six-switch ZV/ZCT, referring to the timings in Figure 5.18, the T_{min} is found to be

$$\begin{aligned} T_{min\_6sw} &= \mathrm{Max}\,(T_{ON} + T_{OFF\,3}, [t_3 + t_4] + T_{OFF\,1}) \\ &= T_{ON} + T_{OFF\,3} \\ &= \frac{T_o}{2\pi}\left(2\pi + \sin^{-1}\frac{IL_n}{1-IL_n} + \cos^{-1}\frac{IL_n}{1-IL_n} + \frac{(1-\sqrt{1-2IL_n})}{IL_n}\right) \end{aligned} . \tag{5.80}$$

For the three-switch ZCT, referring to Figures 5.17, the T_{min} for both I_{Load} directions is derived to be equal, given by

$$\begin{aligned} T_{min\_3sw} &= \mathrm{Max}\,(T_{ON\,3} + T_{OFF\,1}, T_{ON\,1} + T_{OFF\,3}) \\ &= T_{ON\,3} + T_{OFF\,1} \\ &= \frac{T_o}{2\pi}\left(\frac{5}{2}\pi + tg^{-1}(IL_n)\right) \end{aligned} . \tag{5.81}$$

Following Equations (5.80) and (5.81), the minimum phase duty cycle is defined as

$$D_{Limit} = f_s T_{min} . \tag{5.82}$$

Therefore, the range of the effective phase duty cycle D is limited by

$$D_{Limit} \le D \le 1 - D_{Limit} . \tag{5.83}$$

Curves of the minimum phase duty-cycle D_{Limit} are plotted as functions of IL_n and f_sT_o in Figure 5.49. For the designed 55-kW inverters, under f_s=10 kHz, the ranges of effective phase duty cycle are from 0.077 to 0.923 for the six-switch ZCT, and from 0.066 to 0.934 for the three-switch ZCT. These limits become larger with higher f_s or larger resonant period T_o. In control implementations, in order to avoid malfunction of the resonant tanks due to the overlap between consecutive resonant cycles, a detection circuit is designed to prevent the very short or long control signals that are beyond the range specified in Inequality (5.83) from being passed to the corresponding main switch gate drivers. For situations in which the controller demands either a very large or small duty cycle in each phase, the pulse-width limits may cause distortion in the output current. One solution is to make full use of the zero vectors in the SVM schemes. Under the same modulation index, by properly selecting the zero vectors, the duty cycle required for each phase can avoid the very high or very low regions. Thus, the effect of duty-cycle limits can be alleviated. The selection of zero vectors is discussed in [F15] [F16].

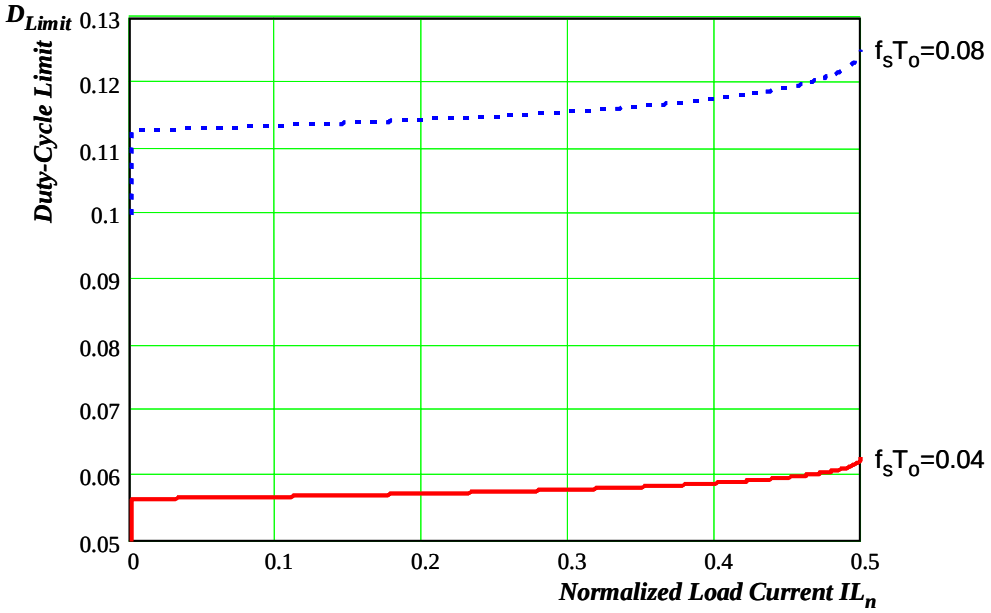

(a)

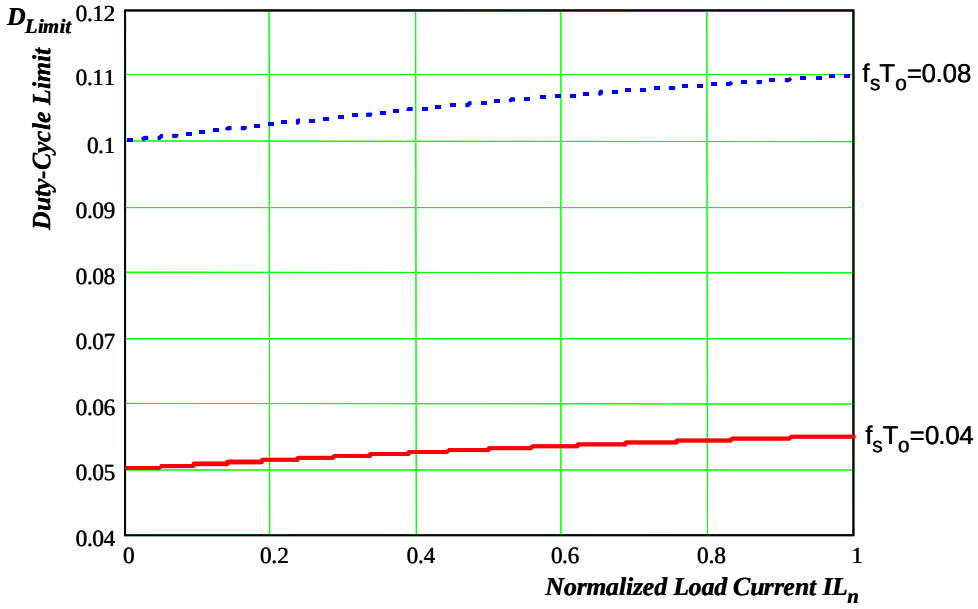

(b)

Figure. 5.49. Duty-cycle limits as functions of IL_n and f_sT_o:
(a) six-switch ZV/ZCT inverter; and
(b) three-switch ZCT inverter.

5.7.3. Transient Behavior

In certain soft-switching inverters, such as the RDCL [B2] [B8], additional circuits and controls are required to start the soft commutations and to build up the initial inductor current. For ZCT inverters, however, the startup is not an issue. In the six-switch ZV/ZCT inverter, the load current I_{Load} charges the resonant capacitor C_x through S_{x1} at [t_7, t_8] (Figure 2.5). In the three-switch ZCT inverter, the DC bus voltage V_{dc} charges C_x through S_1 and S_{xa} at [t_5, t_7] for $I_{Load}>0$ (Figure 3.6), and I_{Load} charges C_x through S_{xa} at [t_7, t_8] for $I_{Load}<0$ (Figure 3.8). These intervals provide ways to transfer energy between the main and auxiliary circuits and to build up the initial capacitor voltage v_x at startup. As a result, the ZCT inverters are easy to start.

Prior to turn-on at t_0, the amplitude of $v_x(t_0)$ equals V_{dc}-$I_{Load}Z_o$ in the six-switch ZV/ZCT and in the three-switch ZCT for $I_{Load}<0$, and equals $I_{Load}Z_o$ in the three-switch ZCT for $I_{Load}>0$. For each I_{Load} direction, the $v_x(t_o)$ is adaptive to the variation of I_{Load}. However, the polarity of $v_x(t_o)$ is opposite between different I_{Load} directions. Referring to the polarity defined in Figures 2.2 and 3.5, when $I_{Load}>0$, $+V_{dc}>v_x(t_0)>0$; when $I_{Load}<0$, $-V_{dc}<v_x(t_0)<0$. It is necessary to investigate how the $v_x(t_0)$ is built up under the bi-directional inverter load current. Figure 5.50 illustrates one scenario for the build-up of $v_x(t_0)$ in the three-switch ZCT, which is also applicable to the six-switch ZV/ZCT. In the beginning, $I_{Load}<0$, $v_x<0$, the switching state is such that S_1 is off and S_2 is on, and I_{Load} flows through IGBT S_2. Then, I_{Load} reverses to $I_{Load}>0$ and starts to freewheel through diode D_2. If for any reason the polarity of v_x is still $v_x<0$, then the bottom auxiliary diode D_x will be forward-biased. Through half of a resonant cycle, the polarity of v_x is then reversed to $v_x>0$. After that, if for any reason $v_x>V_{dc}$, then the top auxiliary diode D_c will conduct, and some of the energy in the capacitor will return to the DC power source through *Dc*. Finally, v_x will stay

at $V_{dc}>v_x>0$, and thus is ready for the turn-on of S_1. Therefore, the ZCT inverters have smooth transitions with bi-directional load currents.

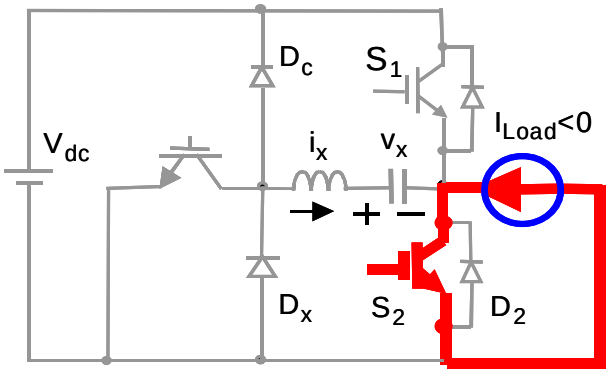

[*Before* t_0]: $I_{Load}<0$, and $v_x<0$.

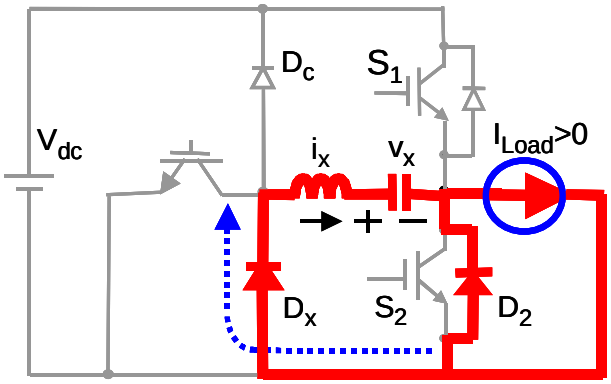

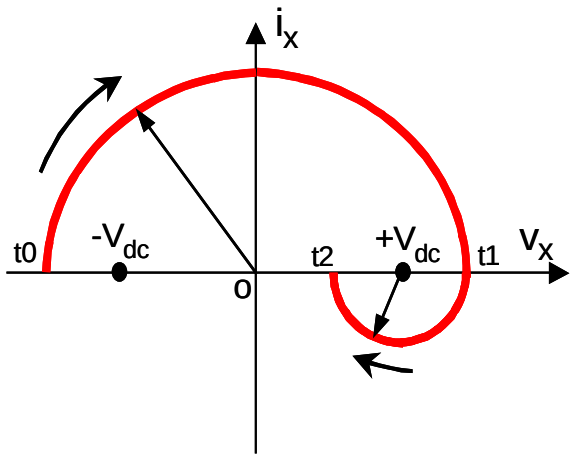

[t_0, t_1]: Polarity of v_x reverses after $I_{Load}>0$.

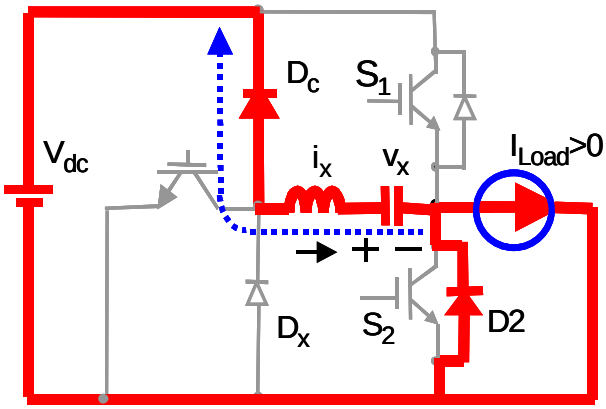

[t_1, t_2]: Operational stage making $v_x<V_{dc}$.

Figure 5.50. Build-up of initial capacitor voltage under a bi-directional load current: topological stages and their corresponding state-plane trajectory.

5.8. Layout and Parasitic Considerations

One advantage of ZCT commutations is that they can absorb the stray inductance as part of the resonant inductance such that the stray inductance can become a useful contributor to the desirable soft commutations [F17]. However, the variation and uncertainty of the stray inductance can cause both a variation in the actual resonant time period T_o as well as incorrect control timings. Moreover, unbalanced T_o among the three phases increases the difficulty in timing control implementations. Therefore, it is necessary to investigate the inverter layout and its impact on the system's sensitivity.

Figure 5.51 illustrates the distribution of stray inductance caused by layout in the three-switch ZCT inverter, which is similar to that of the six-switch ZV/ZCT. There are two major contributors to the stray inductance. One part is L_{con}, caused by the connections between the main and auxiliary switches (A to A_x, B to B_x, and C to C_x). The connections among the three phases should be of equal lengths in order to achieve balanced inductance. The other part of the stray inductance is caused by the DC bus connection ($L_{bus1,}$ L_{bus2} and L_{bus3}); this effect can be reduced by a laminated bus bar.

From Equation (3.1), the relationship between the variation of T_o and the variations of LC resonant tank parameters is derived as

$$\frac{\Delta T_o}{T_o} = \frac{\Delta C_x}{2C_x} = \frac{\Delta L_x}{2L_x}. \tag{5.84}$$

The tolerance to ΔT_o is related to the control timings and device characteristics. In practical implementations, ΔT_o should not be larger than the resolution of the digital controller. For the designed 55-kW inverters, the controller resolution is 0.1 μs. Following Equation (5.84), the tolerance to ΔL_x is found to be around 40 nH in the three-switch ZCT and 30 nH in the six-switch

ZV/ZCT. Under this tolerance, with the stray inductance of the bus connections being equal, the acceptable difference between the lengths of the connections of A to A_x, B to B_x, and C to C_x is about 1~2 inches, which is physically feasible in the implementations. The length of these connections is around 12 inches in the designed power stages, which generates an inductance of around 240 nH.

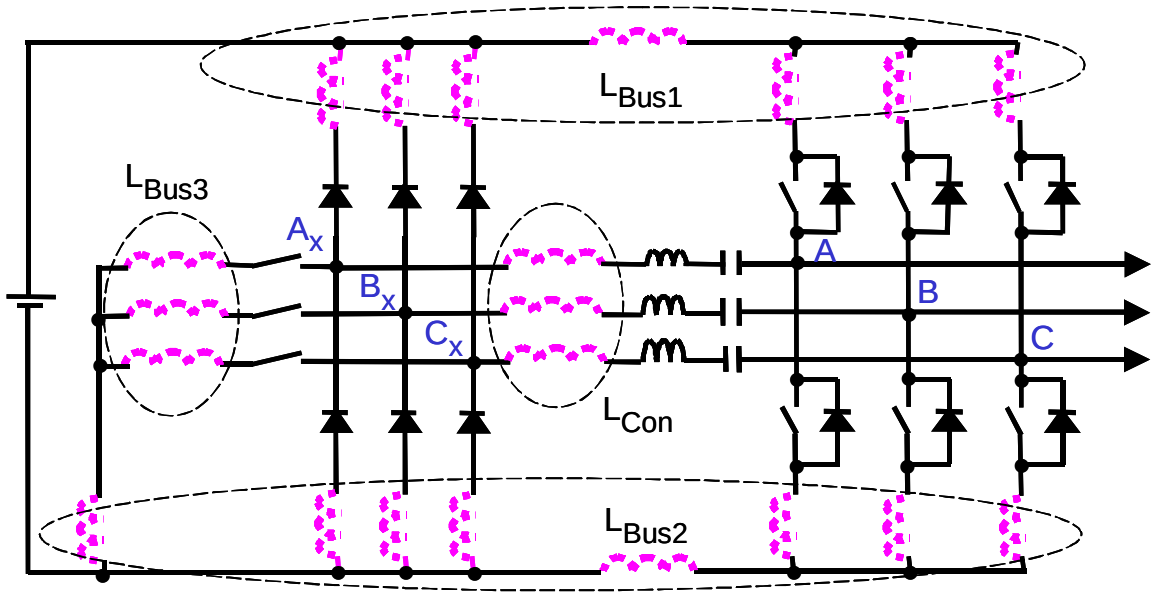

Figure. 5.51. Stray inductance distributed in the three-switch ZCT inverter layout.

In addition to reducing the stray inductance for the purpose of timing control, the laminated bus bars help to protect the main and auxiliary devices from over voltage that occurs due to the reverse recovery in the auxiliary and main diodes. Figure 5.52 illustrates the auxiliary diode reverse-recovery effect, using the turn-on transition of the six-switch ZV/ZCT as an example, for which the theoretical waveforms are shown in Figure 2.5. At the end of this turn-on transition, resonant current i_x drops to zero at t_4, and then a reverse-recovery current starts to flow through the auxiliary diode D_{x2} in the negative direction to remove the charge stored in the junction of D_{x2}, Q_r. After the reverse-recovery current reaches its peak I_{rr}, D_{x2} starts to support a reverse

voltage. Then, through S_1-C_x-L_x, i_x charges C_{j2} (the junction capacitor of D_{x2} and S_{x2}), and discharges C_{j1} (the junction capacitor of D_{x1} and S_{x1}). Since C_x is normally much larger than C_{j1} and C_{j2}, the ringing frequency is mainly determined by L_x as well as the total capacitance of C_{j1} and C_{j2} in parallel, which is in the megahertz range. Because the auxiliary circuit is connected to the DC bus in a totem-pole configuration, the voltage across one auxiliary diode can be clamped by the opposite diode if the bus connection stray inductance is small enough. For example, if C_{j1} is charged up to V_{dc}, D_{x2} will be forward-biased and will conduct the resonant current, or vice versa. Finally, the ringing is damped by parasitic losses, and the reverse voltage supported by D_{x2} is the difference between V_{dc} and v_x.

The diode reverse-recovery time and peak current I_{rr} are related to the decrease rate of i_x prior to t_4, which is controlled by the resonance of L_x and C_x. Unlike the hard-switching turn-on, the turn-off of the auxiliary diode is not accompanied by a turn-on of the opposite auxiliary switch. Thus, the power consumption of the reverse-reverse recovery current effect is negligible.

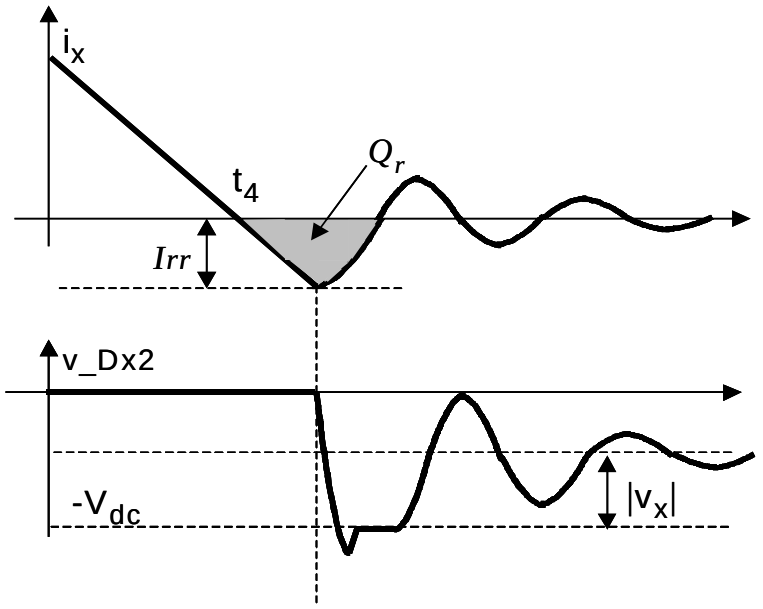

Figure 5.52. High-frequency parasitic ringing caused by the reverse-recovery current of auxiliary diodes in the ZCT inverters.

Similarly, when the current in auxiliary diode D_{x1} falls to zero at t_{10} at the turn-off of the six-switch ZV/ZCT, when the current in auxiliary diode D_x falls to zero at t_4 and t_{10} for the three-switch ZCT (Figures 3.6 and 3.8), and moreover when the surplus current in the main diodes falls back to zero at the turn-off transitions (t_7 in Figures 2.5 and 3.8, and t_8 in Figure 3.6), reverse-recovery current also flows and causes high-frequency parasitic ringings. The laminated bus bar can suppress the voltage spikes Ldi/dt by reducing the bus connection stray inductance. There is no need for additional protection circuits in practical implementations.

It is worthwhile to compare the auxiliary diode reverse-recovery effects with those of other types of soft-switching inverters, such as the ARCP, which is a typical ZVT inverter. As shown in Figure 5.53, the ARCP inverter adds two auxiliary switches in a back-to-back configuration for each phase in order to generate the resonance. At the end of each ZVT commutation, the resonant inductor current drops to zero and is blocked by the diode that is anti-paralleled with the auxiliary switch; thus, a reverse-recovery process will occur, which is similar to what was described in the preceding paragraphs. However, unlike in the ZCT inverters, there is no returning current path from the resonant inductor to the DC bus, so the voltage stress across the auxiliary devices cannot be clamped. Therefore, the diode reverse-recovery current not only causes a high-frequency ringing, but also can create excessive voltage spikes across the auxiliary devices due to the high $L_x di/dt$.

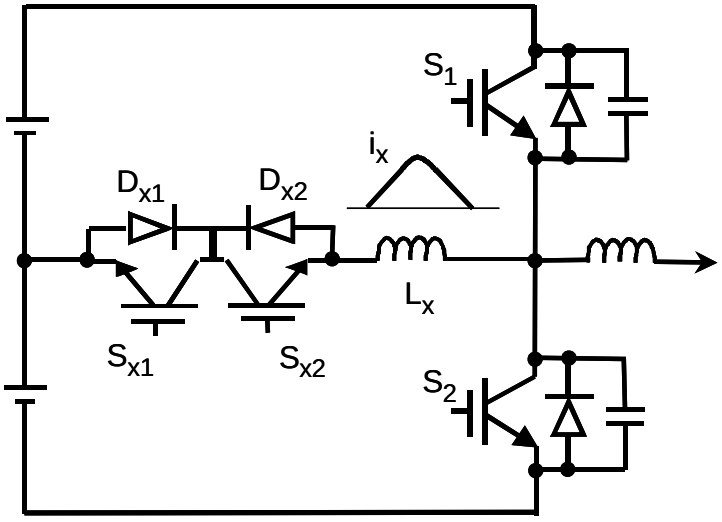

Figure 5.53. Auxiliary diode reverse-recovery effects in the ARCP inverter.

The laminated bus bars designed for both ZCT inverters are made of two pieces of 32-mil-thick copper sheets insulated by Mylar tape, as shown by the photos in Figure 5.54. After the bus bars were fabricated, verification tests were conducted, and the testing circuit and waveforms are shown in Figure 5.55. With the main IGBTs connected to the bus bar, turned off with 300-A current under hard switching and V_{dc}=300 V, which represents the worst switching condition, the switch voltage overshoots were measured as about 90 V within 0.2 μs. Based on the *Ldi/dt*, the DC bus inductance was then estimated to be about 60 nH, which provides important information for the resonant inductor design.

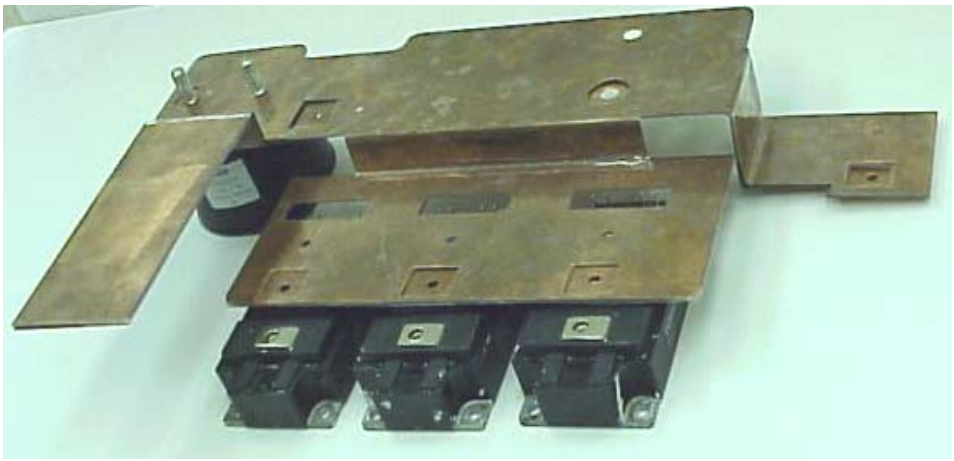

(a)

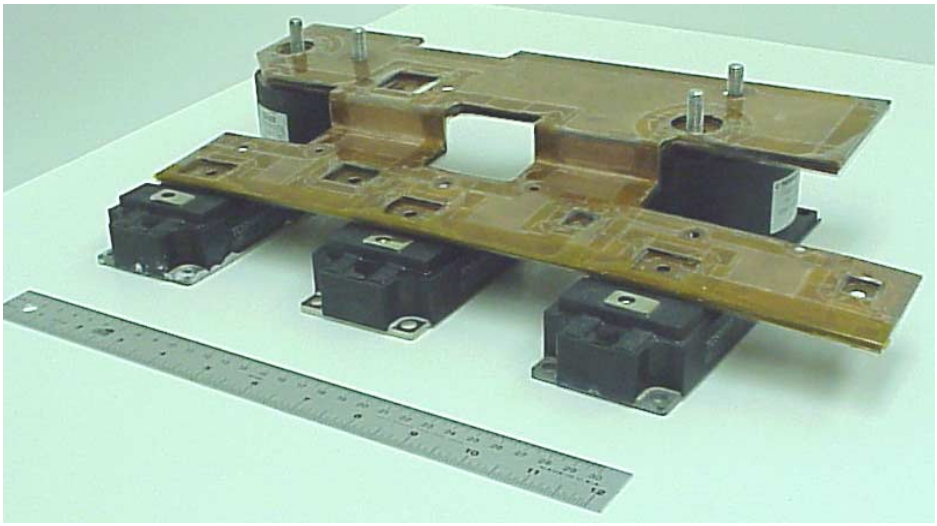

(b)

Figure 5.54. Photos of the laminated bus bars designed and fabricated for the 55-kW inverters:
(a) six-switch ZV/ZCT; and
(b) three-switch ZCT.

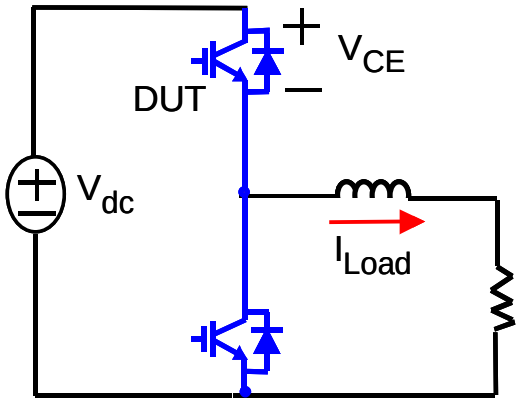

(a)

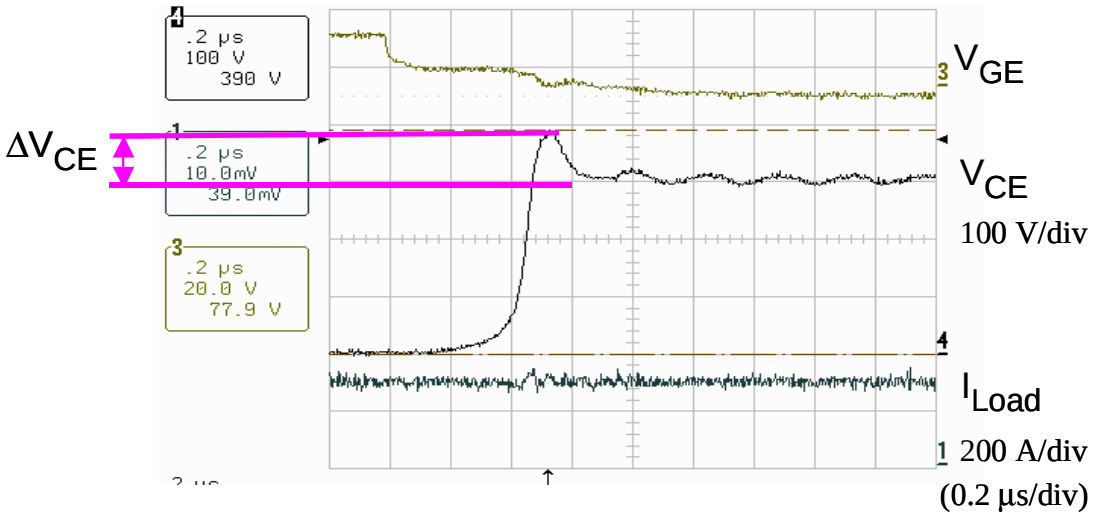

(b)

Figure 5.55. Verification test of the laminated bus bars:
(a) testing circuit; and
(b) measured waveforms of hard-switching turn-off under 300-A current and 300-V voltage.

5.9. Summary of Design Considerations

This chapter has devoted effort to developing systematic design methodologies for high-power ZCT inverters. The methodologies are elaborated via the design process of two 55-kW prototypes for EV motor drives, which are the six-switch ZV/ZCT and three-switch ZCT inverters. Different design aspects between these two inverters are compared. The design approach integrates system optimization with switching characterizations of main devices,

design, selection and characterization of auxiliary devices and components, loss modeling and analysis, system-level operation aspects, and layout and parasitic considerations.

The switching characterization of the main IGBT (MG300J2YS50, 300-A/600-V, half-bridge) shows that both ZCT operations almost eliminate the turn-off loss, and the difference mainly occurs to the turn-on loss. Under resonant tank elements of L_x=1 μH and C_x=1 μF, compared to hard switching, the three-switch ZCT reduces the turn-on loss by about 40%, and the total switching loss by about 70%; the six-switch ZV/ZCT reduces the turn-on loss by about 75%, and the total switching loss by about 90%. The effect of the conductivity modulation lag, which is common in the turn-on process of most ZVS converters, is observed for the first time in the six-switch ZV/ZCT inverter. Moreover, with different resonant tank designs, the ZCT turn-off loss is basically unchanged, but the turn-on loss and behaviors vary quite significantly between the two ZCT operations. For the three-switch ZCT, reducing L_x can significantly increase the turn-on loss, while increasing L_x on the other hand has a limited effect in reducing the turn-on loss. For the six-switch ZV/ZCT, reducing L_x does not significantly increase the turn-on loss. Resonant tanks also affect the diode reverse recovery and the range of ZCT operations.

The design of resonant tanks aims to optimize the total inverter losses over the entire speed/torque range of EV drives. Generalized equations of auxiliary circuit current stresses are developed, which provide assistance in the selection of the resonant capacitors. The resonant inductor core losses, which are caused by nonsinusoidal flux excitations, are modeled and calculated based on the modified Steinmetz equation (MSE). Following the core loss model, optimization of the inductor design is performed, which results in low loss and smaller size.

The selection of the auxiliary switches is mainly determined by the peak current handling capability, and is quite different from those of conventional applications. It is found that current

ratings specified in data sheets of commercial IGBT devices can not match the non-conventional requirements of the auxiliary switches: low average (10~20 A), high peak (400 A), sinewave of 3~6μs pulse width, repetitive frequency of 10~20 kHz, and zero-current turn-off. Therefore, both a single-shot and a continuous resonant tester are proposed for the auxiliary device selection and characterization. The tests on a group of IGBTs show that a sample 39-A IGBT can continuously operate to 400-A peak current with 200-kHz resonant frequency under a repetitive frequency of 10 kHz, and the IGBT peak current capability suitable for the auxiliary switches is largely dependent on manufacturers. A method of estimating the IGBT peak current handling capability from data sheets is recommended, which utilizes the transfer characteristics curves as a comparison index. A new parameter, namely the DC transconductance G_{DC}, is defined to quantify the difference in the peak current handling capabilities. It is suggested that IGBTs with higher G_{DC} tend to have higher peak current capability.

An analytical ZCT inverter loss model is developed to assist the design optimization and to predict the trend in loss reduction. Numerical analysis based on the model shows that the proposed threshold control is effective in achieving a proper trade-off between the switching losses and additional conduction loss, and thus minimizing the total inverter loss. The different loss mechanisms and distributions between the two ZCT inverters are demonstrated. The calculation results on the two 55-kW ZCT inverters suggest that both can reduce the total loss from the hard-switching inverter; however, the efficiency benefit can be limited because the conduction losses in the main circuits are much dominant in the total inverter loss.

Analysis of the system-level operations indicates that the ZCT inverters are easy to start and have smooth transitions with bi-directional load current. Generalized equations are developed for the duty-cycle difference between the ideal and actual PWM control signals and the pulse-width

limits. The duty-cycle difference is almost negligible, but the pulse-width limits may have a negative impact on the control performance. Methods to alleviate this impact are discussed. Layout and parasitic issues are addressed. The ZCT commutations can absorb the stray inductance as part of the resonant inductance, and the sensitivity analysis indicates that the layout of the 55-kW prototypes is physically feasible in implementations. Laminated bus bars are designed and built to reduce the parasitic effects.

The next chapter will present implementation, testing and evaluation of the two 55-kW ZCT inverter prototypes.

Chapter 6

Two 55-kW ZCT Inverter Prototypes for EV Motor Drives — Implementations, Experimentation, and Evaluation

Chapter 5 has described the design considerations of two 55-kW ZCT inverters, which are based on the proposed six-switch ZV/ZCT scheme and three-switch ZCT topology. Following the designs, two prototypes for EV traction motor drives have been built and tested to the full-power level with a closed-loop controlled induction motor dynamometer. This chapter presents the prototype implementations, reports the steady-state test results, and performs an experimental evaluation of the ZCT techniques for the EV drive application.

6.1. Prototype Implementations

6.1.1. System Configurations

The EV motor drive system consists of a battery pack, a ZCT inverter, and a three-phase induction motor. As discussed in Chapter 5, the ZCT inverters are designed to provide a maximum power of 55 kW, and to operate under 10-kHz switching frequency. The nominal DC input voltage from the battery pack is 325 V.

Figure 6.1 illustrates the system configuration, which is applicable for both ZCT inverters. The universal field orientation (UFO) and six-step SVM are used for the closed-loop induction motor drive, which are realized in a main control board with an ADMC300 digital-signal processor (DSP). General system-level functions, such as A/D scaling, torque/speed limitation, input/output ports management, communication, and fault protections, are also implemented in this board. Since the auxiliary switches need to be activated for a short time prior to the main switch turn-on and turn-off transitions, the main control signals generated in the DSP are passed

to an interface board with an Altera EPM9400 erasable programmable logic device (EPLD). Based on the algorithms discussed in Chapters 2 and 3, the ZCT control timing parameters are pre-calculated and stored as a table in the memory of the DSP. According to the load current information, which is available from other control functions for the motor drive, the DSP looks up the timing parameters and transfers them to the EPLD. With the updated timing parameters, the EPLD generates control signals for both the main and auxiliary switches, and sends them to the corresponding gate drivers. No additional sensors are needed for the ZCT control implementations.

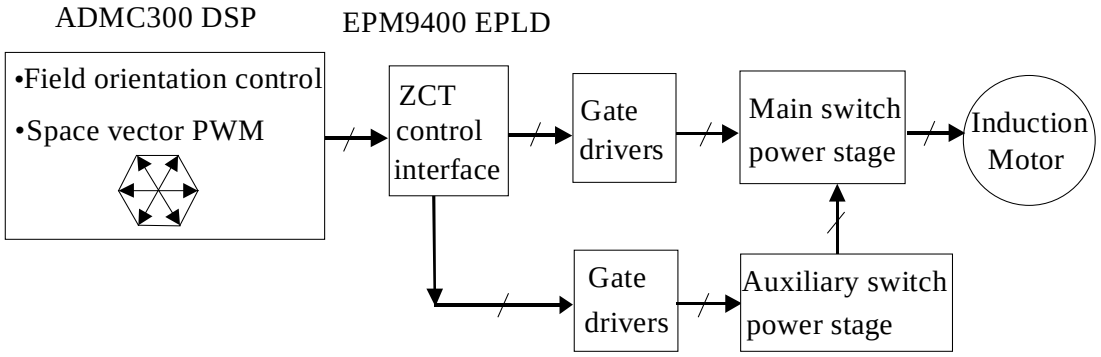

Figure 6.1. System configuration of the ZCT inverters for EV motor drives.

Figure 6.2 is a flowchart of the main program of the closed-loop control in the DSP. The main program sets up interrupts for the DSP, and then enters an infinite loop. The main program also initializes the EPLD. The points in the program at which the EPLD is set up are shown as shaded areas in Figure 6.2. Figure 6.3 describes the sequence of events that occurs during a PWM synchronization (PWM_SYNC) interrupt, which is triggered once per switching cycle. During this interrupt, the DSP performs SVM and UFO. The PIOwrite subroutines write the updated timing parameters to the EPLD.

Both ZCT inverters require no modification to the conventional SVM schemes developed for hard-switching inverters. As a result, the EPLD interface board and the DSP program are designed as piggyback structures. Compared to the DSP program designed for hard-switching inverters, the only difference is the addition of the control-timing table stored in the memory of the DSP. In fact, by setting all of the time widths of the auxiliary switching in the table to zero, the same DSP program can also be used for hard-switching inverters. These piggyback structures provide simple and flexible implementation for soft-switching inverters.

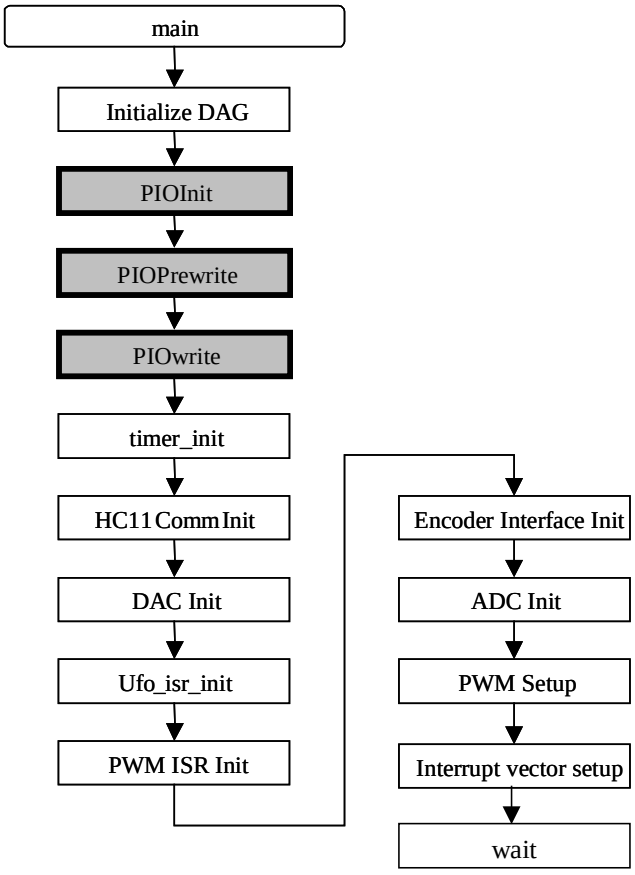

Figure 6.2. Flowchart of the main DSP program.

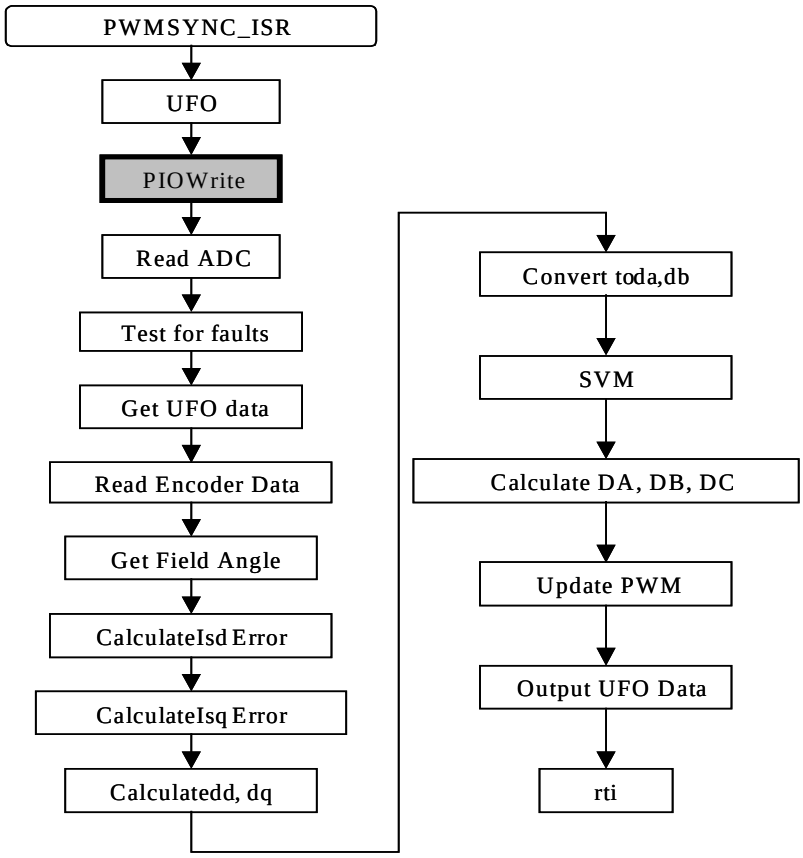

Figure 6.3. Flowchart of the PWM_SYNC interrupt.

6.1.2. Hardware Fabrications

Both ZCT inverters are built on the modified water-cooled chassis that are used in the GM EV-1 cars. Besides considerations given to the mechanical limitation of the chassis, i.e., the inverters must fit into the same mechanical housings, the compatibility issues brought by soft-switching topologies need to be addressed. There are two major concerns.

One concern involves DC capacitors. The ZCT inverters have the true piggyback feature. Unlike the ARCP inverter, they do not require special circuit structures such as the midpoint in the DC bus. Thus, DC capacitors suitable for hard-switching inverters can be directly used. In the 55-kW prototypes designed, two 150-μF polypropylene film capacitors in parallel are chosen to

be the total DC capacitors. The implementations require no additional bulky DC capacitors, which could be 4000~5000 μF, either for balancing the midpoint voltage in the ARCP inverter [F18], or for maintaining a correct DC bus resonance in the RDCL inverter [F7]. This feature can reduce the cost and size.

The other concern involves gate drivers. Regarding gate drivers for the main switches, since the *di/dt* and *dv/dt* of ZCT commutations are different from those of hard-switching inverters, gate drivers for hard-switching inverters need modifications, mainly to the IGBT de-saturation (de-sat) protection sub-circuit. On the other hand, consideration is given to the gate drivers of the auxiliary switches, especially in the three-switch ZCT inverter, in which there is no current path to shoot through the auxiliary switches from the DC bus. Thus, there is no need for the de-sat sub-circuit, which is conventionally built into IGBT gate drivers. This feature simplifies the implementations.

Figure 6.4 illustrates the six-switch ZV/ZCT inverter layout, and Figure 6.5 shows photos of the hardware implementation. Two 150-μF DC film capacitors and an input filter are mounted on the left side of the water-cooled chassis. The main switches, three MG300J2YS50 300-A/600-V half-bridge IGBT modules, are located on the left side of the chassis, near the DC capacitors. This location is beneficial to the thermal management of the main devices, because exactly underneath this position, the contact area between the coolant and the heat sink is larger than that in other positions. To reduce the EMI, three gate driver boards are placed close to their corresponding main switches. The auxiliary device, one BSM150GD60DLC 150-A/600-V six-pack IGBT module, is located on the right side of the chassis, adjacent to the DC capacitors. This module is located underneath the control board, in which six gate-driver circuits for the auxiliary IGBTs are built. This layout results in a short distance between the auxiliary switches and their

gate drivers. The height of the control board is limited to a certain height to allow the cover of the chassis to be closed. Three resonant tanks, comprised of the resonant inductors and capacitors in series, are placed between the main devices and the auxiliary device.

As discussed in Section 5.8, in order to reduce the parasitic effects, a laminated bus bar made of copper sheets is designed and built to connect the DC capacitors and the three main IGBT modules, and another laminated bus bar made of PCB is designed to connect the "six-pack" auxiliary IGBT module. These two bus bars are interconnected as a unit and they cover the power stage. The stray inductance caused by the layout is counted into the total desired resonant inductance, and the lengths of the three-phase connections should be equal in order to balance the stray inductance.

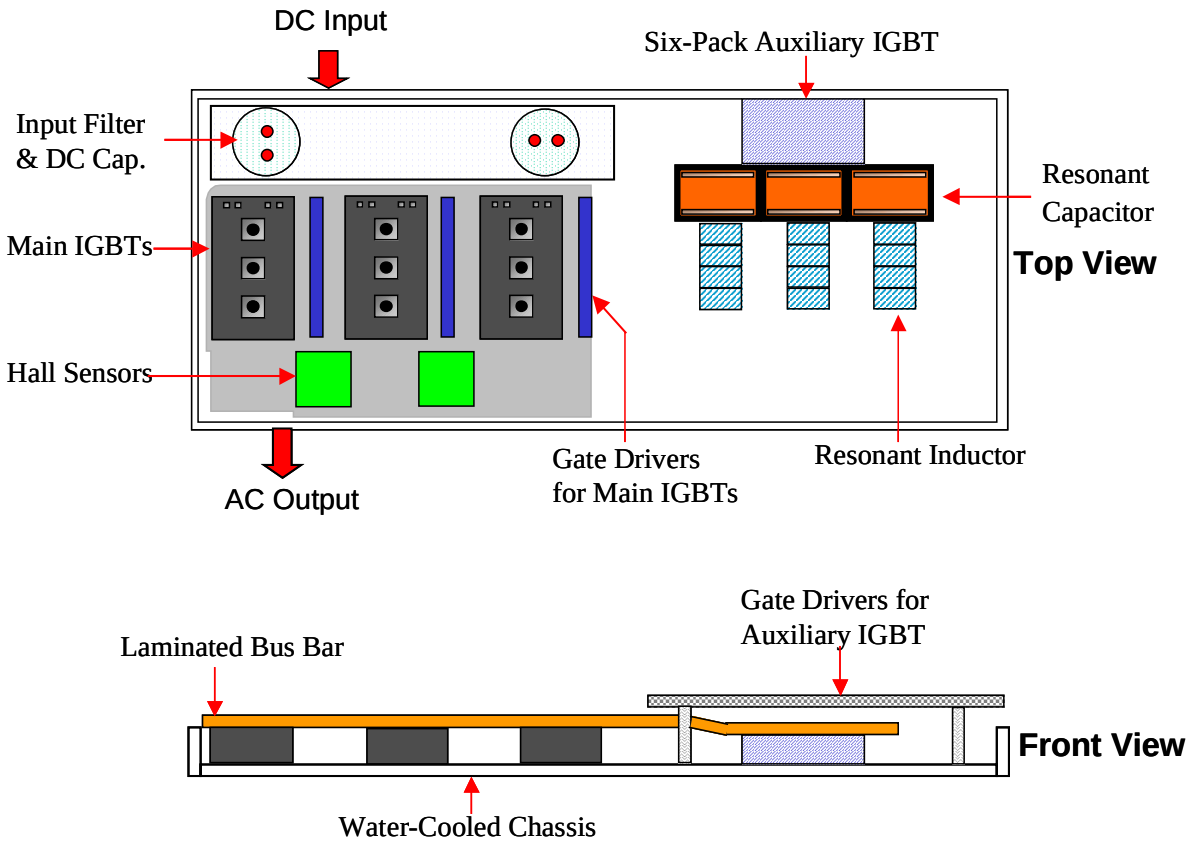

Figure 6.4. Layout design of the 55-kW six-switch ZV/ZCT inverter.

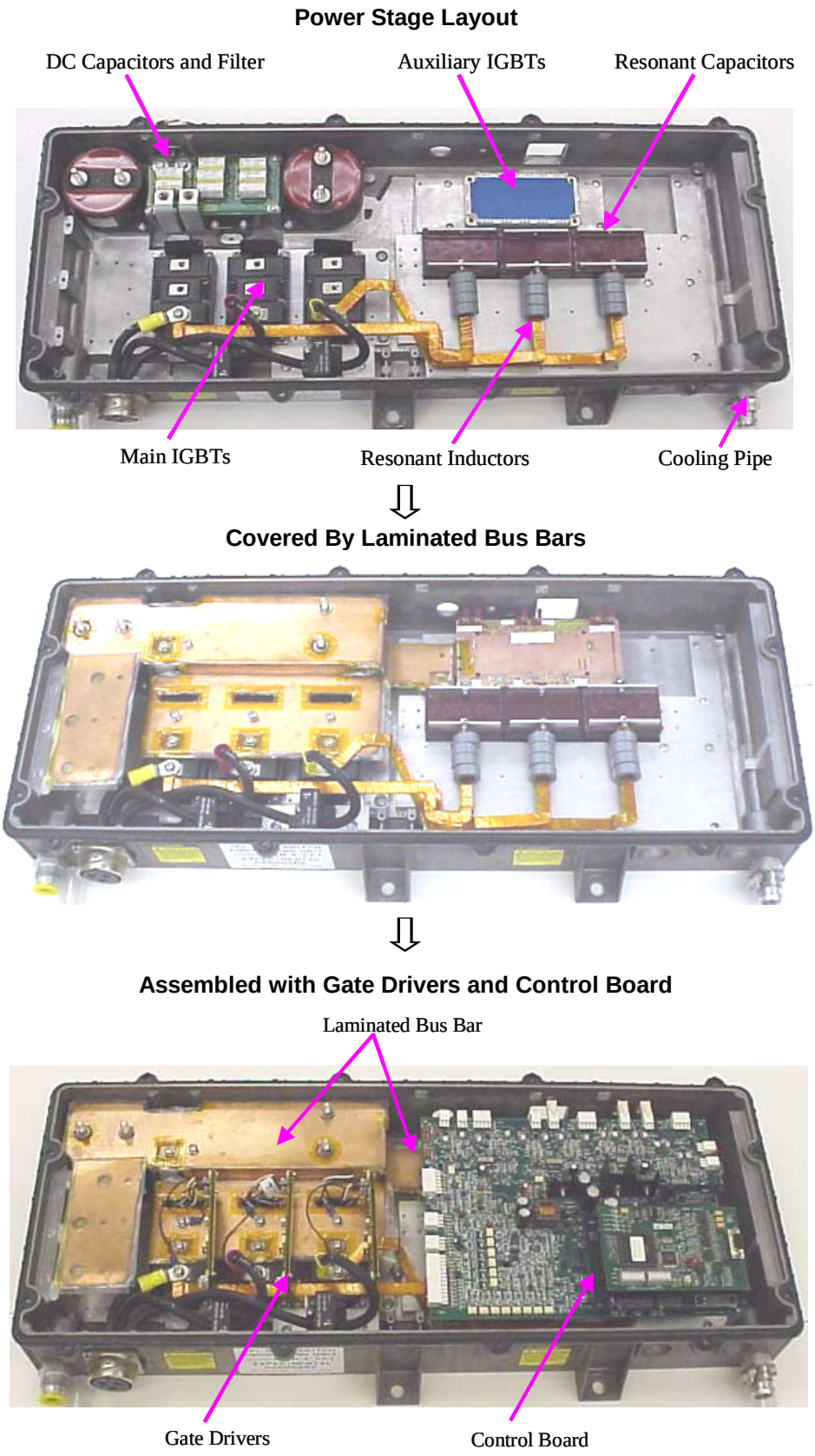

Figure 6.5. Photos of the 55-kW six-switch ZV/ZCT inverter hardware implementation.

Figure 6.6 illustrates the three-switch ZCT inverter layout, and Figure 6.7 shows photos of the hardware implementation. Similar to the six-switch ZV/ZCT inverter, the DC capacitors, filters and main IGBTs are mounted on the left side of the chassis, and a laminated bus bar interconnects and covers the power stage. The major difference in the layout, however, is that all the auxiliary devices and components are located only on the left side of the chassis, which saves significant space on the right side. Each auxiliary switch package, which consists of an IRG4ZC70UD 100-A/600-V IGBT with an IR60EPF06 60-A/600-V diode and which is surface-mounted on an IMS board, is located adjacent to the corresponding main IGBTs. The resonant tank for each phase is also located adjacent to the corresponding main IGBTs. On top of the laminated bus, the gate drivers for both main and auxiliary switches are mounted on a steel plate. This also results in a short distance from the switches to their gate drivers, and can reduce EMI.

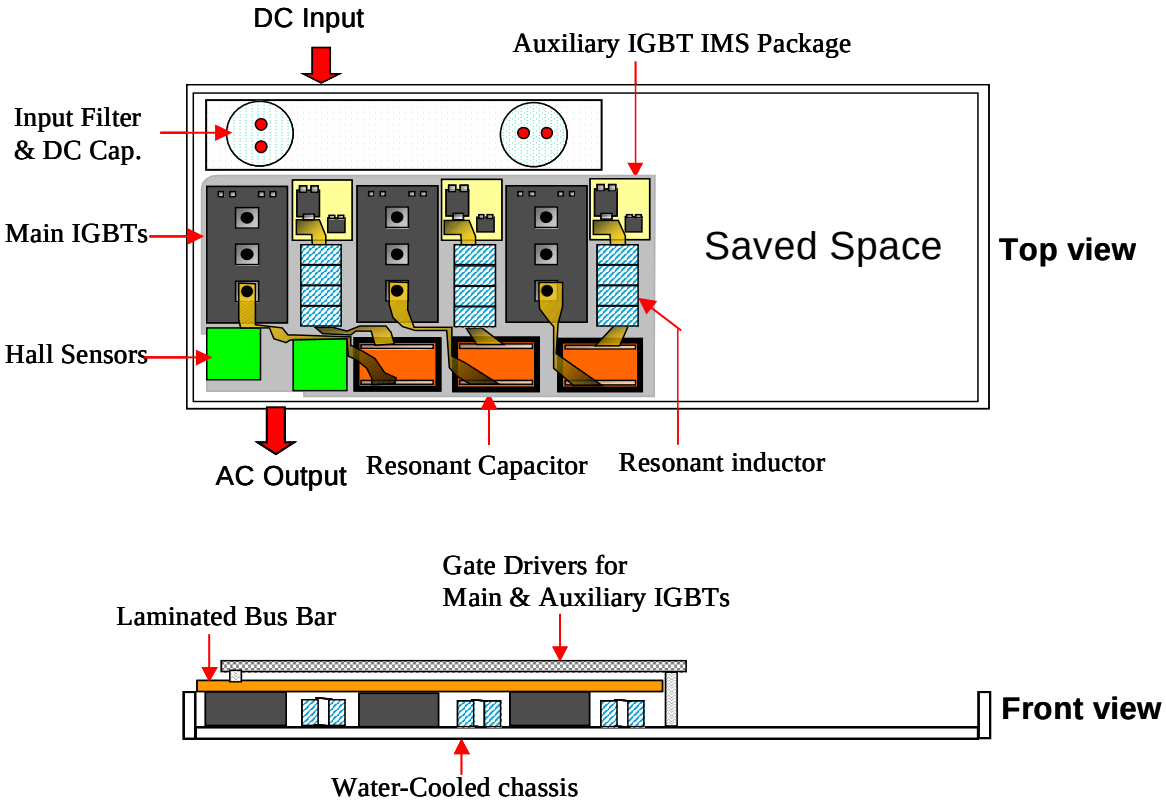

Figure 6.6. Layout design of the 55-kW three-switch ZCT inverter.

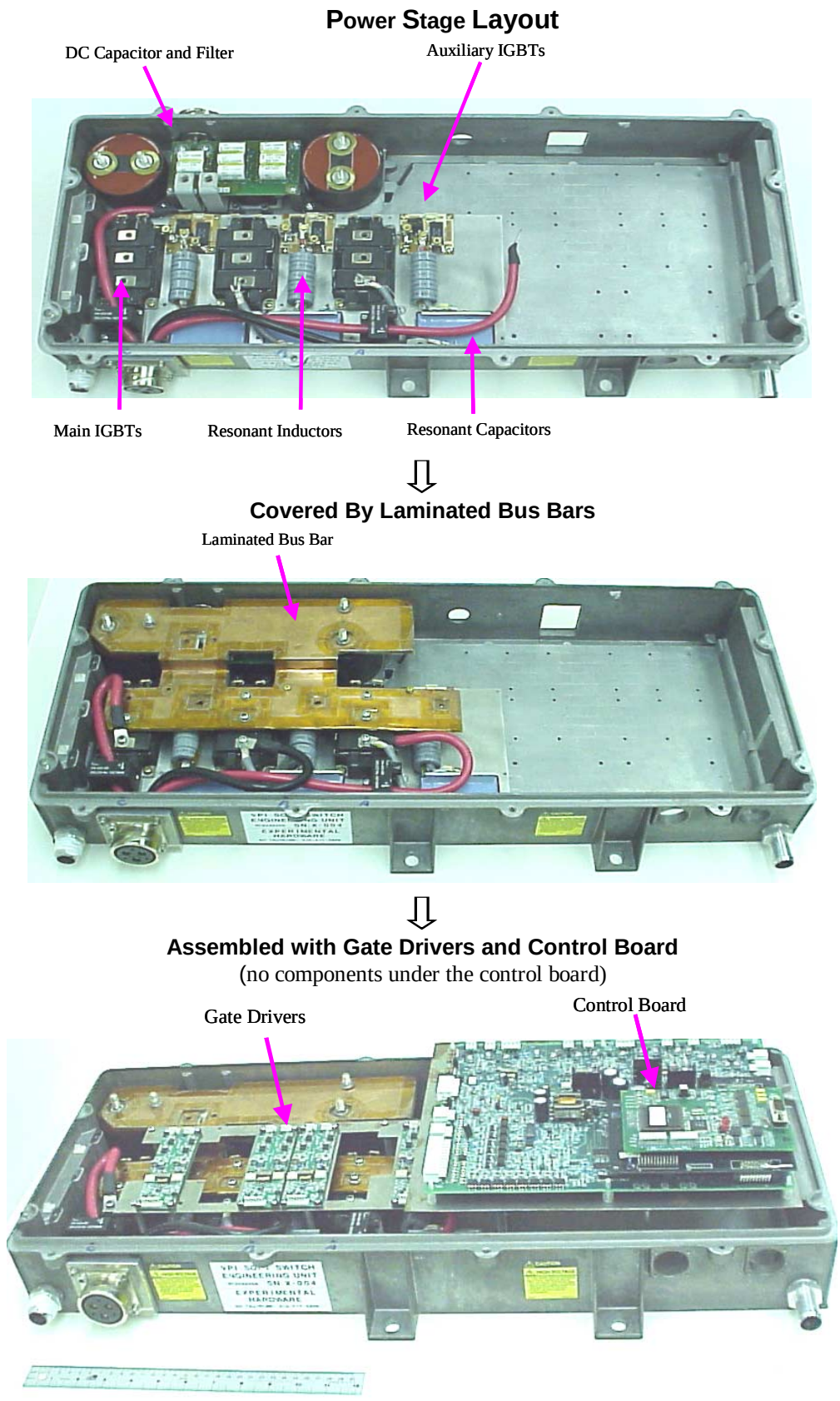

Figure 6.7. Photos of the three-switch ZCT inverter hardware implementation.

6.1.3. Complexity Comparison

Since the issues of cost, quality and reliability are difficult to judge, indirect measures of the 55-kW prototypes are compared, as shown in Table 6.1. This table compares the numbers and ratings of all devices and components that are actually used in the implementations, and the overall inverter sizes. In addition to the six-switch ZV/ZCT and the three-switch ZCT inverters, a 55-kW ARCP ZVT inverter that is designed and built to the same set of requirements with identical mechanical chassis [F18] [F19] is also compared.

Table 6.1.
Complexity Comparison of Three 55-kW Soft-Switching Inverter Prototypes

	ARCP ZVT	Six-Switch ZV/ZCT	Three-Switch ZCT
Main IGBTs	Three 300-A/600-V Half-Bridge (MG300J2YS50)	Same as the Left	Same as the Left
Auxiliary IGBTs	Six 100-A/600-V Discrete (IRG4ZC70UD)	One 150-A/600-V Six-Pack (BSM150GD60DLC)	Three 100-A/600-V Discrete (IRG4ZC70UD)
Discrete Auxiliary Diodes	Not Used	Not Used	Three 60-A/600-V (IR60EPF06)
Resonant Inductors	Three, 1 μH	Three, 0.6 μH	Three, 0.85 μH
Resonant Capacitors	Six, 0.22-μF/600-V	Three, 1-μF/630-V	Three, 0.625-μF/1000-V
Additional Saturable Inductors	Three	Not Used	Not Used
Additional Clamping Diodes	Six	Not Used	Not Used
Additional Capacitors across C_1 and E_2 of Main IGBTs	Not Used	Three, 1-μF/600-V	Three, 1-μF/600-V
Total DC Capacitance	4600 μF	300 μF	300 μF
Overall Size	65 cm x 27 cm x 7 cm	60 cm x 27 cm x 7 cm	39 cm x 27 cm x 7 cm

In the auxiliary IGBT modules for these three inverters, there are built-in anti-parallel diodes. In addition, for the three-switch ZCT, three discrete auxiliary diodes are required, as the topology shown in Figure 3.3. Besides the components required in the theoretical topology shown in Figure 1.5, in each phase of the ARCP inverter, one additional saturable inductor is used to suppress the voltage spikes across the auxiliary devices that occur due to the reverse-recovery current, and two additional clamping diodes are used to protect the auxiliary devices from over voltage. On the other hand, in both ZCT inverters, the voltage stress across an auxiliary switch is clamped by its opposite diode, so no additional components are needed for the over voltage protection. In the ARCP inverter, six snubber capacitors, serving as the resonant capacitors, are connected across the collector and emitter of each of the main IGBTs. In both ZCT inverters, resonant capacitors are connected in series with the resonant inductors. This allows space for one additional high-frequency capacitor to be connected across the C_1 and E_2 terminals of each main IGBT module to absorb some high-frequency ringing in the DC bus. Because the ARCP inverter requires a midpoint in the DC bus, its total DC capacitance is much larger than both ZCT inverters. Overall, the three-switch ZCT inverter has the simplest structure and smallest size. It reduces the size by about 35% from that of the six-switch ZV/ZCT, and by about 40% from that of the ARCP inverter. In addition to reducing the number of auxiliary switches (and their gate drivers) by half, the three-switch ZCT inverter is essentially immune to the shoot-through failure in the auxiliary switches, which enhances its reliability. As a result, the conventional de-sat sub-circuits in the auxiliary gate drivers are removed. As shown by practical experience, the de-sat sub-circuits in the auxiliary circuits of both the six-switch ZV/ZCT and ARCP inverters are prone to being falsely triggered. Therefore, the simplification of the gate drivers makes the three-switch ZCT inverter less susceptible to noises.

6.2. Closed-Loop Dynamometer Tests and Evaluation

6.2.1. Test Setup

Since the ZCT inverters are designed with piggyback structures, the dynamometer test setup is similar to that for a hard-switching inverter. The dynamometer consists of two motors, batteries, and control and measuring equipments, as shown in Figure 6.8. These two motors are oil-cooled squirrel-cage induction motors rated at 35 kW, with maximum speed of 14000 rpm, and maximum torque of 190 N-m at 6435 rpm. They are connected with a gear-coupling ratio of 4.9. The motor under test is in the torque-controlled mode, driven by the ZCT inverter under test. The load motor is in the speed-controlled mode, driven by a conventional hard-switching inverter. Installed on the dynamometers, all parts of both ZCT inverters, including the control boards, hall sensors, input filters, DC capacitors, etc., fit well into the chassis provided by GM. The cover of the chassis can therefore be closed so that further vehicle tests can be performed. The battery packs are connected to the DC input of the inverters without additional bulky DC capacitors. Outside of the chassis, there are no extra devices or components that are indispensable parts of the ZCT inverters.

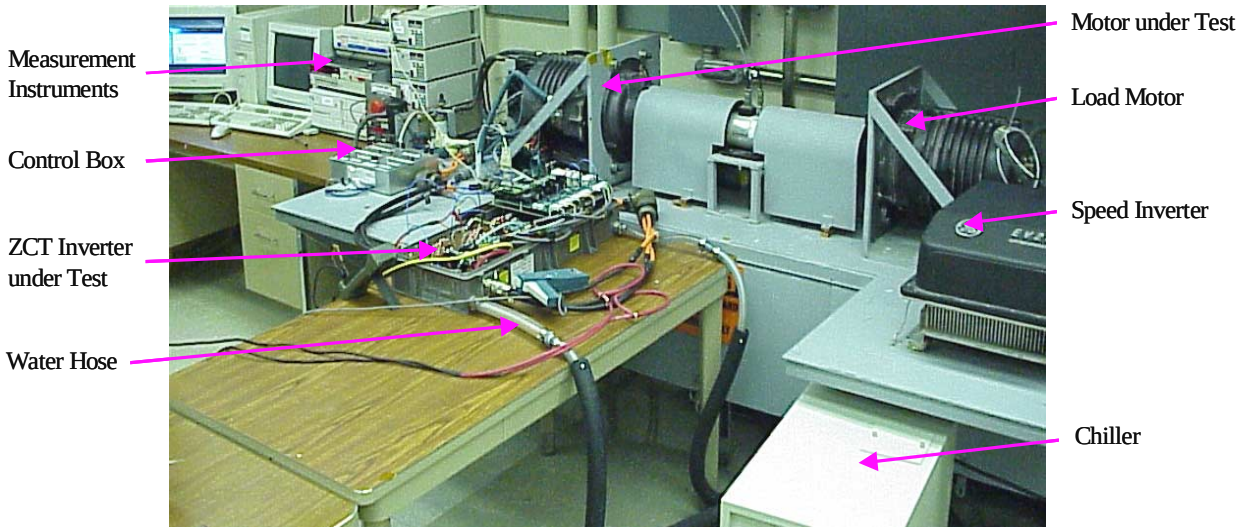

(a)

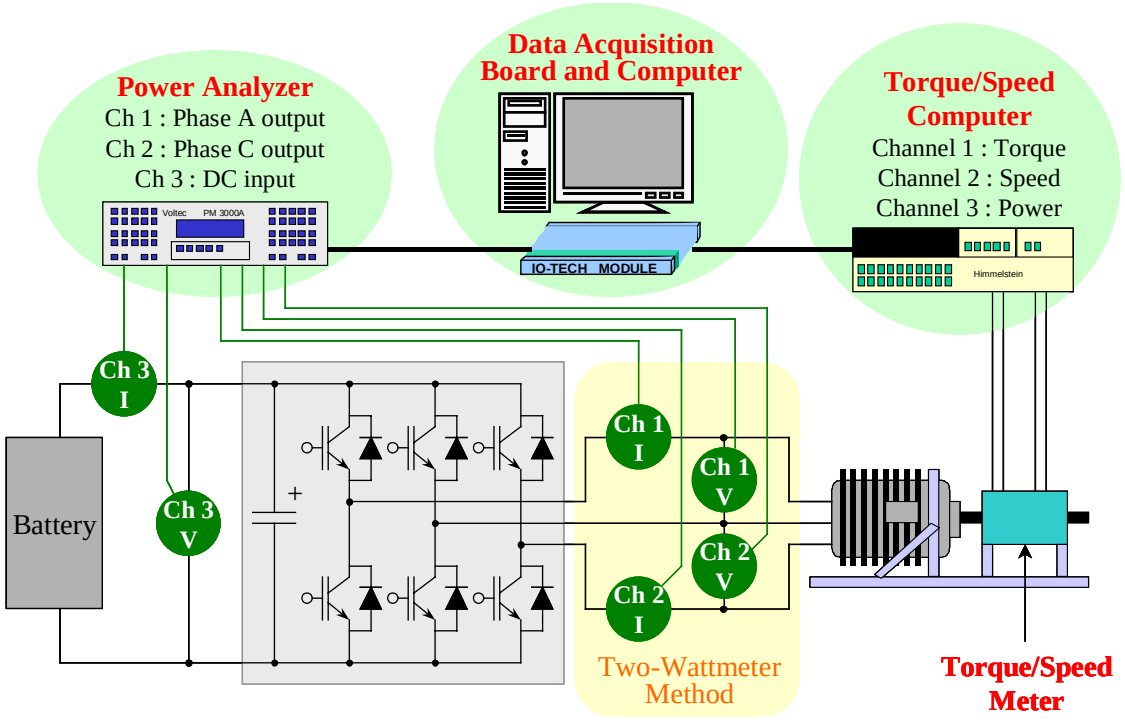

(b)

Figure 6.8. The dynamometer testing setup:
(a) A photo of overall structure with a tested ZCT inverter; and
(b) measurement equipment connections.

6.2.2. Dynamometer Characterization of the ZCT Inverter Operations

Both ZCT inverter prototypes have been tested with the dynamometer. The maximum power reaches 48 kW at the DC input and 40 kW at the induction motor shaft. The desirable ZCT soft transitions are realized together with closed-loop motor drive functions. The switching frequency is 10 kHz, the DC bus voltage is 325 V, and water-cooling is used.

6.2.2.1. Electrical Characterization

A. Line-Cycle Operations

Figure 6.9 shows line-cycle waveforms of both ZCT inverters operating under an output power of about 47 kW. The waveforms are for the load currents I_{Load} of phases A and B, and the upper main switch voltage v_{ce} and resonant current i_x of phase A. It can be seen that both inverters produce balanced sinusoidal three-phase currents, which indicates that the soft transitions do not affect fundamental inverter operations. Thanks to the ZCT operation, there is almost no overshoot or high-frequency ringing in the switch voltage waveforms during the line cycles. It can be seen that, as a result of threshold control, no resonant current is produced at the zero-crossing regions of the load current. As discussed in Chapter 5, the threshold control disables the auxiliary switches when the instantaneous load current is below a specified value and can minimize the total inverter losses through a proper trade-off between the switching and conduction losses. The threshold is set to be 50 A for both inverters during the tests.

It is also observed that between alternate half-line cycles, the envelope of the resonant current is symmetrical in the six-switch ZV/ZCT inverter (Figure 6.9(a)), but is asymmetrical in the three-switch ZCT inverter (Figure 6.9(b)). This asymmetry reflects the different ZCT operational stages and control timings under different load current commutation patterns. In

addition, due to the six-step SVM used and the high power factor of the motor drive, there is no switching action when the load current is at its highest; this further reduces the switching losses.

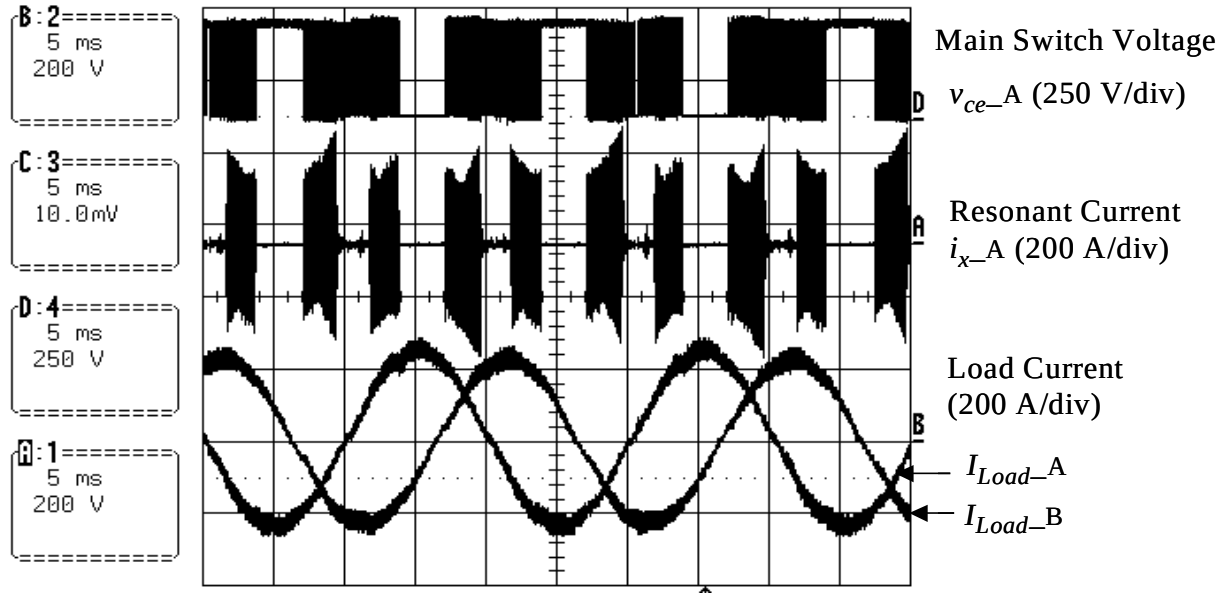

(a)

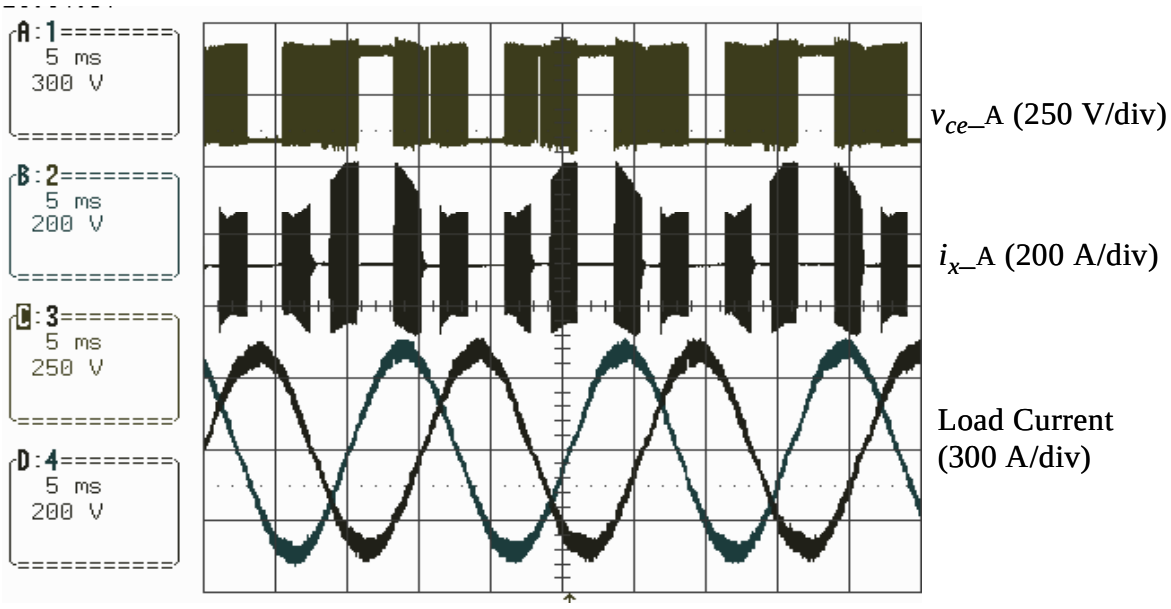

(b)

Figure 6.9. Line-cycle waveforms with the dynamometer test under an output power of around 47 kW (5 ms/div):
(a) six-switch ZV/ZCT inverter; and
(b) three-switch ZCT inverter.

B. Switching-Cycle Operations

Since the soft transition is symmetrical between alternate half-line cycles in the six-switch ZV/ZCT inverter, its switching-cycle waveforms need to be investigated for $I_{Load}>0$ only, as shown in Figure 6.10. On the other hand, for the three-switch ZCT inverter, its switching-cycle waveforms for both $I_{Load}>0$ and $I_{Load}<0$ need to be investigated, as shown in Figure 6.11— For $I_{Load}>0$, in which I_{Load} is conducted through the top IGBT and bottom diode, the main switch voltage v_{ce} waveform is measured across the top main IGBT; for $I_{Load}<0$, the v_{ce} waveform is measured across the bottom main IGBT. It is found that the amplitude of I_{Load} at turn-on is smaller than that at turn-off. This is due to the current ripple associated with finite inductance of the motor stator winding.

Because of the laminated bus bars used, the switch current cannot be measured directly; however, the i_x and I_{Load} waveforms are indications of soft transitions. Both Figures 6.10 and 6.11 show similar traits. At turn-on, i_x reaches I_{Load}, indicating that the current in the main diode has already been diverted to the auxiliary circuit when the opposite main switch is turned on. Particularly, the switch voltage v_{ce} in Figure 6.10 is reduced to near zero before the switch is turned on. Thus, the diode reverse-recovery current and turn-on loss are reduced significantly. At turn-off, i_x exceeds I_{Load}, indicating that the anti-parallel diode across the switch is conducting the surplus current when its gate signal is removed, and that the switch is turned off under zero current. Almost no overshoot is observed in the switch voltage waveforms within the switching cycles. It can also be observed that at the moment when v_{ce} rises to the DC bus voltage at turn-off, the resonant current actually decreases slightly below the level of the load current for a short interval. As discussed in Section 5.8, this is due to the reverse-recovery current that occurs after the surplus current through the anti-parallel diode falls to zero.

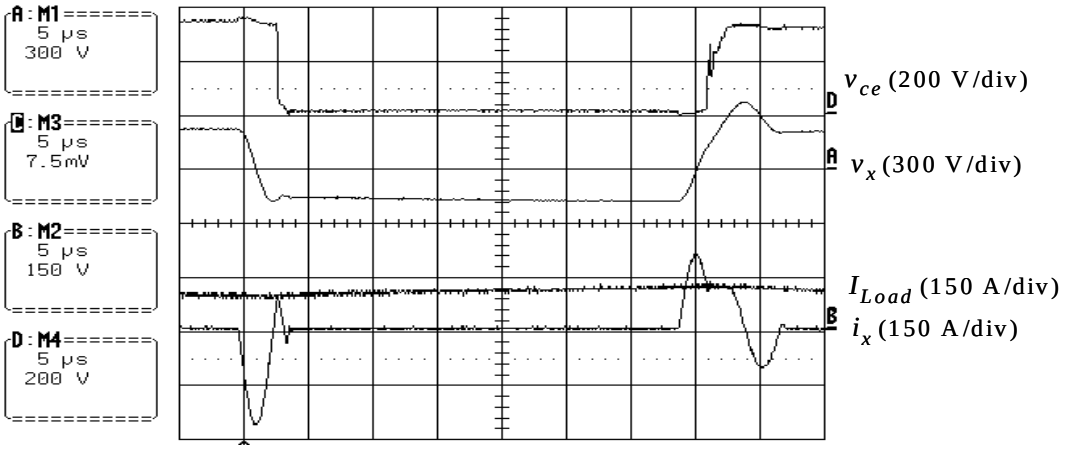

Figure 6.10. Switching-cycle waveforms of the six-switch ZV/ZCT inverter with the dynamometer test.

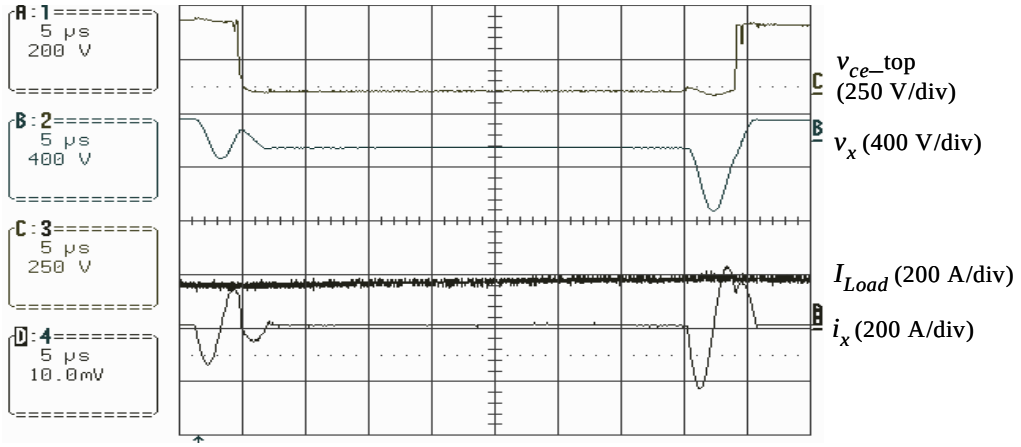

(a)

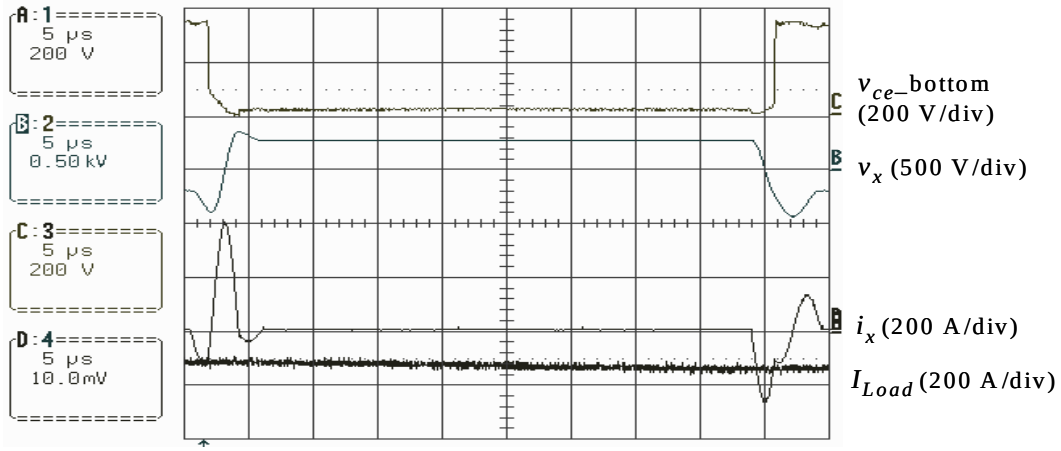

(b)

Figure 6.11. Switching-cycle waveforms of the three-switch ZCT inverter with the dynamometer test, under different load current directions: (a) I_{Load} >0; and (b) I_{Load} <0.

C. State-Plane Visualizations

Figures 6.12~14 show the state-plane trajectories of the ZCT inverters, which are obtained by simultaneously measuring the resonant current i_x and capacitor voltage v_x at the X-Y display mode of the oscilloscope. The switching-cycle trajectories shown in Figures 6.12(a) and 6.13 match the theoretical ones presented in Chapters 2 and 3, which provide visual aids to derive the design methods in Chapter 5. The *line*-cycle trajectory shown in Figures 6.12(b) and 6.14 is composed by all of the *switching*-cycle sub-trajectories within this line cycle, and the trajectory in one complete line cycle is the combination of the trajectories of alternate half-line cycles. Clearly, the trajectories between alternate I_{Load} directions are symmetrical in the six-switch ZV/ZCT inverter, but are asymmetrical in the three-switch ZCT inverter. Moreover, the line-cycle trajectories visualize the dynamic change of resonant voltage and current stresses in the auxiliary circuits under the bi-directional load current. It can be seen that in both ZCT inverters, the transitions between alternate half-line cycles are smooth, and there is no over current or over voltage within either complete line cycles.

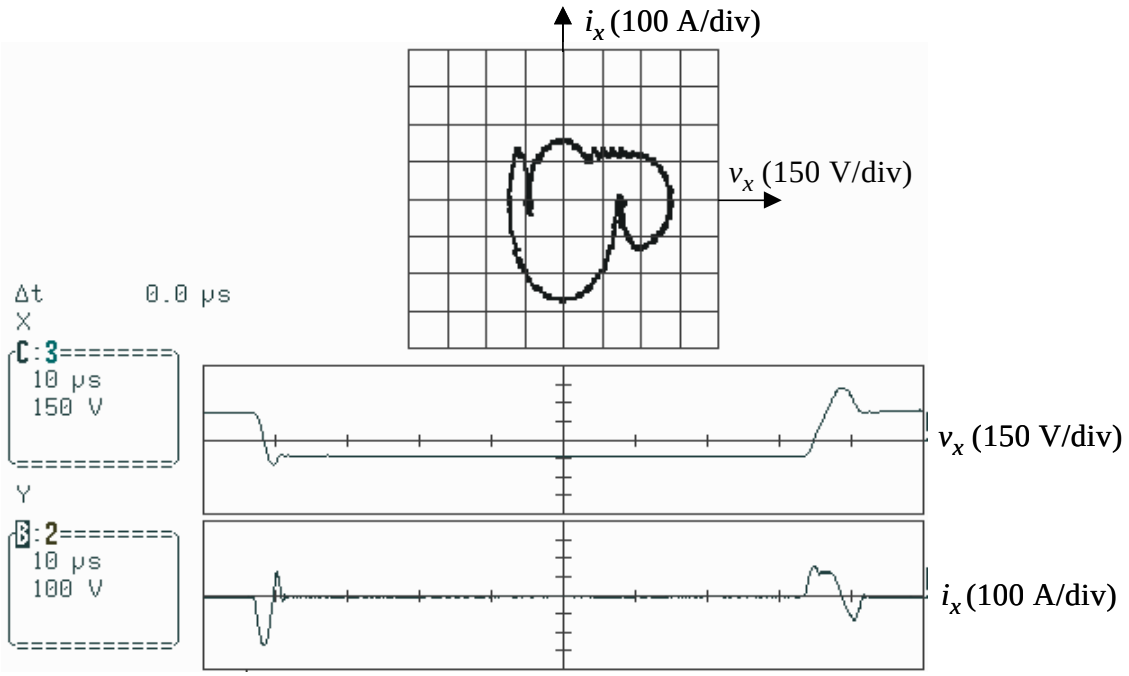

(a)

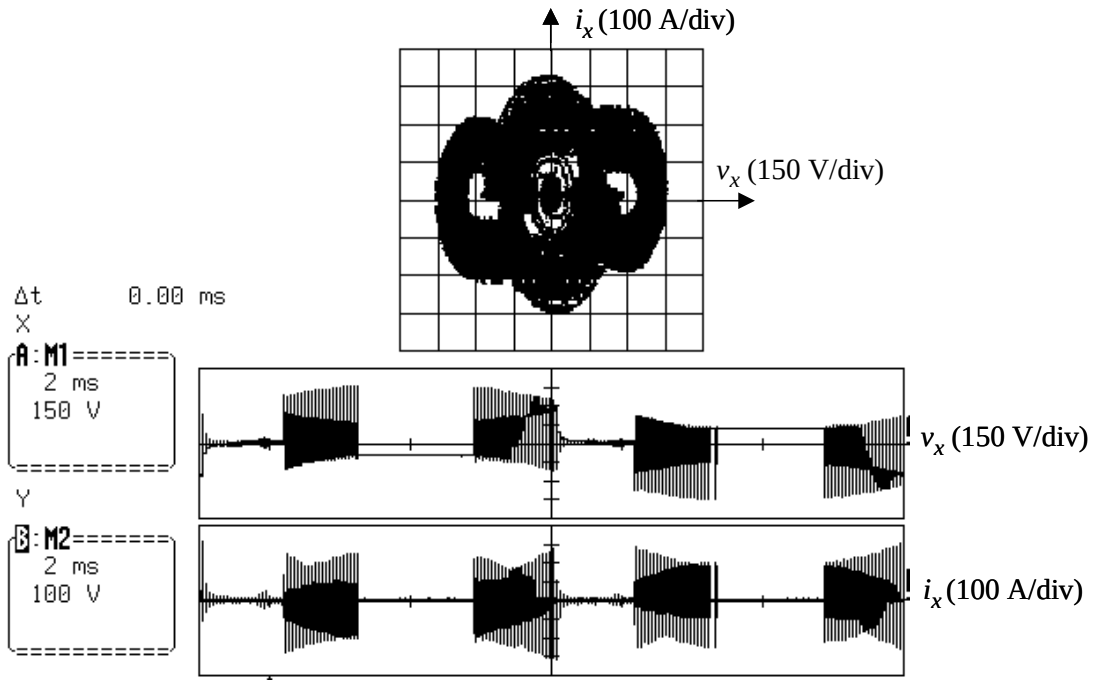

(b)

Figure 6.12. Measured state-plane trajectories of the six-switch ZV/ZCT inverter with the dynamometer test:
(a) *switching*-cycle trajectory; and
(b) *line*-cycle trajectory.

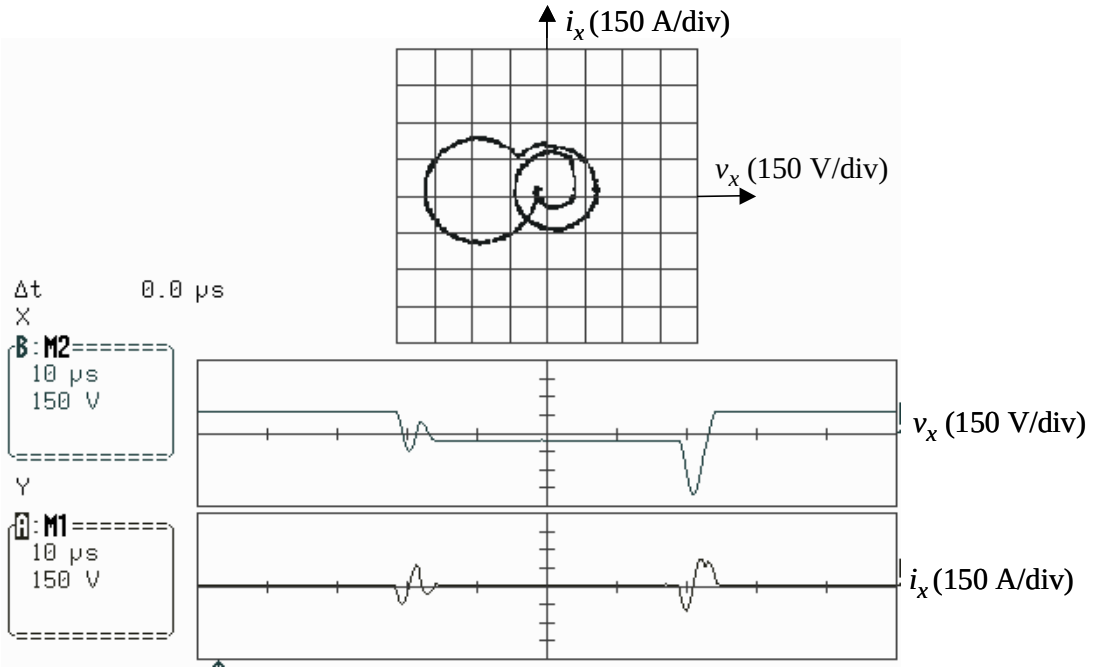

(a)

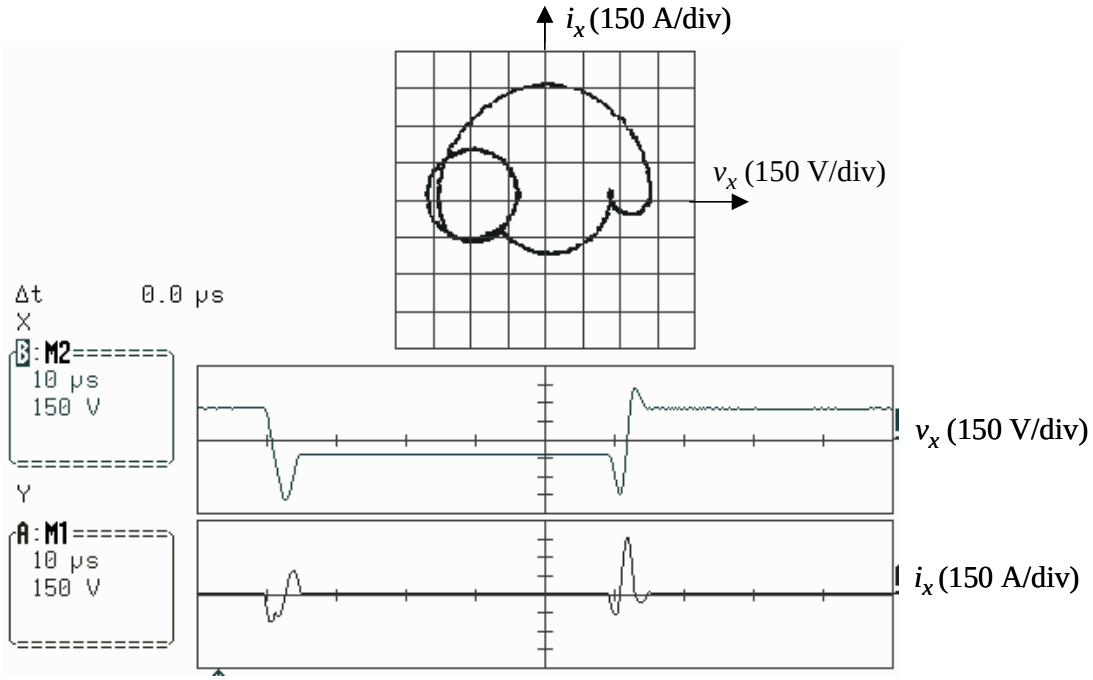

(b)

Figure 6.13. Measured *switching*-cycle state-plane trajectories of the three-switch ZCT inverter with the dynamometer test under different load current directions:

(a) I_{Load}>0; and (b) I_{Load}<0.

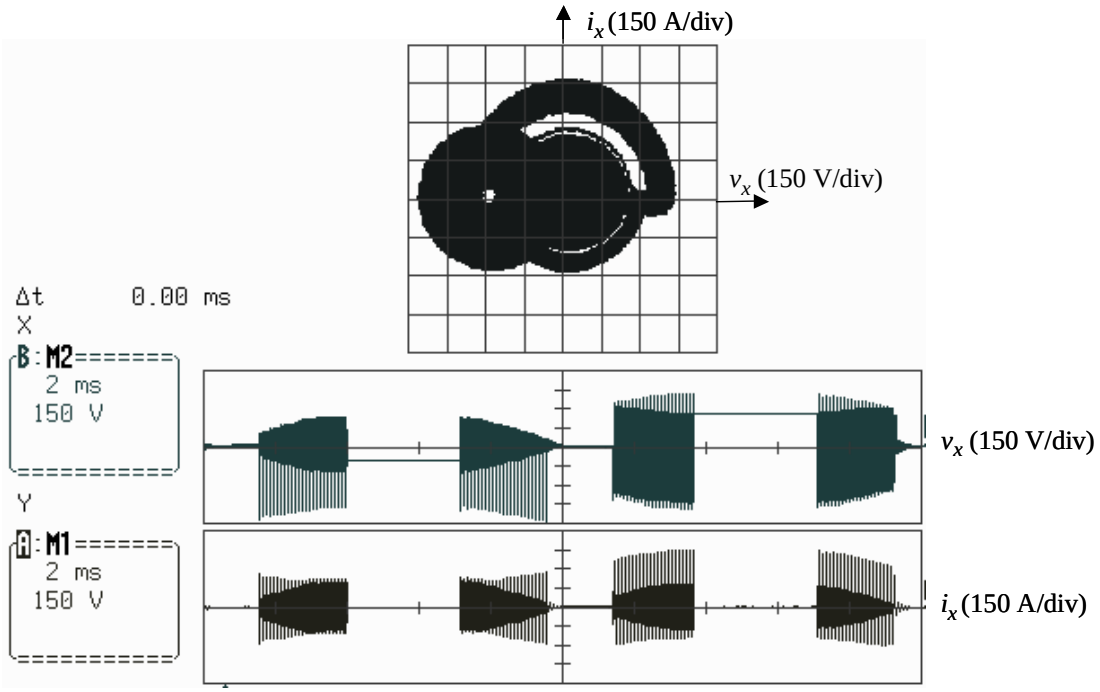

Figure 6.14. Measured *line*-cycle state-plane trajectory of the three-switch ZCT inverter with the dynamometer test.

D. DC-Link Voltage and Current

In both ZCT inverters, the total DC capacitance is 300 μF, generated by two 150-μF film capacitors in parallel. These two capacitors are provided together with the GM chassis as a common practice in hard-switching inverters for EV motor drives. As shown in Table 6.1, the 55-kW ARCP inverter that is designed with the same requirements uses an additional 4300 μF in the total DC capacitance, and a 55-kW RDCL inverter that is also designed with the same requirements must use an additional 5000 μF DC capacitance at heavy load conditions to stabilize the DC-link voltage [F7]. Thus, it is necessary to investigate if the 300-μF DC capacitance is adequate for ZCT inverter operations. As shown by the experimental waveforms in Figure 6.15, there is a ripple in the DC-link voltage V_{dc}, which is directly measured across one of the DC capacitors in the six-switch ZV/ZCT inverter. The ripple frequency is 10 kHz, which

corresponds to the switching frequency. The peak-to-peak amplitude of the ripple is measured at around 20 V under the heavy load condition, which is about 6% of the nominal DC input voltage. The three-switch ZCT inverter also shows a similar ripple in the V_{dc}. This ripple is insignificant and does not affect the fundamental inverter operations and ZCT soft transitions. As a result, no additional DC capacitance was used in the entire torque/speed range of the dynamometer tests. For further characterization, Figure 6.16 shows a waveform of the DC input current I_{dc}, which is measured between the battery packs and the DC capacitors in the six-switch ZV/ZCT inverter.

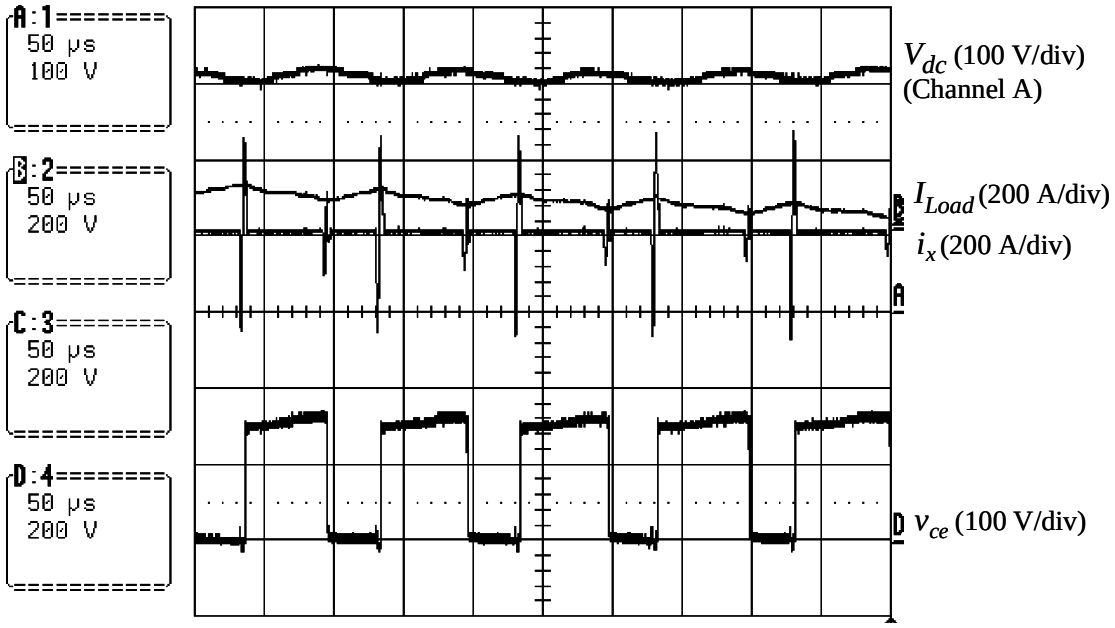

Figure 6.15. The DC-link voltage V_{dc} waveform of the six-switch ZV/ZCT inverter measured under an output power of about 47 kW (50 µs/div).

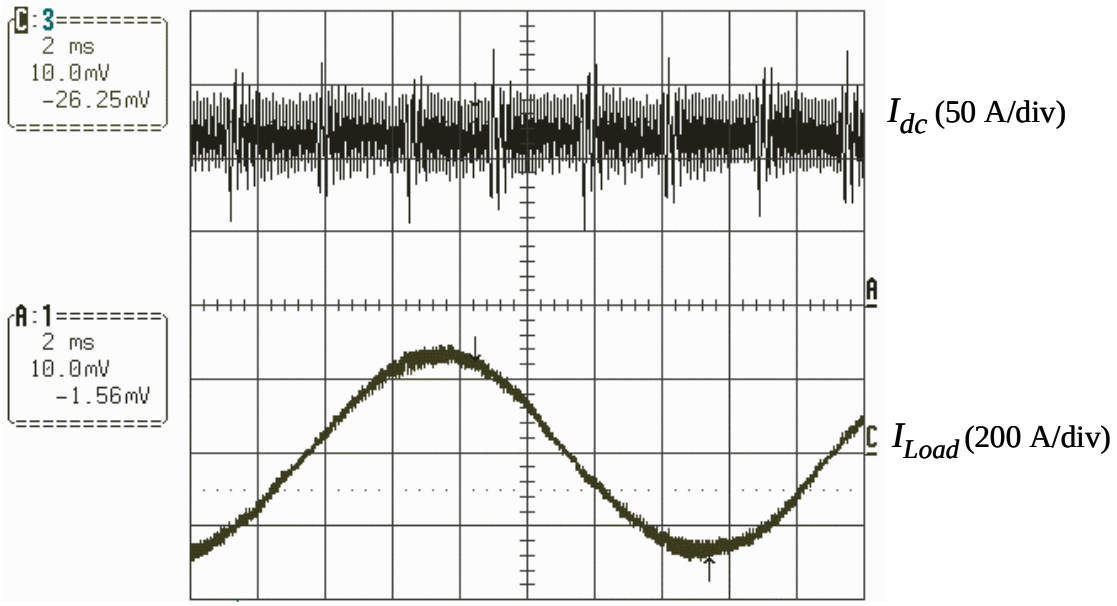

Figure 6.16. The measured DC input current I_{dc} waveform of the six-switch ZV/ZCT inverter with the dynamometer test (2 ms/div).

6.2.2.2. Thermal Characterization

Temperature rises are important indicators of inverter operations. They can also indirectly expose the power dissipation in the auxiliary circuits and verify the auxiliary circuit design. During the dynamometer tests, no devices or components showed any signs of over-heating, abnormality or failure. Table 6.2 lists the temperatures of major devices and components of the two ZCT inverters; these measurements are taken after the main IGBT temperatures become stable when the inverters operate under a 200-A peak load current, using a Raytek laser radiation non-contact thermal probe. Although they may need further calibration, the measured temperatures can reflect the basic thermal stresses. It can be seen that the temperature rises of the auxiliary IGBTs are quite low: about 2°C from the heat sink to the case in the six-pack auxiliary IGBT module in the six-switch ZV/ZCT inverter, and about 4°C from the heat sink to the case in the discrete auxiliary IGBTs in the three-switch ZCT inverter. The detailed thermal analysis and modeling of the 55-kW prototypes, such as extraction of the actual case-to-heat-sink thermal

resistance, are complicated and beyond the scope of this dissertation, but certainly these low temperature rises indicate small amounts of power dissipation in the auxiliary devices.

Moreover, the measured temperature rises of the resonant inductor cores are close to those predicted in Section 5.4.2. Because of the difficulties in precisely predicting the core temperature rises (which depends heavily on environmental factors such as ambient temperature, airflow, and the physical layout of the prototypes), the difference between the predicted and measured temperature rises are within an acceptable range. This result verifies the design and analysis of the resonant inductors.

Table 6.2.
Measured Temperatures of the 55-kW ZCT Inverter Prototypes
(Conditions: 200-A peak load current, 14°C cooling water, 24°C heat sink, and 25°C ambient)

	Six-Switch ZV/ZCT	Three-Switch ZCT
Main IGBT Case	38°C (MG300J2Y50, 300-A/600-V)	40°C (Same as Left)
Auxiliary IGBT Case	26°C (One BSM150GD60DLC, 150-A/600-V, six-pack)	28°C (Three IRG4ZC70UD, 100-A/600-V, discrete)
Resonant Inductor Cores	58°C (Four MPP 55894 cores, one turn)	49°C (Seven MPP 55894 cores, one turn)
Resonant Capacitors	32°C (Metalized polypropylene)	33°C (Same material as left)

6.2.3. Steady-State Tests and Efficiency Evaluation

6.2.3.1. Test Results

For steady-state measurement and evaluation, 14 test points are selected based on typical EV driving cycles. Figure 6.17 shows the 14 test points in the torque-speed plane, which cover 1920~9470 rpm and 5~101 N-m. The maximum power occurs at 3790 rpm/101 N-m, which is

about 48 kW at the DC input and 46.5 kW at the inverter output. The minimum power occurs at 3790 rpm/5 N-m, which is about 2.9 kW at the DC input and 2.7 kW at the inverter output.

Both ZCT inverters are tested under the 14 points. Figures 6.18 and 6.19 show their measured load current and resonant current waveforms under different speed and torque conditions, respectively. It can be seen that the load current waveforms are quite close to sinusoidal at all points, which demonstrates that the ZCT implementations do not interfere with the fundamental control functions of the closed-loop motor drive system within the entire drive cycle. Otherwise, the load current waveforms would be distorted, and the system would even become unstable at certain points. The waveforms also clearly show the effect of threshold control. For Figures 6.18(a) and 6.19(a), which show the torque at its smallest, the peak load current is less than the threshold (50 A), so during the entire line cycle the auxiliary switches are disabled and no resonant current is produced. For other test points, within the intervals when the instantaneous load current is less than the threshold, the auxiliary switches are again disabled, and no resonant current is produced either.

Tables 6.3 and 6.4 list the test results of the two ZCT inverters. Shown in the tables are the operating conditions (voltage, current, power factor, line frequency, and modulation index), measured powers (DC input, AC output, and motor output), and efficiencies (inverter, motor, and system). The DC input power and AC output power are measured via a Voltech PM3000 power analyzer, and the motor output power is calculated from the product of the speed and torque. The induction motor is a two-pole motor, so the line frequency is calculated by *speed/60*. The modulation index is calculated by Equation (5.2). The range of the measured inverter efficiencies is around 92~96.5%, and with higher speed and/or higher torque, the efficiencies tend to increase.

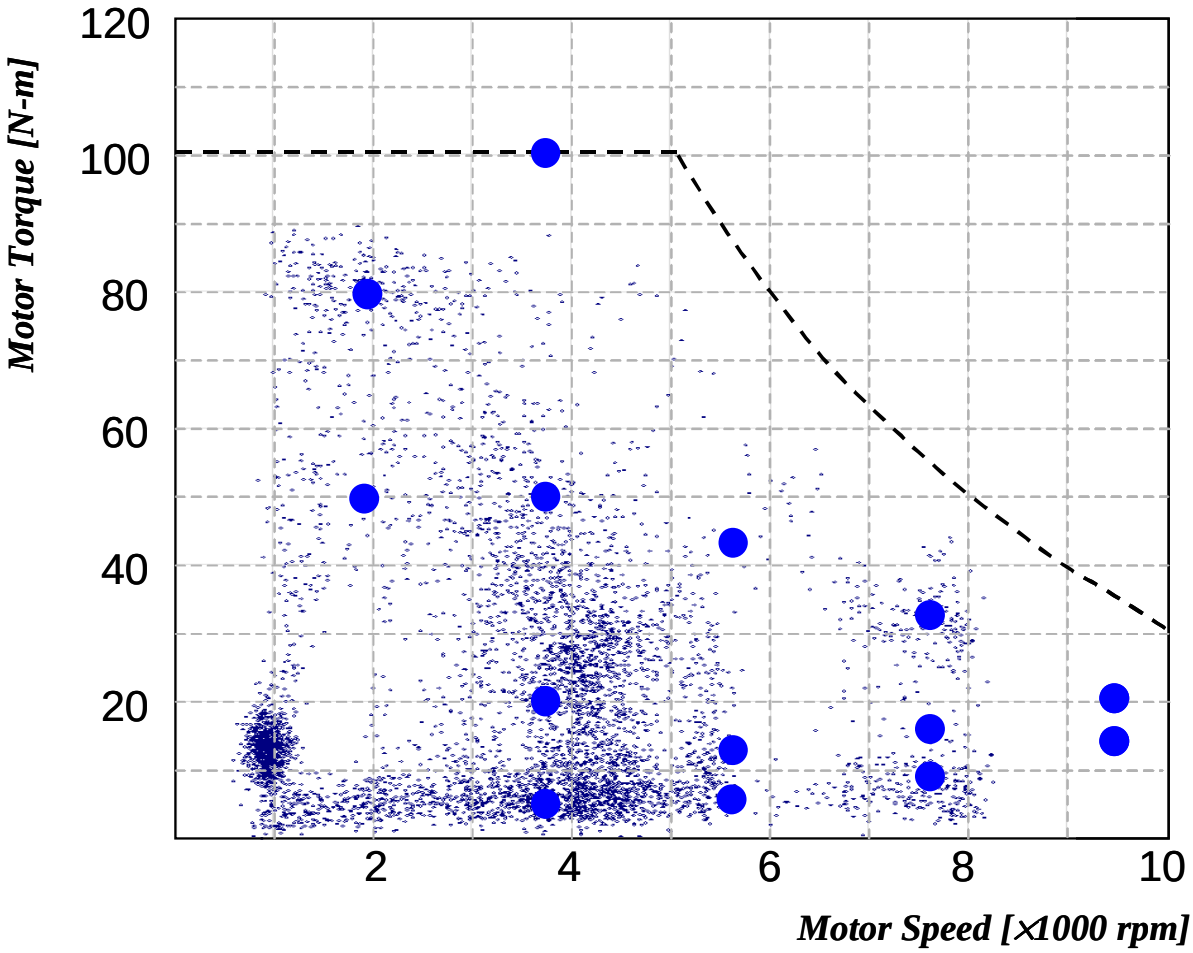

Figure 6.17. The 14 dynamometer test points (●) mapping into a typical EV driving-point density on the torque-speed plane.

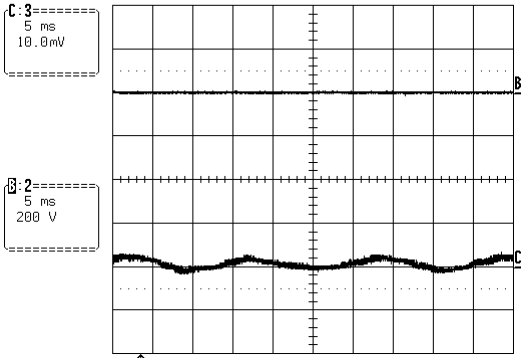

(a) S=3840 rpm, T=5 N-m.

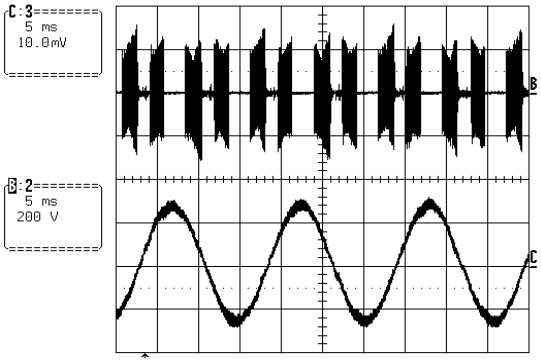

(b) S=3760 rpm, T=101 N-m.

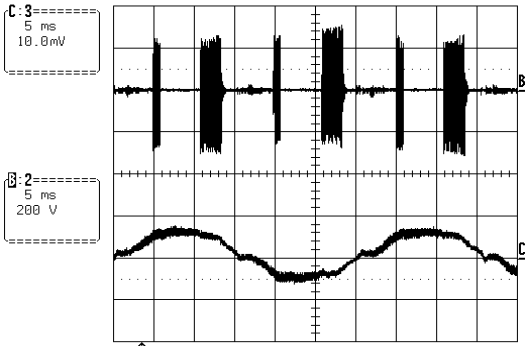

(c) S=1950 rpm, T=51 N-m.

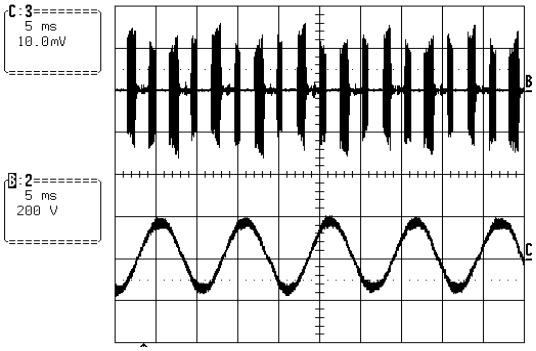

(d) S=5695 rpm, T=42 N-m.

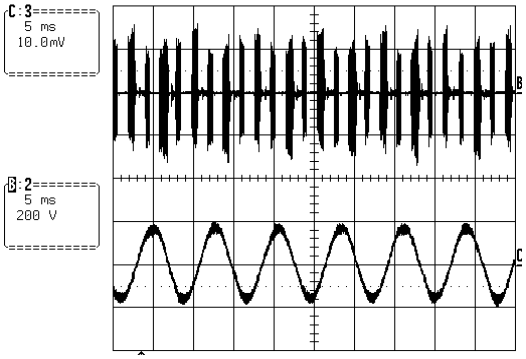

(e) S=7570 rpm, T=31 N-m.

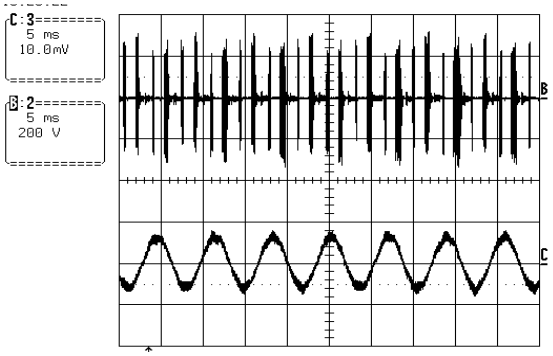

(f) S=8585 rpm, T=20 N-m.

Figure 6.18. Measured current waveforms of the *six*-switch ZV/ZCT inverter under different speed/torque (S/T) points during the steady-state dynamometer test.

Channel C (top): resonant current (200 A/div);
Channel B (bottom): load current (200 A/div);
Time (5 ms/div)

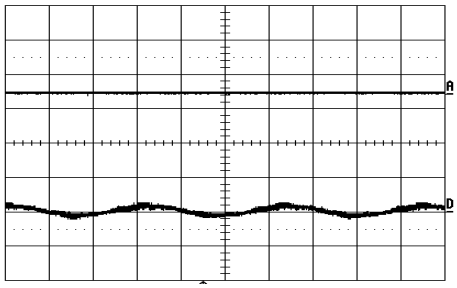

(a) S=3770 rpm, T=5 N-m.

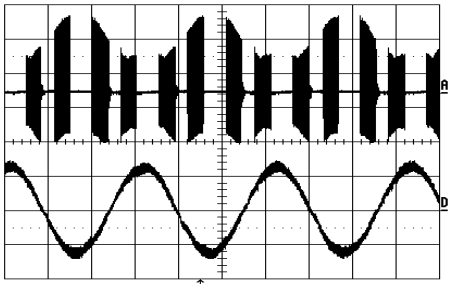

(b) S=3770 rpm, T=101 N-m.

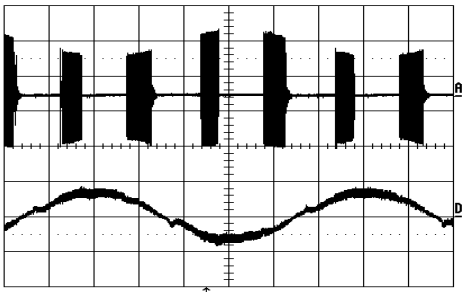

(c) S=1920 rpm, T=50 N-m.

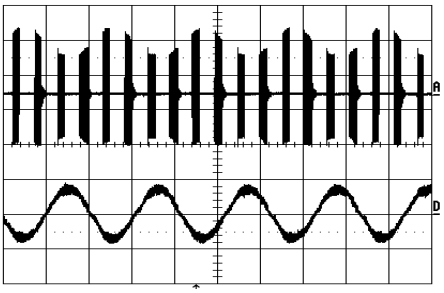

(d) S=5680 rpm, T=42 N-m.

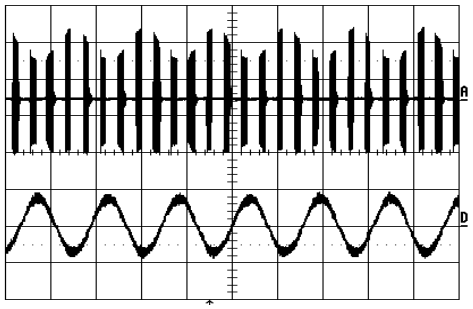

(e) S=7550 rpm, T=31 N-m.

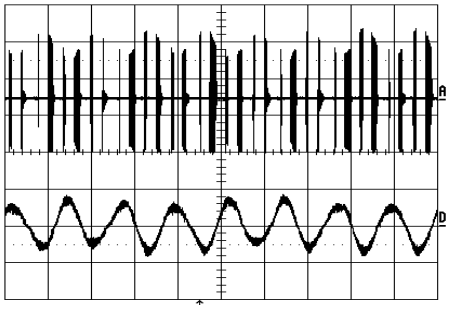

(f) S=9470 rpm, T=20 N-m.

Figure 6.19. Measured current waveforms of the *three*-switch ZCT inverter under different speed/torque (S/T) points during the steady-state dynamometer test.

Channel A (top): resonant current (200 A/div);
Channel D (bottom): load current (200 A/div);
Time (5 ms/div)
(The load current waveform in Figure 6.19(f) has slight low-frequency oscillation. This is probably due to increasing severe mechanical vibration of the encoder that measures the shaft speed. The vibration worsens as the rotation of the rotor reaches its peak S=9470 rpm.)

Table 6.3.
Steady-State Test Results of the *Six*-Switch ZV/ZCT Inverter

(a) Measured Data

Test No.	Speed (rpm)	Torque (N-m)	DC Current [A]	AC Voltage [V]	AC Current [A]		Power Factor	DC Input Power [kW]	AC Output Power [kW]
					Total	Fund.			
1	1920	50.30	39.28	71.5	100.39	99.34	0.938	12.67	11.84
2	1918	80.59	65.49	75.8	156.47	155.58	0.954	21.14	19.78
3	3786	5.10	9.14	103.8	21.38	20.62	0.667	2.91	2.68
4	3782	20.54	30.18	109.5	52.58	51.65	0.922	9.74	9.32
5	3786	50.66	72.21	140.8	98.66	97.68	0.928	23.34	22.49
6	3779	101.57	149.80	153.2	184.24	182.05	0.942	48.30	46.48
7	5624	5.70	13.99	156.0	22.27	21.59	0.690	4.48	4.23
8	5626	12.02	26.25	137.2	37.50	36.63	0.907	8.47	8.13
9	5641	41.78	89.09	150.9	110.42	109.63	0.958	28.76	27.80
10	7512	10.09	29.24	173.1	33.65	32.91	0.900	9.42	9.09
11	7555	14.75	42.64	146.3	54.87	54.09	0.950	13.77	13.29
12	7570	31.79	92.64	149.9	116.27	115.48	0.951	29.88	28.85
13	9374	13.17	48.77	143.0	63.31	60.05	0.952	15.32	14.77
14	9455	20.54	76.88	149.0	97.16	95.36	0.946	24.48	23.63

(b) Calculated Values

Test No.	Speed (rpm)	Torque (N-m)	Line Frequency (Hz)	Modulation Index	Motor Output Power (kW)	Efficiency (%)		
						Inverter	Motor	System
1	1920	50.30	32.0	0.31	10.11	93.47	85.38	79.81
2	1918	80.59	32.0	0.33	16.27	93.58	82.28	77.00
3	3786	5.10	63.1	0.45	2.02	92.07	75.37	69.39
4	3782	20.54	63.0	0.48	8.14	95.64	87.33	83.52
5	3786	50.66	63.1	0.61	20.08	96.36	89.32	86.07
6	3779	101.57	63.0	0.67	40.20	96.24	86.49	83.24
7	5624	5.70	93.7	0.68	3.36	94.29	79.47	74.93
8	5626	12.02	93.8	0.60	7.08	96.02	87.15	83.68
9	5641	41.78	94.0	0.66	24.68	96.66	88.79	85.83
10	7512	10.09	125.2	0.75	7.93	96.48	87.30	84.23
11	7555	14.75	125.9	0.64	11.67	96.49	87.81	84.73
12	7570	31.79	126.2	0.65	25.20	96.54	87.36	84.33
13	9374	13.17	156.2	0.62	12.93	96.45	87.50	84.39
14	9455	20.54	157.6	0.65	20.34	96.51	86.10	83.09

Table 6.4.
Steady-State Test Results of the *Three*-Switch ZCT Inverter

(a) Measured Data

Test No.	Speed (rpm)	Torque (N-m)	DC Current [A]	AC Voltage [V]	AC Current [A]		Power Factor	DC Input Power [kW]	AC Output Power [kW]
					Total	Fund.			
1	1922	50.65	40.01	69.0	104.53	103.43	0.947	12.90	12.02
2	1918	80.76	65.79	74.0	159.51	158.34	0.955	21.21	19.78
3	3835	5.27	9.45	104.0	21.71	20.72	0.672	3.01	2.78
4	3797	20.72	30.77	110.4	53.09	52.11	0.922	9.93	9.50
5	3777	50.57	71.79	140.9	97.87	96.69	0.925	23.18	22.33
6	3792	100.78	148.25	158.3	177.93	175.31	0.932	47.78	45.99
7	5678	6.19	15.55	152.2	23.60	22.52	0.732	4.97	4.70
8	5605	12.47	27.77	134.4	38.48	35.23	0.902	8.89	8.54
9	5592	41.61	88.01	151.2	108.62	107.78	0.958	28.38	27.42
10	7546	10.01	29.52	179.4	33.06	32.25	0.891	9.50	9.17
11	7572	15.28	44.02	152.8	54.32	53.32	0.949	14.15	13.67
12	7531	32.39	94.10	157.9	111.11	109.33	0.955	30.33	29.32
13	9470	13.17	49.09	155.8	59.63	57.35	0.953	15.59	15.08
14	9470	20.11	75.43	152.4	92.64	90.36	0.949	24.02	23.22

(b) Calculated Values

Test No.	Speed (rpm)	Torque (N-m)	Line Frequency (Hz)	Modulation Index	Motor Output Power (kW)	Efficiency (%)		
						Inverter	Motor	System
1	1922	50.65	32.0	0.30	10.19	93.22	84.81	79.05
2	1918	80.76	32.0	0.32	16.20	93.26	81.89	76.38
3	3835	5.27	63.9	0.45	2.12	92.36	76.21	70.39
4	3797	20.72	63.3	0.48	8.24	95.69	86.75	83.01
5	3777	50.57	63.0	0.61	20.00	96.33	89.57	86.29
6	3792	100.78	63.2	0.69	40.02	96.26	87.02	83.77
7	5678	6.19	94.6	0.66	3.68	94.60	78.24	74.01
8	5605	12.47	93.4	0.58	7.32	96.08	85.71	82.35
9	5592	41.61	93.2	0.66	24.37	96.62	88.88	85.88
10	7546	10.01	125.8	0.78	7.91	96.52	86.22	83.22
11	7572	15.28	126.2	0.66	12.11	96.65	88.59	85.63
12	7531	32.39	125.5	0.69	25.55	96.65	87.15	84.23
13	9470	13.17	157.8	0.68	13.06	96.70	86.61	83.75
14	9470	20.11	157.8	0.66	19.94	96.65	85.90	83.02

6.2.3.2. Efficiency Comparison and Evaluation

The 55-kW ARCP ZVT inverter (its implementation is listed in Table 6.1) and a 55-kW hard-switching inverter are also tested under the same speed/torque points in the PNGV project. Table 6.5 lists the measured efficiency data of the hard-switching, two ZCT and ARCP inverters.

Table 6.5.
Measured Efficiencies of Four 55-kW Inverter Prototypes

Test No.	Speed (rpm)	Torque (N-m)	Inverter Efficiency (%)			
			Hard Switching	Six-Switch ZV/ZCT	Three-Switch ZCT	ARCP ZVT
1	1921	50.48	93.46	93.47	93.22	93.42
2	1918	80.68	93.28	93.58	93.26	93.08
3	3810	5.19	91.84	92.07	92.36	90.81
4	3790	20.63	95.52	95.64	95.69	95.22
5	3782	50.62	96.41	96.36	96.33	96.23
6	3786	101.2	96.20	96.24	96.26	95.95
7	5651	5.95	94.02	94.29	94.60	93.36
8	5616	12.25	95.92	96.02	96.08	95.58
9	5616	41.70	96.65	96.66	96.62	96.57
10	7529	10.05	96.40	96.48	96.52	96.06
11	7564	15.02	96.49	96.49	96.65	96.28
12	7551	32.09	96.66	96.54	96.65	96.53
13	9422	13.17	96.53	96.45	96.70	96.35
14	9463	20.33	96.68	96.51	96.65	96.52

Based on Table 6.5, the measured efficiencies at different operating points are plotted as a graph, as shown in Figure 6.20. It can be seen that there is a small difference between the efficiencies of the hard-switching inverter and the soft-switching inverters. However, this small difference is actually within the margin of the measurement error. The inverter efficiencies are obtained based on the measured input DC power and three-phase output power. The accuracy of the efficiency measurement, which counts the accuracy of the current and voltage sensors and

the accuracy of the power analyzer, can be ±1.2% [F19]. This observation suggests that under the tested operating conditions of V_{dc}=325 V and f_s=10 kHz, neither of the ZCT inverters, nor the ARCP ZVT inverter, makes a remarkable efficiency improvement over the hard-switching inverter.

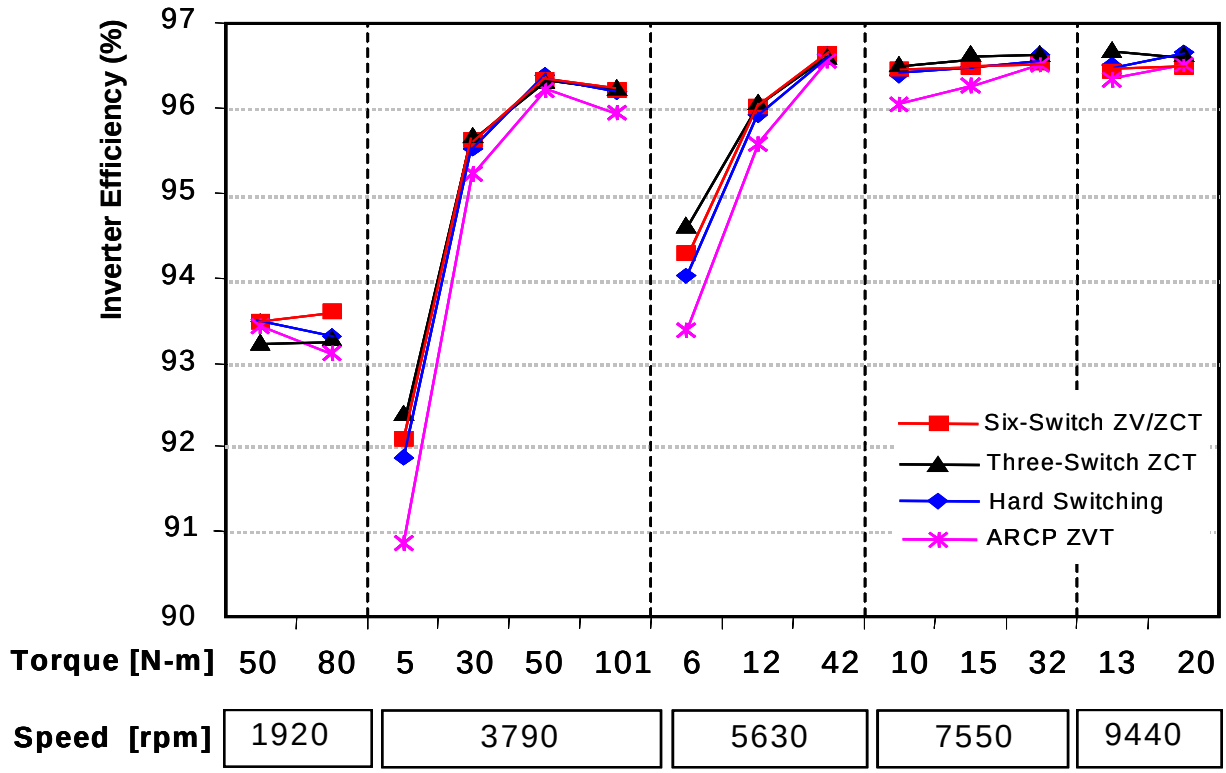

Figure 6.20. Comparison of the *measured* inverter efficiencies.

To investigate the reasons behind the efficiency measurement results, especially for those of the ZCT inverters, the inverter efficiencies are calculated under the same operating conditions (load current, power factor, line frequency and modulation index), using the loss models and MathCAD program developed in Section 5.6. As shown by the graph in Figure 6.21(a), the calculated efficiencies follow almost the same basic trend as the measured data, and they also tend to increase under higher speed and/or higher torque conditions. The calculated results also

indicate only a small difference between the efficiencies of the hard-switching inverter and the ZCT inverters at most points. Due to the approximation and simplification of the loss models and the error in the measurement, the difference in the exact data between the calculation and measurement is acceptable. This confirms that the loss models and mechanisms discussed in Section 5.6 are applicable to the EV motor drive application. It should be mentioned that the results for points No. 3 and 7 in Figure 6.21 are deducted from the measurement data, and are not calculated from the loss models. This is because these two points have low power factors (0.67 and 0.73, respectively), and one of the assumptions of the loss models is that the power factor should be high enough that the six-step SVM can effectively reduce the switching losses.

As analyzed in Section 5.6, the major reason why the ZCT inverters do not show noticeable efficiency improvement over the hard-switching inverter for this particular EV motor drive application lies in the characteristics of the main IGBTs. The main switches used in the 55-kW prototypes are MG300J2YS50, which is the third-generation (3rd-gen) IGBT made by Toshiba. As shown in Figure 6.22, compared to the second-generation IGBT, which is the MG300J2YS45, the 3rd-gen IGBT has much lower switching losses (the turn-off loss in particular is reduced by about 60%), but higher conduction losses. Because the conduction losses are dominant in the total losses, the efficiency benefit of soft switching is limited under the switching frequency of 10 kHz, even though the switching losses are significantly reduced by both ZCT commutations. If the switching frequency is increased, the switching loss can become dominant, and the soft switching will gain further benefits in efficiency. Figure 6.21(b) shows the inverter efficiencies under a switching frequency of 20 kHz, calculated using the loss model. It can be seen that the efficiencies for both the hard-switching and ZCT inverters decrease from those under 10-kHz switching frequency; however, the difference between the efficiencies of the

hard-switching inverter and the ZCT inverters apparently becomes large, in particular at points with high torques. At these points, it is evident that both ZCT inverters have higher efficiency than the hard-switching inverter, and the six-switch ZV/ZCT inverter has higher efficiency than the three-switch ZCT inverter.

The other reason is related to the implementations of the auxiliary circuits. Research efforts have been conducted to develop a design methodology for reducing as much as possible the additional conduction losses caused by ZCT commutations; these efforts are presented in Chapter 5. However, because of the availability of existing devices and components during the project and the mechanical constraints of the chassis, the auxiliary circuits that were actually implemented may need to be optimized further. The control timings also may need further tuning based on the physical hardware. This reason does, however, confirm that the design and implementations of auxiliary circuits are critical for maximizing the overall improvement of inverter efficiencies, and that the related research efforts are necessary and important.

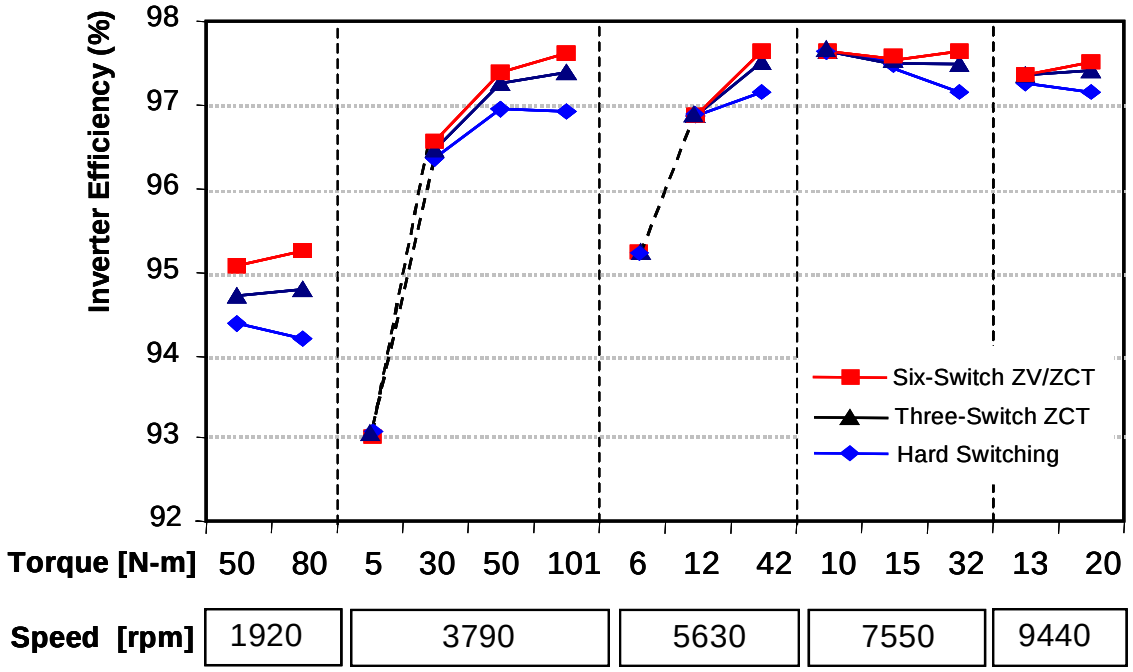

(a)

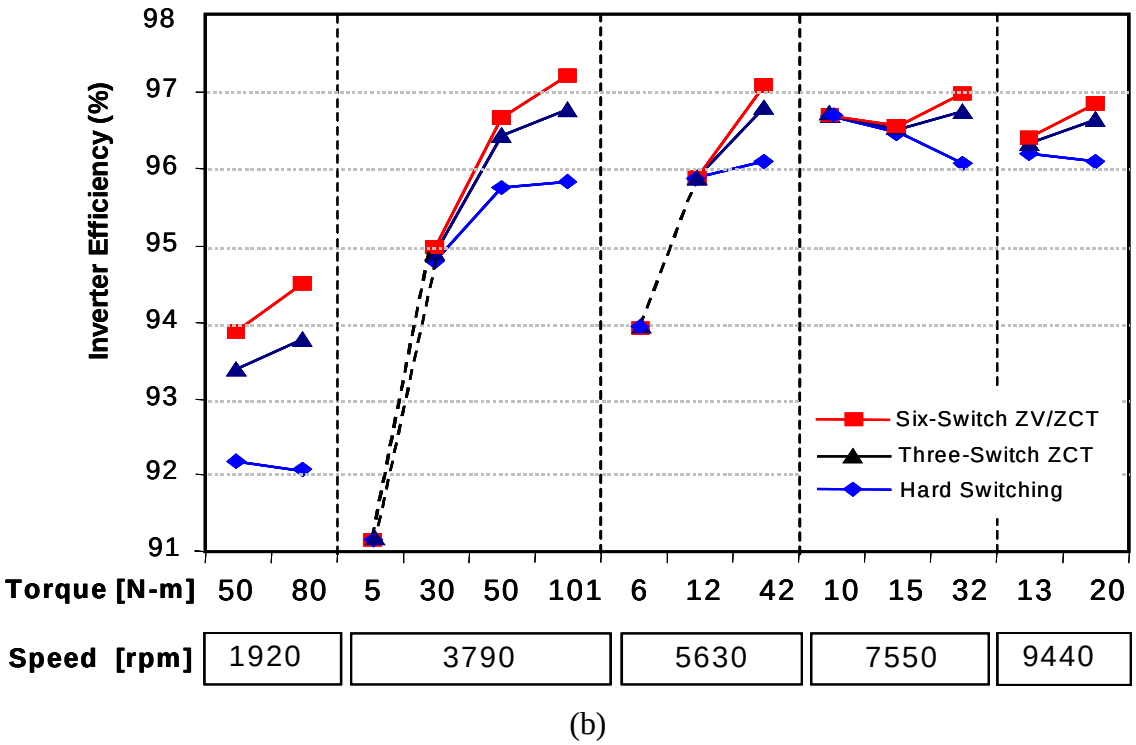

(b)

Figure 6.21. *Calculated* inverter efficiencies using the *loss models* developed in Section 5.6: (a) f_s=10 kHz; and (b) f_s=20kHz.
(Results for points No.3 and 7 are deducted from the measurement data, and are not calculated from the loss models due to their low power factors.)

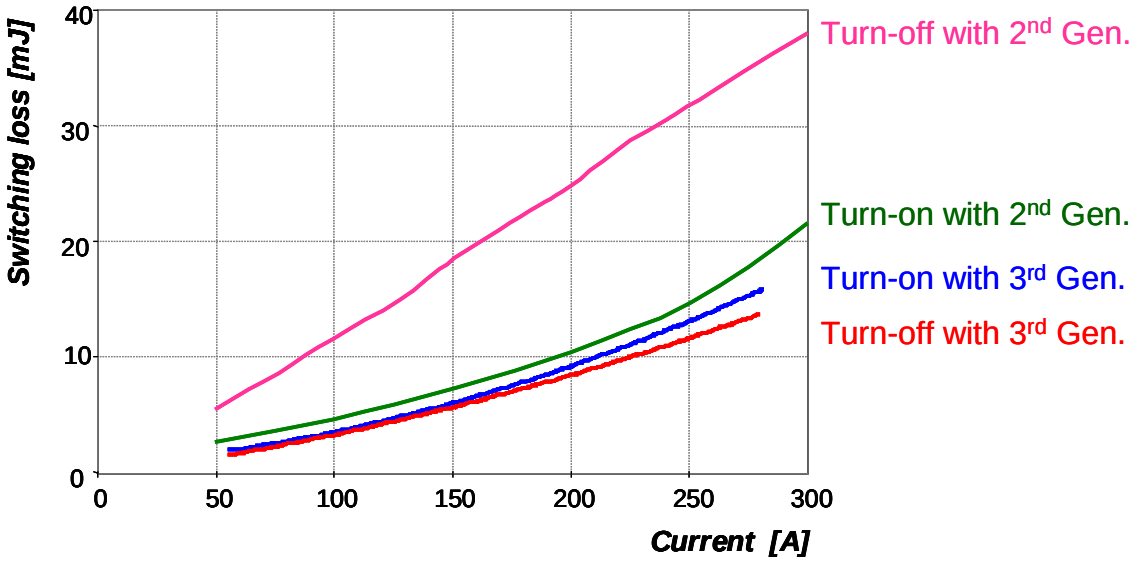

Figure 6.22. Comparison of switching energy losses between the 3rd –generation IGBT (MG300J2YS50) and the 2nd–generation IGBT (MG300J2YS45).

6.3. Summary

Two 55-kW ZCT inverter prototypes, the six-switch ZV/ZCT and the three-switch ZCT, have been completely implemented and tested to the full-power level with a closed-loop controlled induction motor dynamometer. This work enhances the proof of the concepts proposed in Chapters 2 and 3 for high-power AC adjustable speed drive applications, and verifies the design methods presented in Chapter 5. Moreover, it provides a comprehensive evaluation of the ZCT techniques for the EV motor drive application.

As indirect measures of cost, quality and reliability, the complexity of the 55-kW prototypes is compared, in such aspects as the numbers and ratings of all the devices and components that are actually used in the implementations, overall size, and compatibility with hard-switching inverters. The true piggyback merit of both ZCT inverters is demonstrated, which require no modification to normal SVM schemes and the least modification to hard-switching inverters in

terms of both hardware and software. In particular, the three-switch ZCT inverter requires the least cost and space as compared to other soft-switching inverters, and is more reliable.

The ZCT inverter operations are fully characterized under the dynamometer tests, for both electrical and thermal properties. The desirable soft transitions are realized at all testing points, together with motor drive functions. The implementation of ZCT soft switching shows no interference with the closed-loop control of the induction motor within the entire speed/torque range. No devices or components showed any sign of over-heating, abnormality or failure. The measured temperature rises of the auxiliary devices are quite low, which indicates small amounts of power dissipation.

Steady-state tests are carried out at 14 typical speed-torque points in EV driving cycles. The efficiency comparison indicates that under V_{dc}=325 V and f_s=10 kHz and using MG300J2YS50 IGBT as the main switches, the ZCT inverters do not show a noticeable improvement in efficiency over the hard-switching inverter for this EV drive application. This is mainly because the conduction losses in the main IGBTs are dominant in the total inverter losses. It is predicted that with higher switching frequencies and/or higher DC input voltage, the effect of switching loss reduction will have more impact on the total inverter losses, and the soft switching will gain further benefits in efficiency.

Chapter 7

Investigation of the ZCT Concepts for Megawatts High-Frequency Power Conversions

Megawatts high-frequency power conversion is another potential application of the ZCT techniques; this is a situation in which fundamental limits on the high-power devices are being reached. This chapter is an investigation of the ZCT concepts for the megawatts high-frequency power conversion application, in such respects as increasing the switching frequency and current handling capabilities of high-power devices and providing simple low-cost soft-switching solutions.

This chapter first presents an experimental characterization of the IGCT device under the proposed six-switch ZV/ZCT condition. Test results show that ZCT soft switching can dramatically reduce the switching losses of the IGCT device and alleviate the reverse-recovery stress of the high-power diodes. Improvements made to the switching frequency and simplification of the cooling requirements under the ZCT operation are discussed.

Use of multilevel topologies is becoming popular for megawatts power converters. Following the proposed three-switch ZCT inverter that reduces the number of auxiliary switches by half and still maintains desirable soft-commutation features, this chapter also develops a generalized ZCT cell concept to simplify multilevel soft-switching inverters. This concept leads to the discovery of a family of simplified soft-switching inverters, including three-level ZCT inverters using only six auxiliary switches. The simplified three-level ZCT inverters are analyzed in detail, based on PSPICE simulations using actual device models and including parasitic effects.

7.1. Testing and Characterization of Integrated Gate Commutated Thyristor (IGCT) under the ZCT Soft-Switching Condition

7.1.1. IGCT Test Setup

In order to demonstrate the proposed ZCT techniques with state-of-the-art high-power devices, a prototype is developed to test and characterize the IGCT device under the six-switch ZV/ZCT soft-switching condition. The tested device is the ABB IGCT 5SHY35L4503. This IGCT is rated at a permanent DC blocking voltage of 2800 V, repetitive peak off-state voltage of 4500 V, and maximum controllable turn-off current of 4000 A [E22]. Among the available high-voltage high-power devices, this IGCT has the lowest conduction loss and a comparable switching loss; therefore, it is possible that soft switching will be most beneficial for this IGCT. For the purpose of demonstrating the concept, the test setup is configured as a boost-type converter, as shown in Figure 7.1, in which the IGCT S_m is assisted by the auxiliary switch S_{x1} at the turn-on, and by S_{x2} at the turn-off. The operational principles are described in Chapter 2, and the circuit is designed using the guidelines discussed in Chapter 2. The major devices and components are listed as follows:

- *Main diode (D_{M1} and D_{M2}):* ABB 5SDF10H4502, 1000 A/4500 V;
- *Auxiliary switch:* Eupec IGBT FZ1200R33KF2, 1200 A/3300 V;
- *Resonant capacitor*: 6 μF, THY-W4B-6.0-450 oil-filled metallized polypropylene film, rated at 3000-V DC, 4500-V peak; and
- *Resonant inductor*: 7 μH, air-core wound with eight turns of AWG-2 5000-V insulation motor lead on a 4-inch-diameter plastic form.

The IGBTs were selected to be used as auxiliary switches due to the relatively easy mechanical layout of the plastic modules as compared to the hockey-puck package stacks in the

test setup. For practical implementations, GTO-derived devices such as IGCTs would be preferable due to their superior surge current capacities. A photo of the test setup is shown in Figure 7.2.

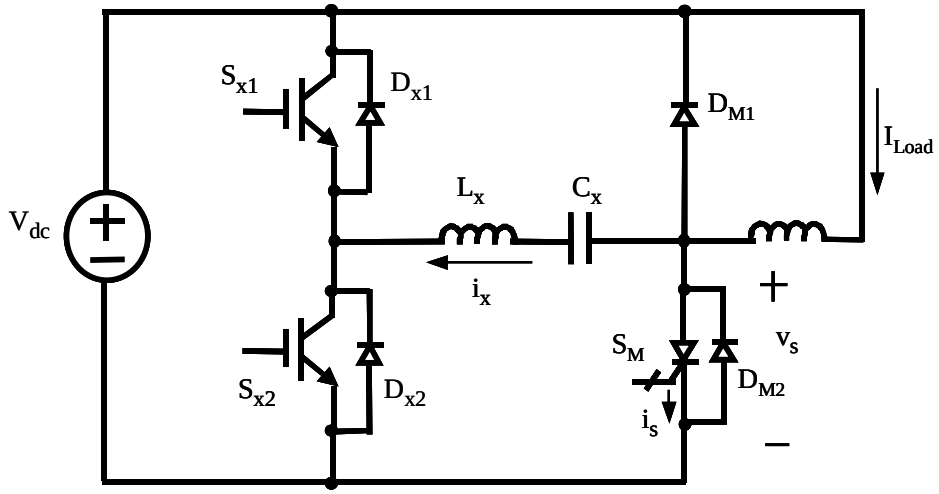

Figure 7.1. ZCT soft-switching test circuit with the IGCT (S_M).

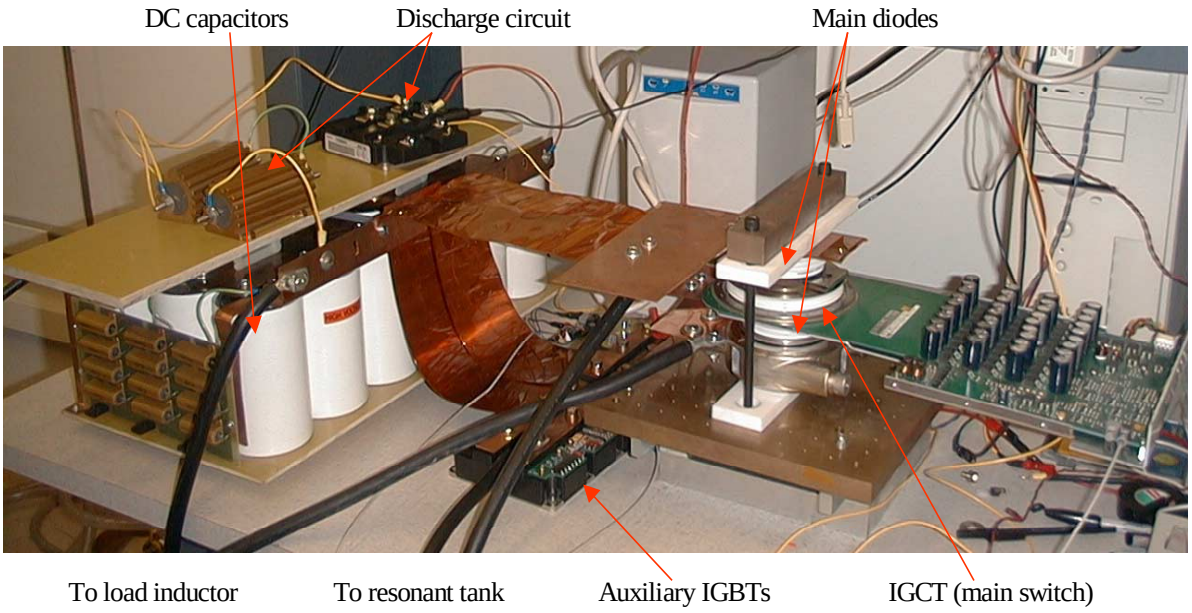

Figure 7.2. A photo of the ZCT test setup with the IGCT.

7.1.2. IGCT Test Results

With the setup shown in Figure 7.2, the IGCT is tested under the six-switch ZV/ZCT condition. The test is performed in a double-pulse sequence, as described in Section 5.1.1. The measured waveforms in one switching cycle are shown in Figure 7.3, where i_x is the resonant inductor current, i_s is the main IGCT current, v_s is the main IGCT voltage, and I_{Load} is the load inductor current. Except that the I_{Load} is not a constant current source (due to the finite load inductance), it can be seen that the experimental waveforms agree with the theoretical waveforms shown in Figure 2.5, which indicates that the desirable ZV/ZCT soft switching is realized in the IGCT. Since the IGCT is in the press-pack packaging, and it does not have an anti-parallel diode built into the package, the i_s represents the measured switch current flowing through the IGCT only. Therefore, the i_s waveform does not have a negative portion at the turn-off transition. (For ZCT turn-off of the IGBT module with an anti-parallel diode, the negative portion of i_s represents the surplus current conducted by the diode.)

At the turn-on transition, the i_x is built up to a level higher than I_{Load}, so the current in the main diode D_{m1} is completely reduced to zero before the S_m is turned on. The interval when i_x is higher than I_{Load} is about 4 μs for this case, and it allows the carriers in D_{m1} to be recombined properly. After i_x begins to decrease from its peak, the difference between i_x and I_{Load} forces the other main diode D_{m2} into conduction and realizes zero-voltage turn-on for the IGCT S_m. The zero-voltage turn-on of S_m is also clearly seen in the zoomed-in turn-on waveforms shown in Figure 7.4, in which the voltage across the main switch decreases to zero for about 1.5 μs before the switch starts to carry current i_s. When the current i_s begins to rise, the resonant inductor limits the rising rate of the current. No reverse-recovery current of main diode D_{m1} flows through the main switch S_m, and the turn-on switching loss is nearly zero. The ZV/ZCT transition has solved

the turn-off problem of the main diode, which normally requires lossy snubbers. It should be noted that with the high-voltage diode, a completely hard commutation of the diode, and therefore a completely hard-switching turn-on of the IGCT, is impossible. Consequently, the *di/dt* must be controlled by either a resonant circuit or a passive snubber. It can be also observed that i_s actually ramps to a point higher than the level of I_{Load} before it finally stays at that level. As discussed in Section 5.1.2.2, this phenomenon occurs because some reverse-recovery current of auxiliary diode D_{x1} flows through the main switch when i_x falls to zero at the end of the turn-on transition. Because the main switch is fully on by the time this recovery occurs, the recovery causes only a slight increase in the conduction loss of the main switch.

At the turn-off transition, it can be seen from Figure 7.3 that the IGCT current (i_s) is reduced to zero, and that the resonant current i_x is built up to a level higher than the load current I_{Load}. The interval when i_x is higher than I_{Load} is about 8 μs for this case, which allows the carriers in the main switch to be recombined. Meanwhile, the gate driver sends out the turn-off command during this interval. Figure 7.5 shows zoomed-in turn-off waveforms. It can be seen that there is a current pulse after i_s falls to zero. This is the circulating current from the gate driver after it sends the turn-off command, and it does not cause any switching loss because the switch voltage is still zero at this moment. When the voltage begins to rise, the *dv/dt* is limited by the charging of the resonant inductor. There is no voltage overshoot or high-frequency ringing beyond the DC bus voltage. When the switch voltage is rising, a small current bump occurs, which causes a slight overlap between the voltage and current. This current bump has two sources. The first source is the charge of the output capacitor of the IGCT. For a large-area device such as the IGCT, a significant output capacitance must be charged in order to establish a depletion region to support the voltage. The other source is the sweep of the free carriers that are not recombined

during the interval when i_x is higher that I_{Load} and the anti-parallel diode D_{m2} conducts the surplus current. However, this current bump is much smaller compared to the current tail that occurs in hard switching, and the dangerous high-stress overlap interval when the switch must handle both full voltage and full current under the hard-switching turn-off does not exist. The measured turn-off energy loss of the IGCT is 70 mJ under 350-A switch current and 1000-V DC bus voltage, which is a reduction of 89% as compared to the hard-switching turn-off at the same current and voltage level (650 mJ).

As discussed in Chapter 2, one advantage of the proposed ZCT scheme is that it can also provide zero-current turn-off to the auxiliary switches. This feature is realized in the IGCT testing circuit. In the measured waveforms shown in Figure 7.3, at the turn-on transition, after i_x reverses from negative to positive, the top auxiliary diode D_{x1} begins to conduct, and the top auxiliary switch S_{x1} turns off under zero current; at the turn-off transition, after i_x reverses from positive to negative, D_{x2} begins to conduct, and S_{x2} turns off under zero current.

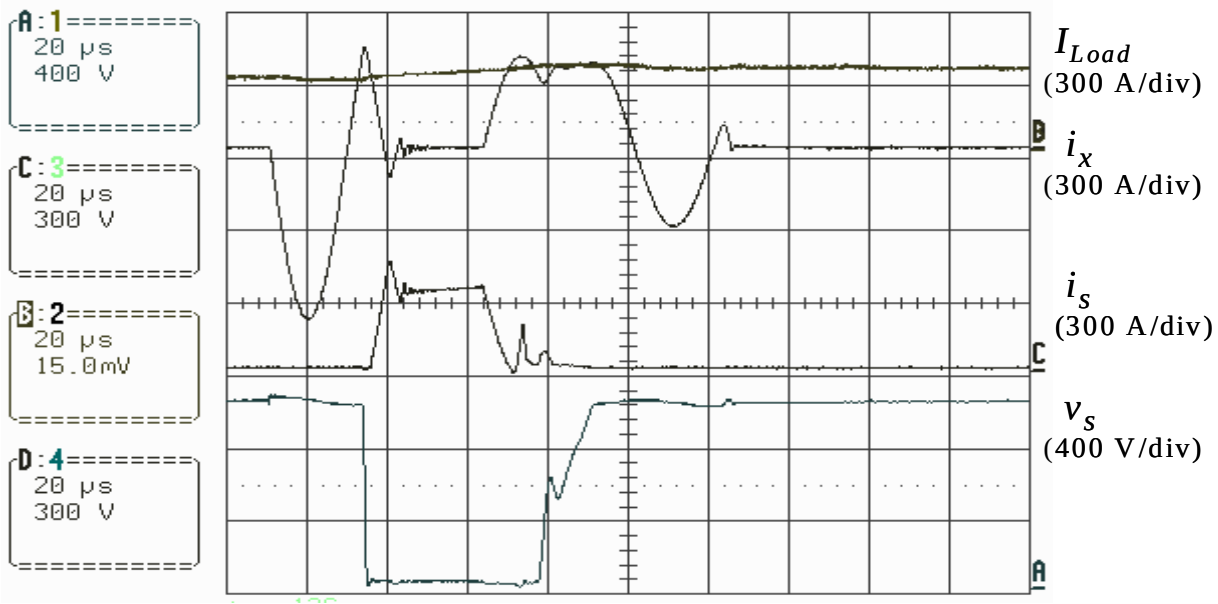

Figure 7.3. Measured waveforms of the IGCT in one switching cycle under the six-switch ZV/ZCT operation.

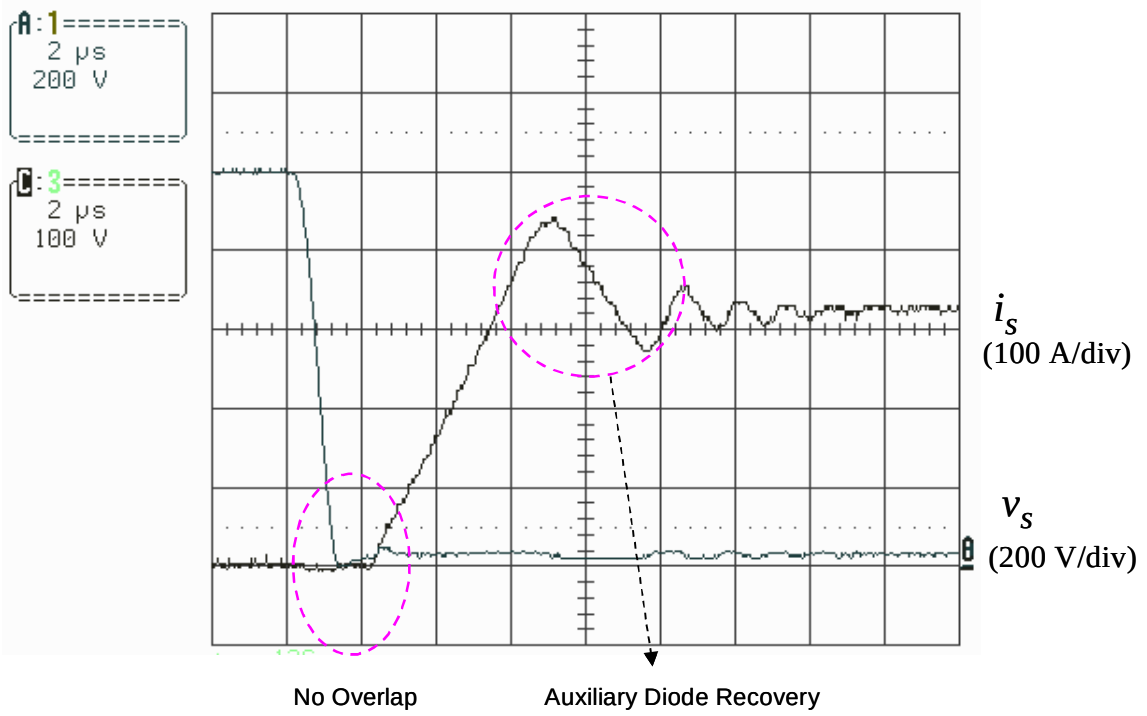

Figure 7.4. Measured turn-*on* waveforms of the IGCT under the six-switch ZV/ZCT operation.

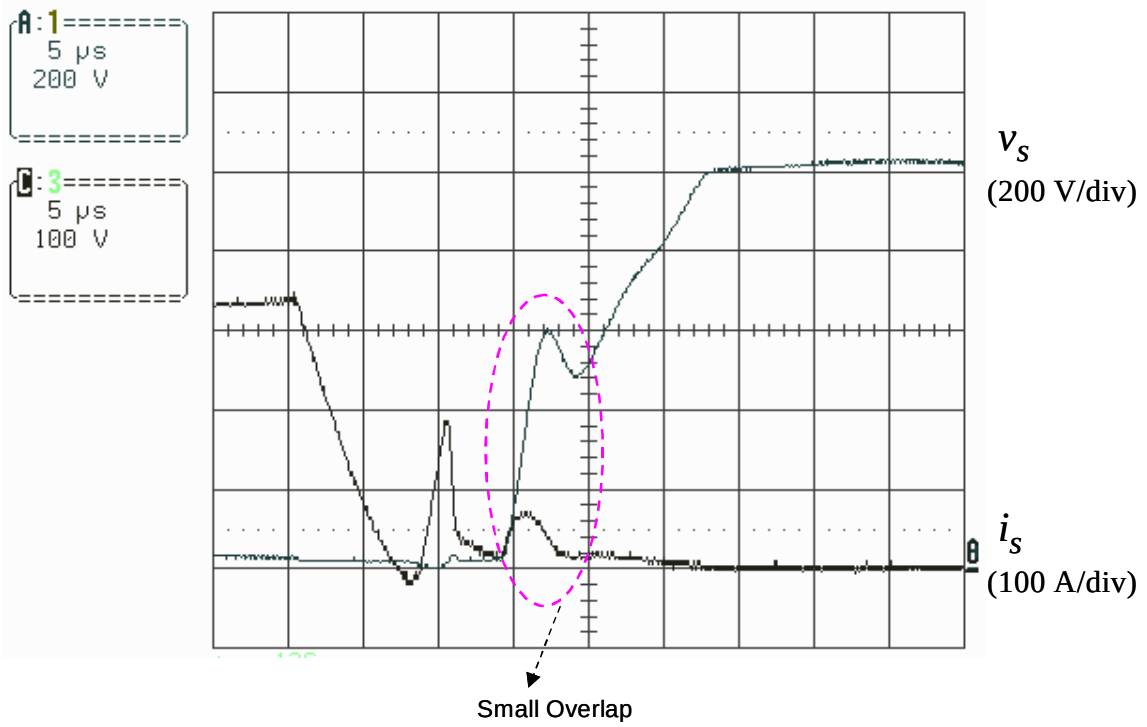

Figure 7.5. Measured turn-*off* waveforms of the IGCT under the six-switch ZV/ZCT operation.

7.1.3. Discussion of the Frequency Limits of ZCT Inverters Equipped with IGCTs

In megawatts power conversion systems, a higher switching frequency is desired, because it can offer such advantages as higher control bandwidth, smaller current ripple and total harmonic distortion (THD), and smaller size of passive components. However, one of the major limitations on the switching frequency is the thermal handling capability of the high-power devices. The experimental results obtained with the IGCT have demonstrated that ZCT soft switching can significantly reduce the switching losses. Therefore, it is necessary to explore how ZCT soft switching will either increase the converter switching frequency f_s, impact the cooling system requirements, or both.

For this purpose, a sample three-phase six-switch ZV/ZCT inverter equipped with the IGCT is analyzed; the circuit diagram is shown in Figure 2.1, and the main switches are the IGCT 5SHY35L4503. The DC bus voltage is assumed to be 2000 V and the maximum output RMS current I_L is assumed to be 2000 A. This condition will produce a maximum of 1400 V line-to-line RMS AC output voltage and a power rating of about 5 MVA. Since our goal is to determine the switching frequency limitation of the IGCT, the maximum power loss per IGCT must be estimated. The worst case conduction loss occurs when the power factor equals one (pf=1) and the IGCT switch conducts for a much longer time than its opposite diode. The average current through the IGCT is

$$I_{avg} = \frac{\sqrt{2}}{\pi} I_L . \tag{7.1}$$

The RMS current through the IGCT is

$$I_{rms} = \frac{\sqrt{2}}{2} I_L . \tag{7.2}$$

Based on the data sheet information, the on-state voltage drop of the IGCT is approximated as

$$V_c = V_o + R_c I\,, \tag{7.3}$$

where V_o=1.205 V and R_c=0.389 mΩ.

The maximum conduction loss in the IGCT is calculated by

$$P_c = V_o I_{avg} + R_c I^2{}_{rms}\,. \tag{7.4}$$

Since a turn-on snubber must be used to limit the *di/dt* in hard switching, the turn-on loss under hard switching can be ignored. The turn-off loss is assumed to be proportional to the DC bus voltage and current. In the worst case, the switching loss under the hard-switching condition is estimated by

$$P_{sw\_hs} = f_s I_{avg} \frac{E_{off}}{800}\,, \tag{7.5}$$

where E_{off} is the tested turn-off energy under 800 A, which is around 4.2 mJ.

The experimental results have demonstrated that the ZV/ZCT operation can nearly eliminate the turn-on loss of the IGCT and can reduce the turn-off loss by 89%. So the switching loss under the ZV/ZCT condition is $0.11P_{sw\_hs}$. Figure 7.6 shows the estimated maximum total power loss per IGCT device under different switching frequencies. It can be seen that the IGCT device power loss is significantly reduced by the ZV/ZCT. This loss can reach 6 kW at f_s=1 kHz under the hard-switching condition, and is still less than 6 kW when f_s increases to 8 kHz under the ZV/ZCT condition.

In the IGCT, the press pack is used. These hockey-puck package stacks allow the double-side cooling, which results in low thermal resistance. In addition to the double-side cooling, the single-side cooling, on either the anode or the cathode side, is also available to the IGCT. The single-side cooling has higher thermal resistance but is a simplified cooling system. On the other hand, the press-pack packaging requires external mechanical clamps for mounting, and relies on the coolant to insulate among the press-pack heatsinks. According to operating conditions of a typical megawatts high-power inverter with IGCT [D1], the IGCT case temperature is assumed to be 50°C, and its maximum allowable junction temperature is 125°C. Figure 7.7 shows the estimated IGCT device junction temperature as a function of the switching frequency under different cooling conditions. It can be seen that for hard switching, the switching frequency is limited to below 1 kHz, and the double-side cooling must be used. In contrast, for the ZV/ZCT operation, under the double-side cooling, the IGCT can operate up to 9 kHz; under the single-side cooling, the IGCT maximum switching frequency is still much higher than that in the hard-switching condition.

In practical implementations, however, due to the minimum pulse-width limits caused by the resonant process and other issues such as the gate driver losses, the feasible conditions for this case are to operate the IGCT under a 4-kHz switching frequency, and in the meantime to use the anode-side cooling. In this way, the switching frequency is increased by three times, and the cooling system can be simplified, which reduces both the cost and complexity of the megawatts power conversion system.

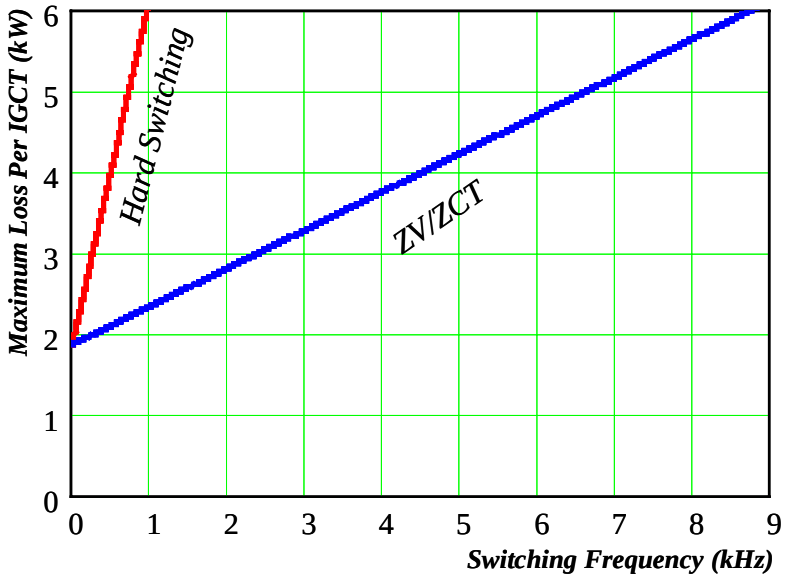

Figure 7.6. Estimated maximum power loss per IGCT device under the hard-switching and ZV/ZCT conditions as a function of the switching frequency.

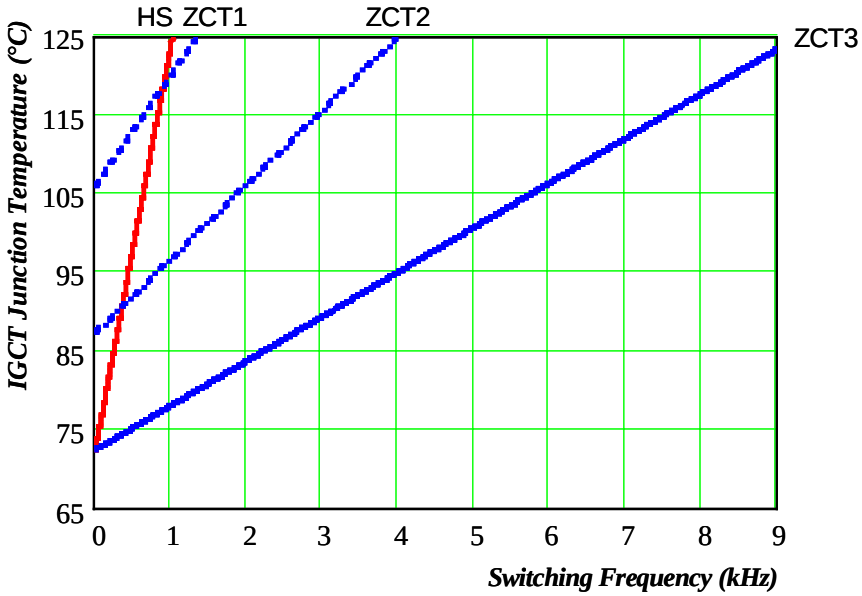

Figure 7.7. Estimated IGCT device junction temperatures as a function of switching frequency, under different operation conditions with different cooling methods:

HS: hard switching, double-side cooling, R_{thjc}=0.012 K/W;
ZCT1: ZV/ZCT, cathode-side cooling, R_{thjc}=0.03 K/W;
ZCT2: ZV/ZCT, anode-side cooling, R_{thjc}=0.02 K/W; and
ZCT3: ZV/ZCT, double-side cooling, R_{thjc}=0.012 K/W.

7.1.4. Summary

The ZCT soft-switching test on the IGCT has shown promising results. The turn-on loss is almost eliminated for the main switch, and meanwhile the reverse-recovery problem of the main diode is solved. The turn-off loss is reduced by 89% compared to hard switching, and the voltage overshoot at turn-off is eliminated. It is important to remember that a complete hard-switching turn-on of the IGCT is impossible. Either passive snubbers or soft-switching circuits are needed to control the turn-off of the main diode. When the ZCT circuit is used to replace the conventional RLD turn-on snubber, the power consumption associated with the snubber can also eliminated. The IGCT testing described in Sections 7.1.1 and 7.1.2 is a joint effort with the work in [E21].

System-level benefits of the ZCT inverter equipped with the IGCT devices are discussed. By reducing the switching loss, the ZCT technique can significantly increase the switching frequency and simplify the cooling system. Analysis of a 5-MVA sample three-phase inverter shows that under the ZCT soft-switching condition, the IGCT switching frequency can be increased from 1 kHz to 4 kHz, and in the meantime the cooling method for the press-pack IGCT can be simplified from the double-side cooling to the single-side cooling.

7.2. A Generalized ZCT Cell Concept to Simplify Multilevel Soft-Switching Inverters

7.2.1. Existing Multilevel Soft-Switching Topologies

With state-of-the-art high-power devices, the operating DC voltage across each device is limited to the 2-kV range. Multilevel inverters are needed in high-voltage applications with power levels of megawatts and above, since they can provide higher voltage capability and lower

output voltage distortion using existing devices without the complications brought by the voltage sharing of series connected low-voltage devices. Soft switching is useful for increasing the switching frequency and current handling capabilities of the multilevel high-power inverters. Most existing multilevel soft-switching topologies are extensions of their counterparts in two-level inverters. As discussed in Chapter 3, according to most existing soft-switching techniques, which cover DC-side and AC-side topologies and which include zero-voltage switching and zero-current switching, for a two-level three-phase soft-switching inverter, six auxiliary switches are required in order to achieve both the following features: 1) soft commutation for all main switches, auxiliary switches and diodes at all operation modes; and 2) in the meantime, no modification to normal PWM schemes. Similarly, three-level inverters face the same problem. The three-level quasi-resonant DC-link inverters require four auxiliary switches for three-phase circuits; however, these auxiliary switches are turned off under hard-switching conditions with high current, resulting in enormous losses [D9] [D10]. Those using AC-side soft-switching techniques, on the other hand, require four auxiliary switches for each phase leg, thus 12 auxiliary switches for three-phase circuits [D11]-[D16].

7.2.2. The Generalized ZCT Cell Concept

To reduce the high cost and large space associated with the auxiliary switches and meanwhile to maintain desirable soft-switching features, the three-switch ZCT inverter topology is proposed for two-level inverters, as documented in Chapter 3, and a 55-kW prototype is developed and tested, as documented in Chapters 5 and 6. Starting from the three-switch ZCT topology, this section will generalize the ZCT concept in order to simplify auxiliary circuitry for multilevel soft-switching inverters.

As discussed in Chapter 3, the three-switch ZCT topology fully utilizes the bi-directional property of the *LC* resonant current, and thus employs only one auxiliary switch to assist the soft transition in each phase leg. As a result, it reduces the number of auxiliary switches by half and still achieves soft commutation at every switching transition in all operation modes without requiring modification to normal PWM schemes. The concept of using one auxiliary switch to realize soft switching in one phase leg is generalized to multilevel inverters. The general statement is as follows: If a circuit (or a sub-circuit in a converter) is in a half-bridge PWM configuration, with bi-directional current flow and a totem-pole commutation pattern, then by the addition of one auxiliary switch S_x, one *LC* resonant tank and two diodes, soft commutation is achieved for all the devices (main switches, diodes, and the auxiliary switch). The circuit with the auxiliary switch and components is called a generic half-bridge ZCT cell, and is shown in Figure 7.8.

For the generic half-bridge ZCT cell, there are two configurations for the connection of S_x, which are equivalent from the standpoint of soft-switching operation, but may result in differences in implementations, such as layout, device selection and packaging, and EMI. Moreover, it should be emphasized that the switches and diodes are defined and identified based on current commutation patterns, and are not based on the physical circuit connection. As long as the totem-pole commutation is identified (which means that a bi-directional current I_{Load} flows into and out of node A, conducted by the top switch S_1 and bottom diode D_2, and vice versa), the generic ZCT cell is applicable. For certain applications, S_1 and S_2 are not necessarily in direct physical series connection, and D_1 and D_2 are not necessarily the physically connected anti-parallel diodes across S_1 and S_2. This feature is especially important for multilevel inverters.

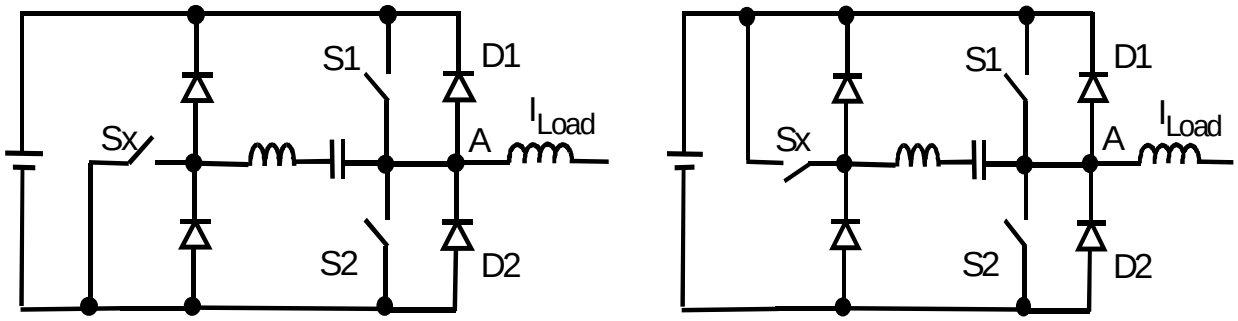

Figure. 7.8. Two configurations of the generic half-bridge ZCT cell.

7.2.3. Applying the ZCT Cell Concept to Simplify Three-Level Soft-Switching Inverters

For two-level inverters, clearly, by replacing each half-bridge phase leg with the generic ZCT cell, the simplified three-switch ZCT inverter can be obtained, as shown in Figure 3.3. It is more meaningful to investigate how the concept of the generic ZCT cell will simplify multilevel soft-switching inverters. In this section, using the three-level inverter as an example, the half-bridge PWM cells will be identified first, and then the ZCT cell will be applied to simplify three-level ZCT inverters.

7.2.3.1. Derivation of Simplified Three-Level ZCT Inverters

Figure 7.9(a) shows one phase-leg circuit of the neutral-point-clamped (NPC) three-level inverter, which is the most popular multilevel topology [D2]. Based on the existing ZCT scheme [C20], a three-level ZCT inverter was proposed and used for superconductive magnetic energy storage and power electronics building block (PEBB) applications [D14]-[D16]. As shown in Figure 7.9(b), this existing three-level ZCT inverter requires four auxiliary switches in one phase, and thus 12 auxiliary switches in the three-phase circuit.

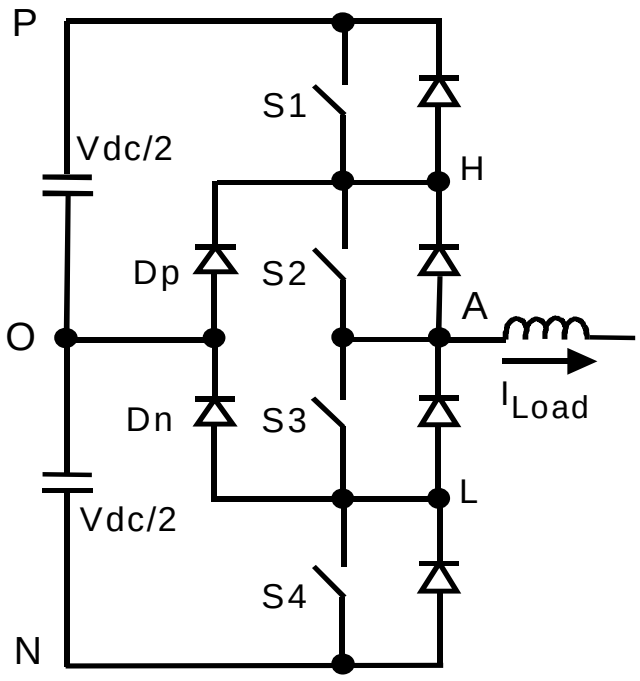

(a)

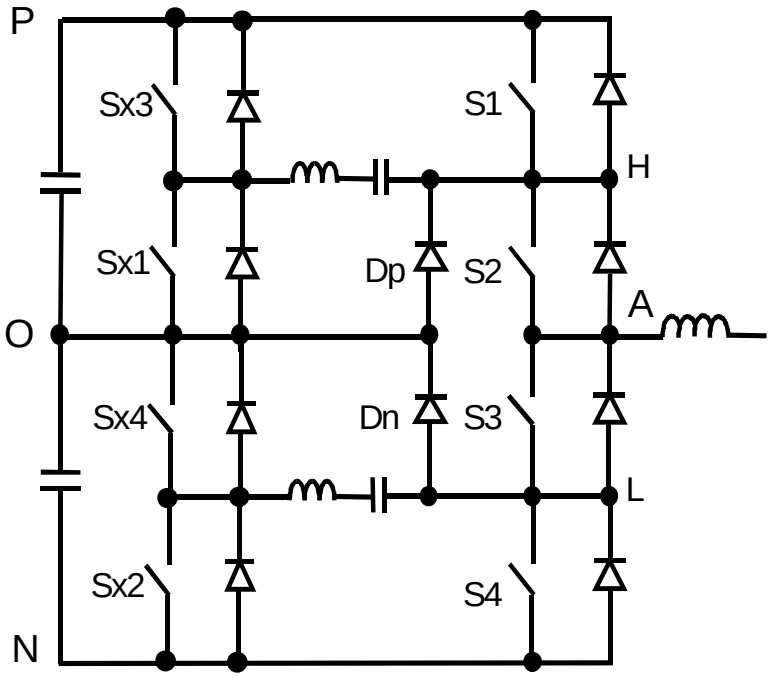

(b)

Figure. 7.9. One phase leg of the three-level NPC inverter:
(a) the basic hard-switching topology; and (b) the existing three-level ZCT topology.

One phase leg of the three-level inverter consists of four switches connected in series (S_1~S_4), two clamping diodes (D_p and D_n), and two capacitors to divide the DC bus voltage. S_1 and S_4 are called the outer switches, and S_2 and S_3 are called the inner switches. Based on switching states, phase node A can be connected to three points: positive DC rail "P," center point "O," and negative DC rail "N"; thus, each phase has three voltage levels: $V_{dc}/2$, 0, and $-V_{dc}/2$. In a three-phase three-level inverter, 24 non-zero and three zero voltage vectors can be produced by different switching combinations. However, in normal modulation schemes, the phase voltage is switched only between two adjacent voltage levels at each switching transition. Thus, there are four possible current commutation patterns in each phase leg, which are shown in Figure 7.10: (a) between S_1 and D_p; (b) between D_1 and S_3; (c) between S_4 and D_n; and (d) between D_4 and S_2.

During patterns (a) and (b), the inner switch S_2 is kept on, and the load current flows into and out of node A, commutated through two switches and two diodes: S_1, S_3, D_p and D_1. According to the discussion of the ZCT cell in Section 7.2.2, combining patterns (a) and (b) therefore yields a half-bridge PWM cell (the top cell). Complementarily, during (c) and (d), S_3 is kept on, and combining (c) and (d) yields another half-bridge PWM cell (the bottom cell), composed of S_4, S_2, D_n and D_4. As a result, the four current commutation patterns in one phase leg are grouped into two half-bridge PWM cells. By replacing the half-bridge PWM cells with the proposed half-bridge ZCT cells, simplified three-level ZCT topologies are obtained, in which one phase needs two auxiliary switches, and the three-phase circuit needs only six auxiliary switches. This represents a reduction by half compared to those required by existing three-level AC-side soft-switching topologies [D11]-[D16].

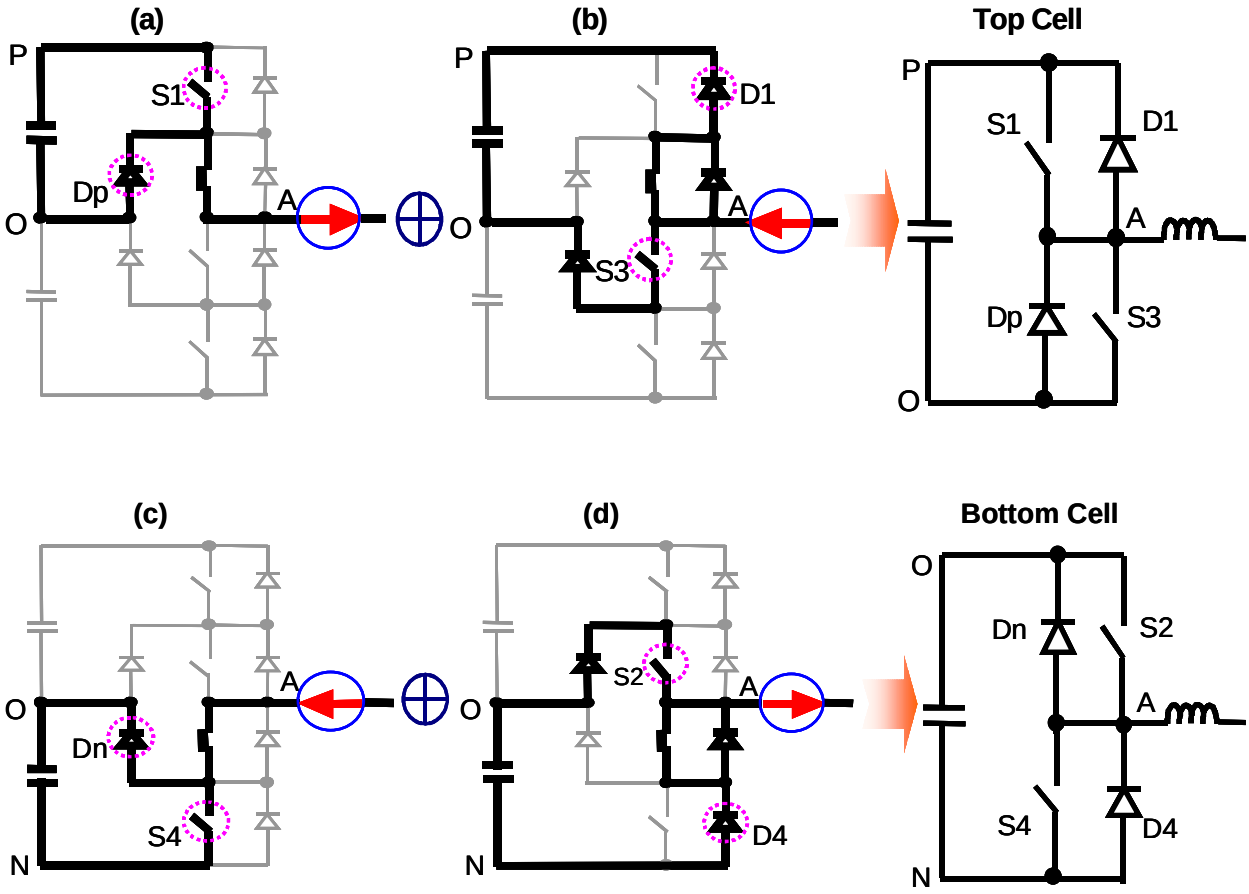

Figure 7.10. Grouping the four commutation patterns in one phase leg of the three-level NPC inverter into two half-bridge PWM cells.

As shown in Figure 7.11, there are four configurations of the simplified three-level ZCT inverters; all are equivalent in terms of soft-switching operation. The auxiliary switch S_{xp} is responsible for the soft switching of the top cell (S_1, D_1, D_p, and S_3) and S_{xn} is responsible for those of the bottom cell (S_2, D_n, S_4, and D_4). For the configuration shown in Figure 7.11(a), since S_{xp} and S_{xn} are physically connected as a half bridge, they can be implemented with standard modules. Therefore, this configuration is preferable for implementations, and will be used as the example for detailed analysis.

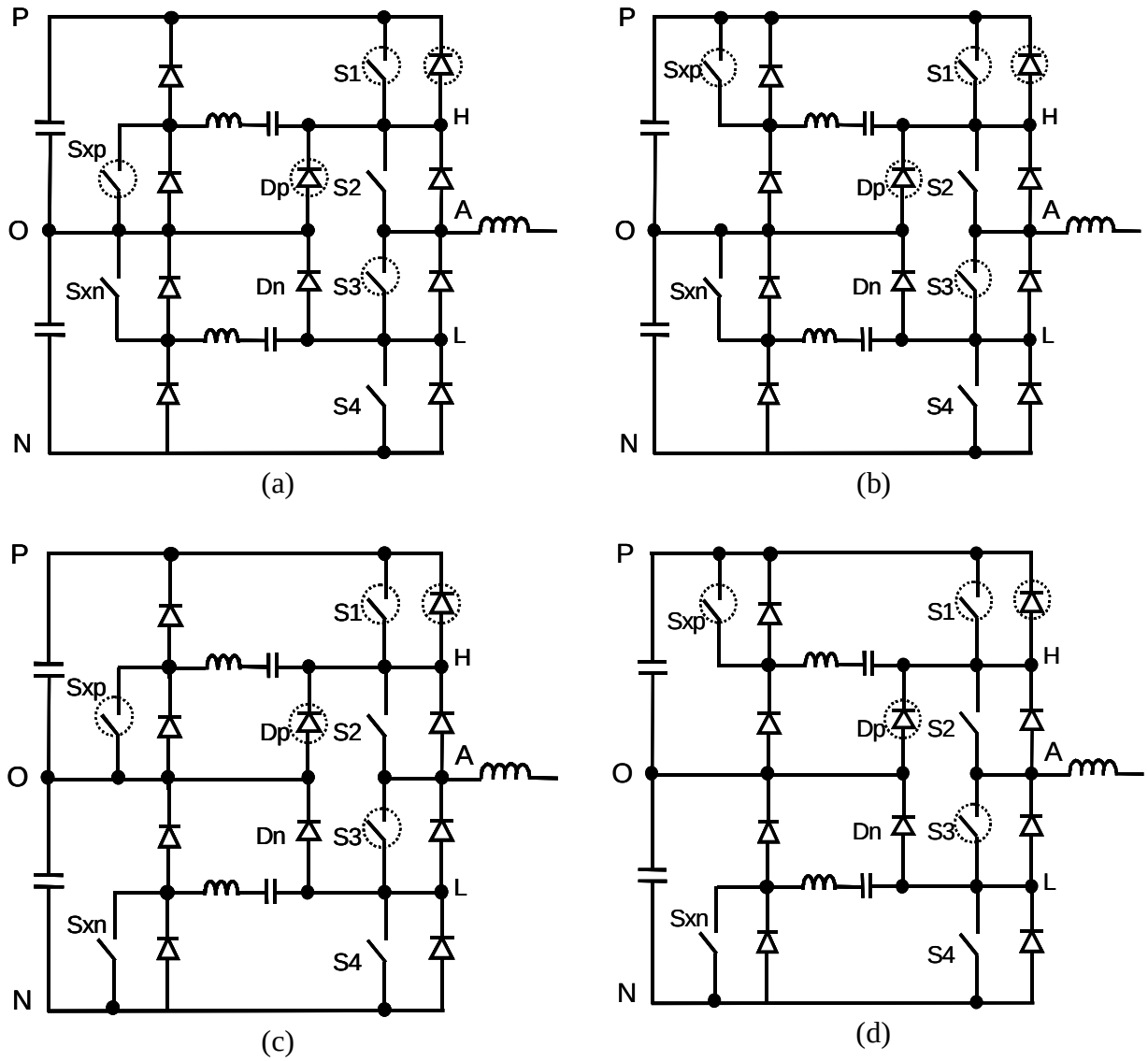

Figure 7.11. Four configurations of the simplified three-level ZCT inverter.

7.2.3.2. Analysis of the Simplified Three-Level ZCT Inverters Using PSPICE Simulations

For the configuration shown in Figure 7.11(a), there are four soft-commutation patterns, which are illustrated in Figure 7.12. These patterns correspond to those in the hard-switching topology, as shown in Figure 7.10. With the identification of the ZCT cells, the soft commutations between an outer switch and a clamping diode (Figures. 7.12(a) and 7.12(c)) are theoretically equivalent to those of the two-level three-switch ZCT inverter at $I_{Load}>0$, as

previously described in Section 3.3.1; those between an inner switch and an outer diode (Figures. 7.12(b) and 7.12(d)) are theoretically equivalent to those of the two-level three-switch ZCT inverter at I_{Load}<0, as described in Section 3.3.2.

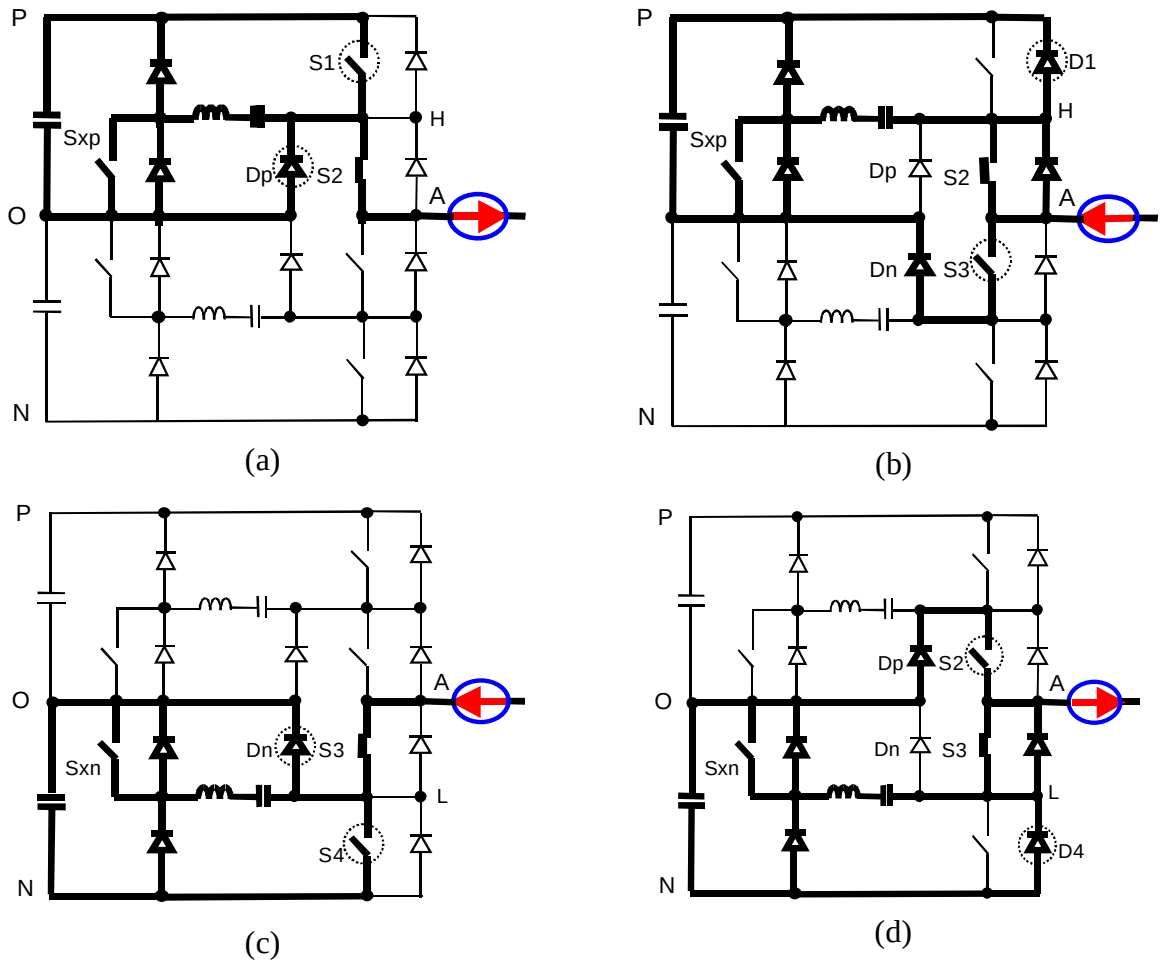

Figure 7.12. Four soft-commutation patterns in one phase leg of the simplified three-level ZCT inverter (for the configuration shown in Figure 11(a)):
(a) between S_1 and D_p; (b) between D_1 and S_3;
(c) between S_4 and D_n; and (d) between D_4 and S_2.

In order to verify and analyze the simplified three-level ZCT operations, PSPICE simulations are conducted using the circuit model shown in Figure 7.13. Soft-switching parameters for the simulation are set to be the same as those of the 55-kW two-level prototype for the EV motor drives, as presented in Chapter 6: L_{xp}=L_{xn}=850 nH and C_{xp}=C_{xn}=0.625 μF. The DC bus voltage

for the soft transition is also the same: V_{dc}=650 V (the switches withstand only half of V_{dc}). Actual device models are used: CM300DY-12H, 300-A/600-V IGBTs for the switches, the same ratings as those of the 55-kW prototype (the PSPICE model of the MG300J2Y50 IGBT was not available during the simulation). Two MUR20020CTs (200-A/200-V) are connected in series to represent one diode, which can closely simulate device behaviors associated with the voltage stress. Parasitic inductance in the critical current paths is considered in the simulation and is represented as lumped parameters (L_{s1}~L_{s8}); each is set to be 20 nH. The simulation conditions are quite close to those in experimental implementations.

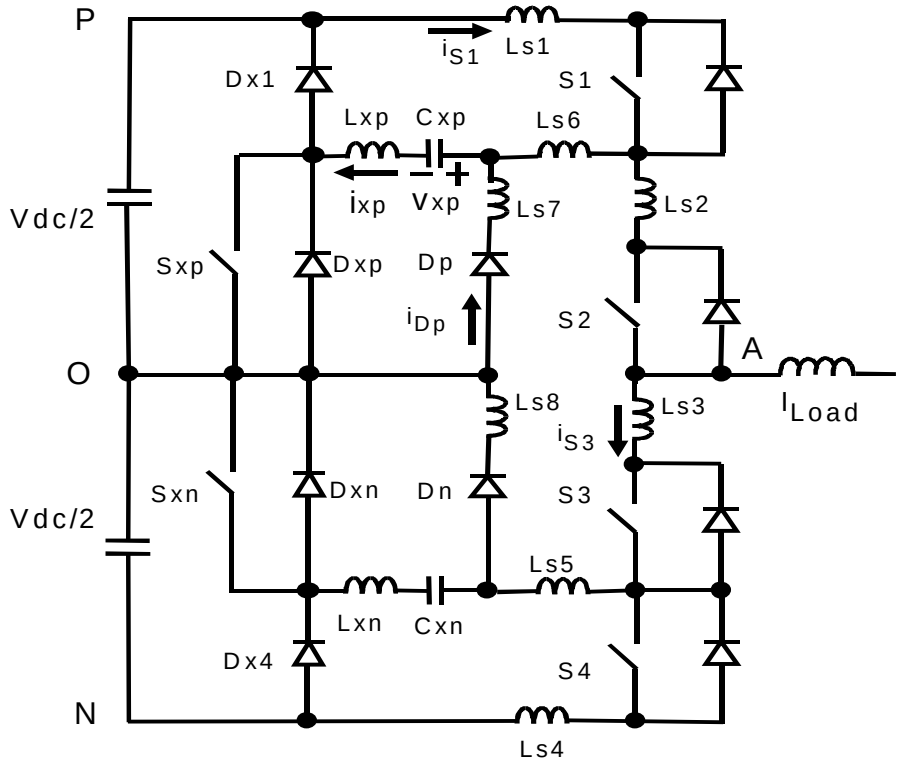

Figure 7.13. The PSPICE simulation circuit model of the simplified three-level ZCT inverter including the parasitic inductance L_{s1}~L_{s8}.

A. Soft Commutation between the Outer Switch and Clamping Diode

Figure 7.14 shows simulation waveforms of the soft commutation between the outer switch S_1 and clamping diode D_p. It can be seen that the simulation waveforms match those of the two-

level ZCT inverter at I_{Load}>0, as shown in Figure 3.6. The same features are achieved: zero-current turn-off for main and auxiliary switches, and soft turn-off for diodes.

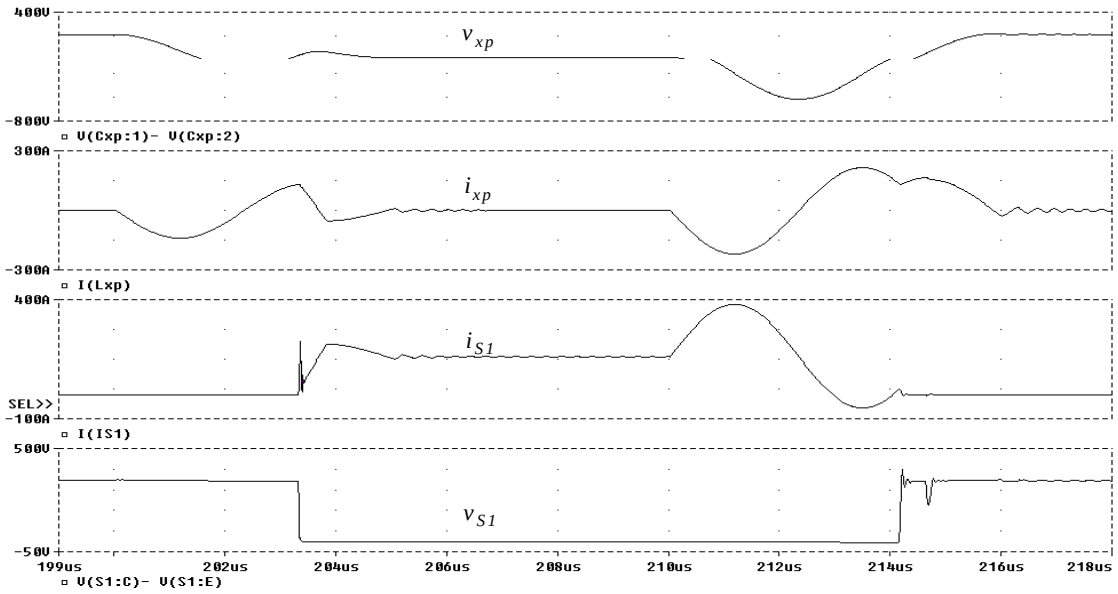

Figure 7.14. Simulation waveforms of soft commutation of the simplified three-level ZCT inverter: between the outer switch (S_1) and clamping diode (D_p).

B. Soft Commutation between the Inner Switch and Outer Diode

Figure 7.15 shows simulation waveforms of the soft commutation between the inner switch S_3 and outer diode D_1. However, some differences appear as compared to the waveforms of the two-level three-switch ZCT inverter at I_{Load}<0 (Figure 3.8). The major difference occurs at the turn-off of S_3. As can be seen from Figure 7.15(a), after the resonant current i_{xp} is built up higher than the load current, the switch current i_{s3} does not drop to zero, while for the two-level ZCT inverter, the switch current is reduced to zero when the resonant current is higher than the load current. As illustrated in Figure 7.16, this variation occurs due to the presence of clamping diode D_p. When i_{s3} decreases, D_p becomes forward-biased by the voltage induced by the parasitic inductance L_{s2}, L_{s3}, and L_{s5}~L_{s8}. Part of the resonant current flows through D_p, which forms a

freewheeling path to prevent i_{s3} from decreasing further. As a consequence, S_3 is turned off under a reduced, but not completely zero-current, condition. Nevertheless, compared to results obtained from the hard-switching turn-off simulation using the same device models and circuit parameters (Figure 7.15(b)), the instantaneous peak turn-off loss p_{s3} is still reduced from 47 kW to 6 kW, and the switch voltage stress is reduced from 430 V to 380 V.

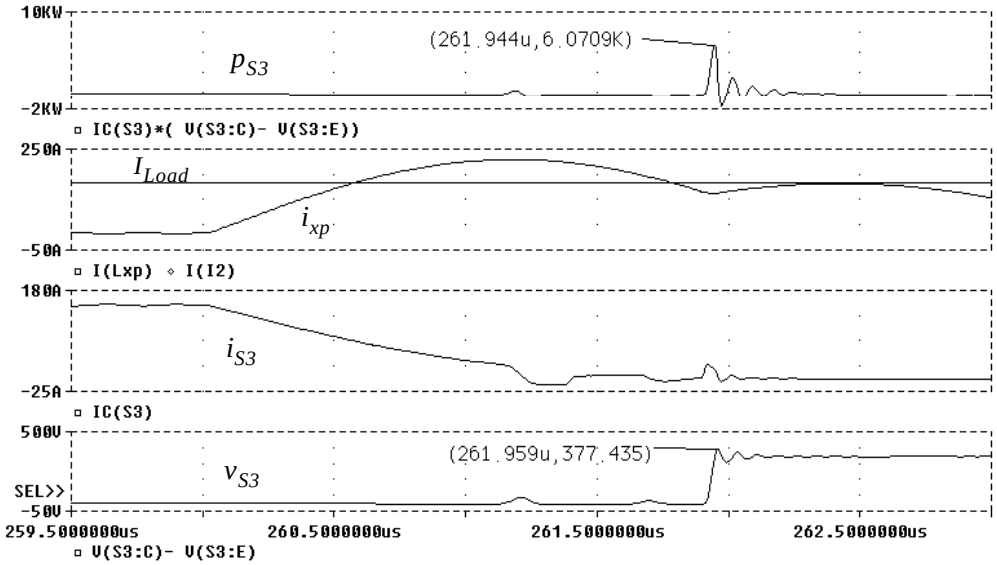

(a)

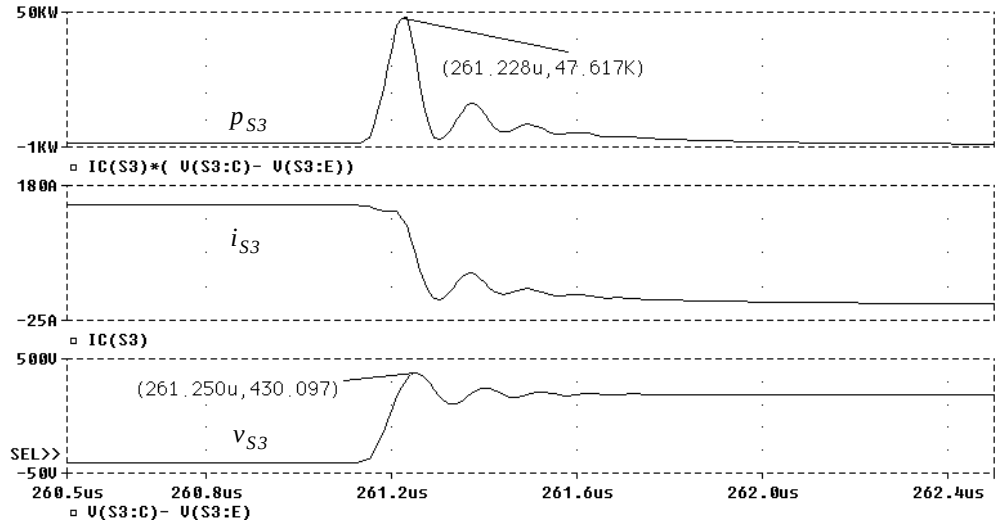

(b)

Figure 7.15. Simulated turn-off waveforms of the commutations between the inner switch S_3 and outer diode D_1 in the three-level NPC inverter:
(a) under ZCT soft switching; and (b) under hard switching.

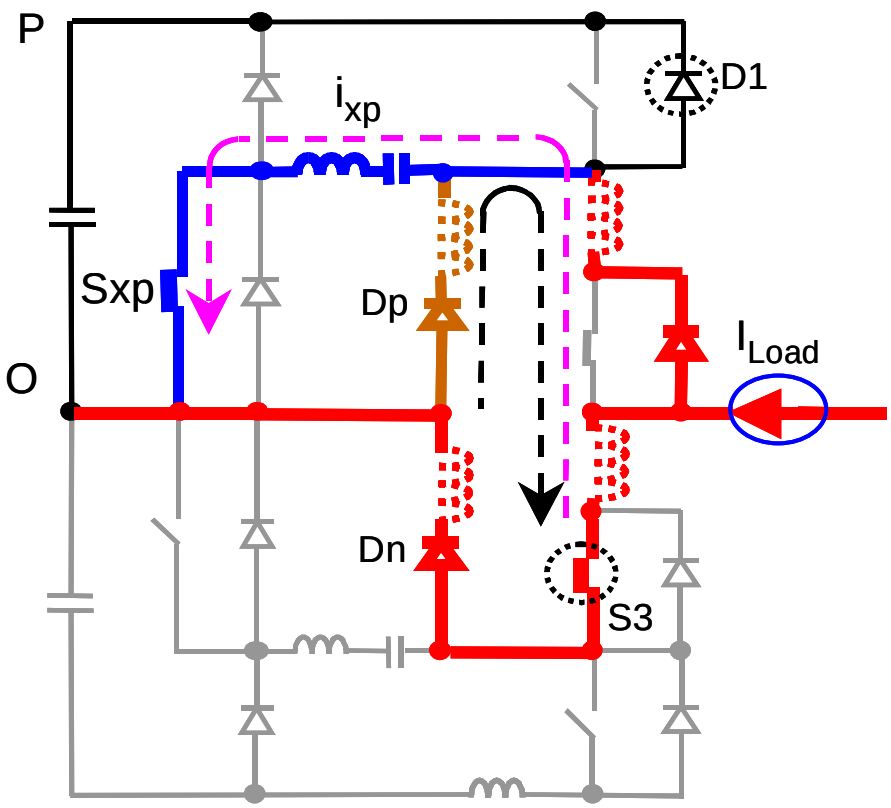

Figure 7.16. During the ZCT turn-off of S_3, clamping diode D_p forms a freewheeling path to prevent the current in S_3 from dropping to zero.

Referring to Figures 7.17 and 7.18, the detailed soft commutation between S_3 and D_1 in one switching cycle, including the parasitic effects, is described as follows.

a) *[t_0, t_1]:* Initially, load current I_{Load} flows through D_2 and D_1. Auxiliary switch S_{xp} is turned on at t_0. At t_1, i_{xp} reaches its peak and the current through D_1 is reduced to near zero.

b) *[t_1, t_2]:* S_3 is turned on at t_1 with reduced diode reverse-recovery current and switching loss. Diode D_p is forward-biased due to the voltage induced by the parasitic inductance.

c) *[t_2, t_3]:* Since the resonant tank is shorted, the currents through L_{xp}, D_p and D_2 decrease. These currents drop to zero at t_2, and D_p turns off. Since v_{xp} has increased to a peak that is higher than $V_{dc}/2$, the resonance continues, and i_{xp} is driven in the direction in which D_{xp} conducts. S_{xp} is

turned off under zero current. After a quarter of a resonant cycle, the current through switch S_3 (i_{S3}) begins to decrease. D_p is again forward-biased.

d) [t_3, t_4]: At t_3, i_{xp} returns to zero, and D_{xp} turns off. Since the magnitude of v_{xp} is still greater than $V_{dc}/2$, i_{xp} is driven in the direction in which auxiliary diode D_{x1} conducts. As the voltage across PO is applied to the resonant tank, both i_{xp} and the current through D_p decrease.

e) [t_4, t_5]: i_{xp} returns to zero at t_4, and D_{x1} and D_p turn off. I_{Load} flows through S_3 and D_n, and PWM operation resumes.

f) [t_5, t_6]: Before S_3 is turned off, S_{xp} is turned on again at t_5. As i_{xp} increases, i_{s3} decreases, and D_p is again forward-biased by the induced voltage. Because part of i_{xp} flows through D_p, i_{s3} can not drop to zero even after i_{xp} is built up higher than I_{Load}. At t_6, i_{xp} peaks, and S_3 is turned off with reduced current and switching loss.

g) [t_6, t_7]: The i_{xp} decreases, and the surplus current between i_{xp} and I_{Load} flows through D_p.

h) [t_7, t_8]: The i_{xp} falls to I_{Load} at t_7, and D_p turns off. I_{Load} flows through D_2 and charges C_{xp}.

i) [t_8, t_{10}]: C_{xp} is charged to $V_{dc}/2$, and diode D_1 starts to conduct. The resonance resumes. After t_9, i_{xp} reverses its direction and is carried by D_{xp}. S_p is turned off under zero current.

j) [After t_{10}]: The i_{xp} returns to zero at t_{10}, I_{Load} flows through D_2 and D_1, and PWM resumes.

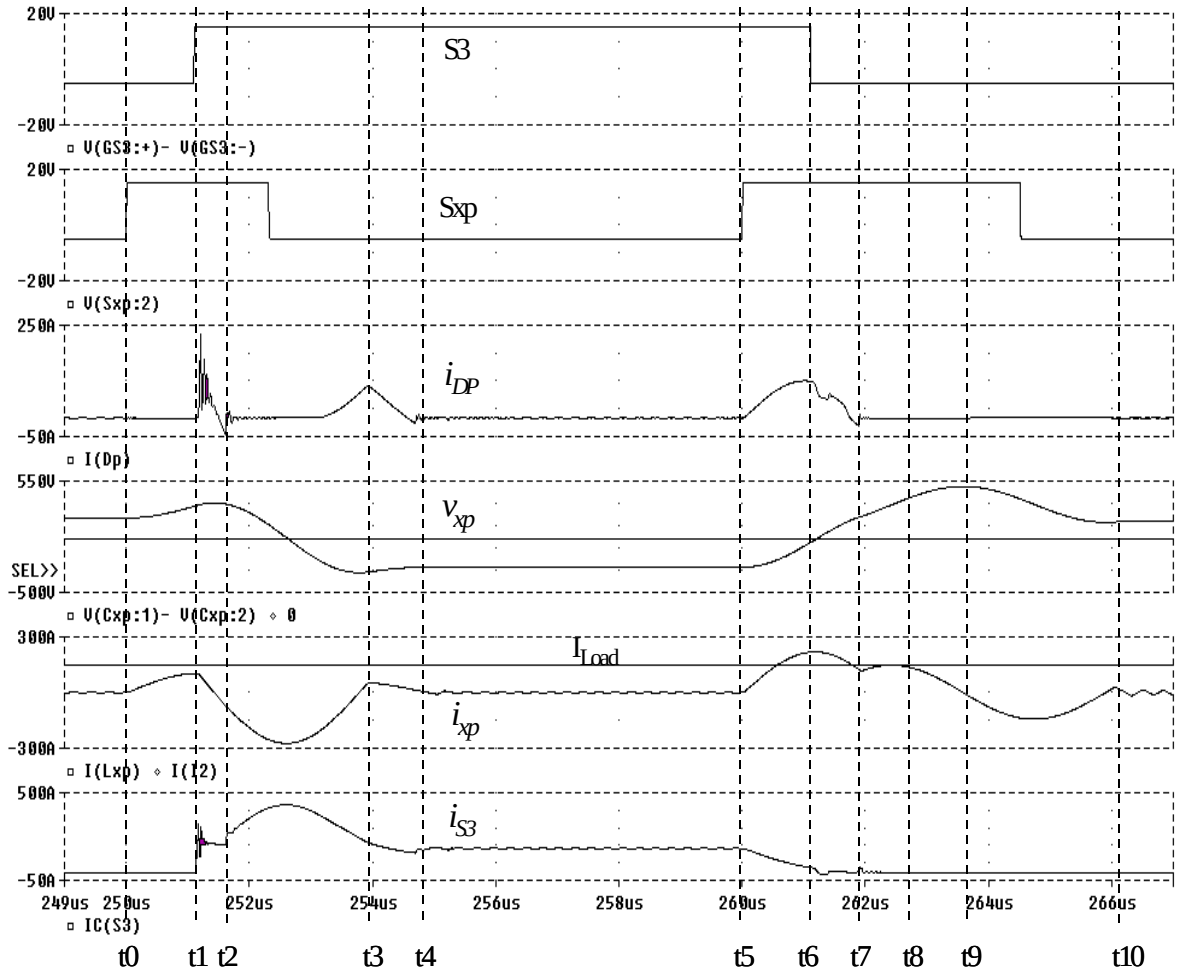

Figure 7.17. Simulation waveforms of soft commutation between inner switch S_3 and outer diode D_1 of the simplified three-level ZCT inverter in one switching cycle, including the parasitic effects.

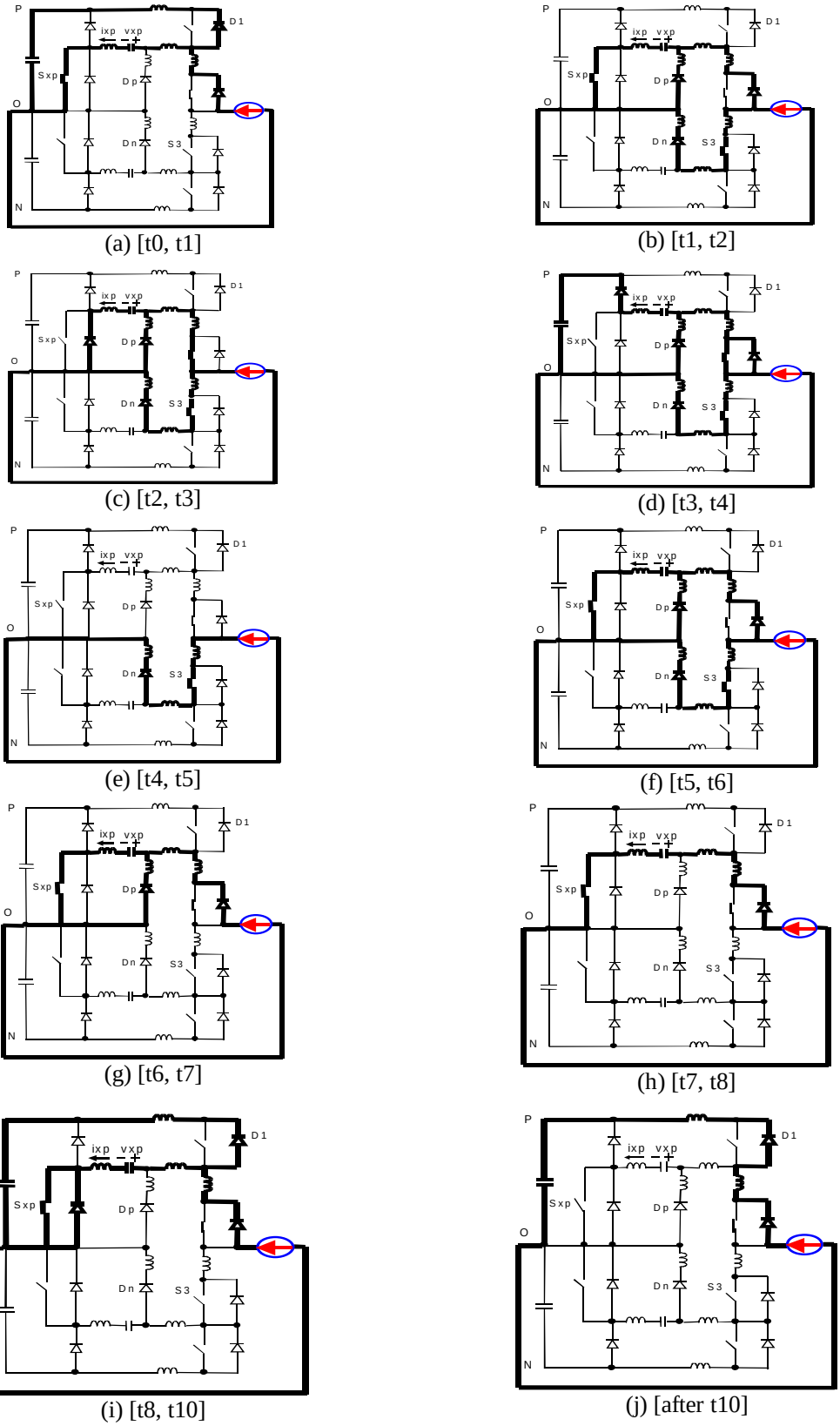

(a) [t0, t1] (b) [t1, t2]

(c) [t2, t3] (d) [t3, t4]

(e) [t4, t5] (f) [t5, t6]

(g) [t6, t7] (h) [t7, t8]

(i) [t8, t10] (j) [after t10]

Figure 7.18. Topological stages of the soft commutation between inner switch S_3 and outer diode D_1 in one switching cycle, including the parasitic effects.

7.2.4. Summary

The concept of the generic half-bridge ZCT cell is developed; it employs one auxiliary switch and one *LC* resonant tank to assist switching transitions. Application of the concept has led to a family of simplified multilevel soft-switching inverters. These inverters reduce the number of auxiliary switches by half from existing topologies and still achieve soft commutation at every switching transition in all operation modes; and in the meantime they require no modification to normal PWM schemes.

For two-level three-phase inverters, the three-switch ZCT inverter is the embodiment of this concept; it realizes both zero-current turn-off for all main and auxiliary switches as well as near-zero-current turn-off of the diodes.

For three-level three-phase inverters, only six auxiliary switches are needed for soft commutations. The simplified ZCT three-level NPC inverters have been analyzed in detail based on PSPICE simulations using actual device models and including parasitic effects. For commutations between an outer switch and a clamping diode, the same soft-switching features as the two-level ZCT inverter are realized. For commutations between an inner switch and an outer diode, due to the presence of the clamping diode that is connected to the outer diode, the inner switch can only achieve near-zero-current turn-off. This is because the clamping diode forms a freewheeling path to prevent the current in the inner switch from dropping to zero. However, the turn-off loss and voltage stress are still substantially reduced compared to hard-switching turn-off, and zero-current turn-off for auxiliary switches and soft turn-off for diodes are achieved.

The essence of the ZCT cell concept is modularity. It can be extended to other multilevel topologies with higher levels, and offer the potential to achieve simple low-cost soft-switching solutions for multilevel inverters.

Chapter 8
Conclusions and Future Work

8.1. Conclusions

Soft-switching techniques can increase both the switching frequency and current handling capability of the devices. While minimizing switching losses is a major expectation, the piggyback architecture is desired in soft-switching topologies, such that their implementation requires no modification to normal PWM algorithms. Meanwhile, attractive soft-switching topologies must use simple low-cost auxiliary circuits, in particular those with a minimum count of auxiliary switches. Practical issues, including design methodologies for optimizing soft-switching performance and evaluations of the advantages and limitations of soft-switching inverters for particular applications using state-of-the-art devices and components, are also important and challenging.

Motivated by these challenges, this dissertation has been dedicated to a unified and comprehensive study of the ZCT techniques for high-power three-phase PWM inverter applications. Major efforts in this study are as follows: 1) Conception of one new ZCT scheme and one new ZCT topology; 2) Systematic comparison of a family of ZCT inverters; 3) Design, implementation and experimental evaluation of two 55-kW prototype inverters for EV motor drives that are developed based on the proposed ZCT concepts; and 4) Investigation of the ZCT concepts in megawatts high-frequency power conversions. The major accomplishments and conclusions are summarized below.

1) Conception of One New ZCT Scheme and One New ZCT Topology

In order to minimize the switching losses, Chapter 2 proposes a new ZV/ZCT control scheme for the six-switch ZCT inverter circuit that improves performance by providing an opportunity to achieve zero-voltage turn-on for the main switch, and in the meantime enabling all main switches, diodes and auxiliary switches to be turned off under zero-current conditions. Meanwhile, the proposed ZV/ZCT scheme requires no modification to normal PWM algorithms. The philosophy behind the ZV/ZCT scheme is as follows: It fully utilizes the bi-directional property of the inverter load current and thus uses two auxiliary switches to alternately assist the turn-on and turn-off transitions of one main switch without adding extra devices or components to the existing ZCT inverter circuit. As a result, it can generate sufficient resonant energy to build up resonant currents that totally diverts the currents in the main circuit to the auxiliary circuit at both the turn-on and turn-off transitions.

However, a big drawback of the six-switch ZV/ZCT inverter, as well as with other types of soft-switching topologies using six auxiliary switches, is the high cost and large space associated with the auxiliary switches. To overcome this drawback, Chapter 3 proposes a simplified three-phase ZCT inverter topology that uses only three auxiliary switches. The significance of the proposed three-switch ZCT topology is that, among three-phase soft-switching inverters developed so far, this is the only one that uses *fewer* than six auxiliary switches and still has the following three features: 1) soft commutation for all main switches, diodes and auxiliary switches in all operation modes; 2) no modification to normal PWM schemes; and 3) in practical implementations, no need for extra resonant current sensing, saturable cores, or snubbers to protect the auxiliary switches. The philosophy behind the three-switch ZCT topology is as follows: It fully utilizes the bi-directional property of the *LC* resonant current, and thus instead of

assigning one auxiliary switch to each main switch, it employs only one auxiliary switch per phase leg to assist the soft transitions of all switches and diodes in this phase leg. As a result, it reduces the number of auxiliary switches by half from the existing topologies and still achieves similar soft-commutation features.

2) Systematic Comparison of a Family of Three-Phase ZCT Inverters

Chapter 4 conducts a systematic comparative study of the family of ZCT inverters, which consists of five schemes for the six-switch inverter circuit (including the proposed ZV/ZCT scheme) and the proposed three-switch ZCT topology. A simplified equivalent circuit is presented to unify the common traits of ZCT commutations. With the visual aid of state planes, the evolution of the ZCT inverter technique is examined, and the inherent connections and differences between these ZCT inverters are identified. The comparative study indicates that the step-by-step improvements of switching conditions are normally associated with trade-offs, on such aspects as the time occupied by the resonant process, circulating energy, voltage/current stresses, and/or auxiliary switch counts. It suggests that the six-switch ZV/ZCT has the best overall soft-switching features, and that the three-switch ZCT can be a simple low-cost soft-switching solution.

3) Design, Implementation, and Experimental Evaluation of Two 55-kW ZCT Prototype Inverters for EV Motor Drives

3.A. Design Considerations

Chapter 5 presents in detail the design considerations two 55-kW prototype inverters for EV motor drives, which are developed based on the six-switch ZV/ZCT scheme and three-switch ZCT topology. Different design aspects of these two inverters are compared. The design approach integrates system optimization with switching characterizations of main IGBT devices,

design, selection and characterization of auxiliary devices and components, loss modeling and analysis, system-level operation aspects, and layout and parasitic considerations. Some important results are listed as follows.

a) Switching Characterization of the Main IGBT (MG300J2YS50, 300-A/600-V, Half-Bridge) under the ZCT Conditions

Both ZCT operations almost eliminate the turn-off loss, and their difference mainly occurs in the turn-on loss. Compared to hard switching, the three-switch ZCT can reduce the turn-on loss by about 40%, and the total switching loss by about 70%; the six-switch ZV/ZCT can reduce the turn-on loss by about 75%, and the total switching loss by about 90%. The effect of the conductivity modulation lag, which is common in the turn-on process of most ZVS inverters, is observed for the first time in the six-switch ZV/ZCT inverter. Moreover, with different resonant tank designs, the ZCT turn-off loss is basically unchanged, but the turn-on losses and behaviors vary quite substantially between the two ZCT operations. For the three-switch ZCT, reducing L_x can significantly increase the turn-on loss, but increasing L_x on the other hand has a limited effect in reducing the turn-on loss. For the six-switch ZV/ZCT, reducing L_x does not significantly increase the turn-on loss. Resonant tanks also affect the diode reverse recovery and the range of ZCT operations.

b) Design of Resonant Tank Components

The design of resonant tanks aims to optimize the total inverter losses over the entire speed/torque range of EV drives. Generalized equations of auxiliary circuit current stresses are developed, which provide assistance to select the resonant capacitors. The resonant inductor core losses, which are caused by discontinuous nonsinusoidal flux excitations, are modeled and calculated based on the modified Steinmetz equation. Following the core loss model, optimization of the inductor design is performed, which results in low loss and small size.

c) Selection, Testing, and Characterization of Auxiliary Devices

The selection of auxiliary switches is mainly determined by the peak current handling capability, and is quite different from conventional applications. It is found that current ratings specified in data sheets of commercial IGBT devices cannot match the requirements for the auxiliary switches: low average (10~20 A), high peak (400 A), sinewave of 3~6 μs pulse width, repetitive frequency of 10~20 kHz, and zero-current turn-off. A single-shot and a continuous resonant tester are proposed for the auxiliary device selection and characterization. The tests on a group of IGBTs show that a sample 39-A IGBT can continuously operate to 400-A peak current with 200-kHz resonant frequency under a repetitive frequency of 10 kHz, and the IGBT peak current capability suitable for the auxiliary switches is largely dependent on manufacturers. A method for estimating the IGBT peak current capability from data sheets is recommended; this approach utilizes the transfer characteristic curves as the comparison index. A new parameter, namely the DC transconductance G_{DC}, is defined to quantify the difference in the peak current handling capabilities. It is suggested that IGBTs with higher G_{DC} tend to have higher peak current capability.

d) ZCT Inverter Loss Modeling and Numerical Analysis

An analytical ZCT inverter loss model is developed to assist the design optimization and to predict the trend in loss reduction. A threshold control method is proposed to achieve a proper trade-off between the switching losses and additional conduction loss caused by the ZCT commutations. Numerical analysis based on the loss model shows that threshold control is effective in minimizing the total inverter losses. The different loss mechanisms and distributions between the two ZCT inverters are demonstrated. Loss breakdowns are conducted, which provide insights into the operations of both inverters.

e) System-level Operation and Parasitic Effects

Analysis of the system-level operations indicates that the ZCT inverters are easy to start and have smooth transitions with bi-directional load current. Generalized equations are developed for the duty-cycle difference between the ideal and actual PWM control signals and the pulse-width limits, which are caused by the soft commutations. The duty-cycle difference is almost negligible, but the pulse-width limits may have negative impact on the control performance in certain applications. Methods for alleviating this impact are suggested. Layout and parasitic issues are addressed. The ZCT commutations can absorb the stray inductance as part of the resonant inductance, and the sensitivity analysis indicates that the layout of the 55-kW prototypes is physically feasible in implementations.

3.B. Prototype Implementation and Evaluation

As presented in Chapter 6, both 55-kW ZCT inverter prototypes have been completely implemented and tested to the full-power level with a closed-loop controlled induction motor dynamometer. This work enhances the proof of the proposed concepts for high-power AC adjustable speed drives, and verifies the design methods presented in Chapter 5. Moreover, it provides a comprehensive evaluation of the ZCT techniques for the EV motor drive application.

As indirect measures of cost, quality and reliability, the complexity of the 55-kW prototypes is compared, on such aspects as the numbers and ratings of all the devices and components that are actually used in the implementations, overall size, and compatibility with hard-switching inverters. The true piggyback merit of both ZCT inverters is demonstrated; they require no modification to normal SVM and cause the minimal modification to hard-switching inverters in both hardware and software. In particular, the three-switch ZCT inverter requires the least cost and space compared to other soft-switching inverters, and it is also more reliable.

The ZCT inverter operations are fully characterized under the dynamometer tests, for both electrical and thermal properties. The desirable soft transitions are realized at all testing points. The implementation of ZCT soft switching shows no interference with the closed-loop control of the induction motor within the entire speed/torque range. No devices or components showed any sign of over-heating, abnormality or failure. The measured temperature rises of the auxiliary devices are quite low, which indicates that there is only a small amount of power dissipation.

Steady-state tests are carried out at 14 speed/torque points in typical EV driving cycles. The efficiency comparison indicates that under V_{dc}=325 V and f_s=10 kHz, and using MG300J2YS50 IGBT as the main switches, the ZCT inverters do not show noticeable efficiency improvement over the hard-switching inverter for this EV drive application. This is mainly because for the MG300J2YS50 IGBT, the conduction loss is much higher than the switching loss, and thus the conduction loss is quite dominant in the total inverter losses. It is predicted that with higher switching frequencies and/or higher DC input voltage, the effect of switching loss reduction will have more impact on the total inverter losses, and the efficiency benefit of soft switching will be maximized.

4) Investigation of the ZCT Concepts in Megawatts High-Frequency Power Conversions

As documented in Chapter 7, the investigation of the ZCT concepts for megawatts high-frequency power conversions has shown potential benefits. The ZV/ZCT soft-switching test on the IGCT (ABB 5SHY35L4503) is promising. The turn-on loss is almost eliminated for the main switch, and the reverse-recovery problem of the main diode is solved. The turn-off loss is reduced by 89% compared to hard switching, and the voltage overshoot at turn-off is eliminated. It is important to remember that a complete hard-switching turn-on of the IGCT is impossible.

Either passive snubbers or soft-switching circuits are needed to control the turn-off of the main diode. When the ZCT circuit is used to replace the conventional RLD turn-on snubber, the power consumption associated with the snubber is also eliminated.

System-level benefits of the ZCT inverter equipped with the IGCT device are discussed. Preliminary analysis of a 5-MVA sample three-phase inverter shows that under the ZV/ZCT soft-switching condition, the IGCT switching frequency can be increased from 1 kHz to 4 kHz, and in the meantime the cooling method for the press-pack IGCT can be simplified from the double-side cooling to the single-side cooling.

Following the three-switch ZCT topology, a concept of the generic half-bridge ZCT cell is generalized. Application of the ZCT cell concept leads to the discovery of a family of simplified multilevel soft-switching inverters that reduce the number of auxiliary switches by half and still achieve soft commutation at every transition in all operation modes without requiring modification to normal PWM schemes. The simplified ZCT three-level NPC inverters are analyzed in details, based on a PSPICE simulation using actual device models and including parasitic effects. The essence of the ZCT cell concept is modularity. It can be extended to other multilevel topologies with higher levels, and offers the potential to achieve simple low-cost soft-switching solutions.

8.2. Future Work

The effectiveness of soft-switching techniques relies heavily on both the characteristics of the devices used and inverter operation conditions. The dynamometer test on the two 55-kW ZCT inverter prototypes, with V_{dc}=325 V and f_s=10 kHz and using MG300J2YS50 IGBTs as the main switches, did not show a noticeable efficiency improvement over hard-switching inverters for the

EV motor drive application. To further explore the potential for efficiency improvement, one future work would test the inverters under higher switching frequencies. In addition, for the MG300J2YS50 IGBT, the conduction loss is found to be much higher than the switching loss, so investigation into other types of IGBT devices that might be more suitable for soft-switching inverters in the EV application is another area for future research.

This dissertation has also investigated ZCT techniques in megawatts high-frequency power conversion applications, and has shown some promising results. In these applications, the fundamental limits of power devices are being reached, while high switching frequency and small ripples are normally mandatory; thus, the use of soft switching could have a great impact. Another important direction for future work, therefore, is to further characterize the ZCT techniques with state-of-the-art high-power devices, to develop practical design methods for the megawatts high-frequency converters, and to conduct experimental evaluations.

REFERENCES

A. Soft-Switching Techniques for DC/DC Converters

[A1] G. Hua and F. C. Lee, "A new class of zero-voltage-switched PWM converters," in *Proc. IEEE-HFPC*, 1991, pp. 244-251.

[A2] G. Hua, C. S. Leu, and F. C. Lee, "Novel zero-voltage-transition PWM converters," in *Proc. IEEE-PESC*, 1992, pp. 55-61.

[A3] I. Barbi and D. C. Martins, "A true PWM zero-voltage switching pole with very low additional RMS current stress," in *Proc. IEEE-PESC*, 1991, pp. 261-267.

[A4] D. C. Martins, F. J. M. DeSeixas, J. A. Brihante, and I. Barbi, "A family of DC-to-DC PWM converter using a new ZVS commutation cell," *Proc. IEEE-PESC*, 1993, pp. 538-544.

[A5] J. P. Gegner and C. Q. Lee, "Zero-voltage-transition converters using inductor feedback techniques," in *Proc. IEEE-APEC*, 1994, pp. 862-868.

[A6] J. P. Gegner and C. Q. Lee, "Zero-voltage-transition converters using a simple magnetic technique," in *Proc. IEEE-PESC*, 1994, pp. 590-596.

[A7] R. L. Lin and F. C. Lee, "Novel zero-current-switching zero-voltage-switching converters," in *Proc. IEEE-PESC*, 1996, pp. 438-442.

[A8] G. Hua and F. C. Lee, "An overview of soft-switching techniques for PWM converters," in *Proc. IEE-EPE*, 1993, pp. 12-26.

[A9] W. McMurray, "Thyristor commutation in DC choppers— a comparative study," *IEEE Trans. Ind. Applicant*. vol.14-6, 1978, pp. 547-558.

B. Soft-Switching Techniques for DC-Side Three-Phase Converters

[B1] D. M. Divan, "The resonant DC-link converter— a new concept in static power conversion," in *Proc. IEEE-IAS Annu. Meeting*, 1986, pp. 648-656.

[B2] D. M. Divan and G. Skibinski, "Zero switching loss inverters for high power applications," in *Proc. IEEE-IAS Annu. Meeting*, 1987, pp. 627-634.

[B3] G. Venkataramanan, D. M. Divan, and T. M. Jahns, "Discrete pulse modulation strategies for high frequency inverter systems," *IEEE Trans. Power Electron.*, vol. 8, 1993, pp. 279-287.

[B4] G. Venkataramanan and D. M. Divan, "Pulse width modulation with resonant DC link converters," *in Proc. IEEE-IAS Annu. Meeting*, 1990, pp. 984-990.

[B5] S. Chen and T. A. Lipo, "Soft-switched inverter for electric vehicle drives," in *Proc. IEEE-APEC*, 1995, pp. 586-591.

[B6] S. Chen and T. A. Lipo, "A passively clamped quasi resonant DC link inverter," in *Proc. IEEE-IAS Annu. Meeting*, 1994, pp. 841-848.

[B7] V. Ageligis, P. D. Ziogas, and G. Joos, "An optimum modulation strategy for a novel notch commutated 3-Φ PWM inverter," in *Proc. IEEE-IAS Annu. Meeting*, 1991, pp. 809-818.

[B8] J. S. Lai and B. K. Bose, "A high frequency quasiresonant DC voltage notching inverter for AC motor drive," in *Proc. IEEE-IAS Annu. Meeting*, 1990, pp. 1202-1207.

[B9] S. Salama and Y. Tadros, "Novel soft-switching quasi resonant 3-phase IGBT inverter," in *Proc. IEEE-PESC*, 1995, pp. 28-33.

[B10] B. J. Filho and T. A. Lipo, "Space vector analysis and modulation issues of passively clamped quasiresonant inverters," in *Proc. IEEE-IAS Annu. Meeting*, 1996, pp. 1179-1185.

[B11] J. He and N. Mohan, "Parallel resonant DC-link circuit— a novel zero switching loss topology with minimum voltage stresses," in *Proc. IEEE-PESC*, 1989, pp. 1006-1012.

[B12] J. Cho, H. Kim, and G. Cho, "Novel soft-switching PWM converter using a parallel resonant DC-link," in *Proc. IEEE-PESC*, 1991, pp. 241-247.

[B13] R. W. DeDonker and J.P. Lyons, "The auxiliary quasi-resonant DC link inverter," in *Proc. IEEE-PESC*, 1991, pp. 248-253.

[B14] L. Malesani, P. Tenti, P. Tomasin, and V. Toigo, "High efficiency quasi resonant DC-link converter for full-range PWM," in *Proc. IEEE-APEC*, 1992, pp. 472-478.

[B15] Y. Chen, "A new quasi-parallel resonant DC link for soft-switching PWM inverters," *IEEE Trans. Power Electron*. vol. 13, May/June, 1998, pp. 427-435.

[B16] K. Wang, Y. Jiang, S. Dudovsky, G. Hua, D. Boroyevich, and F. C. Lee, "Novel DC-rail soft switching three-phase voltage source inverter," *IEEE Trans. Ind. Applicat.*, vol. 23, no. 2, pp. 509-516, 1997.

[B17] Y. Jiang, H. Mao, F. C. Lee, and D. Boroyevich, "Simple high performance three-phase boost rectifiers," in *Proc. IEEE-PESC*, 1994, pp. 1158-1163.

[B18] P. Tomasin, "A novel topology of zero-current switching voltage-source PWM inverter for high power applications, " in *Proc. IEEE-PESC*, 1995, pp. 1245-1251.

C. Soft-Switching Techniques for AC-Side Three-Phase Converters

[C1] W. McMurray, "Resonant snubbers with auxiliary switches," *IEEE Trans. Ind. Applicat.*, vol. 29, March/April, 1993, pp. 355-362.

[C2] R. W. DeDonker and J.P. Lyons, "The auxiliary resonant commutated pole converter," in *Proc. IEEE-IAS Annu. Meeting*, 1990, pp. 1228-1235.

[C3] S. Frame, D. Katsis, D. H. Lee, D. Boroyevich, and F. C. Lee, "A three-phase zero-voltage-transition inverter with inductor feedback," in *Proc. VPEC Seminar*, 1996, pp. 189-193.

[C4] X. Yuan and I. Barbi, "Analysis, designing, and experimentation of a transformer-assisted PWM zero-voltage switching pole inverter," *IEEE Tran. Power Electron.*, vol. 15, no. 1, Jan. 2000, pp. 72-82.

[C5] J. S. Lai, R. W. Young, G. W. Ott, C. P. White, J. W. Mckeever, and D. S. Chen, "A novel resonant snubber inverter," in *Proc. IEEE-APEC*, 1995, pp. 797-803.

[C6] J. S. Lai, R. W. Young, G. W. McKeever, and F. Z. Peng, "A delta-configured auxiliary resonant snubber inverter," *IEEE Trans. Ind. Applicant.*, vol. 32-3, May/June 1996, pp. 518-524.

[C7] J. S. Lai, "Fundamentals of a new family of auxiliary resonant snubber inverters," in *Proc. IEEE-IECON*, 1997, pp. 645-650.

[C8] H.G. Eckel, L. Sack and K. Rascher, "FPGA based control of an ARCP inverter without additional sensors," in *Proc. IEE-EPE*, 1997, pp. 4385-4390.

[C9] J. Choi, D. Boroyevich, and F. C. Lee, "A novel ZVT inverter with simplified auxiliary circuit," in *Proc. IEEE-APEC*, 2001, pp. 1151-1157.

[C10] V. Vlatkovic, D. Boroyevich, F. C. Lee, C. Caudros, and S.Gatatric, "A new zero-voltage-transition three-phase PWM rectifier/inverter circuit," in *Proc. IEEE-PESC*, 1993, pp. 868-873.

[C11] C. Cuadros, D. Borojevich, S. Gataric V. Vlatkovic, H. Mao, and F. C. Lee, "Space vector modulated zero-voltage-transition three-phase to DC bi-directional converter," in *Proc. IEEE-PESC*, 1994, pp. 16-23.

[C12] H. Mao and F. C. Lee, "An improved zero-voltage-transition three-phase rectifier/inverter," in *Proc. IEEE-IPEC*, 1995, pp. 848-853.

[C13] Q. Li, X. Zhou, and F. C. Lee, "A novel ZVT three-phase bidirectional rectifier with reduced auxiliary switch stresses and losses," in *Proc. IEEE-PESC*, 1996, pp. 153-158.

[C14] J. Choi, D. Boroyevich, and F. C. Lee, "Improved ZVT three-phase inverter with two auxiliary switches," in *Proc. IEEE-APEC*, 2000, pp. 1023-1029.

[C15] J. Choi, D. Boroyevich, and F. C. Lee, "Phase-lock circuit for ZVT inverters with two auxiliary switches," in *Proc. IEEE-PESC*, 2000, pp. 1215-1220.

[C16] J. Choi, D. Boroyevich, and F. C. Lee, "Thyristor-assisted ZVT inverters with single coupled inductor for high power applications," in *Proc. IEEE-IAS*, 2000, pp. 2156-2163.

[C17] W. McMurray, "SCR inverter commutated by an auxiliary impulse," *IEEE Trans. Communications and Electronics*, vol. 8-75, Nov./Dec. 1964, pp. 824-829.

[C18] General Electric Company, *SCR Manual*, 6th ed., New York: GE, 1979.

[C19] G. Hua, E. Yang, Y. Jiang, and F. C. Lee, "Novel zero-current-transition PWM converters," in *Proc. IEEE-PESC*, 1993, pp. 538-544.

[C20] H. Mao, F. C. Lee, X. Zhou, and D. Boroyevich, "Improved zero-current-transition converters for high power applications," in *Proc. IEEE-IAS Annu. Meeting*, 1996, pp. 1145-1152.

[C21] J. Wu, H. Dai, K. Xing, F. C. Lee, and D. Boroyevich, "Implementation of a 100-kW three-phase PFC rectifier with ZCT soft-switching technique," in *Proc. VPEC Seminar*, 1998, pp. 109-116.

D. Multilevel Power Converters

[D1] D. Boroyevich, A. Q. Huang, F. C. Lee, J. D. van Wyk, G. Q. Lu, T. A. Lipo, and G. Venkataramanan, "Advanced high power conversion systems for EMALS/EARS," *Project Proposal Prepared for Office of Naval Research*, April 2001.

[D2] A. Nabae, I. Takahashi, and H. Akagi, "A new neutral-point clamped PWM inverter," *IEEE Trans. Ind. Applicat.*, no. 5, Sept./Oct. 1981, pp. 518-523.

[D3] P. M. Bhagwat and V. R. Stefanovic, "Generalized structure of a multilevel PWM inverter," *IEEE Trans. Ind. Applicat.*, no. 6, Nov./Dec. 1983, pp. 1057-1069.

[D4] T. A. Meynard and H. Foch, "Multilevel conversion: high voltage choppers and voltage source inverters," in *Proc. IEEE-PESC*, 1992, pp. 397-403.

[D5] H. Stemmler, "Power electronics in electric traction applications," in *Proc. IEEE-IECON*, 1993, pp. 707-713.

[D6] C. Hochgraf, R. Lasseter, D. M. Divan, and T. A. Lipo, "Comparison of multi-level inverters for static var compensation," in *Proc. IEEE-IAS Annu. Meeting*, 1994, pp. 921-928.

[D7] J. S. Lai and F. Z. Peng, "Multilevel converters— a new breed of power converters," in *Proc. IEEE-IAS Annu. Meeting*, pp. 2348-2356, 1995.

[D8] B. S. Suh, G. Sinha, M. D. Manjrekar, and T. A. Lipo, "Multilevel power conversion - an overview of topologies and modulation strategies," in *Proc. Optim'98 Conf.*, pp. AD11-AD24, 1998.

[D9] W. Yi and G. H. Cho, "Novel snubberless three-level GTO inverter with dual quasi-resonant DC-link," in *Proc. IEEE-PESC*, 1991, pp. 880-884.

[D10] T. Bruckner and S. Bernet, "Investigation of a high power three-level quasi-resonant DC-link voltage source inverter," in *Proc. IEEE-APEC*, 2000, pp. 1015-1022.

[D11] J. G. Cho, J. W. Baek, D. W. Yoo, and C. Y. Won, "Three-level auxiliary resonant commutated pole inverter for high power applications," in *Proc. IEEE-PESC*, 1996, pp. 1019-1026.

[D12] X. Yuan and I. Barbi, "A transformer assisted zero-voltage switching scheme for the neutral-point-clamped (NPC) inverter," in *Proc. IEEE-APEC*, 1999, pp. 1259-1265.

[D13] X. Yuan and I. Barbi, "ARCPI resonant snubber for the neutral-point-clamped (NPC) inverter," in *Proc. IEEE-IAS Annu. Meeting*, 1999, pp. 1157-1164.

[D14] H. Mao, D. H. Lee, H. Dai, F. C. Lee, and D. Boroyevich, "Evaluation and development of new power electronic technologies for superconducting magnetic energy storage (SMES) using PEBB," in *Proc. 15 th VPEC Seminar*, Sept. 1997, pp. 129-134.

[D15] D. H. Lee, D. Peng, Y. Li, F. C. Lee, D. Boroyevich, D. Y. Chen, J. S. Lai, and A. Huang, "Advanced power electronics techniques for superconducting magnectic energy storage power conditioning system," *SMES 2nd Phase Report*, VPEC, June 30, 1996.

[D16] D. Boroyevich, F. C. Lee, K. Xing, D. H. Lee, and H. Dai, "Use of power electronics building block concept for medium power conversion," *PEBB Workshop*, VPEC, Oct. 1997.

E. Power Devices and Components

[E1] K. Wang, F. C. Lee, G. Hua, and D. Boroyevich, "A comparative study of switching losses of IGBTs under hard-switching, zero-voltage-switching and zero-current-switching conditions," in *Proc. IEEE-PESC*, 1994, pp. 1196-1204.

[E2] A. Kurnia, O. H. Stielau, G. Venkataramanan, and D. M. Divan, "Loss mechanism of IGBTs under zero-voltage switching," in *Proc. IEEE-PESC*, 1992, pp. 1011-1017.

[E3] A. Kurnia, H. Cherradi and D. M. Divan, "Impact of IGBT behavior on design optimization of soft-switching inverter topologies," in *Proc. IEEE-IAS Annu. Meeting*, 1993, pp. 807-813.

[E4] J. G. Kassakin, M. F. Schlecht, and G. C. Verghese, *Principles of Power Electronics*, Addison-Wesley Publishing Company, 1991.

[E5] R. Rangan, D. Y. Chen, J. Yang, and J. Lee, "Applications of insulated gate bipolar transistor to zero-current switching converters," *IEEE Trans. Power Electronics*, vol. 4-1, Jan./Feb. 1989, pp. 2-7.

[E6] *Toshiba IGBT Data Book*, Toshiba Electronics Europe, 1995.

[E7] Terry Hosking, "Application notes for SBE power capacitors with aluminum rail terminals," SBE Company, March 1999.

[E8] M. A. Swihart, "Designing with magnetics cores at high temperatures," *MAGENECTICS Bulletin*, No. FC-xxx, PA, 1999.

[E9] T. Durbaum and M. Albach, "Core losses in transformers with an arbitrary shape of the magnetization current," in *Proc. IEE-EPE*, vol. 1, 1995, pp. 1.171-1.176.

[E10] J. Reinert, A. Brockmeyer, and R. W. DeDonker, "Calculation of losses in ferro- and ferromagnetic materials based on the modified Steinmetz equation," *IEEE Trans. Ind. Applicat.*, vol. 37-4, July/Aug. 2001.

[E11] J. Li, T. Abdallah, and C. R. Sullivan, "Improved calculation of core loss with nonsinusoidal waveforms," in *Proc. IEEE-IAS Annu. Meeting*, 2001, pp. 2203-2210.

[E12] A. P. Steinmetz, "On the law of hysteresis," *AIEE Transactions*, vol. 9, 1892, pp. 3-64. Reprinted under the title "A Steinmetz contribution to the AC power revolution," introduced by J. E. Brittain, *in Proceedings of the IEEE*, vol. 72-2, 1984, pp. 196-221.

[E13] *MAGNETICS MPP Core Data Book*, Magnetics Company, PA, 1999.

[E14] [Online] Available: http:// www.irf.com/, "Current ratings of power semiconductors," Application Note AN-949, International Rectifier Company.

[E15] *IGBT Data Sheets*, International Rectifier Company.

[E16] *IGBT Data Sheets*, Harris Company.

[E17] [Online] Available: http://www.eupec.com/igbt/600VIGBT_half.htm.

[E18] *Powerex IGBT and Intellimod Applications and Technical Data Book*, 1st ed., Powerex Company, 1994.

[E19] [Online] Available: http:// www.irf.com/, "IGBT characteristics", Application Note AN-983, International Rectifier Company.

[E20] K. Motto, Y. Li, and A. Q. Huang, "Comparison of the state-of-the art high power IGBTs, GCTs, and ETOs," in *Proc. IEEE-APEC*, 2000, pp. 1137-1143.

[E21] K. Motto, *Applications of High-Power Snubberless Semiconductor Switches in High-Frequency PWM Converters*, Master Thesis, Blacksburg, VA, Nov. 2000.

[E22] [Online] Available: http:// www. Abbsem. com/english/igct.htm.

F. Soft-Switching Converter Design and Evaluation

[F1] M. Bellar, T. Wu, A. Tchamdjou, J. Mahdavi, and M. Ehsani, "A review of soft-switched DC-AC converters," *IEEE Trans. Ind. Applicat.*, vol. 34-4, July/Aug. 1998, pp. 847-860.

[F2] F. Huliehel, F. C. Lee, and B. H. Cho, "Small-signal modeling of the single-phase boost high power factor converter with constant frequency control," in *Proc. IEEE-APEC*, 1992, pp. 474-482.

[F3] R. B. Sepe and J. H. Lang, "Inverter nonlinearities and discrete-time vector current control," in *Proc. IPEC*, 1992, pp. 494-501.

[F4] W. Dong, J. Choi, Y. Li, H. Yu, J. S. Lai, D. Boroyevich, and F. C. Lee, "Efficiency consideration of load side soft-switching inverters for electric vehicle applications," in *Proc. IEEE-APEC*, 2000, pp. 1049-1056.

[F5] R. Oruganti and F. C. Lee, "Resonant power processors: part I- state plane analysis," *IEEE Trans. Ind. Applicat.*, vol. IA-21, Nov./Dec. 1985, pp. 1453-1460.

[F6] D. M. Divan, G. Venkataraman, and R. W. DeDonker, "Design methodologies for soft switched inverters," *IEEE Trans. Ind. Applicat.* vol. 29-1, Jan./Feb. 1993, pp. 126-135.

[F7] R. Gascoigne, "GM resonant DC link inverter— final test report for PNGV project," SoftSwitching Technologies Corporation, Jan. 2001.

[F8] J. S. Lai, R. W. Young, and J. W. McKeever, "Efficiency consideration of DC link soft-switching inverters for motor drive applications," in *Proc. IEEE-IAS Annu. Meeting*, 1994, pp. 1003-1008.

[F9] S. Clemente and B. Pelly, "An algorithm for the selection of the optimum power device for electric vehicle propulsion," in *Proc. IEEE Workshop on Power Electronics in Transportation*, Oct. 1992, pp. 129-136.

[F10] J. W. Kolar, H. Etrl, and F. C. Zach, "Influence of the modulation method on conduction and switching losses of a PWM converter system," *IEEE Trans. Ind. Applicant.*, vol. 27-6, Nov./Dec. 1991, pp. 1063-1075.

[F11] J. Choi, *Analysis of Inductor-Coupled Zero-Voltage-Transition Converters*, Ph.D. Dissertation, Blacksburg, VA, July 2001.

[F12] J. Wu, F. C. Lee, and D. Boroyevich, "Elimination of low-frequency harmonics caused by PWM in a three-phase soft-switched boost rectifier," in *Proc. IEEE-IAS Annu. Meeting*, 2000, pp. 2305-2310.

[F13] V. Pickert and C. M. Johnson, "Three-phase soft-switching voltage source converters for motor drives- part 1: overview and analysis," in *IEE Proc.-Electr. Power Appl.*, vol. 146, no. 2, March 1999, pp. 147-154.

[F14] C. M. Johnson and V. Pickert, "Three-phase soft-switching voltage source converters for motor drives- part 2: fundamental limitations and critical assessment," in *IEE Proc.-Electr. Power Appl.*, vol. 146, no. 2, March 1999, pp. 155-162.

[F15] W. Dong, J. Francis, F. C. Lee, and D. Boroyevich, "Maximum pulse width space vector modulation for soft-switching inverters," in *Proc. CPES-Seminar*, 2001, pp. 288-292.

[F16] J. Sun and H. Grotstollen, "Optimized space vector modulation and regular-sampled PWM: a reexamination," in *Proc. IEEE-IAS Annu. Meeting*, 1996, pp. 956-963.

[F17] H. Dai, K. Xing, and F. C. Lee, "Investigation of soft-switching techniques for power electronics building blocks (PEBB)," in *Proc. IEEE-APEC*, 1998, pp. 633-639.

[F18] W. Dong, J. Choi, H. Yu, and Fred C. Lee, "A 50-kW auxiliary resonant commutated pole inverter for electric vehicle applications– practical issues," in *Proc. CPES-Seminar*, 2000, pp. 136-141.

[F19] W. Dong, J. Choi, Y. Li, J. Francis, M. Pochet, M. Turner, F. C. Lee, D. Boroyevich, J.S. Lai, H. Yu, X. Jing, D. Katsis, and M. Ye, "Soft-switching inverters for AC adjustable speed drives," *Final Report of PNGV Project*, prepared for General Motors Research Laboratory, Jan. 2001.

G. Patents, Inventions, and Publications during the Ph. D. Study Period

[G1] Y. Li and F. C. Lee, "Three-phase zero-current-transition (ZCT) inverters and rectifiers with three auxiliary switches," *U. S. Patent* (awarded), No. 6337801.

[G2] Y. Li and F. C. Lee, "Novel zero-current-transition and quasi-zero-voltage-transition (ZCQZVT) three-phase inverter/rectifier with optimal variable timing control and reduced stresses on device and component," *Invention Disclosure*, *VTIP* No. 98-056.

[G3] Y. Li, F. C. Lee, and D. Boroyevich, "A three-phase soft-transition inverter with a novel control strategy for zero-current and near-zero-voltage switching," *IEEE Transactions on Power Electronics*, vol. 16, no. 5, Sept. 2001, pp. 710-723.

[G4] Y. Li and F. C. Lee, "A generalized zero-current-transition concept to simplify three-phase soft-switching inverters," in *Proc. IEEE-IAS 2001 Annual Meeting*, pp. 991-998.

[G5] W. Dong, J. Choi, Y. Li, D. Boroyevich, F. C. Lee, J. Lai, and S. Hiti, "Comparative experimental evaluation of soft-switching inverter techniques for electric vehicle drive applications," in *Proc. IEEE-IAS 2001 Annual Meeting*, pp. 1469-1476.

[G6] Y. Li and F. C. Lee, "Design methodologies for high-power three-phase zero-current transition inverters," in *Proc. IEEE-PESC 2001*, pp. 1217-1223.

[G7] Y. Li and F. C. Lee, "Design considerations for a 50-kW soft-transition inverter with zero-current and near-zero-voltage switching," in *Proc. IEEE-APEC 2001*, pp. 931-937.

[G8] Y. Li and F. C. Lee, "A comparative study of a family of zero-current-transition schemes for three-phase inverter applications," in *Proc. IEEE-APEC 2001*, pp. 1158-1164.

[G9] Y. Li, F. C. Lee, D. Katsis, and M. Ye, "Design of a 50-kW three-phase zero-current-transition inverter with three auxiliary switches for electric propulsion drives," in *Proc. CPES-Seminar 2001*, pp. 311-318.

[G10] Y. Li, F. C. Lee, J. S. Lai, and D. Boroyevich, "A low-cost three-phase zero-current-transition inverter with three auxiliary switches," in *Proc. IEEE-PESC 2000*, pp. 527-532.

[G11] Y. Li, F. C. Lee, J. S. Lai, and D. Boroyevich, "A novel three-phase zero-current-transition and quasi-zero-voltage-transition (ZCT-QZVT) inverter/rectifier with reduced stresses on devices and components," in *Proc. IEEE-APEC 2000*, pp. 1030-1036.

[G12] W. Dong, J. Choi, Y. Li, H. Yu, J. Lai, D. Boroyevich, and F. C. Lee, "Efficiency consideration of load side soft-switching inverters for electric vehicle applications," in *Proc. IEEE-APEC 2000*, pp. 1049-1056.

[G13] Y. Li and F. C. Lee, "Characterization and analysis of a novel three-phase zero-current-transition inverter," in *Proc. IEEE-IPEMC 2000*, pp. 163-168.

[G14] W. Dong, Y. Li, and F. C. Lee, "Evaluation of DC-link current in space vector modulated inverters," in *Proc. CPES-Seminar 1999*, pp. 286-291.

Appendix A

A Detailed Analysis of Determining Z_o in the Six-Switch ZV/ZCT Inverter

The state-plane trajectory of the six-switch ZV/ZCT scheme (Figure 2.9) is normalized by V_{dc} and the maximum load current subjected to the zero-current turn-off, I_{max}. (Note: since the purpose of this analysis is to determine the Z_o, the current is not normalized by the factor of V_{dc}/Z_o, as defined in Section 2.4.2.) The resultant normalized state-plane trajectory is shown in Figure A.1, where

$$IL_n = \frac{I_{Load}}{I_{max}}, \tag{A.1}$$

$$V_{xn} = \frac{v_x}{V_{dc}}, \tag{A.2}$$

$$Z_{on} = Z_o \frac{I_{max}}{V_{dc}}, \text{ and} \tag{A.3}$$

$$I_{xn} = \frac{I_x}{I_{max}}. \tag{A.4}$$

Under this normalization, the design variable k becomes

$$k = \frac{I_{xpk}}{IL_n}, \tag{A.5}$$

where I_{xpk} is the normalized resonant current peak during the turn-off transition.

During the interval [t_2, t_3], without considering diode reverse recovery and other parasitic effects, the resonant capacitor is charged linearly by the load current. A variable ΔV_{on} is identified as the corresponding linear voltage variation. Referring to the geometric relationship given in Figure A.1, ΔV_{on} is derived as follows.

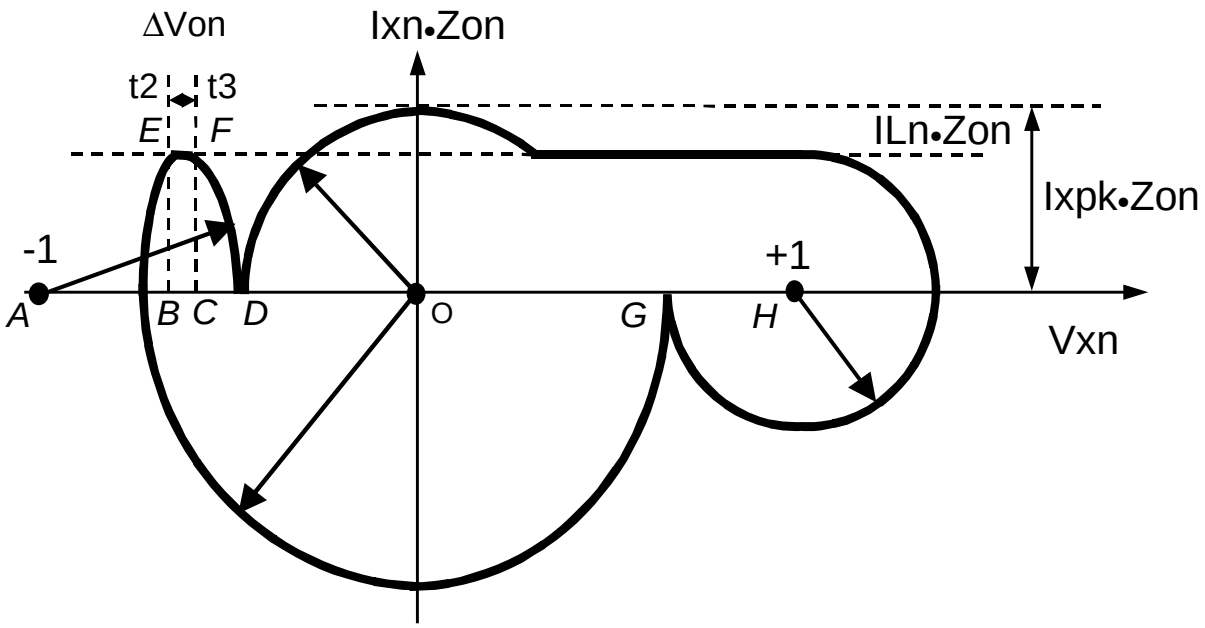

Figure A.1. Normalized state-plane trajectory of the six-switch ZV/ZCT scheme.

$$FC = IL_n \cdot Z_{on}, \tag{A.6}$$

$$AD = 1 - DO = 1 - k \cdot IL_n \cdot Z_{on}, \text{ and} \tag{A.7}$$

$$AC = \sqrt{AF^2 - FC^2} = \sqrt{AD^2 - FC^2}\ . \tag{A.8}$$

Combining (A.6) to (A.8) yields

$$CO = 1 - AC = 1 - \sqrt{(1 - k \cdot IL_n \cdot Z_{on})^2 - (IL_n \cdot Z_{on})^2}\ . \tag{A.9}$$

It is also obtained that

$$EO = OG = 1 - IL_n \cdot Z_{on}, \text{ and} \tag{A.10}$$

$$BO = \sqrt{EO^2 - EB^2} = \sqrt{1 - 2IL_n \cdot Z_{on}}\ . \tag{A.11}$$

Combing (A.9) and (A.11), therefore,

$$\begin{aligned} \Delta V_{on} &= BO - CO \\ &= \sqrt{1 - 2IL_n \cdot Z_{on}} + \sqrt{(1 - k \cdot IL_n \cdot Z_{on})^2 - (IL_n \cdot Z_{on})^2} - 1 \end{aligned}\ . \tag{A.12}$$

Equation (A.12) shows an implicit relationship among the key variables of the circuit operation, based on which the curves of ΔV_{on} against Z_{on} under the full load condition ($IL_n = 1$) are generated and plotted in Figure A.2. Since the purpose of the time between [t_2, t_3] is to ensure that the main diode can be recombined completely before the opposite main switch is turned on, this interval is short, and ΔV_{on} is small. A condition necessary for the circuit to operate in the desired ZV/ZCT mode is that the inequality $\Delta V_{on} \geq 0$ must be satisfied. The physical meaning of this inequality is that the energy stored in the resonant tank must be high enough to ensure that the current in the main circuit can be completely diverted to the auxiliary circuit at both the turn-on and turn-off transitions. As a result, the zero-crossing point of the ΔV_{on} curve in Figure A.2 is the boundary condition to determine the value of Z_{on}. The circuit can only achieve the desired soft-transition feature at the left side of this boundary. For example, in the k=1.2 case, Z_{on} is designated as 0.36. The actual vale of Z_o is then calculated by equation (A.3).

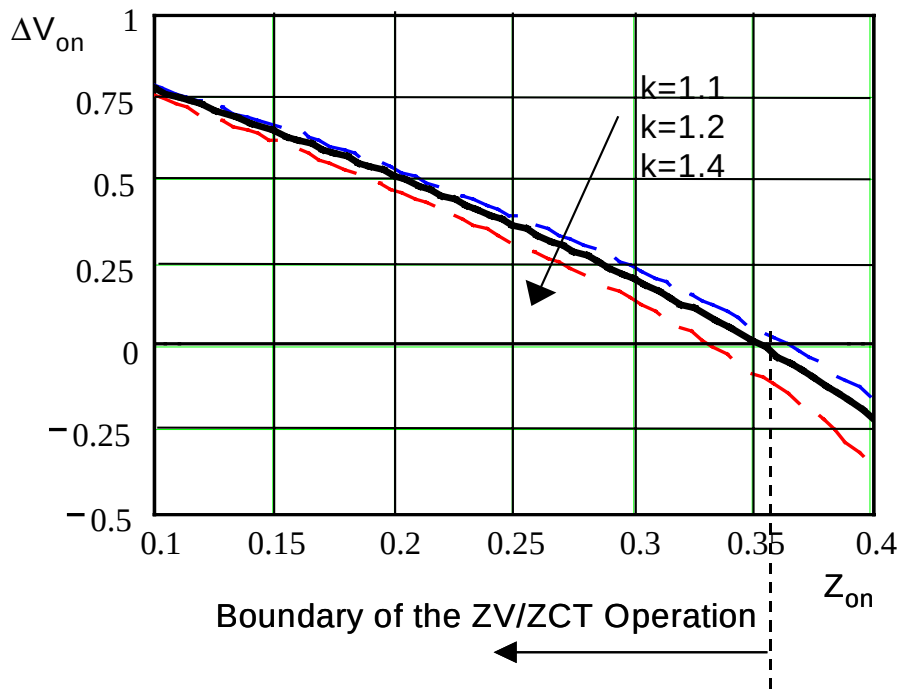

Figure A.2. Curves of ΔV_{on} against Z_{on} under the full load condition ($IL_n = 1$).

Appendix B

Expressions of the Average and RMS Currents in the Auxiliary Circuit of the Three-Switch ZCT Inverter

First, the I_{Load}>0 case, as shown in Figure 5.17(a), is considered. Over switching cycles, the currents in the auxiliary switch at turn-on are

$$I_{avg\_s\_on\_p\_3sw}(t) = I(t)\cdot T_o f_s/\pi \text{, and} \tag{B.1}$$

$$I_{rms\_s\_on\_p\_3sw}(t) = I(t)\cdot\sqrt{T_o f_s}/2. \tag{B.2}$$

The currents in the auxiliary diode at turn-on are

$$I_{avg\_d\_on\_p\_3sw}(t) = I_{avg\_s\_on\_3sw\_p}(t)/2 \text{, and} \tag{B.3}$$

$$I_{rms\_d\_on\_p\_3sw}(t) = I_{rms\_s\_on\_3sw\_p}(t)/\sqrt{2}. \tag{B.4}$$

The currents in the auxiliary switch at turn-off are

$$I_{avg\_s\_off\_p\_3sw}(t) = I_{x\_pk\_off\_3sw}(t)\cdot T_o f_s/\pi \text{, and} \tag{B.5}$$

$$I_{rms\_s\_off\_p\_3sw}(t) = I_{x\_pk\_off\_3sw}(t)\cdot\sqrt{T_o f_s}/2. \tag{B.6}$$

The currents in the auxiliary diode at turn-off are

$$I_{avg\_d\_off\_p\_3sw}(t) = I_{x\_pk\_off\_3sw}(t)\cdot T_o f_s/\pi \text{, and} \tag{B.7}$$

$$I_{rms\_d\_off\_p\_3sw}(t) = I_{x\_pk\_off\_3sw}(t)\cdot\sqrt{T_o f_s}/2. \tag{B.8}$$

Second, the I_{Load}<0 case, as shown in Figure 5.17(b), is considered. Over switching cycles, the currents in the auxiliary switch at turn-on are

$$I_{avg\_s\_on\_n\_3sw}(t) = I(t)\cdot T_o f_s/2\pi \text{, and} \tag{B.9}$$

$$I_{rms\_s\_on\_n\_3sw}(t) = I(t)\cdot\sqrt{T_o f_s}/(2\sqrt{2}). \tag{B.10}$$

The currents in the auxiliary diode at turn-on are

$$I_{avg\_d\_on\_n\_3sw}(t) = I_{x\_pk\_on\_n\_3sw}(t) \cdot T_o f_s / \pi \text{, and} \tag{B.11}$$

$$I_{rms\_d\_on\_n\_3sw}(t) = I_{x\_pk\_on\_n\_3sw\_n}(t) \cdot \sqrt{T_o f_s} / 2 . \tag{B.12}$$

The currents in the auxiliary switch at turn-off are

$$I_{avg\_s\_off\_n\_3sw}(t) = I_{x\_pk\_off\_3sw}(t) \cdot T_o f_s / \pi \text{, and} \tag{B.13}$$

$$I_{rms\_s\_off\_n\_3sw}(t) = I_{x\_pk\_off\_3sw}(t) \cdot \sqrt{T_o f_s} / 2 . \tag{B.14}$$

The currents in the auxiliary diode at turn-off are

$$I_{avg\_d\_off\_n\_3sw}(t) = I(t) \cdot T_o f_s / \pi \text{, and} \tag{B.15}$$

$$I_{rms\_d\_off\_n\_3sw}(t) = I(t) \cdot \sqrt{T_o f_s} / 2 . \tag{B.16}$$

Over the line cycle, the average and RMS currents of the auxiliary switch and diode are obtained as.

$$\begin{cases} I_{avg\_s\_3sw} = \int_0^{T/6} (I_{avg\_s\_sum}(t))dt \cdot 2/T \\ I_{rms\_s\_3sw} = \sqrt{\int_0^{T/6} (I_{rms\_s\_sum}(t))dt \cdot 2/T} \end{cases}, \tag{B.17}$$

and

$$\begin{cases} I_{avg\_d\_3sw} = \int_0^{T/6} (I_{avg\_d\_sum}(t))dt \cdot 2/T \\ I_{rms\_d\_3sw} = \sqrt{\int_0^{T/6} (I_{rms\_d\_sum}(t))dt \cdot 2/T} \end{cases}, \tag{B.18}$$

where

$$\begin{cases} I_{avg\_s\_sum}(t) = I_{avg\_s\_on\_p\_3sw}(t) + I_{avg\_s\_off\_p\_3sw}(t) \\ \qquad\qquad + I_{avg\_s\_on\_n\_3sw}(t) + I_{avg\_s\_off\_p\_3sw}(t) \\ I_{rms\_s\_sum}(t) = I^2_{rms\_s\_on\_p\_3sw}(t) + I^2_{rms\_s\_off\_p\_3sw}(t) \\ \qquad\qquad + I^2_{rms\_s\_on\_n\_3sw}(t) + I^2_{rms\_s\_off\_n\_3sw}(t) \end{cases}, \tag{B.19}$$

and

$$\begin{cases} I_{avg\_d\_sum}(t) = I_{avg\_d\_on\_p\_3sw}(t) + I_{avg\_d\_off\_p\_3sw}(t) \\ \qquad\qquad + I_{avg\_d\_on\_n\_3sw}(t) + I_{avg\_d\_off\_n\_3sw}(t) \\ I_{rms\_d\_sum}(t) = I^2{}_{rms\_d\_on\_p\_3sw}(t) + I^2{}_{rms\_d\_off\_p\_3sw}(t) \\ \qquad\qquad + I^2{}_{rms\_d\_on\_n\_3sw}(t) + I^2{}_{rms\_d\_off\_n\_3sw}(t) \end{cases}. \tag{B.20}$$

Thus, the RMS current flowing through the resonant capacitors is obtained as

$$I_{x\_rms\_3sw} = \sqrt{I^2_{rms\_d\_3sw} + I^2_{rms\_s\_3sw}}\ . \tag{B.21}$$

Appendix C

Expressions of the Additional Main Circuit Conduction Losses Caused by Soft Commutations in the Three-Switch ZCT Inverter

First, the I_{Load}>0 case, as shown in Figure 5.17(a), is considered. The additional main circuit conduction losses occur only at the turn-off: In the main switch during [t_5, t_6], and in the main diode during [t_7, t_8]. The time intervals of both shaded areas at the turn-off in Figure 5.17(a) are approximately equal, as calculated by

$$T_{sh\_p} = 2\cos^{-1}\left(\frac{I(t)}{I_{x\_pk\_off\_3sw}(t)}\right)\cdot\frac{T_o}{2\pi}. \tag{C.1}$$

The additional conduction energy loss in the main switch at I_{Load}>0 is

$$\begin{aligned} &E_{add\_s\_p\_3sw}(t) \\ &= 2\cdot\int_{\frac{T_o}{4}-\frac{T_{sh\_p}}{2}}^{\frac{T_o}{4}} \left(V_{ce\_s\_p\_3sw}\left(I_{x\_pk\_off\_3sw}(t)\sin\left(\frac{2\pi}{T_o}\gamma\right)+I(t)\right)\right., \\ &\left.-(V_t+R_{ce}I(t))\cdot I(t)\right)\cdot d\gamma \end{aligned} \tag{C.2}$$

where

$$V_{ce\_s\_p\_3sw} = V_t + R_{ce}\left(I_{x\_pk\_off\_3sw}(t)\sin\left(\frac{2\pi}{T_o}\gamma\right)+I(t)\right). \tag{C.3}$$

The additional conduction energy loss in the main diode at I_{Load}>0 is

$$\begin{aligned} &E_{add\_d\_p\_3sw}(t) \\ &= 2\cdot\int_{\frac{T_o}{4}-\frac{T_{sh\_p}}{2}}^{\frac{T_o}{4}} \left(V_{ak\_d\_p\_3sw}\left(I_{x\_pk\_off\_3sw}(t)\sin\left(\frac{2\pi}{T_o}\gamma\right)-I(t)\right)\right)d\gamma \end{aligned}, \tag{C.4}$$

where

$$V_{ak\_d\_p\_3sw} = V_f + R_{ak}(I_{x\_pk\_3sw\_off}(t)\sin(\frac{2\pi}{T_o}\gamma) - I(t)). \quad \text{(C.5)}$$

Second, the I_{Load}<0 case, as shown in Figure 5.17(b), is considered. The additional main circuit conduction losses occur at both turn-on and turn-off: In the main switch at the turn-on during [t_2, t_3], and in the main diode at the turn-off during [t_6, t_7]. The time intervals of the shaded areas at the turn-on and the turn-off in Figure 5.17(b) are approximately equal, as calculated by

$$T_{sh\_n} = 2\cos^{-1}(\frac{I(t)}{I_{x\_pk\_on\_n\_3sw}(t)}) \cdot \frac{T_o}{2\pi}. \quad \text{(C.6)}$$

The additional conduction energy loss in the main switch at I_{Load}<0 is

$$\begin{aligned} &E_{add\_s\_n\_3sw}(t) \\ &= 2 \cdot \int_{\frac{T_o}{4}-\frac{T_{sh\_n}}{2}}^{\frac{T_o}{4}} (V_{ce\_s\_n\_3sw}(I_{x\_pk\_on\_n\_3sw}(t)\sin(\frac{2\pi}{T_o}\gamma) + I(t)) \cdot \\ &-(V_t + R_{ce}I(t)) \cdot I(t)) \cdot d\gamma \end{aligned} \quad \text{(C.7)}$$

where

$$V_{ce\_s\_n\_3sw} = V_t + R_{ce}(I_{x\_pk\_on\_n\_3sw}(t)\sin(\frac{2\pi}{T_o}\gamma) + I(t)). \quad \text{(C.8)}$$

The additional conduction energy loss in the main diode at I_{Load}<0 is

$$\begin{aligned} &E_{add\_d\_n\_3sw}(t) \\ &= 2 \cdot \int_{\frac{T_o}{4}-\frac{T_{sh\_n}}{2}}^{\frac{T_o}{4}} (V_{ak\_d\_n\_3sw}(I_{x\_pk\_off\_3sw}(t)\sin(\frac{2\pi}{T_o}\gamma) - I(t))d\gamma \end{aligned}, \quad \text{(C.9)}$$

where

$$V_{ak\_d\_n\_3sw} = V_f + R_{ak}(I_{x\_pk\_3sw\_off}(t)\sin(\frac{2\pi}{T_o}\gamma) - I(t)). \quad \text{(C.10)}$$

Therefore, under threshold control, the main switch additional conduction power loss in the three phases is

$$p_{add\_s\_3sw} = 6(\sum_{n=N_{th}}^{N_S}(E_{add\_s\_p\_3sw}(\frac{n}{f_s}) + E_{add\_s\_n\_3sw}(\frac{n}{f_s}))/T. \quad \text{(C.11)}$$

The main diode additional conduction power loss in the three phases is

$$p_{add\_d\_3sw} = 6(\sum_{n=N_{th}}^{N_S}(E_{add\_d\_p\_3sw}(\frac{n}{f_s}) + E_{add\_d\_n\_3sw}(\frac{n}{f_s}))/T. \quad \text{(C.12)}$$

Vita

The author was born in Dayi, Sichuan, China. He received the B.S. degree (major in electric machines and control in the Department of Electrical Engineering, minor in electronics and computer technology in the Department of Automation) and the M.S. degree in power electronics, both from Tsinghua University, Beijing, China, in 1991 and 1993, respectively. From 1994 to 1995, he was a Lecturer in the Department of Electrical Engineering at Tsinghua University. From 1996 to 1997, he was a Demonstrator in the International Electric Vehicle Research Centre at The University of Hong Kong.

Since August 1997, he has been working towards the Ph.D. degree in the Virginia Power Electronics Center (VPEC) at Virginia Tech, which became the Center for Power Electronics Systems (CPES) in 1998. His research interests include power converters, three-phase inverters and rectifiers, motor drives, soft-switching techniques, digital controllers, and integrated power electronics systems.

The author is a member of IEEE.